Hypersonic Interference Aerothermodynamics

David Estruch-Samper

Submitted for the Degree of Ph.D.

Department of Aerospace Sciences
School of Engineering
Cranfield University
United Kingdom

2009

Cranfield
UNIVERSITY

School of Engineering
Department of Aerospace Sciences
Applied Aerodynamics Group

PhD Thesis

Academic Year 2009-2010

David Estruch-Samper

HYPERSONIC INTERFERENCE AEROTHERMODYNAMICS

Supervisors: Dr. N. J. Lawson and Prof. K. P. Garry

October 2009

For space exploration

"Why should we go into space? (...) Spreading out into space will have an even greater effect (referring to the discovery of America by Columbus in 1492). It will completely change the future of the human race and maybe determine whether we have any future at all. (...)
We could have a base on the Moon within 30 years and reach Mars in 50 years - with manned space flight."

Prof. Stephen Hawking on NASA 50th Anniversary Event, Washington, April 2008.

Abstract

When a vehicle travels at hypersonic speeds during launch, cruise or atmospheric re-entry it is subject to extremely high surface flow temperatures. As well as on the vehicle forebody, extreme heating can take place close to surface protuberances which are almost impossible to avoid in a real flight vehicle. These disturbances interfere with the freestream flow and result in complex viscous interactions which induce a local heat flux augmentation that can become detrimental to the integrity of the vehicle. A greater understanding of these flow phenomena is required.

This thesis develops the understanding of the behaviour of the flow around surface protuberances in hypersonic vehicles and presents an engineering approach to predict the location and magnitude of the highest heat transfer rates in their vicinity. To this end, an experimental investigation was performed in a gun tunnel at freestream Mach numbers of 8.2 and 12.3 and Reynolds numbers ranging from $Re_\infty/m=3.35x10^6$ to $Re_\infty/m=9.35x10^6$. The effects of protuberance geometry, boundary layer state, freestream Reynolds number and freestream Mach number were assessed. Further understanding of the flowfield was obtained through oil-dot visualisations and high-speed schlieren videos taken at frame rates of up to 50 kHz.

Results show the local interference interaction is strongly three-dimensional and is dominated by the incipient separation angle induced by the protuberance. In subcritical interactions - in which the incoming boundary layer remains unseparated upstream of the protuberance - the highest heating occurs adjacent to the device. In supercritical interactions - in which the incoming boundary layer is fully separated ahead of the protuberance - the highest heating generally occurs on the surface just upstream of it. An exception is for low-deflection protuberances under low-Reynolds freestream flow conditions in which case the heat flux to the side is greater.

Acknowledgements

During the course of this research project I have had the chance of working under Dr. David MacManus, Prof. em. John Stollery, and my supervisors Dr. Nicholas Lawson and Prof. Kevin Garry. It is their combined collaboration which has made this project possible. As well, I thank the technical staff of the Aerospace Sciences workshop for their assistance throughout the experimental programme, in particular Lynton Banks-Davies for the operation of the tunnel.

Finally, I want to dedicate this thesis to my family and closest friends.

Contents

List of Tables

List of Figures

Nomenclature

Latin symbols

a, b	correlation exponents
A	attachment location, m
	or area, m^2
C	correlation constant
C_∞	constant in temperature-viscosity law, (= 0.9)
C_D	drag coefficient, $= D/\left(0.5\rho u^2 A\right)$
C_f	friction coefficient, $= \tau_w/\left(0.5\rho_e u^2{}_e\right)$
C_H	heat transfer coefficient, $= q/\rho_\infty V_\infty c_p(T_{0\infty} - T_w)$
c_p	specific heat capacity at constant pressure, $J{\cdot}kg^{-1}{\cdot}K^{-1}$
C_p	pressure coefficient, $=\left(p - p_\infty\right)/\left(0.5\rho_\infty u_\infty^2\right)$
Ch	Chapman-Rubesin parameter, $=\left(\rho_w\mu_w\right)/\left(\rho_e\mu_e\right)$
d	distance , m
D	drag, N
	or diameter, m
D_i	mass diffusivity, $= \alpha / Le$
G	system gain, =2.06 at 0.1kHz – 5kHz signal frequency
h	protuberance height, m
H	total enthalpy, J
i	specific enthalpy, $J{\cdot}kg^{-1}$
I	pixel intensity, on a scale from 0 to 255
k	thermal conductivity, $W{\cdot}m^{-1}{\cdot}K^{-1}$
l	length or characteristic linear dimension, m
L	lift, N
	or separation length ahead of protuberance-plate junction, m
Le	Lewis number, $= \alpha / D$
M	Mach number, $= V/\left(\gamma RT\right)^{0.5}$
n	refractive index
Nu	Nusselt number, $= St\,\mathrm{Re}\,\mathrm{Pr}$
p	static pressure, Pa
P_D	drive pressure, Pa
Pr	Prandtl number, $=\left(c_p\mu\right)/k$
q	heat flux, $=\left(\sqrt{\rho c_p k}\right)_g \overline{V_2}\Big/\left(\alpha_R V_1 G\right)$, $W{\cdot}m^{-2}$
r	recovery factor, assumed r=1 in calculation of St

r_n	nose radius, m
R	gas constant, $=287.05\ J{\cdot}kg^{-1}{\cdot}K^{-1}$ or radius, m
Re	Reynolds number, $=\rho Ul/\mu$
Re/m	Reynolds number per unit length, $=\rho U/\mu$
Re_L	Reynolds number based on L, $=\rho_\infty U_\infty L/\mu_\infty$
$Re_{x,k}$	Reynolds number based on x_k, $=\rho_\infty U_\infty x_k/\mu_\infty$
$Re_{y,cl}$	Reynolds number based on y_{cl}, $=\rho_\infty U_\infty y_{cl}/\mu_\infty$
s	Reynolds analogy factor
S	separation location, m
St	Stanton number, $=q/\left(\rho_\infty U_\infty c_p\theta\right)$
t	time, s
T	temperature, K
U	longitudinal velocity, $m{\cdot}s^{-1}$
V	total velocity, $m{\cdot}s^{-1}$
V_1	initial voltage across gauge, V
$\overline{V_2}$	average output voltage of integrated signal across effective run duration, $V{\cdot}s^{-0.5}$
W	protuberance width, m
x	longitudinal distance, m
y	lateral distance from centreline, m
z	normal distance from flat plate, m

Greek symbols

α	protuberance deflection angle, *degrees* or thermal diffusivity, $=k/\left(\rho c_p\right)$
α_R	coefficient of resistivity, K^{-1}
$\overline{\chi}$	viscous interaction parameter, $=M_0^3\sqrt{Ch/\mathrm{Re}}$
δ	boundary layer thickness with edge at $U=0.99U_\infty$, m
δ^*	boundary layer displacement thickness, m
Δm	distance margin, m
ε	light deflection angle, *degrees*
ϕ	geometrical angle, *degrees*
γ	ratio of specific heats, = 1.4
μ	dynamic viscosity, $kg{\cdot}m^{-1}{\cdot}s^{-1}$ or Mach angle, *degrees*
θ	temperature relative to wall, $=T_{aw}-T_w$
$\varnothing$	diameter, m
ρ	density, $kg{\cdot}m^{-3}$
$\left(\sqrt{\rho c_p k}\right)_g$	thermal property of gauges, $J{\cdot}K^{-1}{\cdot}m^{-2}{\cdot}s^{-0.5}$
τ_w	surface shear stress, $=\mu_w\left(\partial u/\partial y\right)_w$
ω	exponential constant from $\mu\propto T^\omega$ $(\omega=0.76)$

Subscripts and Superscripts

1	upstream of shock
2	downstream of shock
∞	freestream conditions
*	reference value
ahead	ahead of protuberance
av	averaged
aw	adiabatic wall
axisym	axisymmetrical
cl	relative to centreline
coarse	coarse grid
e	conditions at boundary layer edge
eff	effective
exp	experiments
fplate	flat plate
gw	conditions of gas at the wall
h	based on protuberance height
i	referring to incipient conditions or to incompressible flow
k	relative to protuberance leading edge
lam	laminar conditions
le	relative to flat plate leading edge
max	maximum value
min	minimum value
n	nose
o	total or stagnation conditions, or initial conditions
prot	protuberance
r	recovery
rad	radiation
ref	reference value
run	referring to gun tunnel run
s	shock wave
side	to protuberance side
t	transition location
T	total
te	trailing edge
th	theory
turb	turbulent conditions
u	undisturbed conditions at protuberance location
w	conditions on the wall
x	based on local values

Abbreviations

BOS	background oriented schlieren
CARS	coherent anti-Stokes Raman spectroscopy
CCD	charge-coupled device
CFD	computational fluid dynamics
DGV	Doppler global velocimetry
L2F	laser-two-focus anemometry
LCT	liquid crystal thermography
LDA	laser Doppler anemometry
LED	light emitting-diode
LIF	laser induced fluorescence
MTV	molecular tagging velocimetry
PIV	particle image velocimetry
PLIF	planar laser induced fluorescence
PNS	parabolised Navier-Stokes
PSP	pressure sensitive paint
PTV	particle tracking velocimetry
RANS	reynolds averaged Navier-Stokes
SA	Spalart-Allmaras
SLR	single lens reflex
SST	shear stress transport
SWTBLI	shock-wave/turbulent boundary-layer interaction
TSP	temperature sensitive paint
VG	vortex generator

Coordinate System

The coordinate system uses as a reference the protuberance leading edge:

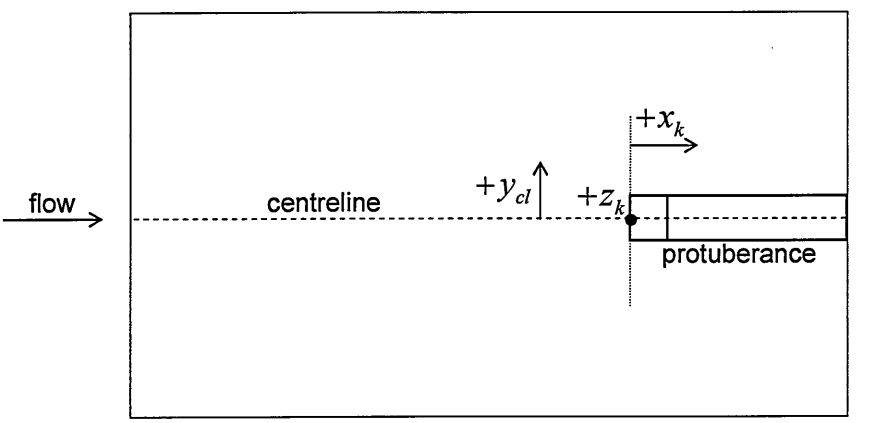

Terminology

The following terms are used to classify the interference interactions:

SUBCRITICAL: The incoming boundary layer remains unseparated upstream of the protuberance

SUPERCRITICAL: The incoming boundary layer is fully separated ahead of the protuberance

CHAPTER 1

Introduction

Forty years after man first stepped on the Moon there seems to be a re-surging interest in the exploration of space with proposed goals as challenging as building a base on the Moon and bringing man to Mars. These challenges, along with the continued aim of flying faster, are reviving interest in hypersonic transport vehicles and related hypersonic aerothermodynamics. As these vehicles travel at hypersonic speeds during their launch, cruise or/and re-entry phases, the high kinetic energy of the flow results in extremely high temperatures that dominate their design. While special consideration has typically been paid to the heating of the vehicle forebody where the stagnation of the flow results in very high heat transfer rates to the surface, extreme heating can also take place close to surface protuberances which interfere with the incoming flow and give rise to complex local viscous interactions (Fig. 1.1). The very high temperatures induced at the regions of the protuberances constitute one of the principal hazards regarding the safety of hypersonic vehicles.

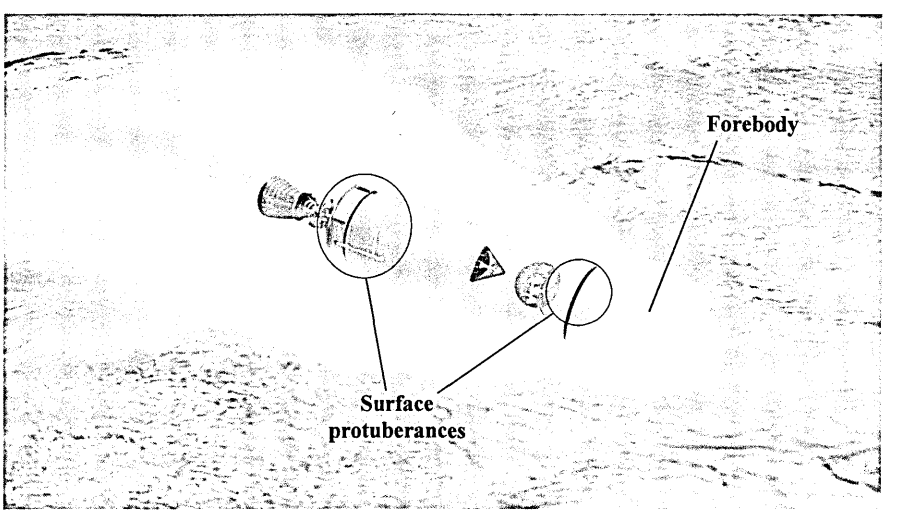

Figure 1.1 Artist's impression of ARES I Upper Stage vehicle during re-entry. ©NASA 2009

1.1 Context

Surface protuberances are frequently unavoidable in the design of hypersonic vehicles in the form of control surfaces but also as smaller elements of the order of the boundary layer thickness. As an example, Fig. 1.2 shows a close-up view to some of the protuberances on the ARES I launch vehicle, which is currently being developed by the National Aeronautics and Space Administration (NASA, USA) for the Constellation program, to replace the Space Shuttle program and to provide human access to low-Earth orbit, the Moon, and even Mars in a farther perspective (Davis, 2008). As shown in more detail in Fig. 1.3, protuberances on the ARES I vehicle surface are found as instrumentation and cable protection pads, stiffeners, control modules and motors, feed and drain lines, etc. In any of these forms, the protuberance interferes with the freestream flow and results in a three-dimensional interaction which may induce extremely high heat transfer rates that can become detrimental to the integrity of the vehicle. While the expected high heat flux rates on the actual protuberances can be tackled by the use of advanced heat-resistant materials, it is the heating of the vehicle surface which generally becomes a concern in practical engineering applications (Stollery et al., 2008). Being able to predict the heat flux at the location of surface protuberances is an important design aspect in the development of new-generation hypersonic vehicles (Huebner et al., 2009; Wang et al., 2009).

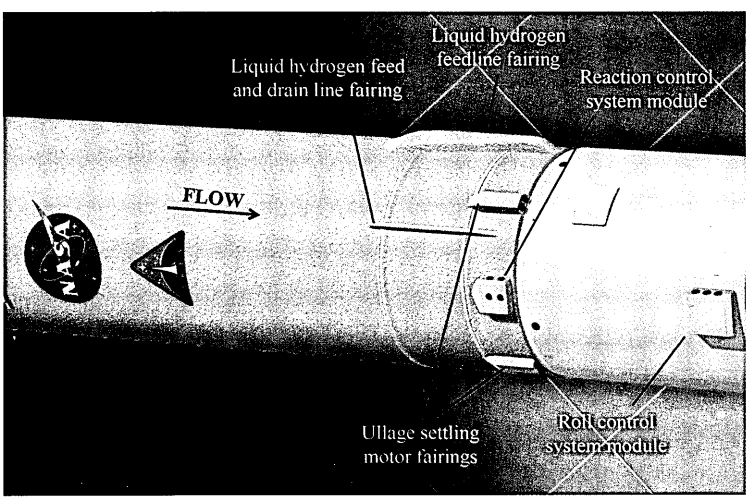

Figure 1.2 Close-up view to surface protuberances on ARES I Upper Stage vehicle. Based on original design by ©NASA 2009

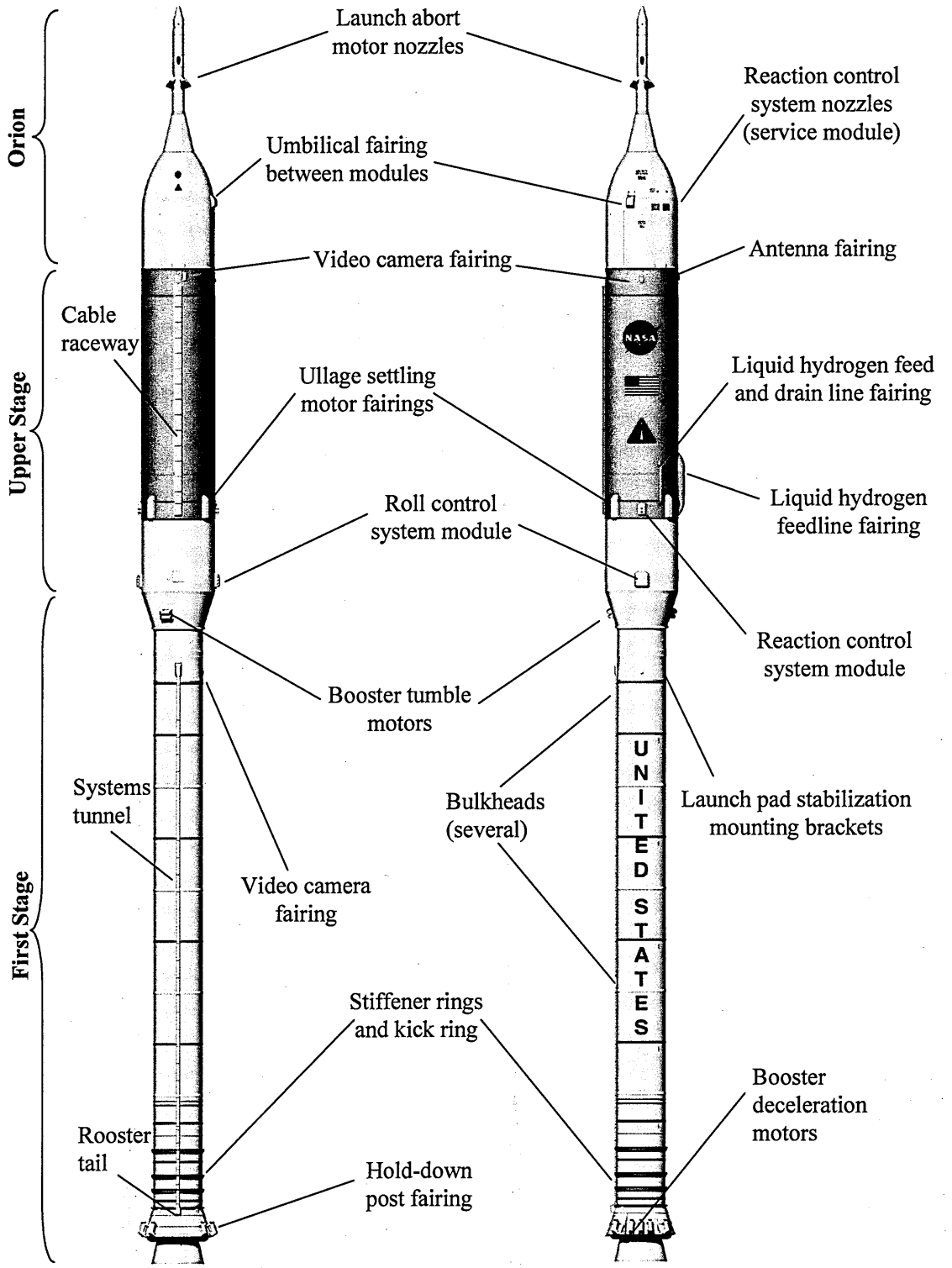

Figure 1.3 Surface protuberances on Ares I launch vehicle.
Based on original vehicle design by ©NASA 2009

1.2 Scope of the present investigation

The aim of the present work is to further develop the understanding of the behaviour of the flow around surface protuberances in hypersonic vehicles and the corresponding effects on the aerodynamic heating on the area surrounding the protuberance rather than on the protuberance itself.

The capability to predict computationally the heat transfer augmentation in interference regions is generally poor and therefore a greater understanding is required based on experimental studies. For this, an experimental program is carried out in the Cranfield University gun tunnel. The heat flux at different locations around the protuberances and at a range of different freestream conditions is measured by means of thin-film heat transfer gauges. A digital high-speed schlieren system is also developed to obtain flow visualisations that are used to determine unsteady features in the flow and to further explain the flow mechanisms around the protuberances. Oil flow visualisations are also obtained to determine the trajectory of the skin friction lines on the surface.

The case of three-dimensional compression ramps with finite span (W) and height (h) and semi-infinite length (l) is investigated in detail. The h/δ_u ratio of the datum configuration is 1 and the width is $W/\delta_u=2.7$. These dimensions are representative of generic surface protuberances such as those shown in Figs. 1.1 - 1.3, which are considered to have a height of the same order of the boundary layer thickness. This is expected for most of the cases regardless of the many different functions and shapes the protuberances may have. The different effects that are investigated are as follows:

i. The effect of h/δ_u and W/δ_u ratio
ii. Deflection angle effect
iii. Effect of forward deflection
iv. Effect of boundary layer state
v. Reynolds number effect
vi. Mach number effect

Through understanding of the flow field around these well-defined forms of protuberances and the effects on the local heat flux a generic engineering approach for predicting the induced heat flux augmentation to the surface surrounding the protuberances is developed. This approach provides rapid estimates of the location and magnitude of the hot spot in the vicinity of the protuberances for application during the different development phases of hypersonic vehicles, throughout which improved modifications are considered (e.g. to instrumentation, propulsion systems, control systems, etc.) which often imply changes to the vehicle's protuberances. Following the previous example, as it has been seen throughout the maturing design of the ARES I launch vehicle, the changes to the protuberances are sometimes quite significant (Huebner et al., 2009). In general, when protuberances cannot be avoided, their surface is kept smooth with the purpose of minimising their interference with the flow as for example done with the roll control system module (Fig. 1.4). However, no clear guidelines to predict or minimise the induced heat transfer to the surface seem to be established as yet and modifications are believed to be unfavourable in some cases. Hence, the work presented in this thesis addresses these problems as well by developing the aforementioned hot spot predictive approach.

As a whole, the present work contributes to the development of more efficient designs of future hypersonic vehicles in terms of reliability, time, cost but most importantly safety.

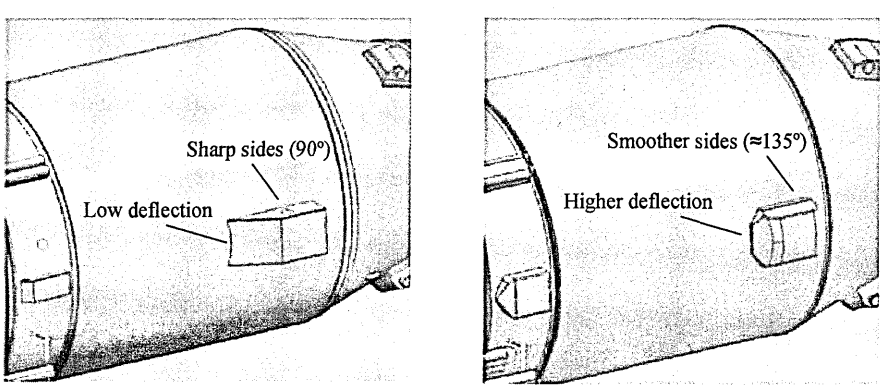

(a) Protuberance in preliminary test vehicle (b) Current protuberance design

Figure 1.4 Modified roll control system module on ARES I vehicle (Huebner et al., 2009). ©Elsevier 2009

1.3 Content

This thesis is divided into 9 chapters. Following the present introduction, Chapter 2 offers a review of background knowledge and existing literature relevant to this investigation. This is followed by a description of the experimental programme in Chapter 3 which also provides details on the flow diagnostic methods developed and applied. Chapter 4 goes on to present the part of the investigation that concerns heat flux in regions of attached flow. Since heat flux predictive methods for such cases are already available, this serves at the same time as a demonstration of the reliability of the experimental rig. After that, the results from the extensive experimental investigation on the interference interaction induced by surface protuberances are presented in Chapter 5. The development of the heat transfer predictive approach based on these results is then shown in Chapter 6, followed by a further insight into the behaviour of the flow field in such interactions in Chapter 7. This is followed by a further consideration of three specific protuberances in Chapter 8 which demonstrates the applicability of the method. Chapter 9 closes the study with the conclusions. Supporting documentation is presented in Appendices A – D.

CHAPTER 2

Background and Literature Review

In this chapter, an insight is given into the problem of hypersonic aerodynamic heating and its significance in the development of vehicles flying at hypersonic speeds. A review of literature regarding high aerodynamic heating regions in hypersonic flows is included followed by an overview of the role of experimental aerodynamics in hypersonic flow research. An outline of the main flow diagnostic techniques used in high-speed wind tunnel testing is also presented followed by a description of the current computational capability to simulate such flows. An overview of the current knowledge on hypersonic interference aerothermodynamics closes the chapter.

2.1 Hypersonic vehicles

When a vehicle flies at velocities faster than the speed of sound the flow disturbances it generates cannot travel upstream and result in the formation of shock waves through which static pressure and temperature are rapidly increased. At high supersonic velocities the high kinetic energy of the freestream flow results in particularly significant temperatures in a layer close to the surface. This is known as the thermal layer and is mainly caused by flow compression and skin friction (van Driest, 1956). The high temperatures in this layer may cause the molecules in the air to dissociate into atoms and to later ionise, sometimes even resulting in radiation effects. These effects are distinguished as a subset of supersonic flows known as the hypersonic flow regime. Hypersonic flow is generally considered as this that travels at velocities of Mach 5 or greater ($M_\infty \geq 5$).

Supersonic vehicles ($M_\infty > 1$) are generally slender and have sharp edges in order to avoid strong shock waves which may result in excessive pressure loads affecting their performance. Whereas pressure is the dominating flow property in the design of supersonic vehicles, hypersonic vehicles are generally considered to be temperature-dominated (Hirschel, 2007). This is because excessive thermal loads may not only become critical for the performance of the vehicle but also for its structural integrity (Bertin and Cummings, 2006). A well-known example is the disintegration of the Space Shuttle Columbia during re-entry in 2003 (Mazaheri and Wood, 2008).

Different aerothermodynamic effects may take place depending on the nature of the vehicle under consideration. A first distinction can be made between two main types of hypersonic vehicles: re-entry vehicles and cruise and acceleration vehicles (Fig. 2.1). The characteristics of re-entry vehicles are compared with those of cruise and acceleration vehicles in Table 2.1.

2.1.1 Re-entry vehicles

When a vehicle enters a planetary atmosphere this generally reaches high hypersonic speeds. The first known vehicle ever to reach hypersonic velocity was the WAC Corporal, a US Army rocket which in February 1949 was mounted on a German V2 rocket and launched to an altitude of 390 km reaching over 8200 km/h upon re-entry. The first manned re-entry vehicle however was not seen until 1961, when Yuri Gagarin piloted Russia's Vostok-1 reaching Mach 25 during its entry into the atmosphere. Other well known re-entry vehicles are NASA's Mercury, Gemini, and Apollo spacecrafts together with the Space Shuttle, the Russian Sputnik and Soyuz, the Chinese Shenzhou, and the European Atmospheric Re-entry Demonstrator (ARD), amongst others.

Re-entry vehicles can reach very high Mach numbers, up to approximately Mach 30 - e.g. the Apollo vehicle (Lee et al., 1970) - depending on their entry strategy. Since they need to be slowed down before reaching the ground, large drag (D) is usually preferred. In order to obtain high drag and low lift to drag ratios (L/D) re-entry vehicles are usually found at high angles of attack and thus in blunt configurations. This generally results in the appearance of strong detached shock waves with extremely high

temperatures downstream of the shock. Flow compressibility effects can thus become particularly critical, especially on the windward side of the vehicle. Due to the high temperatures, special account needs to be taken of possible dissociation and ionisation effects of the air around re-entry vehicles. Radiation effects, usually from the vehicle to the flow, also need to be considered at even higher temperatures.

2.1.2 Cruise and acceleration vehicles

Hypersonic cruise vehicles are aircraft-like vehicles designed to travel at altitudes generally up to 30 to 40 km and at maximum Mach numbers of about 8 (Polezhaev, 2000). The difference between hypersonic cruise vehicles and acceleration vehicles is that thrust needs to be constantly produced in the latter. In contrast to re-entry vehicles, cruise and acceleration vehicles generally require high L/D ratios, for which the drag needs to be minimised. They are therefore slender and fly at low angle of attack. Due to the lower Mach numbers and angle of attack in comparison with re-entry vehicles, the shock wave on the windward side of cruise vehicles is generally not so strong and real-gas effects are weaker. The flow field around this type of vehicle is generally dominated by viscous effects that may result in elevated surface temperatures especially in regions of viscous interactions (Boutry and Vital-Durand, 2003).

The first hypersonic cruise vehicle was the X-15 in 1959, which reached its top speed in 1967 when it flew at Mach 6.7 conditions and at an altitude of 31 km. The impact of the thermal loads on the vehicle was noticed by its pilots, who could hear the airframe cracking as it heated up and as some parts of the vehicle's skin glowed red (Thompson, 1992). The second time the X-15 was flown at Mach 6.7 conditions, excessive surface heating resulted in structural melting damage due to viscous interactions and the end of the X-15 programme (Watts, 1968a, 1968b). Further hypersonic research programmes have been carried out since then. Recent projects involving hypersonic cruise vehicles are the X-43 (NASA) and the X-51 (by NASA, DARPA and US air force), the Sharp Edge Flight Experiment (SHEFEX, by DLR) and the Sustained Hypersonic Flight Experiment (SHYFE, by QinetiQ, UK MoD), among others. Examples of accelerator vehicles are the National Aerospace Plane (NASP, by NASA) and Sanger (Germany).

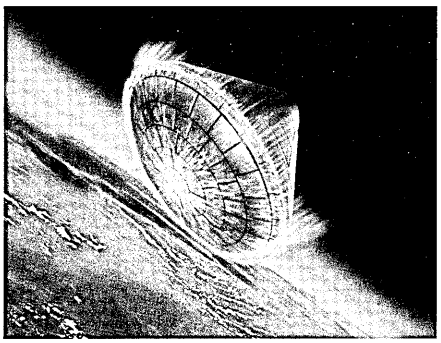

(a) ARD re-entry vehicle. ©ESA 1998

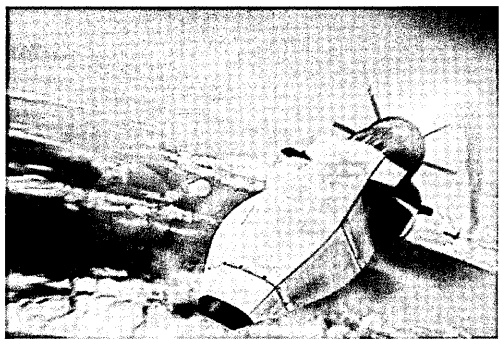

(b) X-51 cruise vehicle. ©NASA 2009

Figure 2.1 Sample re-entry and hypersonic cruise vehicles.

	Re-entry vehicles	Cruise and acceleration vehicles
Mach number	0-30	0-8
Configuration	Blunt	Slender
Angle of attack	Large	Small
Drag	Large	Small
Lift / Drag	Small	Large
Flight time	Short	Long
Dominating effects	Compressibility	Viscosity
Real-gas effects	Strong	Weak

Table 2.1 Characteristics of re-entry vehicles and cruise and acceleration vehicles.

2.2 Hypersonic aerodynamic heating

The area of fluid dynamics that studies the effects of aerodynamic heating at hypersonic speeds is known as aerothermodynamics. Despite the existence of aerothermodynamic theoretical and computational prediction methods, these are in general not sufficiently established for most current applications and experimental studies are routinely required (Gnoffo et al., 1999; Bertin and Cummings, 2006). An introduction to hypersonic aerodynamic heating together with a review on critical heating regions on hypersonic vehicles follows.

2.2.1 Aerothermodynamics

Aerothermodynamics considers the thermodynamics of high-speed air in which real-gas effects need to be taken into account due to the high temperatures present. Air is formed by molecular nitrogen (N_2, 78%) and molecular oxygen (O_2, 21%), argon, carbon dioxide and other spurious gases (Ar, CO_2 and others, 1%). At hypersonic speeds, air is heated close to the surface due to compressibility and viscosity effects. At sufficiently high temperatures, air molecules may become excited and dissociation and recombination effects take place. The gas will then become a mixture of molecules and atoms mostly of nitrogen and oxygen. At higher temperatures ionization is likely to occur. As shown in Section 2.1, these effects are of particular importance in re-entry vehicles.

Typical aerothermodynamic phenomena around hypersonic vehicles are shown in Fig. 2.2. These are mainly dependent on the flight Mach number, altitude, angle of attack and Reynolds number. The state of the surface viscous layer (i.e. the boundary layer) is a key aspect to determine the thermal state of the vehicle's surface. As a general rule, the thickness of this layer is directly proportional to the square of the Mach number and inversely proportional to the square root of the local Reynolds number: $\delta \propto M^2 \, \mathrm{Re}_x^{-0.5}$. Thick boundary layers are therefore generally found in hypersonic flows together with thin shock layers around the body which give place to strong viscous interaction effects.

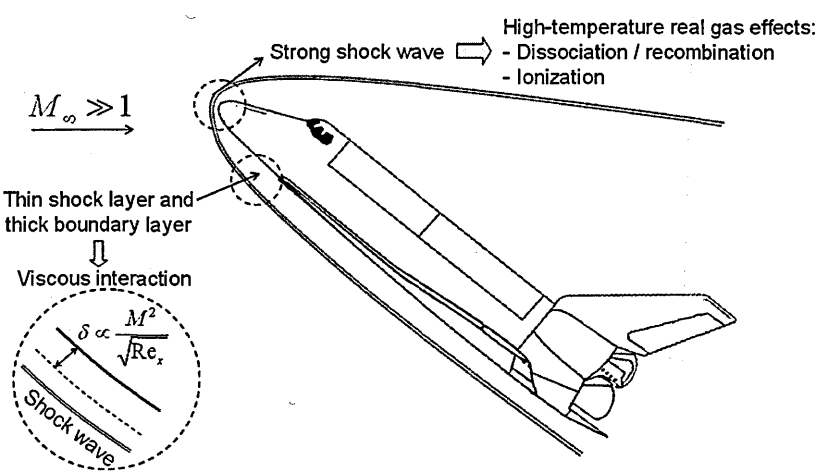

Figure 2.2 Basic aerothermodynamic flow features around a hypersonic vehicle. Example based on Space Shuttle vehicle.

2.2.2 Viscous flow layer

The boundary layer on a hypersonic vehicle governs the shear stress and the thermal state of the surface. At flight below approximately 50km of altitude the boundary layer is generally laminar only at the front of the vehicle and it transitions naturally to a turbulent state as the local Reynolds number increases (Anderson, 2006). Even in flight conditions in which the boundary layer may be laminar, this may be easily triggered to a turbulent state by small surface irregularities (Babinsky, 1994).

Whether the state of the boundary layer is laminar or turbulent generally has a significant effect on surface heating. Given that turbulent boundary layers have a fuller velocity profile than laminar boundary layers, the displacement and momentum thickness of a turbulent boundary layer in proportion to any characteristic length is smaller. The higher flow momentum close to the vehicle's surface in turbulent boundary layers generally results in higher wall shear stress and consequently in higher aerodynamic heating than when the boundary layer is laminar. A more detailed description of these effects can be found in the book by Hirschel (2007).

2.2.3 Thermal state of the surface

A significant part of the heat transported towards a hypersonic vehicle is transported by diffusion mechanisms towards the vehicle surface. The thermal state of a hypersonic vehicle's surface majorly depends on the temperature of the gas close to the wall and on the wall temperature. A heat flux normal to the surface, i.e. heat transferred over unit area per unit time, is generally considered to determine its thermal state, as shown in Fig. 2.3. In some cases, a radiation heat flux from the surface to the air can be considered (Anderson, 2006). The thermal state of the surface can then give an indication of the thermal loads on the vehicle, which also depend on the structure and materials used.

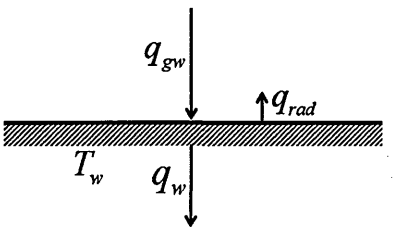

Figure 2.3 Schematic diagram of thermal state of the surface.

As the surface is heated up, the local boundary layer thickness increases and the turbulent skin friction decreases thus resulting also in a decrease in heat flux (Hirschel, 2007). Given that heat flux is a function of time, there may be a point when equilibrium is reached and no more heat is transferred to the surface. This takes place when the surface reaches the recovery temperature (T_r), which is in general slightly lower than the total temperature of the flow ($T_r \approx 0.9T_o$). An accurate prediction of the recovery temperature is not always possible.

2.3 Regions of high aerodynamic heating

High heat transfer rates on a hypersonic vehicle are generally found in the forebody or windward side, where stagnation regions may take place mainly due to the strong compression of the incoming flow (Fig. 2.4). High aerodynamic heating can also be found near surface discontinuities, in which strong interference effects may occur and give place to complex viscous interactions.

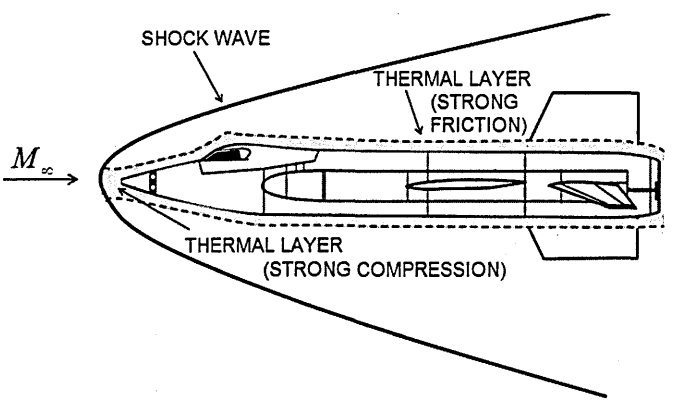

Figure 2.4 Aerodynamic heating caused by compression and friction effects. Example based on X-15 vehicle.

2.3.1 Forebody

In vehicles flying at zero angle of attack, stagnation conditions generally take place at the nose or forebody. As the flow moves away from the stagnation region, the heat flux over the surface generally decreases. Whereas robust theoretical models to predict stagnation heat flux in hypersonic dissociated air are available (Fay and Riddell, 1958), the trend followed by the heat flux downstream of the stagnation region is strongly dependent on the actual geometry of the forebody. A number of experimental investigations have been carried out in the past to determine the aerodynamic heating along different forebody geometries. Common geometries investigated have been hemisphere-cylinders, flat-faced cylinders and hemisphere-cones (Kemp et al., 1959; Crabtree et al., 1965). The trend of the heat flux along these geometries is shown in Fig. 2.5 based on previous experimental studies and non-dimensionalised with respect to the stagnation heat flux.

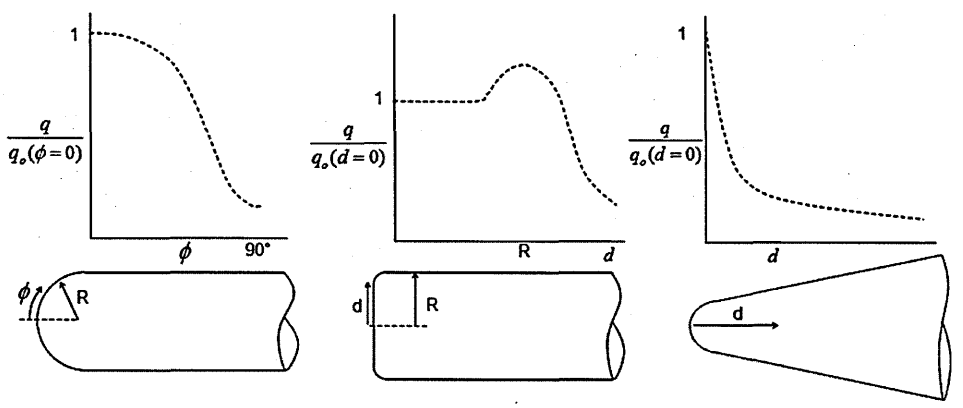

(a) Hemisphere-cylinder (b) Flat-faced cylinder (c) Hemisphere-cone

Figure 2.5 Typical hypersonic forebody geometries.

Early studies on hemisphere-cylinders were performed by Stine and Wanlass (1954) at supersonic Mach numbers (M_∞ = 2-3) and at laminar conditions. It was shown that for these geometries, the stagnation heat transfer (q_0) was lower for large leading edge diameters ($\varnothing_{le}$) according to the proportionality $q_0 \propto \varnothing_{le}^{-0.5}$ (van Driest, 1956). Further studies on hemisphere-cylinders were performed by Kemp et al. (1959) at Mach numbers between 7 and 14 and at laminar conditions. In their studies, a flat-nosed body with a corner radius of 1/4th of the cylindrical radius (R) was also investigated. Different semi-empirical methods to estimate the heat transfer to sharp cones, hemisphere-

cylinders and hemisphere-cones with different cone semi-angles (5° to 30°) in hypersonic flows (Mach 5 to 10) were developed by Crabtree et al. (1965). Similar studies were performed by Holden (1964) at Mach numbers of 7, 10 and 15.

More specific applications looked at conical aeroshell forebodies for investigations related to the Apollo entry vehicle (Lee et al., 1970). Other geometries which have received attention are cone-cylinder-flares and hemisphere-cylinder-flares (Coleman and Stollery, 1973). Further experimental measurements can be found in Holden and Moselle (1992), who put together a database of aerothermal measurements in hypersonic flows, including hemispherical noses under laminar and turbulent conditions at Mach 11, blunt cone forebodies under laminar and turbulent conditions at Mach 11-13 and large cone-flare models at Mach 11-16. Other specific forebody geometries such as biconic noses were also considered in their work.

2.3.2 Surface discontinuities

As well as on the forebody of a vehicle, high heat transfer rates can be found close to surface discontinuities that interfere with the incoming attached boundary layer. Not only can these irregularities provoke the transition of the boundary layer to a turbulent state when the incoming flow is laminar but they also can result in the presence of strong viscous effects that may induce high local heating.

2.3.2.1 Two-dimensional discontinuities

Common discontinuities found in hypersonic vehicles can be simplified in the form of two-dimensional rearward and forward facing steps, cavities, gaps, compression corners and protuberances (Nestler, 1985). Typical surface heating trends along these discontinuities are summarised in Fig. 2.6, where the local heat transfer rate (q) respect the undisturbed heat transfer (q_u) is plotted for turbulent interactions. In the case of forward-facing steps, large separated regions are found ahead of the protuberance. The heat flux in the separation region ahead of the protuberance is reduced in fully laminar interactions (Needham, 1965), but in contrast, for turbulent interactions a progressive increase in heat transfer is found from the location of separation with a second and more marked increase on the surface just ahead of the step, followed by a decrease in heat

flux downstream (Needham and Stollery, 1966a, 1966b). Some studies considering freestream laminar flow have reported an increase in heat flux along the separation region (Zakkay and Wang, 1973) believed to be due to the transitional behaviour of the boundary layer induced by the step and to the associated re-energising process. Such a difference between fully laminar and turbulent interactions is of high importance.

In rearward-facing steps, a low heat-transfer region appears on the surface just behind the step, followed by a slight increase as the boundary layer reattaches. Downstream of the reattachment region the heat flux starts approaching the undisturbed value. This is consistent with the case of a two-dimensional step, where similar effects as in the forward-facing step are found upstream of the protuberance and similar effects to rearward-facing steps are found downstream of it. It must be noticed that along the separated region the heat flux does not always follow a constant trend since this is strongly dependent on the number and location of vortices. The same is also observed in the case of cavity flows where, depending on cavity dimensions and incoming flow conditions, different recirculations may reattach inside the cavity and separate again (closed cavity flow) or skip the cavity and reattach at the other side (open cavity flow), giving place to different heat flux trends. The same is observed in the case of compression corners with turbulent boundary layer separation. In this case, an increase in heat flux is noticed as the incoming turbulent boundary layer separates from the wall followed by a much higher increase at the location of reattachment (Coleman, 1973b). Downstream of the reattachment region the heat flux starts decreasing until reaching similar values to the undisturbed heat flux. In the same way as in steps, in fully laminar separation regions the heat flux is decreased (Needham and Stollery, 1985) but transitional behaviour can be induced at reattachment just ahead of the ramp as suggested by the measurements from Holden (1964).

In conclusion, it must be taken into account that the heat transfer trend caused by surface discontinuities is principally sensitive to the separation and reattachment of the boundary layer to the surface as well as on its state (laminar/turbulent). The location and number of vortices in the flow is therefore a dominant aspect of these interactions. This is further complicated in surface protuberances given that these effects by themselves are three-dimensional and in many cases they are also fundamentally unsteady.

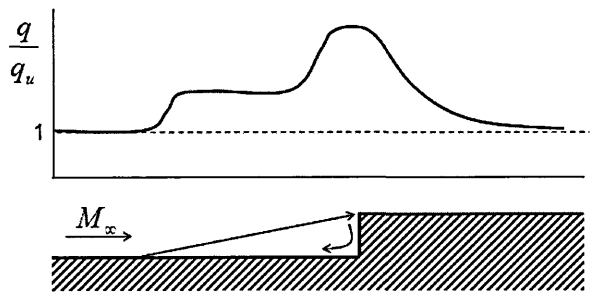

(a) Forward-facing step

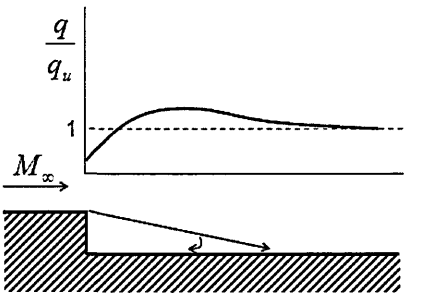

(b) Rearward-facing step

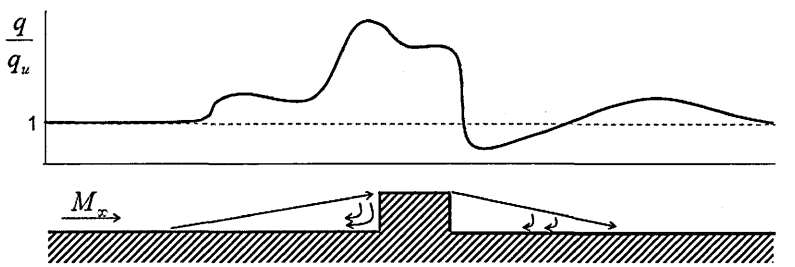

(c) Step

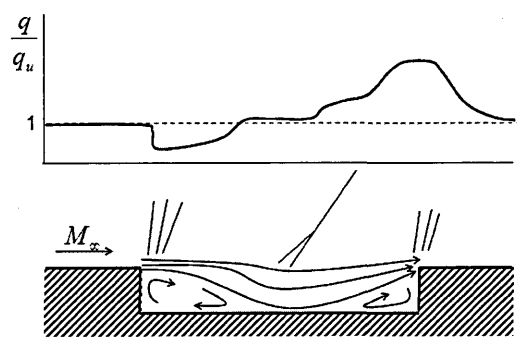

(d) Closed cavity flow

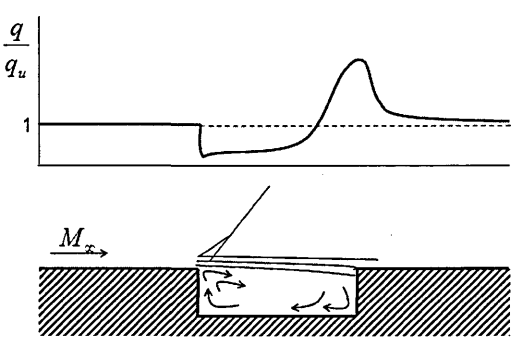

(e) Open cavity flow

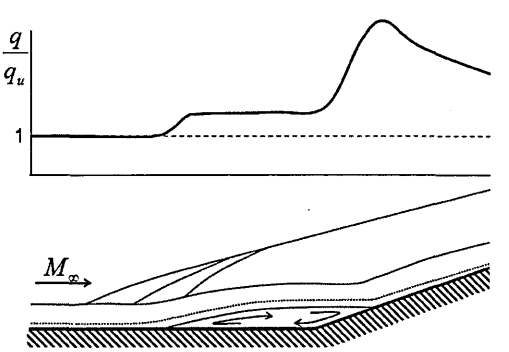

(f) Compression corner

Figure 2.6 Hypersonic flow in simple surface discontinuities under turbulent conditions.

2.3.2.2 Flow three-dimensionality around protuberances

In real applications, surface protuberances generally have markedly three-dimensional geometries. Given the complexity and three-dimensionality of the flow around them and due to the flow sensitivity to the specific geometry, no general approach to determine the heat flux in their vicinity has been derived to date (Truitt, 1965; Surber, 1965; Fox et al., 2001). A representation of the three-dimensional flow field around a blunt fin and a cylinder is shown in Fig. 2.7. The appearance of a horseshoe vortex in the separated region is seen in both cases followed by secondary vorticities. Similar vortex systems were noticed by Giles and Thomas (1966) and Stainback and Weinstein (1967) around blunt swept and unswept fins. These vortices, together with the appearance of a complex shock structure ahead of the model, dominate the three-dimensionality of the flow field and thus the distribution of the thermal heating on the surface surrounding the protuberance.

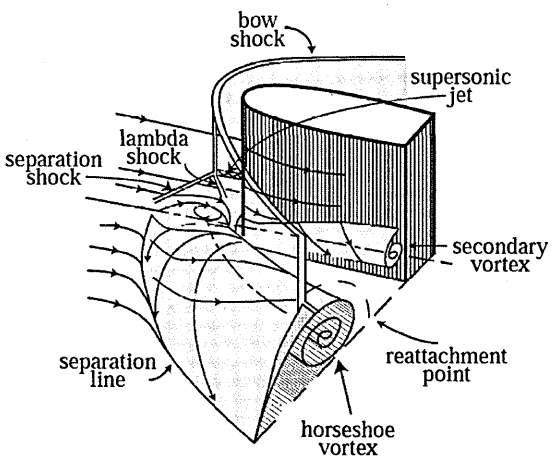

(a) Flow around a blunt fin (Houwing et al., 2001). ©Springer 2001

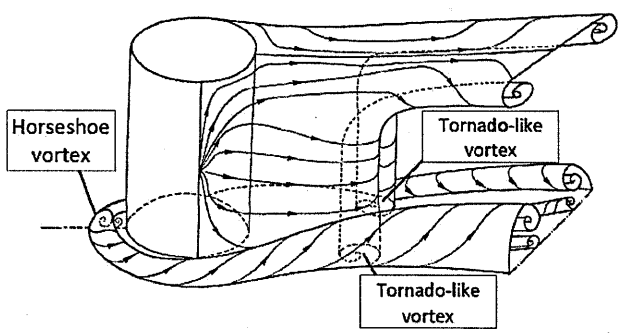

(b) Flow around a cylinder (Delery, 2001). ©Onera 2001

Figure 2.7 Features associated with hypersonic flow over surface protrusions.

Examples of different possible vortical structures ahead of protuberances are also shown in Fig. 2.8 for the case of cylinders on a flat plate based on the work by Sedney and Kitchens (1977). The appearance of one, two or three pairs of vortices upstream of the protuberance is observed. In regions of flow separation, low heat transfer is present whereas in reattachment regions the heat flux to the surface is high (Sedney, 1973).

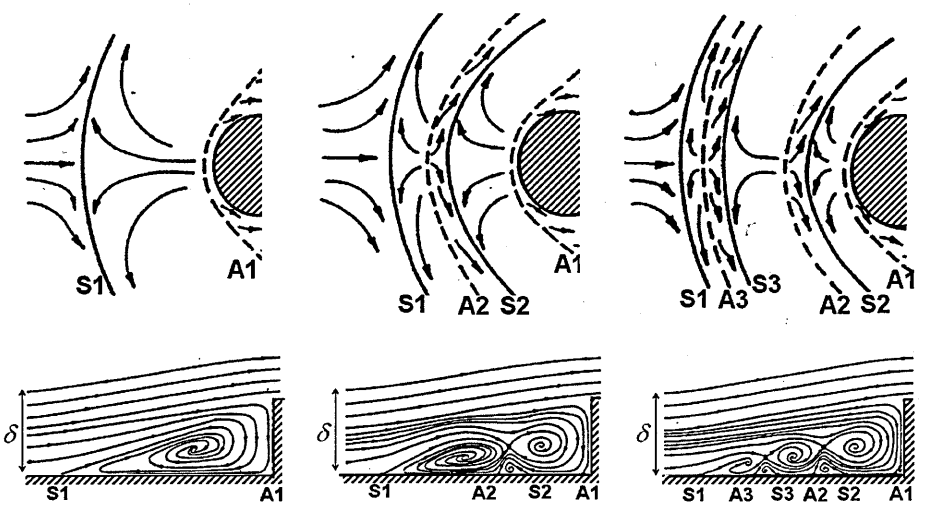

(a) 2 vortices (b) 4 vortices (c) 6 vortices

Figure 2.8 Possible flow structure upstream of a cylinder. Separation=S and Attachment=A. Based on the findings by Sedney and Kitchens (1977).

2.3.2.3 Region of separated flow

The increased heat flux in interaction regions is thus clearly linked to the separation and reattachment of the flow. For example, the typical trend in skin friction, pressure and heat flux on a compression corner interaction with a turbulent separated boundary layer is shown in Fig. 2.9 based on the results of Stollery and Coleman (1975). A correlation between pressure and heat flux along the separated region is observed. The skin friction in the separated region is indicated as negative to represent the upstream influence of the flow. These trends show that the highest pressure and heat flux take place on the compression ramp but they do not reflect the sharp heat flux peaks that occur in front of the discontinuity in some cases (Nestler, 1985).

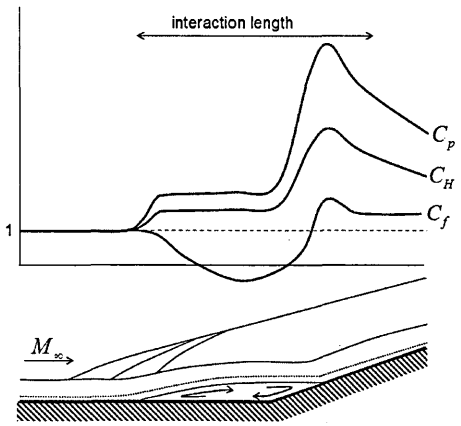

Figure 2.9 Pressure, heat flux and friction coefficients on 2-dimensional compression ramp for turbulent flow.

Large stand-off distances are present ahead of supercritical protuberances (i.e. with upstream boundary layer separation), that is in relation to the usually much lower stand-off distances ahead of simple hypersonic blunt geometries, e.g. 0.08r for the case of a sphere with radius r at Mach 8.9 (Miller, 1975). For example, Burbank et al. (1962) measured the heat transfer in the vicinity of a 2-inch by 4-inch (50.8mm x 101.6mm) rectangular stiffener at high supersonic speeds (Mach 3.5) under turbulent flow and observed interactions of approximately 3 times the height of the protuberance (Fig. 2.10). Larger interactions of up to 6 times the height of the protuberance were observed in further studies on 2-dimensional steps at higher Mach numbers as shown in Fig. 2.11, based on Nestler (1985). Increased heat transfer rates take place along these large separation regions. Upstream of the separation and downstream of the reattachment the heat transfer becomes similar to the undisturbed flat plate value.

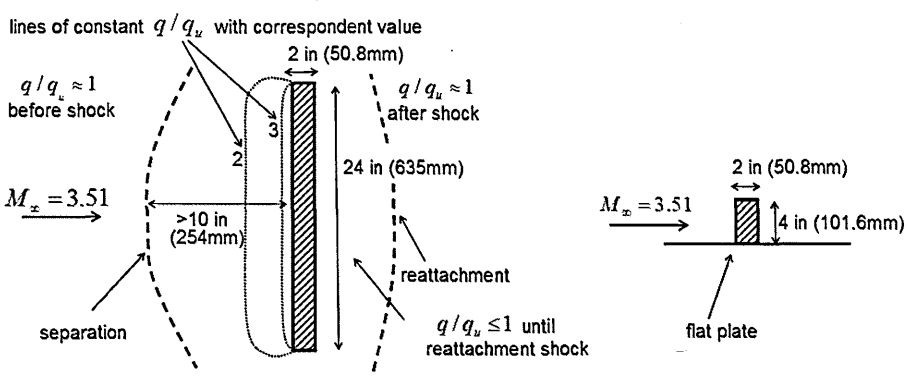

(a) Plan view (b) Side view of the model

Figure 2.10 Heat transfer in the vicinity of a stiffener, based on Burbank et al. (1962). Turbulent flow.

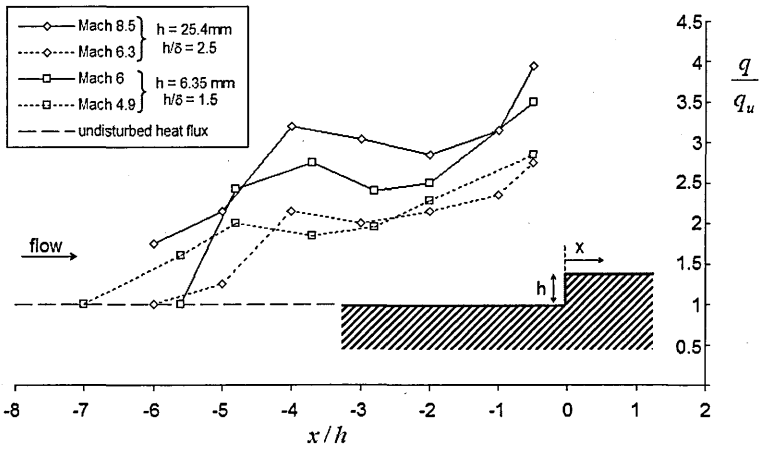

Figure 2.11 Heat transfer ahead of hypersonic 2-dimensional steps in turbulent flow, based on the work by Nestler (1985).

2.3.2.4 Effect of protuberance h/δ ratio

As well as the freestream properties, including those of the incoming boundary layer, the ratio between protuberance height (h) and local boundary layer thickness (δ_u), h/δ_u ratio, has been shown to have a strong effect in some cases on the heat transfer around surface protuberances (Nestler, 1985). Hung and Patel (1984) measured the heat transfer in the vicinity of cylindrical and rectangular protuberances and showed the effect of h/δ_u ratio on their heat transfer measurements at a freestream velocity of Mach 5.3. In their work, distinction was made between tall ($h>2Ø$ or $h>2W$), short ($h<Ø$ or $h<W$) and wide protuberances ($Ø \rightarrow \infty$ or $W \rightarrow \infty$, i.e. quasi-two-dimensional). Their main results showed that the highest heat transfer in the vicinity of tall protuberances is independent of their height (h) whereas around short and wide protuberances this is independent of the width or span (W) but strongly dependent on the protuberance height. Figure 2.12 shows the correlation of the results from Hung and Patel (1984) for turbulent interactions plotting the ratio of maximum interference heat transfer rate over undisturbed heat transfer versus the h/δ_u ratio for each protuberance to show this effect. Further consideration to the different type of interactions is taken in Section 2.6.

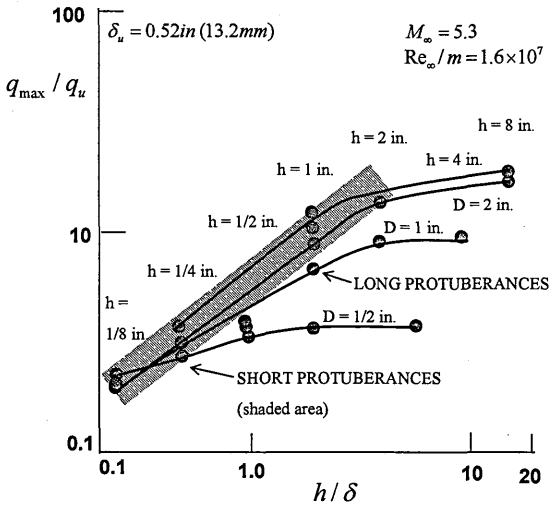

Figure 2.12 Correlations for short protuberances in turbulent flow, based on the results of Hung and Patel (1984).

2.3.2.5 Previous experimental studies on protuberances

Previous experimental studies on the aerodynamic heating caused by surface protuberances in high-speed flows are listed in Table 2.2. Most of the studies consider freestream Mach numbers of 5 or higher and have been carried out with freestream Reynolds numbers between $Re_\infty/m = 1x10^6$ and $3x10^7$. In the cases where laminar incoming boundary layers are considered, investigations are often based on the effectiveness of the protuberances being used as boundary layer trips. Some of them consider irregularities such as sinusoidal waves which may appear on the surface of high-speed vehicles due to expansion or contraction of the surface material during changing temperatures. Investigations with turbulent incoming boundary layers have mostly considered swept and unswept blunt fins, cylindrical protuberances, forward and rearward steps, blocks and wedges, for example. The measurement region considered in these studies is also indicated in Table 2.2: on the protuberance (prot) or/and on the surface around the protuberance (surf).

Incoming b.l.	Configuration	M_∞	Measurement	Reference
Lam	Different roughness elements (e.g. spheres, cylinders, wire) as trip elements on a 5° semi-angle blunt cone.	8	Surf	Stainback (1969)
Lam	Different roughness elements (e.g. spheres, triangular rods, spherical rods) on a flat plate and on a 20° wedge.	6	Surf	Sterret et al. (1967)
Lam	Different roughness elements on a 9° semi-angle blunt cone.	8	Surf	Nestler (1982)
Lam	Sinusoidal waves on flat plate.	8	Prot	Weinstein (1970)
Lam	Sinusoidal waves on flat plate.	20	Prot	Arrington (1968)
Lam	Swept fin on a 9° semi-angle blunt cone.	10	Prot	Bramlette et al. (1975)
Lam/Turb	Small steps and sinusoidal wave on plate.	7, 10	Surf/Prot	Bertram and Wiggs (1963)
Lam/Turb	Sinusoidal waves on a plate.	2-10	Prot	Bertram et al. (1967)
Lam/Turb	Waves, grooves and steps on flat plate, cylinder and delta wings.	7-15	Surf/Prot	Jaeck (1966)
Lam/Turb	Cylinder on flat plate.	5	Surf/Prot	Hung and Clauss (1980)
Lam/Turb	Cylinders and blocks on flat plate.	5	Surf/Prot	Hung and Patel (1984)
Lam/Turb	Sinusoidal waves on flat plate.	6	Prot	Cary and Morrisette (1968)
Turb	Blunt fin on flat plate.	6	Surf	Neumann and Hayes (1981)
Turb	Fin on a 5° semi-angle blunt cone.	5	Surf/Prot	Gillerlain (1975)
Turb	Fin on tunnel wall.	5	Surf	Winkelmann (1972)
Turb	Blunt fin on flat plate.	8	Surf	Wang et al. (1998)
Turb	Blunt swept fin on a cone and a 6° semi-angle blunt cone.	2-5	Prot	Coleman and Lemmon (1973)
Turb	Blunt swept fin on a 10° semi-angle blunt cone.	2-4	Prot	Lemmon and Coleman (1973)
Turb	Blunt swept fin on tunnel wall.	2-5	Surf/Prot	Price and Stallings (1967)
Turb	Swept cylinders, stiffeners, 30° ramp and blocks on a flat plate.	3-4	Surf/Prot	Burbank et al. (1962)
Turb	Blunt swept fin on a flat plate.	6	Surf/Prot	Jones (1964)
Turb	Sinusoidal waves on a flat plate.	6	Surf/Prot	Watts and Olinger (1968)
Turb	Cylinders on plate.	3, 4	Surf/Prot	Burbank and Strass (1958)
Turb	Forward and rearward steps.	2	Surf	Gadd et al. (1960)
Turb	Forward steps.	8	Surf	Shifen and Qingquan (1990)
Turb	Sinusoidal protuberances on a flat plate.	3	Surf	Shore et al. (1963)

Table 2.2 Experimental studies on surface protuberances in supersonic/hypersonic flow.

2.4 Experimental methods in hypersonic flow research

Several hypersonic research flight programmes have been carried out to date with the purpose of developing the technologies necessary to establish hypersonic flight. However, real flight projects are limited by their complexity and high costs involved. Most of the data on hypersonic flows generated to date have been obtained from ground facility testing. Despite the increasing use of computational fluid dynamics (CFD) as reviewed in Section 2.5, ground-test experimental studies are still of high importance in hypersonic flow research for both data generation and validation of numerical results.

2.4.1 Ground facility simulation

The most commonly used ground test facilities in hypersonic flow research are cold hypersonic wind tunnels (Needham, 1963). The main limitation of these, however, is their inability to simulate either the high temperatures or the high Reynolds numbers generally present in real hypersonic flight. Despite early concerns that low-temperature wind tunnel data would not be applicable to real hypersonic vehicles, this was proven wrong by the X-15 flight data, which showed excellent agreement with the pressure and force predictions from wind tunnel tests (Thompson, 1992).

In heat transfer studies, the wall heat flux is in most cases assumed to be equal to the heat flux in the gas at the wall. As explained in the previous sections, in some real flight conditions, real-gas effects which are not reproducible in low-temperature facilities may be present and give place to a radiation heat flux emanating from the vehicle. The heat flux predictions obtained in these facilities are thus of a conservative nature given they do not account for energy radiation effects from the vehicle to the surrounding air. Following the previous example, the X-15 flight data showed that the heat flux during hypersonic flight was about 35% lower than predicted by the well-established semi-empirical models of Eckert (1955) and van Driest (1956).

A restricted number of high-enthalpy hypersonic tunnels exist which may simulate real gas effects. However, these have significant operational and interpretational limitations and so they are only considered useful in most cases in hypersonic combustion studies where high-energy conditions are present such as in scramjet combustor development (Becker, 1968; Smart and Suraweera, 2009). Low-temperature hypersonic wind tunnels are therefore the accepted generic tool in fundamental applications such as this considered in the present work.

2.4.2 Simulation of turbulent flow

A common constraint of cold wind tunnels is that they generally provide laminar conditions as a consequence of the usually low Reynolds numbers. When turbulent conditions need to be reproduced the transition of the boundary layer from laminar to turbulent has to be forced. This can be usually done by placing either distributed or discrete roughness trips close to the leading edge of the model. The trip effectiveness depends strongly on its geometry and on the local Reynolds number (Thyson et al., 1978; Nestler, 1982). The effect of h/δ_u ratio - h being in this case the height of the tripping element - has also been observed to have a strong effect in some cases (Schrijer, 2003).

Boundary layer trips may also result in spanwise non-uniformities which affect the recreation of a homogeneous turbulent flow (Stainback, 1969; Sedney, 1973). In ideal applications, spanwise distortions need to be kept to a minimum and a fully developed turbulent boundary layer should be achieved (Sterret et al., 1967; Nestler, 1985). Further details on the effectiveness of boundary layer trips in hypersonic flows can be found in the studies by Stainback (1969), Schrijer et al. (2004) and Berry and Horvath (2007). While the forced transition of the boundary layer is known to be subject to a number of different factors such as freestream Reynolds number, Mach number and incoming boundary layer momentum thickness among others, all these investigations agree on the fact that there is an apparent compromise between trip effectiveness and the creation of spanwise non-uniformities. A careful selection of the boundary layer trip needs therefore to be made when a fully turbulent boundary layer is to be recreated.

2.4.3 Flow diagnostics

Different flow diagnostics have been developed to date with the purpose of obtaining information from hypersonic flows such as pressure, density, velocity, temperature and species concentrations. Such methods are generally restricted by the short test durations - generally a few milliseconds - and small test regions, which constrain models to small scales and thus require high spatial resolution and fast response systems. The application of optical diagnostics, which allow non-intrusive imaging and data recording from the flow is furthermore limited by the high velocity, strong gradients and restricted optical access generally encountered. The main flow diagnostics used in high-speed wind tunnel testing are described in this section. A more detailed review on the development of optical measurement techniques and their application to supersonic and hypersonic aerospace flows in recent years can be found in Estruch et al. (2009a).

2.4.3.1 Qualitative and semi-quantitative diagnostics

Qualitative diagnostics such as oil-flow visualisations are used to obtain qualitative information from the flow. In this technique, a suitable mixture is placed on a surface prior to testing and its displacement due to wall shear stress can reveal the trajectory of the skin friction lines. The most common qualitative and semi-quantitative flow diagnostics are shadowgraph and schlieren, which are based in the concept of light refraction (Hayes and Probstein, 1959; McIntyre et al., 2007). Interferometry is also sometimes used to image phase changes in the light which depend on flow density. In shadowgraph, a beam of collimated light is directed to the flow and visualisations in the form of a flow field shadow are obtained (Porcar and Prenel, 1982). Density gradients in the flow cause a deflection (ε) of the light beams which results in an image with darker or lighter regions (Wood et al., 1988). The deflection of the light (ε) depends on an index of refraction which in its simplest definition is dependent on the local fluid density (ρ). Shadowgraph is considered to be proportional to the second derivative of local density ($d^2\rho/dy^2$) and is generally sensitive to flows with large density gradients (Pianthong et al., 2003). Its main disadvantages are that weak density gradients such as these through expansion regions cannot be easily distinguished and there is no direct geometric correlation between the test region and its shadow (O'Byrne et al., 1999).

In the schlieren technique a spatial filter is used to select the direction of the density gradients sensitivity and to obtain image intensity proportional to the first derivative of the density gradient ($d\rho/dy$) (Fig. 2.13). Schlieren visualisations offer a geometrically correct image based on the density gradients averaged through the test section. A more detailed explanation of these techniques can be found in the literature by Shapiro (1953), Liepmann and Roshko (1957) and Settles (2001).

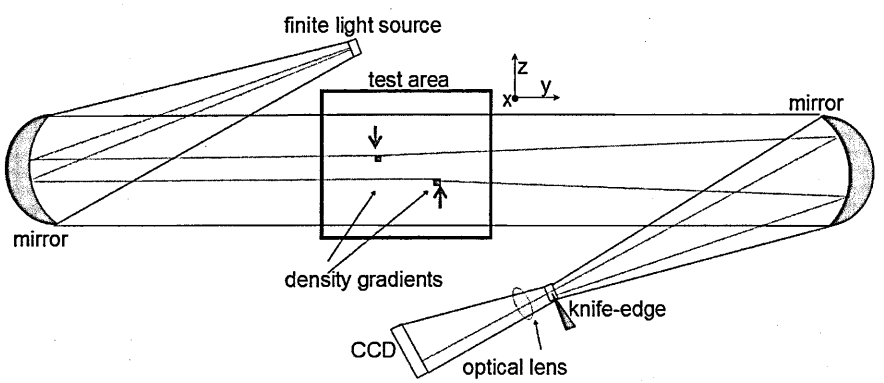

Figure 2.13 Schematic diagram of a two-mirror Z-type Toepler schlieren system.

2.4.3.2 Quantitative diagnostics

Measurement of quantitative flow data in hypersonic facilities is most commonly performed through intrusive methods. In most applications measurements are performed by monitoring the voltage across variable resistors designed to have resistance values proportional to the measured property. Laser-based techniques that are gaining importance due to their ability to yield non-intrusive velocity data are laser Doppler anemometry (LDA), particle image velocimetry (PIV), particle tracking velocimetry (PTV), Doppler global velocimetry (DGV) and laser-two-focus anemometry (L2F). Despite being generally established for the investigation of supersonic flows, limited applications have been performed on hypersonic flows. This is partly due to the difficulty in seeding this type of flow with solid or liquid particles, which is required by these techniques. Light reflections are another common difficulty in such methods and need to be avoided in order not to damage the recording device and retain data quality (Hamel et al., 2001).

Whereas LDA and L2F yield high accuracy and spatial resolution velocity measurements from a point in the flow, PIV offers measurement of the velocity of the flow either in a plane or from a volume in its most advanced form. Two or three velocity components can be measured depending on the system. A review on this technique can be found in Grant (1997), Adrian (2005) and more recently in Raffel et al. (2007). Similarly to PIV, PTV measures velocity data in a planar or volumetric region but with the difference that the latter tracks the particles individually in time and space (Adrian, 1991). Another technique is DGV, which offers three-dimensional velocity data from a plane in the flow (Ainsworth et al., 1997). This has not had so many applications given that it generally requires one view for every different component of the velocity and thus a more complex imaging system than PIV.

Other optical laser-based diagnostics are the MTV, RELIEF and PLIF techniques, which are based on the insertion of a fluorescent agent or dye in the fluid and also yield velocity data. In these techniques, the fluorescent dye absorbs the laser light energy and reemits it at a different wavelength, which is then collected by the receiving apparatus and used for obtaining the required data (Gochberg, 1997). Fluorescence techniques may offer quantitative data typically in terms of concentrations, temperatures and velocity from the flow. PLIF can also measure temperature, pressure and species concentrations in a plane in the flow.

Other optical methods are based on spectroscopy. These include Raman spectroscopy and CARS, which measure temperature and species concentrations, and Rayleigh spectroscopy, which measures temperature and pressure. These techniques can be applied to both reacting and non-reacting flows and their main advantage is that the flow does not need to be seeded but instead is based on the molecular properties of the gas.

A schematic diagram based on the comprehensive review of non-intrusive techniques and their application to supersonic and hypersonic flow in Estruch et al. (2009a) is shown in Fig. 2.14 with a classification of these techniques according to flow property measured and degree of optical complexity.

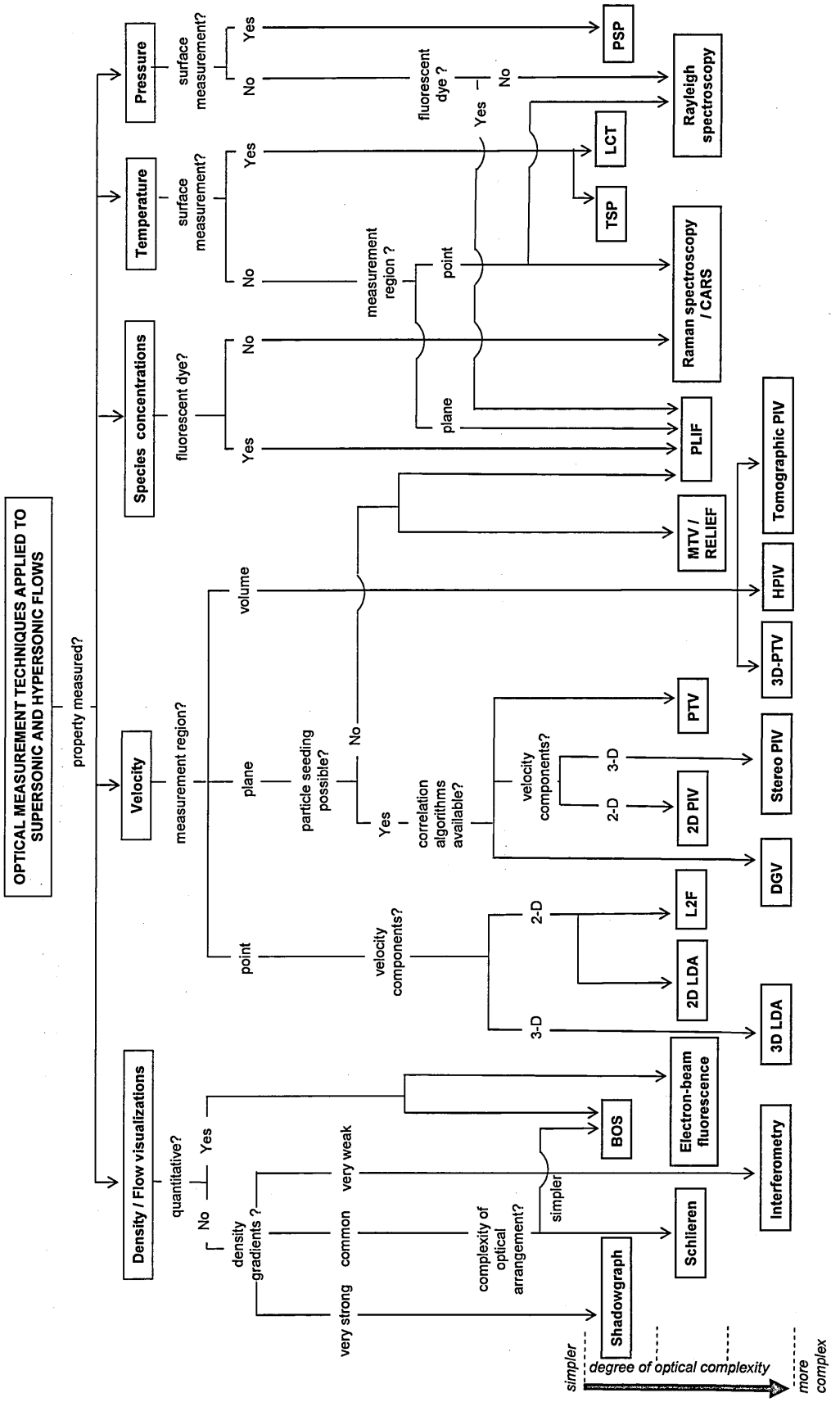

Figure 2.14 Main optical techniques applied to supersonic and hypersonic flows, reproduced from Estruch et al. (2009a). ©ASCE 2009

2.5 CFD studies of hypersonic flows

Computational Fluid Dynamics (CFD) simulations are today extensively used in aerospace engineering to obtain numerical predictions of high-speed flows (Hung and MacCormack, 1976; Brenner et al., 1993; Birch et al., 2001; Hirsch, 2007). However, the application of CFD to hypersonic flows is not fully established in many aspects.

2.5.1 Current CFD capability

Different CFD codes have been used to date in studies involving hypersonic flows. The commercial package Fluent is certainly the most commonly used at present for generic low-speed applications (Estruch and Elsari, 2007); however, its suitability for hypersonic flow studies is not well established given the limited applications that have been performed to date (Lofthouse et al., 2002; Savino and Paterna, 2005 and Menezes et al., 2005). Other codes that have been used for the study of hypersonic flows are based on the Parabolised Navier-Stokes equations (PNS), which neglect the streamwise diffusion and unsteady terms from the complete Navier-Stokes equations (Ludlow et al., 2001a, 2001b; Shoesmith et al., 2006). Recent studies have demonstrated their applicability to hypersonic flows but as with Fluent the number of investigations are very limited (Birch et al., 2001). Another commercial code which is starting to show particular suitability for the study of hypersonic flows is Cobalt (Srinivasan and Bowersox, 2004); however, previous applications of Cobalt to predict hypersonic heat transfer do not appear to be available in the literature.

In general, regardless of the code employed, the computation of hypersonic heat transfer with suitable accuracy is more difficult than this of the surface pressure to the same accuracy and very fine computational grids are necessary to accurately represent the large velocity and temperature gradients normal through the surface boundary layer (Stetson, 1992). Further complications come when turbulent flows need to be simulated since turbulence models are generally not validated for the prediction of heat transfer in hypersonic flow (Rumsey, 2009).

2.5.2 CFD studies on interference heating

Since early studies by Polak (1974) and Pai (1978) the heat transfer in regions of separated flow has been found to be generally subject to very large underprediction errors, i.e. with computational predictions usually falling well below corresponding experimental results. Since then, the number of CFD studies that have looked at the surface heat transfer induced by protuberances in hypersonic flows has been very limited. One relevant study is by Grotowsky and Ballmann (2000) on laminar hypersonic forward and backward facing steps. Another more recent study was on the Space Shuttle Orbiter plug repair protuberances, which consisted of swept cylinder models with short rounded protuberances ($h/\delta < 0.3$) under Mach 11.5 laminar flow (Mazaheri and Wood, 2008). In both cases the flow features and pressure along the surface were well predicted but significant errors in the prediction of wall heat flux were observed. The same was also observed in the results by Gaitonde and Shang (1993) on 2-dimensional blunt body and compression corner flows and by Knight et al. (1995) on impinging shock-wave/boundary-layer interactions (SWTBLIs).

The application of CFD to predict hypersonic heat transfer is thus clearly subject to large uncertainties in regions of separated flow. Since the heat flux augmentation in interference interactions occurs in such regions, the current CFD capability to predict hypersonic interference heat transfer is not considered sufficiently well established so as to perform a consistent investigation of interference interactions. This is even subject to higher errors if turbulent flows are considered. It is therefore essential to reach a further understanding based on experimental investigations. To this end, the present investigation is principally carried out from an experimental approach. A complementary computational study on the interference interactions considered in the present work was performed by Haas (2009). Among the different possible approaches reviewed in Section 2.5.1 the commercial code Cobalt was identified as the most suitable for the present application. Further details on this computational work are presented in Appendix D where the significant limitations of numerical studies for such applications are outlined.

2.6 Hypersonic interference heating

The relevant background on hypersonic interference aerothermodynamics has been presented. It has been shown that the interference of the flow at the location of surface protuberances on both re-entry and acceleration vehicles can induce very high heat transfer rates to the surface and become critical to their integrity. The current capability to predict the heat flux in interference regions is poor and therefore a better understanding of the mechanisms that induce the local heat flux augmentation in the vicinity of surface protuberances is required.

2.6.1 Current understanding

The main concluding points based on the background and literature review are the following:

i. The highest heat flux usually takes place on the protuberance; however, since protuberances can be made of advanced heat-resistant materials in practical design applications it is the very high heat flux to the surface surrounding the protuberance which is usually of the highest concern.

ii. Most relevant studies to date have considered interactions induced by two-dimensional discontinuities such as compression ramps and steps. There are some physical mechanisms of interactions causing boundary layer separation upstream – referred in this work as supercritical interactions – which are not totally understood as yet. The current semi-empirical and computational capability to predict the heat flux to the surface in these cases is also limited.

iii. The interaction induced by protuberances such as blunt fins and cylinders is strongly three-dimensional and the increase in heat flux occurs over the region of separated flow. This is in turn an even more complex flow case than this in 2-dimensional discontinuities and the understanding of the local heat flux augmentation is further limited.

iv. The interaction induced by a surface protuberance depends on protuberance geometry (height, diameter/span, etc.) and on freestream conditions (thickness and state of the incoming boundary layer, Reynolds number, Mach number, etc.). A number of different parameters are therefore involved in these interactions.

v. Very few experimental investigations have measured the surface heat flux induced by three-dimensional protuberances on hypersonic flows. That together with the large number of parameters involved in these interactions has hindered the development of a generic heat flux predictive approach to date. The current knowledge in this area is thus limited.

vi. Careful consideration of the measurement techniques to be applied in the investigation of such flows needs to be taken. The application of optical methods to hypersonic gun tunnels is generally restricted by the very short run duration of these facilities, restricted optical access and strong gradients in the flow, among other reasons. Non-intrusive measurement of the surface heat transfer can be further complicated if different Reynolds and Mach number flows are to be studied.

2.6.2 Interference heating prediction

Despite the effort in developing empirical or semi-empirical correlations that provide heat flux predictions for simple protuberance geometries (Murphy, 1965), these are generally limited by the dearth of experimental data (Hung and Patel, 1984; Nestler, 1985). In some correlations, the peak heat transfer is assumed as a reference, but given the complex three-dimensionality of the flow and the measurement resolution restrictions caused by the size and location of the gauges, erroneous peak heating values are suspected to have been considered in some studies as noticed by Neumann and Hayes (1981). In addition, correlations are also limited by the number of parameters

considered and in many cases measurements are non-dimensionalised without a total understanding of the actual dependence on the reference value. For example, Fig. 2.11 presents the heat flux measurements ahead and along two-dimensional steps as the ratio between local heat flux and the corresponding undisturbed heat flux; however, the dependence on the undisturbed heat flux is not totally clear. This implies that the non-dimensioning of the heat flux routinely performed in previous studies does not always have a physical explanation and therefore care needs to be taken in the misconceptions induced when interpreting such results since direct scaling rules are unlikely to be obeyed (Truitt, 1965; Surber, 1965). Other studies that non-dimensionalise the measurements with respect to the stagnation heat flux are also subject to the same limitations.

One of the main difficulties in the development of a generic predictive approach that can be used for different type of protuberances is the very different geometries that these can have. As mentioned in Section 2.3, a suitable distinction among three different types of protuberances was made in the work of Hung and Patel (1984) and Nestler (1985). Distinction was made between long ($h>2Ø$ or $h>2W$), short ($h<Ø$ or $h<W$) and large protuberances ($Ø \to \infty$ or $W \to \infty$, i.e. quasi-two-dimensional). In the present work it has been preferred to refer to these protuberances as tall, short and wide respectively, but the same definitions are followed. As summarised in Fig. 2.15, the following effects on the peak heat transfer are expected:

i. *Tall protuberances* ($h>2Ø$ or $h>2W$):
   The peak heat flux in their vicinity is independent of protuberance height.
   The effect of protuberance width/span is unclear.

ii. *Short protuberances* ($h<Ø$ or $h<W$):
   The peak heat flux in their vicinity is independent of protuberance width/span.
   The highest heat flux increases with protuberance height.

iii. *Wide protuberances* ($Ø \to \infty$ or $W \to \infty$):
   As in short protuberances, the magnitude of the peak heat flux is strongly dependent on protuberance height.

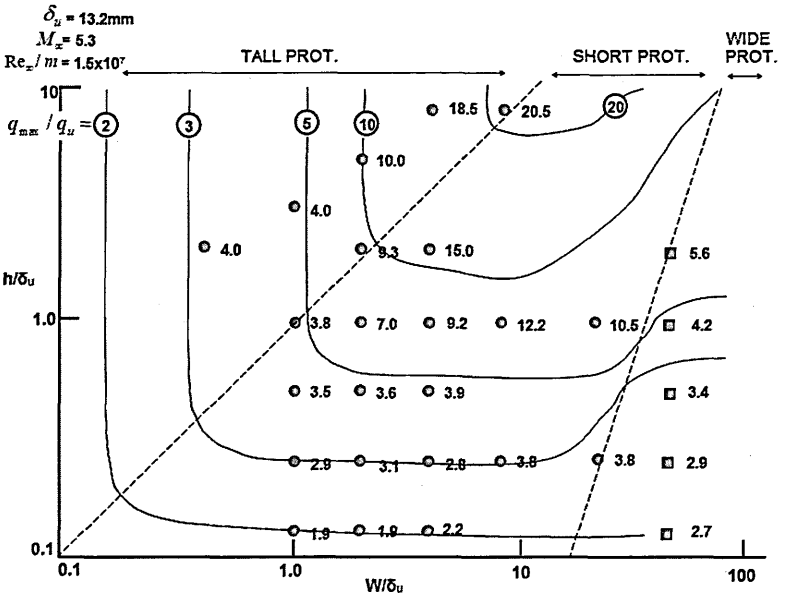

Figure 2.15 Effect of h/δ_u and W/δ_u ratios on peak heat flux in the vicinity of a protuberance under turbulent flow based on experiments from Hung and Patel (1984).

Overall, previous experimental studies have shown that the local interaction induced by the presence of a protuberance in hypersonic flow depends mainly on its geometry and on the freestream flow conditions. Nevertheless, most studies to date have considered tall protuberances in the form of control surfaces and a generic predictive approach is not available due to the lack of experimental data encompassing all the main parameters involved (Nestler, 1985). To this end, using a hypersonic gun tunnel, the present investigation presents an experimental dataset of heat flux measurements in the vicinity of surface protuberances from a Mach 8.2 and 12.3 flow. In particular, 3-dimensional short compression ramp protuberances with finite span and of the order of the boundary layer thickness are considered to represent generic protuberance geometries such as those shown in Chapter 1. Further details on the investigation are given in the following chapter, where the experimental programme is described.

CHAPTER 3

Experimental Programme

An extensive experimental investigation was performed in the Cranfield University gun tunnel. A description of the experimental programme comprising the design of the models and the development of the measurement diagnostics applied is included in this chapter. High-resolution quantitative heat flux measurements were performed by means of thin-film gauges and further understanding of the flowfield was obtained through oil-dot visualisations and high-speed schlieren videos taken at frame rates of up to 50 kHz.

3.1 Hypersonic gun tunnel

Gun tunnels were first developed by the Ames Aeronautical Laboratory in U.S.A. (Eggers et al., 1955) and have since then been the most common tool used to reproduce hypersonic flow conditions for ground testing (Section 2.4). The Cranfield University gun tunnel is a one-shot, blow-down wind tunnel capable of simulating hypersonic flow conditions for durations of the order of a few milliseconds. As in all hypersonic facilities, the available optical access is limited and fast-response measurement systems are necessary principally due to the short durations and high speed of the flow. Further details on this facility can be found in Needham (1963).

3.1.1 Operation

A schematic diagram of the Cranfield University gun tunnel is shown in Fig. 3.1, followed by two photographs in Figs. 3.2 and 3.3. This facility comprises a high-pressure reservoir at one side ($0.113m^3$) and a vacuum dump tank at the other end ($8.5m^3$). The drive of the tunnel is the high pressure air, which is compressed up to 2000 psig ($13.8x10^6$ Pa) in the reservoir. A double diaphragm arrangement separates the high pressure vessel from a shock-compression tube. The two diaphragms used are made of aluminium and their thickness is designed so that they break when the pressure across them is slightly over half of the pressure in the drive tank. Before starting the tunnel, air is compressed to the driver pressure inside the high pressure reservoir and to half of this pressure between the two diaphragms, while inside the barrel air is still at atmospheric conditions. Both diaphragms are subject to half of the driver pressure. The tunnel is subsequently started by venting the air between the two diaphragms causing their immediate rupture.

The gas in the compression tube has an initial volume of $0.032m^3$ (6.096m-long and 81.39mm in diameter). An aluminium piston (100gr mass and 81.38mm-diameter) placed at the beginning of the tube is accelerated after the rupture of the diaphragms and compresses the initially atmospheric air in the barrel. This compression process gives rise to multiple shock reflections between the blanked end of the barrel and the piston increasing both the temperature and pressure of the gas in a highly non-isentropic manner. The piston then comes to rest close to the end of the barrel when the pressures at both sides of it become equal. At the end of the barrel a convergent-divergent nozzle is connected to the wind tunnel test section and then to a dump tank. Before each test the nozzle, test section and dump tank are evacuated to about 50Pa by a vacuum pump. A tape diaphragm is placed at the inlet of the nozzle in order to stop air flowing inside the test section prior to the run. This provides a sufficiently strong start pressure ratio through the nozzle throat. When the high-pressure high-temperature air in the shock tube breaks the tape diaphragm, air flows through the nozzle and produces a uniform hypersonic flow stream in the open jet test section. Air is then dumped into the vacuum tank and evacuated to the atmosphere immediately after each run.

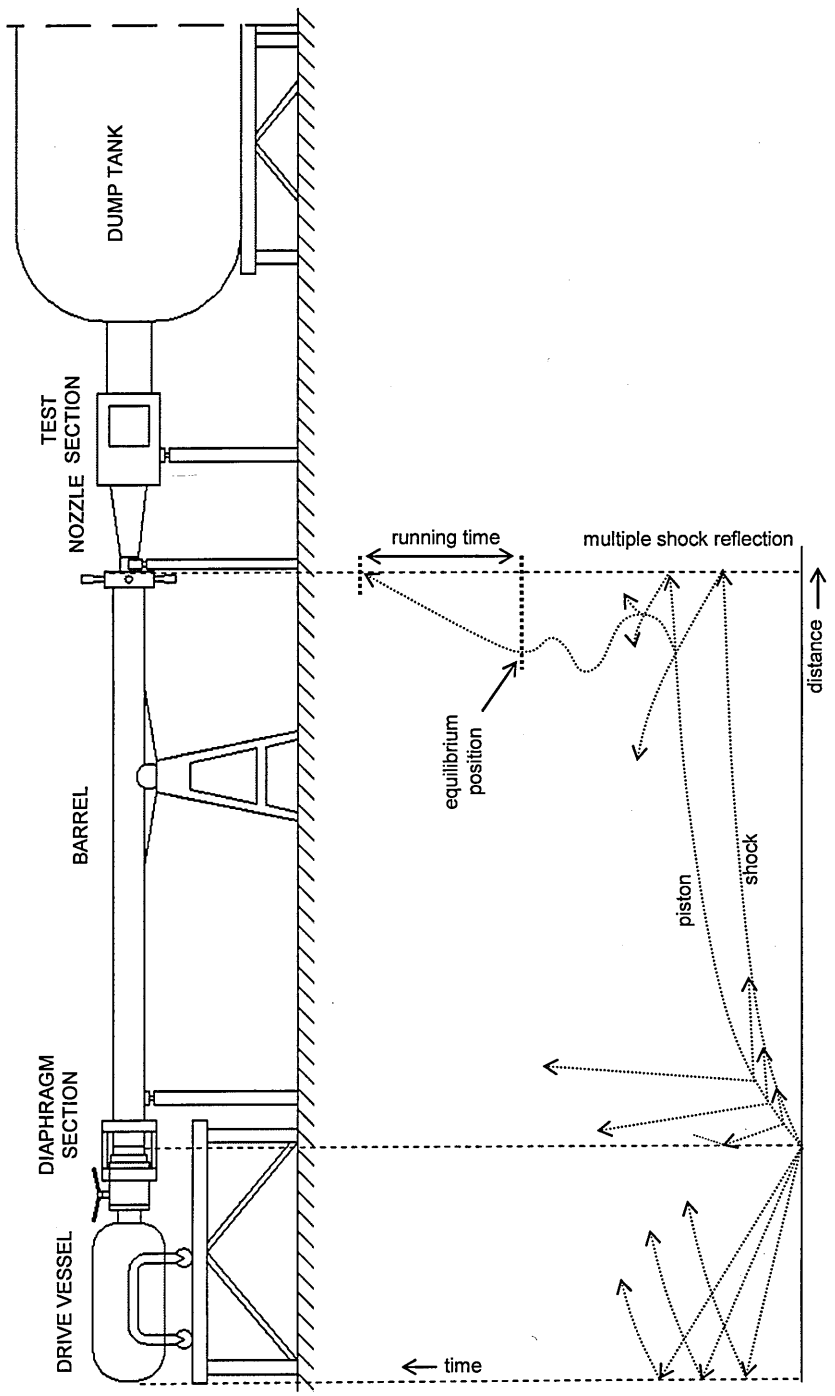

Figure 3.1 Schematic diagram of Cranfield University Hypersonic gun tunnel.

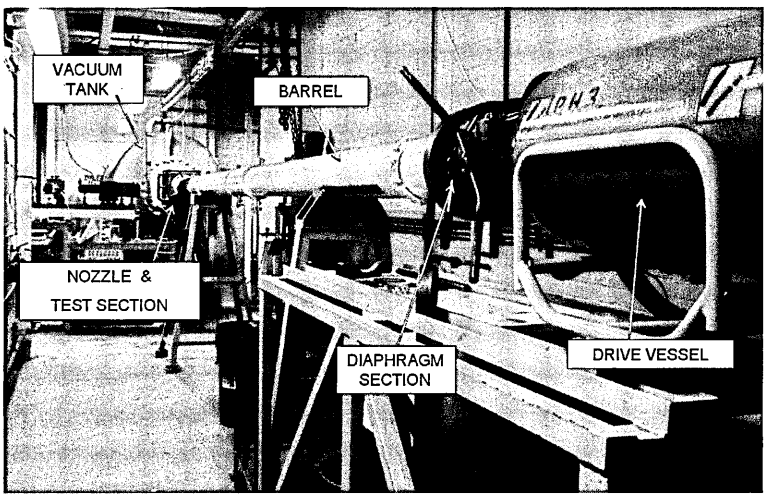

Figure 3.2 Photograph of Cranfield University Hypersonic gun tunnel.

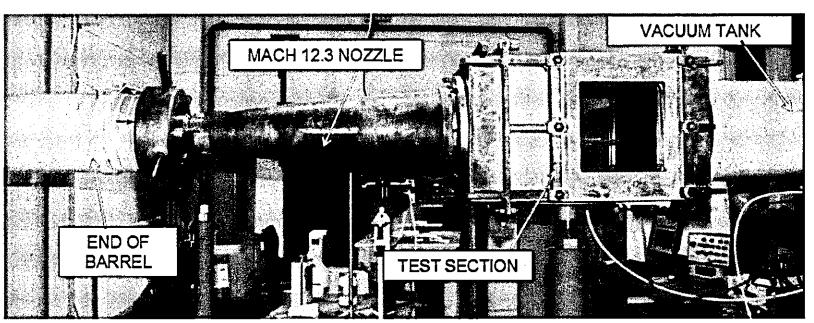

Figure 3.3 Close up view to test section of Cranfield University Hypersonic gun tunnel with Mach 12.3 nozzle on.

3.1.2 Test conditions

Two different nozzles are available at present which allow obtaining Mach 8.2 and Mach 12.3 freestream conditions. The duration of the effective hypersonic flow varies depending on the nozzle used and on the operating conditions (which were changed by using different driver pressures) in such a way that reduced throat diameters (i.e. higher flow Mach numbers) provide longer duration running times (Table 3.1).

Depending on the operating Mach number and on the reservoir pressure, different Reynolds number conditions can be simulated. The initial barrel pressure was atmospheric for all the tests. At a freestream Mach number of 8.2, $Re_\infty/m=4.84x10^6$ ($T_\infty=56.8K$) is obtained with drive pressures of 500 psig ($3.5x10^6$ Pa), $Re_\infty/m=6.57x10^6$ ($T_\infty=72.0K$) at 1000 psig ($6.9x10^6$ Pa), $Re_\infty/m=8.06x10^6$ ($T_\infty=81.7K$) at 1500 psig

($10.3x10^6$ Pa) and $Re_\infty/m=9.35x10^6$ (T_∞=89.3K) at 2000 psig ($13.8x10^6$ Pa). At Mach 12.3 conditions, $Re_\infty/m=3.35x10^6$ (T_∞=41.3K) is obtained at 2000 psig ($13.8x10^6$ Pa). Lower driver pressures are not used at Mach 12.3 conditions due to the extremely low temperatures and pressures of the hypersonic jet which could lead to air liquefaction and possible damage to the facility and instrumentation. At freestream Mach numbers of 8.2 and 12.3 and Reynolds numbers ranging from $Re_\infty/m=3.35x10^6$ to $Re_\infty/m=9.35x10^6$ natural transition of the boundary layer does not occur as also found in a number of previous studies in the same facility (Coleman, 1973b; Vannahme, 1994). The boundary layer thus needs to be tripped if turbulent conditions are to be simulated (Section 2.4).

A list of the test conditions used in the present study is shown in Table 3.1. The initial wall temperature during the tests was T_w =295±5 K. The rapid establishment of the flow (1-2 ms) - even in cases involving strong separation regions - was assessed from the high-speed schlieren results during all the tests. Although flat plate measurements were performed at a drive pressure of 500 psig ($3.5x10^6$ Pa), these conditions were not used in the study on the interference interactions due to the frequent premature fracture of the diaphragms and the consequent unwanted start of the tests in this case. That was because the thickness of the aluminium diaphragms was 22 SWG (0.7mm) at 500psig and that made them more sensitive to weak pressure differences between both sides than at the other test conditions, in which thicker diaphragms were used: 18 SWG (1.2mm) at 1000psig, 14 SWG (2.0mm) at 1500psig and 10 SWG (3.3mm) at 2000psig.

M_∞	P_D [MPa]	$P_{0,\infty}$ [MPa]	$T_{0,\infty}$ [K]	ρ_∞ [kg·m^{-3}]	U_∞ [m·s^{-1}]	Re_∞/m [m^{-1}]	t_{run} [ms]
8.2±0.05	13.8 ± 1%	10.9 ± 1%	1290 ± 3%	0.0371 ± 7.1%	1553 ± 1.6%	$9.35x10^6$ ± 7.6%	31±0.5
8.2±0.05	10.3 ± 1%	8.2 ± 1%	1180 ± 3%	0.0304 ± 7.1%	1486 ± 1.6%	$8.06x10^6$ ± 7.7%	39±0.5
8.2±0.05	6.9 ± 1%	5.4 ± 1%	1040 ± 3%	0.0230 ± 7.1%	1395 ± 1.6%	$6.57x10^6$ ± 7.7%	52±0.5
12.3±0.05	13.8 ± 1%	10.9 ± 1%	1290 ± 3%	0.0054 ± 6.2%	1584 ± 1.5%	$3.35x10^6$ ± 7.5%	176±0.5

Table 3.1 Experimental test conditions indicating uncertainty as further described in Appendix C.

3.2 Case study

To simulate the case of generic surface protuberances on a hypersonic vehicle, a flat plate which replicates the surface of the vehicle was used and different protuberance models were fixed on it as shown in Fig. 3.4. The investigation aimed at measuring the surface heat transfer rate at different locations around the protuberance and high-speed schlieren videos were obtained simultaneously for all the tests. Oil surface visualisations were performed separately. These data were used to provide an understanding of the flow interference effects induced by the protuberance and the effects on the aerodynamic heating. The protuberances were three-dimensional compression corners with finite span and height. The investigation was centred on the datum case of an $\alpha = 30°$ protuberance at a freestream Mach number of M_∞=8.2, Reynolds number of Re_∞/m=9.35x10^6 in a turbulent flow. The dimensions of the datum protuberance were 80mm in length, 5mm in height and 13.5mm in width. Further details on the test models can be found in Section 3.4.

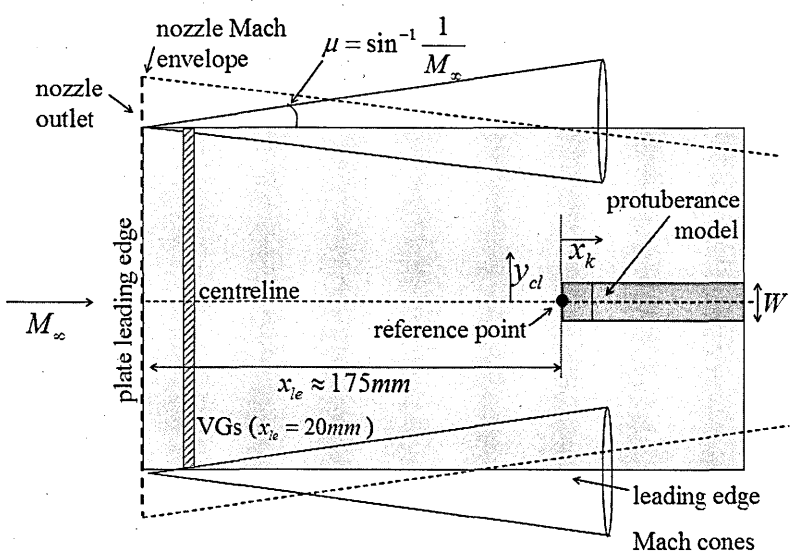

Figure 3.4 Test model arrangement plan view.

Table 3.2 summarises the present case study. Due to the complexity involved in the operation of the facility and the complete experimental rig, and also to the costs, the investigation was limited by the number of runs. A careful selection of the tests required was done. Departing from the datum case, the following features were investigated:

i. A protuberance twice the height and another one twice the width with respect to the datum configuration were considered to assess the effects of protuberance dimensions. A wider range of h/δ_u and W/δ_u ratios was not possible due to the design constraints present in this facility (Section 3.3).

ii. The effect of protuberance deflection angle was studied with similar models but with deflection angles of $\alpha = 15°$, 45°, 60° and 90°.

iii. The case of a surface protuberance with forward deflection was also considered ($\alpha = 135°$).

iv. The effect of boundary layer state, Reynolds number and Mach number on the magnitude of the highest heat flux was assessed for almost the full range of deflection angles ($\alpha = 15°$ to $\alpha = 135°$). Only the $\alpha = 15°$ protuberance was not considered in the study of Reynolds number effect due to the limited information this configuration was expected to provide.

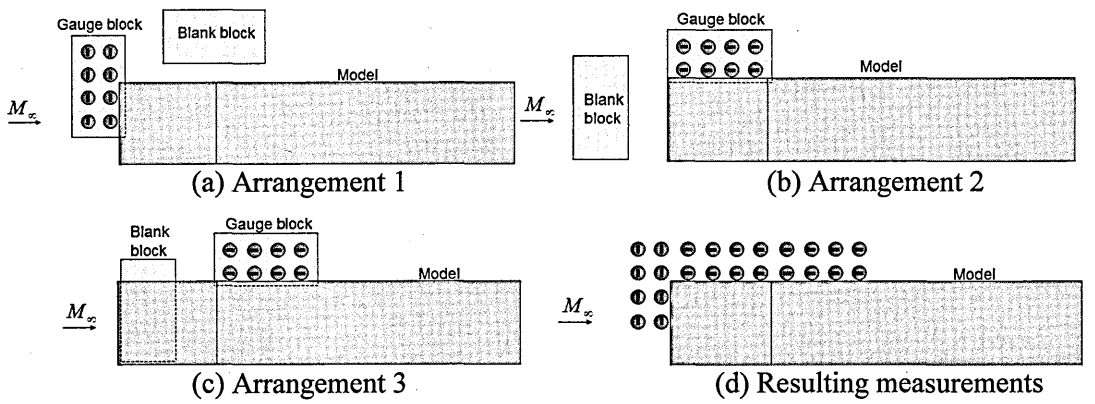

Figure 3.5 Three hypothetical arrangements and resulting measurements.

Study	M_∞	Re_∞/m [m^{-1}]	α [°]	h [mm]	W [mm]	VGs
datum	8.2	$9.35x10^6$	30	5.0	13.5	Yes
h/δ_u effect	8.2	$9.35x10^6$	30	10.0	13.5	Yes
W/δ_u effect	8.2	$9.35x10^6$	30	5.0	27.0	Yes
α effect	8.2	$9.35x10^6$	15,45,60,90	5.0	13.5	Yes
forward α effect	8.2	$9.35x10^6$	135	5.0	13.5	Yes
b.l. state effect	8.2	$9.35x10^6$	15,30,45, 60,90,135	5.0	13.5	No
Re_∞ effect	8.2	$8.06x10^6$	30,45,60,90,135	5.0	13.5	Yes
	8.2	$6.57x10^6$	30,45,60,90,135	5.0	13.5	Yes
M_∞ effect	12.3	$3.35x10^6$	15,30,45, 60,90,135	5.0	13.5	Yes

Table 3.2 Summary of present study.

Optical methods are usually preferred to obtain non-intrusive measurements in high-speed wind tunnel testing but their application to measure surface heating in hypersonic flows is particularly restricted by a number of factors as reviewed by Estruch et al. (2009a). Consequently, eight thin-film gauges were used in the present study with the purpose of obtaining high-resolution high-accuracy measurements of the flux of heat to the surface surrounding the protuberance models. The sensor elements were approximately 1.2mm-long and 0.3mm-wide and were very fragile (see more details in Section 3.7). One possible approach for these measurements would have been to use a model at a fixed position and with different insert locations on the flat plate where gauges could be placed. However, this would not have allowed for small measurement resolutions and would have limited the experiments by having to change the gauges of location for each specific test so that its relative distance to the gauges would allow a final distributed pattern of measurement points around the protuberance. Instead, a module with the 8 gauges was made and two different insert cavities of this module on the flat plate were designed: one for measurements ahead of the protuberance and another for side measurements. A prescribed set of fixing points on the flat plate was then used to fix the protuberance model at different positions relative to the sensing gauge module. The vacant cavity during each test was filled with a blank insert placed flush to the flat plate surface as shown in Fig. 3.5. Care was taken to ensure that the gauges, mounting block and the blanking piece were flush with the surface.

A further analysis of the results shows that the interaction was unaffected by the small changes in the longitudinal and spanwise location of the protuberance on the flat plate. The change in the undisturbed boundary layer heat flux between the different locations also was small (≈2%) and not expected to affect the results as considered in the uncertainty analysis in Appendix C. Measurements were performed with a maximum spatial resolution of 2mm in the longitudinal (x) and lateral directions (y) in the cases required. Special care was taken in the selection of the measurement points so that enough resolution would be obtained in the vicinity of the model to capture the hot spot. The thin film elements were also oriented perpendicular to the direction of the highest heat flux gradients (which take place normal to the front and side of the model) to improve discretisation of the hot spot.

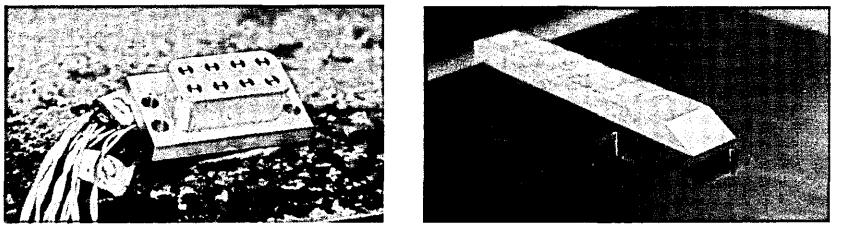

(a) Thin-film module (b) Inserts and model on flat plate

Figure 3.6 Thin-film module and insert cavities on the flat plate.

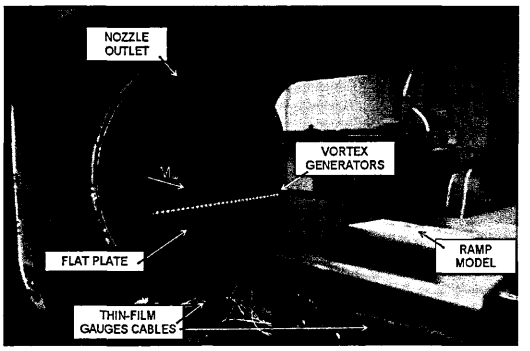

Figure 3.7 Photograph of models in gun tunnel test section.

3.3 Test constraints

The design of the experiments was restricted by different factors including: the useful jet diameter, Mach cones created by the models, test section blockage, regions of interest and spatial resolution, flexibility of the models, boundary layer thickness and protuberance geometry.

3.3.1 Jet diameter

The tunnel nozzles have an outlet of 196mm in diameter (Fig. 3.8). A Mach wave originates at the end of the nozzle with an angle $\mu = \sin^{-1}(1/M)$. A larger angle is obtained at Mach 8.2 freestream conditions: $\mu = 7°$, while $\mu = 5°$ is obtained at Mach 12.3. Considering the limiting case at Mach 8.2, the useful test section is reduced with the relation $\varnothing_{eff} = (196 - 2x\tan 7°)$ mm, where x is the axial distance from the nozzle outlet (Fig. 3.9).

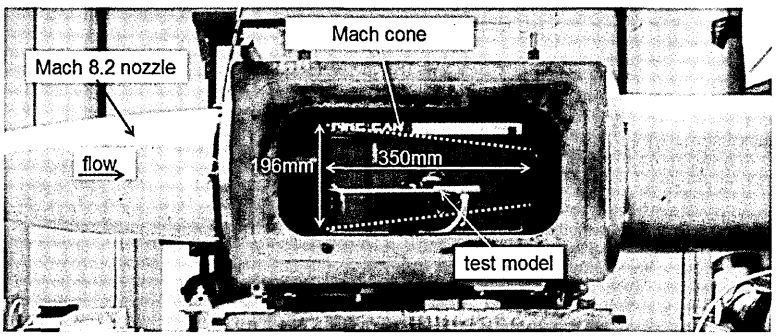

Figure 3.8 Mach wave envelope in Cranfield University gun tunnel test section with Mach 8.2 nozzle on.

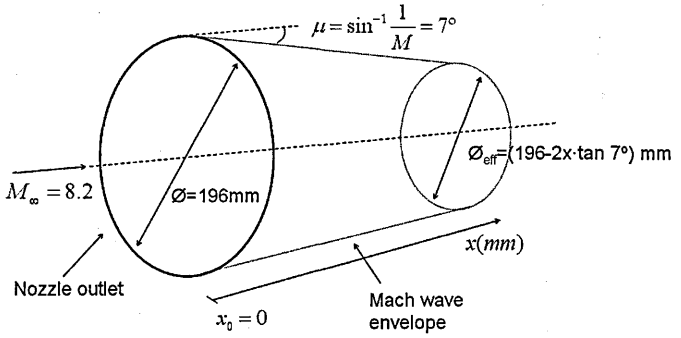

Figure 3.9 Perspective diagram of Mach wave envelope from nozzle.

3.3.2 Leading edge Mach cones

Mach cones also originate at each corner of the flat plate leading edge. These result in a reduced effective width of the flat plate with the following limiting relation at Mach 8.2 conditions: $W_{eff} = W - 2x\tan 7°$ (see Fig. 3.10). Sufficient margin needs to be allowed in order to avoid interference of the flat plate leading edge Mach cones with the interaction induced by the protuberance.

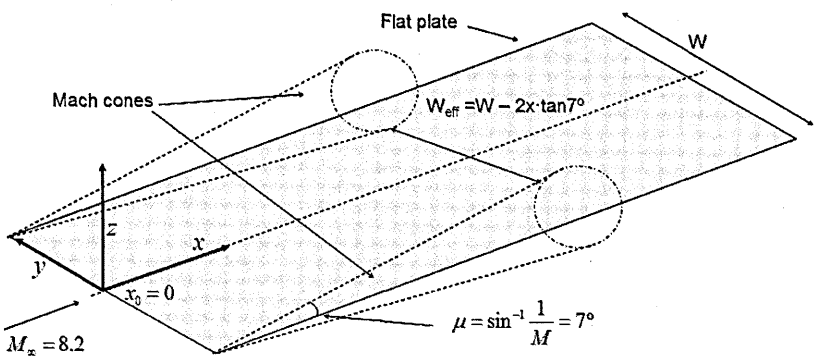

Figure 3.10 Mach cones from flat plate leading edge at Mach 8.2 freestream conditions.

3.3.3 Test section blockage

In previous experimental studies performed in the same facility and at operating conditions of Mach 8.2 and $Re_\infty/m = 9.35 \times 10^6$, test section blockage was observed to take place with cross-sectional model areas of about $3500mm^2$ (Vannahme, 1994). This was using a flat plate with a width of 102mm, thickness of 6mm and with a 44mm-long flap at 40° deflection. The frontal area of the flat plate and models thus needed to be kept below approximately $3500mm^2$ in order to prevent test section blockage.

3.3.4 Measurement regions and resolution

Based on the information gathered in the literature review (Chapter 2), it was expected that high spatial resolution would be required at distances close to the protuberance models. If the measurement surface of the thin-film probes had been relatively large with respect to the size of the model, high heat flux regions would have risked being underpredicted. At the same time, fine measurement resolution was necessary to capture the sharp heat flux gradients found with some of the configurations. Larger protuberance models thus resulted in improved measurement resolution; however, their size was also strongly restricted by the design constraints just discussed.

3.3.5 Flexibility of the models

The protuberance models were fixed at different positions relative to the thin-film modules. These needed to be moved laterally in some configurations and there was the possibility that Mach cones from the plate leading edge or from the nozzle outlet would interfere with the interaction region caused by the protuberance models. Considering the reference protuberance location of x_{le}=175mm, the model width of W=13.5mm (refer to Section 3.4) and based on the literature review (Section 2.3), an expected lateral clearance of about 30mm respect the centreline was considered (Fig. 3.11). Allowing for a 10mm margin from each side, the total effective width (W_{eff}) required on the flat plate was approximately 80mm at x_{le}=175mm. This was subsequently corroborated with the oil surface visualisations (Appendix B).

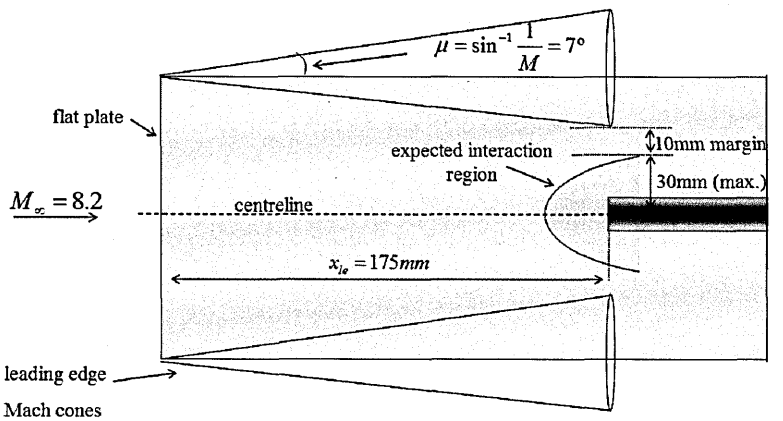

Figure 3.11 Maximum clearance for lateral movement of protuberance models on plate.

3.3.6 Boundary layer thickness

A fully developed turbulent boundary layer was required in the main part of the investigation. In practical applications, the thickness of a turbulent boundary layer is also dependent on the height and location of the vortex generators (VGs) which are used to trip the originally laminar boundary layer. Based on previous experiments at Mach 8.2 freestream conditions and Reynolds number of $\mathrm{Re}_\infty / m = 9.35x10^6$, it was expected that δ=10mm would be obtained at x_{le}=200mm downstream of the leading edge using a VG height of 4mm. It was also expected that δ=4.3mm would be obtained at x_{le}=159mm with a VG height of 1mm (Vannahme, 1994). A slightly thicker boundary layer should be obtained at Mach 12.3 conditions. While the reference enthalpy method predicted a boundary layer thickness of δ=5mm at x_{le}=175mm and $M_\infty = 8.2$ conditions, it predicted δ=7mm at $M_\infty = 12.3$ and at the same location on the plate.

3.3.7 Effect of protuberance geometry

The ratio between the height of the protrusions and the local boundary layer thickness (h/δ_u) was expected to have an effect on the heat transfer measurements for certain protuberance geometries. The effects of the W/δ_u and h/δ_u ratios on the maximum heat flux were previously investigated by Hung and Patel (1984) on supercritical protuberances as already presented in more detail in Chapter 2.

3.4 Test models

The dimensions of the flat plate and models were selected based on the design constraints. The position of the models in the test section was also carefully considered.

3.4.1 Flat plate

The main constraint on the flat plate width (W) was the required lateral clearance of the models. As shown, an effective width of W_{eff}=80mm was needed at x_{le}=175mm. Considering the flat plate would be placed just at the outlet of the nozzle, the nozzle Mach wave would not affect its effective width as long as it would be shorter than the nozzle diameter (196mm). The effective width of the flat plate was then restricted by the leading edge Mach cones.

Different possible values of W were considered to determine the best trade-off between W and the expected boundary layer thickness at the location of the protuberance δ_u based on the test constraints (Section 3.3). These estimations showed that a flat plate width of at least 150mm was required in order to have sufficient mobility of the model. Although the widest plate used in previous studies in this facility was $W = 130$mm (Needham, 1965), previous calibrations had measured the Mach number at distances 3in (76.2mm) above and below the centreline and showed that the Mach number remains practically uniform around this area (Opatowski, 1967) thus confirming that the flow would be suitable for a plate of up to $W = 152$mm (6in). A width of $W = 150mm$ was consequently selected. The chosen flat plate length was 265mm, which allowed placing the protuberance models at the different required locations.

A sharp leading edge was required to reduce the strength of the weak shock produced. For this, a leading edge angle of 10° was selected as a typical angle used in a number of previous studies (Bushnell and Huffman, 1967; Vannahme, 1994 and Kumar, 1991). The same thickness of 6mm used in previous experiments was also selected due to its known suitability (Kumar, 1991; Vannahme, 1994 and Prince, 1995). The final flat plate design is presented in Fig. 3.12.

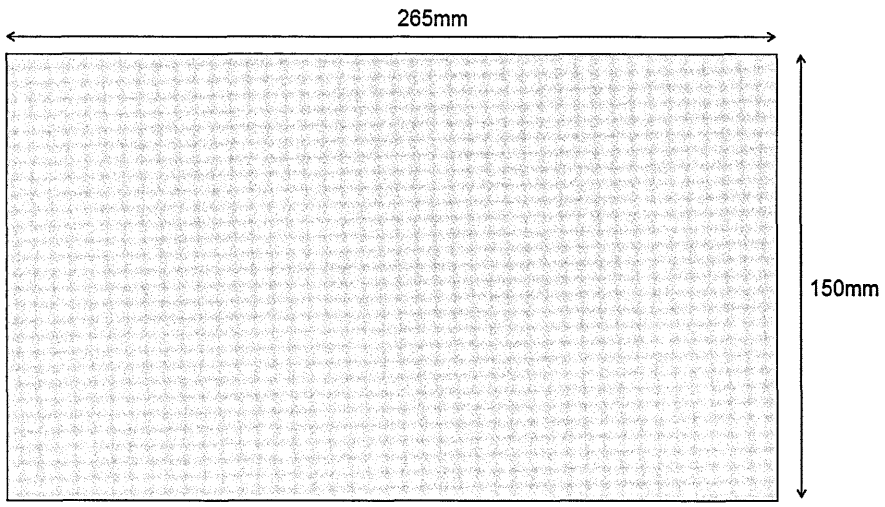

(a) Plan view

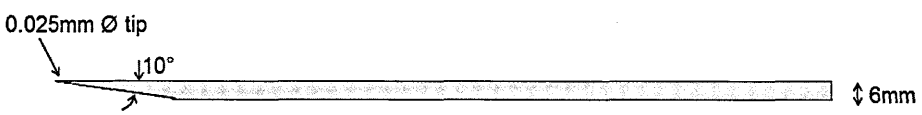

(b) Side view

Figure 3.12 Flat plate design.

The position of the flat plate and protuberance model in the test section is shown in Fig. 3.13. The flat plate leading edge was placed at the nozzle outlet in order to obtain the maximum available effective flow diameter at the location of the protuberance. It was considered suitable to locate the flat plate at a height of 25mm below the nozzle centreline so that a larger margin between the Mach cone from the nozzle and the interference interaction produced by the protuberance models would be allowed.

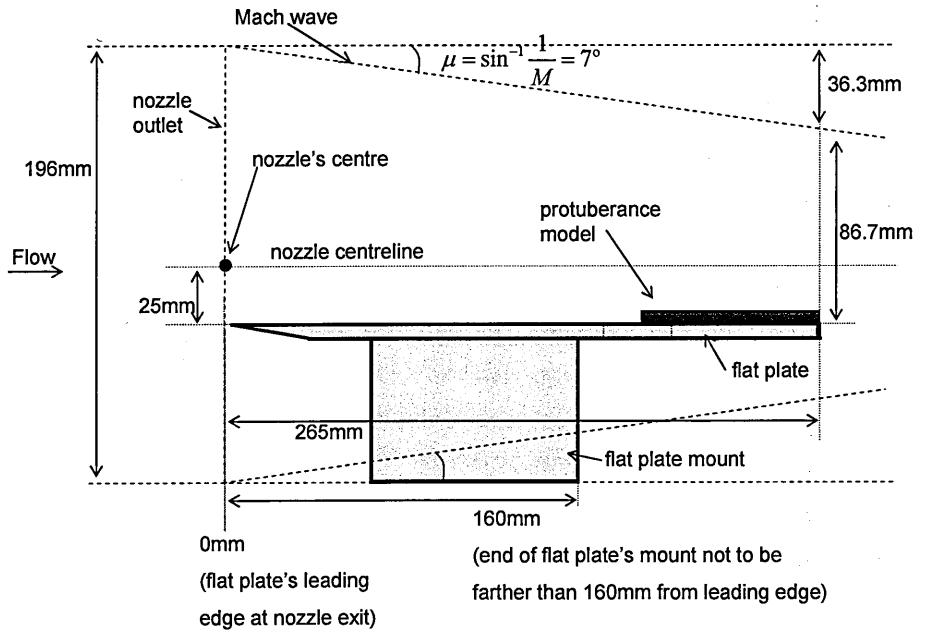

(a) Side view

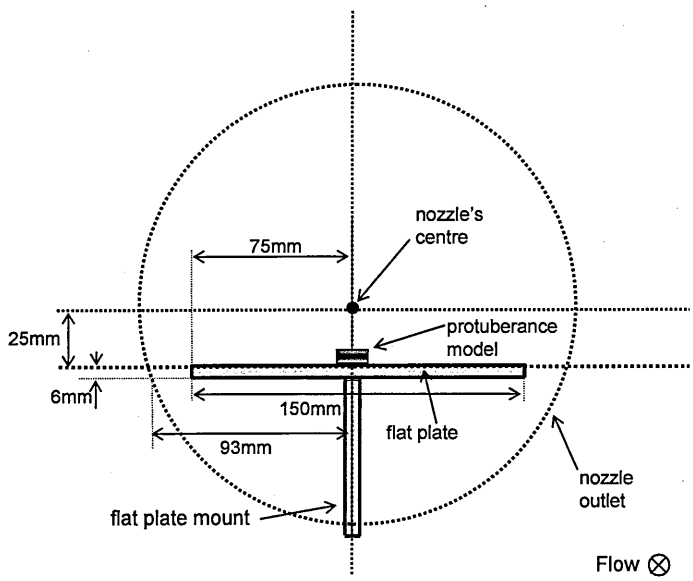

(b) Front view

Figure 3.13 Position of the flat plate in the test section considering Mach 8.2.

3.4.2 Boundary layer trip

A study was done to find a suitable boundary layer trip. The ideal trip would provide a fully developed turbulent boundary layer with no spanwise effects. Based on the applications previously reviewed, two main options were considered: discrete vortex generators or distributed roughness patterns. The use of distributed roughness patterns was discarded given their reduced effectiveness to trip the boundary layer to a fully turbulent state before reaching the location of the protuberance (Section 2.4.2).

Discrete vortex generators were thus used to obtain a fully developed turbulent boundary layer at shorter distances. Although the use of a diamond configuration was shown to be a more effective boundary layer trip, this was not considered due to the strong non-uniformities expected in the downstream flow (Berry and Horvath, 2007). A strip of VGs based on the design used by Coleman (1973) in the same facility was chosen. This was also used by Vannahme (1994) and Prince (1995) at similar operating conditions (Fig. 3.14). Three different VG heights were tested: 1mm (VG1), 4mm (VG2) and 6mm (VG3), refer to Table 3.3. Whereas the shorter VGs provided a turbulent boundary layer thickness of δ_u=5mm at x_{le}=175mm, the others provided approximately δ_u=12mm at the cost of much stronger downstream non-uniformities. No further specific measurements were performed to determine VG effectiveness but VG1 was selected as the most suitable one given that it was expected to provide fully turbulent conditions without spanwise non-uniformities at the location of the protuberance, according to previous studies by Vannahme (1994) and Prince (1995).

	h	d	δ_u
VG1	1mm	3.5mm	5mm
VG2	4mm	15mm	12mm
VG3	6mm	22.5mm	12mm

Table 3.3 Characteristics of VGs tested.

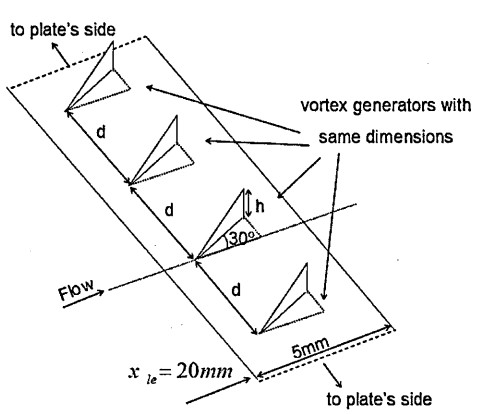

Figure 3.14 Design of VGs used.

A photograph of the 1mm-high 30° triangular vortex generators with a 3.5mm spanwise spacing placed 20mm downstream of the flat plate leading edge is shown in Fig. 3.15 together with the development of the vortices at different distances along the plate based on the liquid crystal flow visualisations by Vannahme (1994). With the same vortex generators and freestream conditions as in the present work, the spanwise 2-dimensionality of the turbulent boundary layer was demonstrated. In particular, it was found that the vortices break down between 100mm and 140mm from the plate leading edge. The two-dimensionality of the flow upstream of the protuberance is therefore ensured.

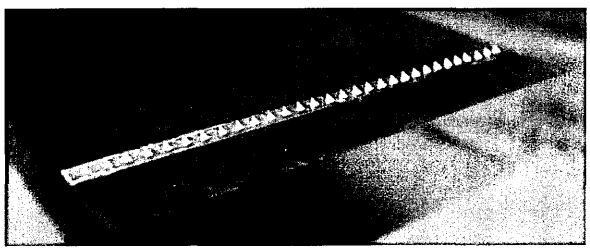

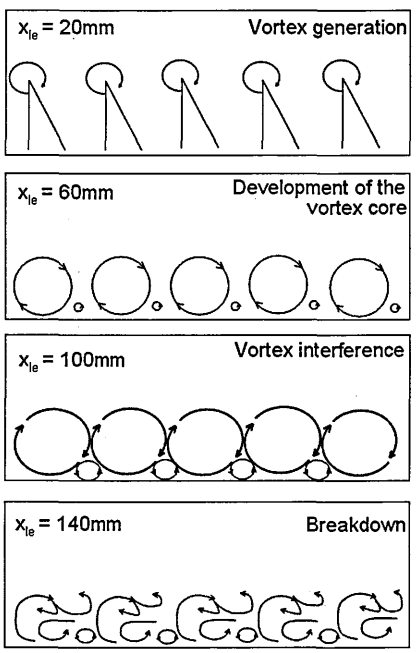

(a) VG1 on plate. $M_\infty = 8.2$, $\mathrm{Re}_\infty / m = 9.35x10^6$ (b) Flow development along plate

Figure 3.15 Photograph of 1mm-high vortex generator (VG1) and corresponding development on the flat plate based on liquid crystal flow visualisations by Vannahme (1994).

3.4.3 Protuberance models

Considering that the expected boundary layer thickness at the location of the protuberance for the datum case was about δ_u=5mm a datum protuberance height of 5mm was chosen to match the reference h/δ_u ratio of 1. Given the design of the thin-film block, 13.5mm had been chosen as a suitable width in order to measure the side heat transfer rates as close to the protuberance as possible with the thin-film module used. The 8 different models considered are shown in Table 3.4, with the corresponding geometrical definitions in Fig. 3.16.

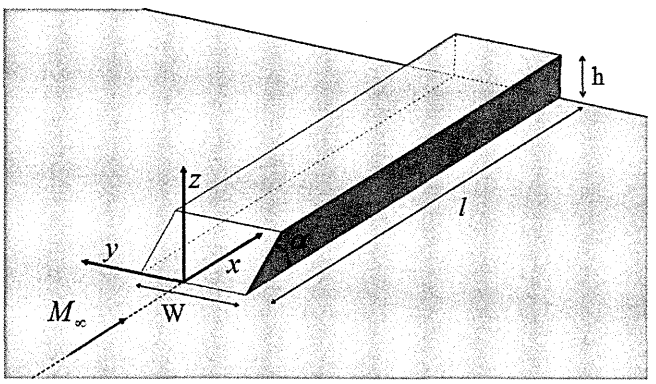

Figure 3.16 Scheme of protuberance models used.

MODELS	α (°)	h (mm)	W (mm)	*l* (mm)
1	15	5	13.5	80
2	30	5	13.5	80
3	45	5	13.5	80
4	60	5	13.5	80
5	90	5	13.5	80
6	135	5	13.5	80
7	30	10	13.5	80
8	30	5	27	80

Table 3.4 Dimensions of models used, according to definitions in Fig. 3.16.

3.5 Surface oil visualisations

Oil flow surface visualisation methods are extensively used in conventional wind tunnel testing but their application in hypersonic gun tunnels is generally limited. This is due to the short test times and very low static pressures which very often result in poor quality visualisations. A suitable variance of this technique consists in applying different oil dots to the surface under study prior to the test. The oil dots are disturbed during the test and thus provide an indication of the limiting streamlines depending on the shear stress direction. The length of the oil streaks gives an indication of the shear stress magnitude at the location of each dot.

Early applications of this technique were performed by Meyer and Vail (1967) and Rao (1970), who looked at the three-dimensional surface flow over delta-wing lifting configurations. Later applications of the oil-dot technique in gun tunnels were performed by Papuccuoglu (1993), Guiming (1994), Singh (1996) and more recently by Kontis (2008). In some of these applications the models were painted in black in order to obtain an improved contrast in combination with a white oil dot mixture.

In the present case the white oil dots could be well appreciated without needing to paint the models in black. Different mixtures were initially tested before a consistent oil blend was obtained. The mixture that was eventually used consisted of linseed oil, titanium dioxide and a few drops of oleic acid, similar to the mixtures used in previous applications (Papuccuoglu, 1993; Singh, 1996). The viscosity of the mixture was suitable to be placed on the flat plate model and the oil dots did not move during the nearly 1 hour preparation time of the gun tunnel. In general, low shear stress was expected over the separating flow regions while stronger skin friction – and therefore longer strakes - was expected in the regions of flow reattachment. This technique was therefore particularly useful in the present case to identify these flow patterns on the surface surrounding the protuberances. The oil-dot flow pattern was recorded immediately after each run. Oil-dot visualisations taken for the present study can be found in Appendix B.

3.6 Time-resolved schlieren diagnostics

A digital high-speed schlieren system was developed to obtain time-resolved information from the flow under test. The first stages of the system development were carried out in the Cranfield University 2.5"x2.5" Supersonic Wind Tunnel given that this facility can provide up to Mach 2.4 conditions with durations of approximately 30 seconds and this preliminarily eliminated the main constraint of the short run duration of the gun tunnel. Subsequently the system was developed in the gun tunnel for simultaneous application with the heat flux measurements. Based on digital image processing routines, semi-quantitative data from the flow was obtained.

3.6.1 Schlieren optical arrangement

A Toepler schlieren arrangement was used in a Z-type configuration (Fig. 3.17). This is the most common schlieren arrangement given that it cancels comatic aberration. The main items used included an LED light source, two parabolic mirrors, a knife-edge and a digital camera (Fig. 3.18).

The light source was placed at the mirror focal length and arranged to bring the light through the test section. In the test section, light was diffracted by spatial density gradients ($\nabla\rho$). The deflection angle (ε) was dependent on the characteristic length of the flow volume (l), on the refractive index (n) and on the density gradients in the form: $\varepsilon = (l/n)\nabla\rho$ (Settles, 1985). The image was then brought to a focal point from the second mirror to the knife-edge. Any misalignment in the optical system resulted in a distortion of the circular shape at this point and hence of the final visualisation. The direction of the density gradients shown in the visualisation was selected at the knife-edge. In this case, a horizontal knife-edge was used with a blockage between 50% and 80%. Vertical density gradients from the flow were thus highlighted in the schlieren images.

In the preliminary stages of the system development in the 2.5" x 2.5" Supersonic Wind Tunnel (Fig. 3.19), a digital SLR camera was used to obtain single images at exposure times of approximately 1 ms. With this arrangement, the camera lens was removed and the schlieren image was projected directly onto the CCD chip of the camera. Further details on this system can be found in Estruch et al. (2008, 2009b).

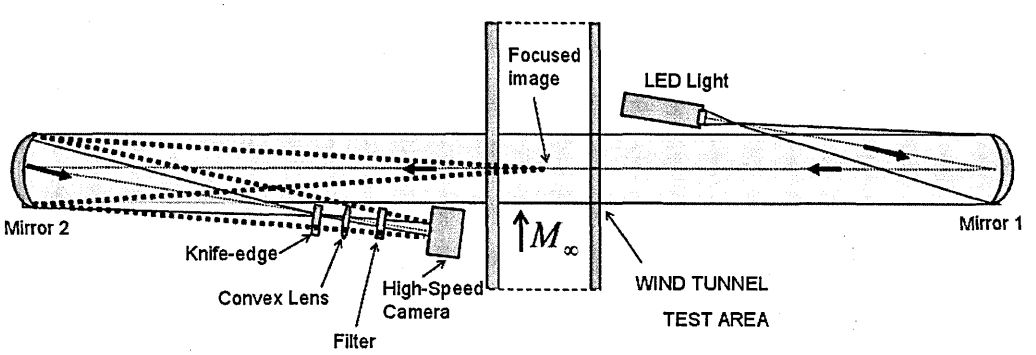

Figure 3.17 Schematic diagram of high-speed schlieren optical arrangement.

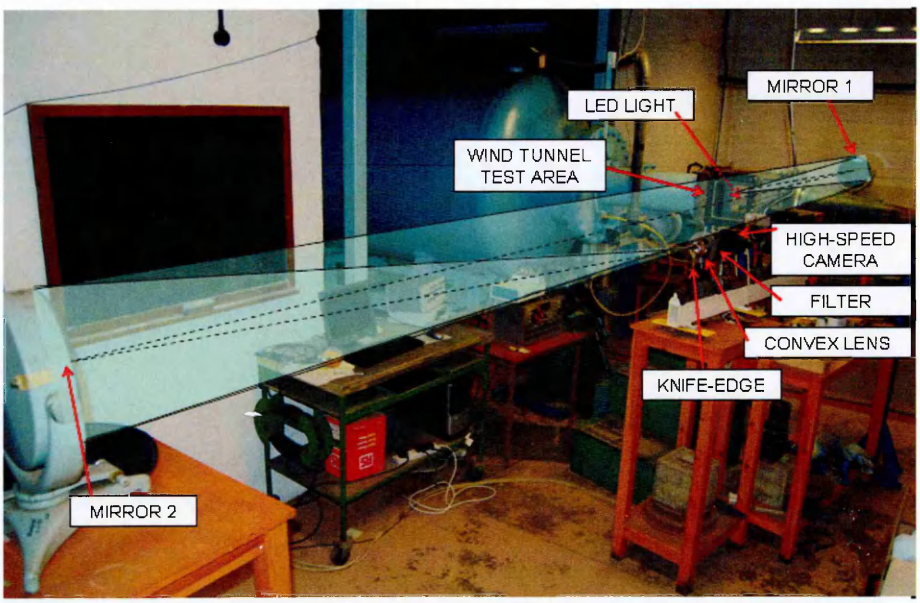

Figure 3.18 Photograph of high-speed schlieren optical arrangement used in Cranfield University gun tunnel.

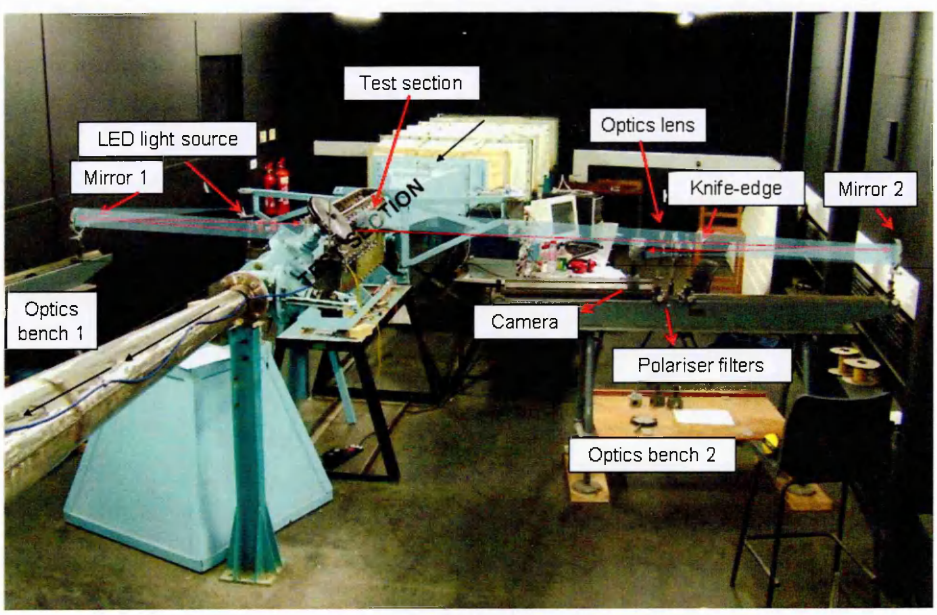

Figure 3.19 Photograph of schlieren optical arrangement in Cranfield University 2.5"x2.5" Supersonic Wind Tunnel.

A sample schlieren image obtained with the present rig is shown in Fig. 3.20. The model in this case is a generic hypersonic blunt body comparable for example to the Apollo re-entry capsule (Section 2.1). The adverse pressure gradients across the shock at the top of the image result in a vertical downwards deflection of the light beams with the knife-edge blocking the bottom of the image horizontally. This occurs because light is always diffracted towards the regions of higher refractive index, which correspond to those with higher air density in this case, i.e. downstream of shock waves. For this reason, the same shock structure at the bottom half of the image appears as a brighter area instead of darker.

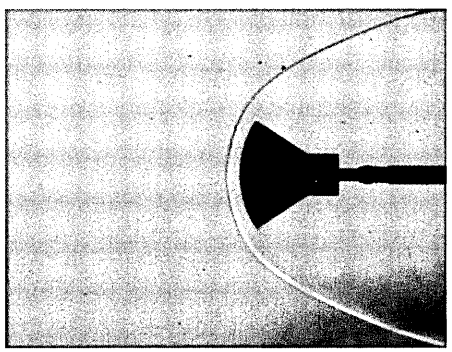

Figure 3.20 Sample schlieren image of hypersonic blunt body, $M_\infty = 8.2$, $\mathrm{Re}_\infty / m = 9.35x10^6$.

3.6.2 LED light source

An argon spark light source in combination with a film photographic camera had been used to date in the present facility to obtain snapshot schlieren images during the tests but this was not suitable for high-speed schlieren imaging. Other similar schlieren systems have typically used incandescent lamps, arc lamps and spark gaps (Smith, 1994). Other light sources that have been successfully applied for schlieren imaging are laser diodes, which have proven to provide sufficient luminosity for high-speed schlieren visualisation (see e.g. Haley and Smy, 1988). Lasers are not so suitable for qualitative schlieren methods due to their coherence (Weinberg, 1963) and the translation of phase differences into amplitudes in this case (Settles, 2001). In large field schlieren applications, extended light sources have been generally used (Weinstein, 2000).

An LED was selected as a potential light source suitable for a high-speed schlieren system. Pawliszyn (1987) reported the suitability of LEDs for schlieren applications, highlighting their good beam pointing characteristics and high stability in light output. The incoherence of the LED light source and their compact design are also an advantage for schlieren applications (Estevadeordal et al., 2007). Similar applications used an LED with large currents for short pulse durations. While typical LED forward currents are only a few milliamps, LEDs can withstand higher intensity currents at microsecond pulse durations (Stasicki et al., 1990). Pulsed LED light sources were used in conventional and high-speed schlieren applications (Tsai and Bakos, 1998). Hiller et al. (1987) used a similar light source for unsteady flow investigation in a Mach-Zehnder interferometer system. Circuit designs suitable for this type of light source are outlined in the literature (Buttsworth and Ahfock, 2003). Pulsed LEDs have also had successful application in Cranz-Schardin cameras for high-speed shadowgraphy and interferometry (e.g. Bretthauer et al., 1991; Lu and Liu, 1997).

A preliminary investigation was therefore done to select possible potential LED light sources. Three LEDs with different wavelength, luminous intensity and viewing angle were initially tested and used in a continuous mode. Other LEDs examined in the present investigation were discarded due to the non-uniformity of their output light. This was mainly due to the encasement of the LED, which acts as a lens on the light produced and this has a strong effect on the quality of the visualisations. Although visualisations with a longer wavelength light source were expected to be more sensitive to weaker disturbances, other factors were shown to have a stronger impact on the quality of the visualisations such as light uniformity and optical alignment. As shown in Figs. 3.21 and 3.22, the three LEDs that were initially tested were a NSPW510BS Nichia white LED (9200mcd, 20° viewing angle), L-7113VGC-H Kingbright green LED (18000mcd, 20° viewing angle) and TLSH180P Toshiba red LED (10000mcd, 8° viewing angle). They allowed for image exposure times of up to 0.5ms proving suitable for visualisation of steady flows.

Although the initial aim was to design a circuit providing the LED with high-intensity currents at short pulse durations, a new-technology high-power LED (3-Watt CREE Q5) which came onto market during the time of the investigation (2008) could be

eventually used in a continuous mode. This LED provided sufficient light so as to obtain images at frame rates of up to 50000 fps (Fig. 3.23). In particular, the dominant wavelength of this LED was in the blue spectrum and visualisations were of a similar quality as those obtained with the NSPW510BS Nichia white LED, which had a dominant wavelength also in the blue spectrum of light and was the most suitable one among all the three initial LEDs as shown by the plots of intensity levels in Fig. 3.23. No other alterations needed to be made to the rest of the optical system.

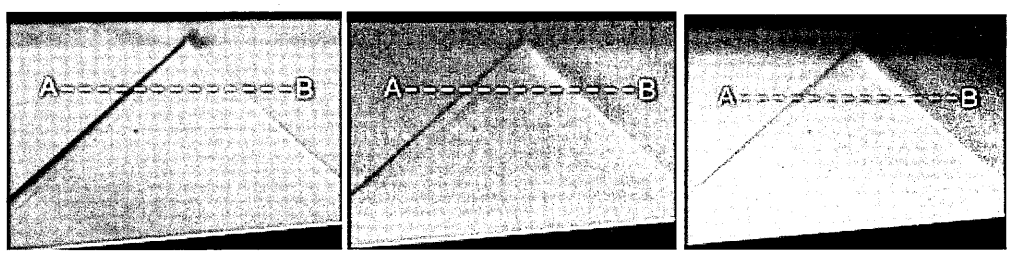

(a) NSPW510BS Nichia (b) L-7113VGC-H Kingbright (c) TLSH180P Toshiba

Figure 3.21 Schlieren images of supersonic SWTBLI with different light sources

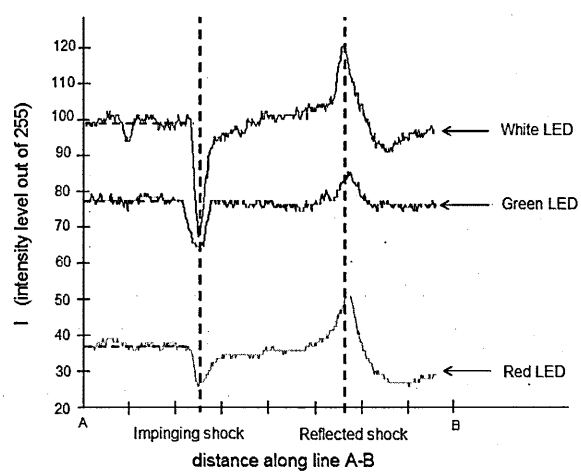

Figure 3.22 Intensity levels along lines A-B from Fig. 3.21.

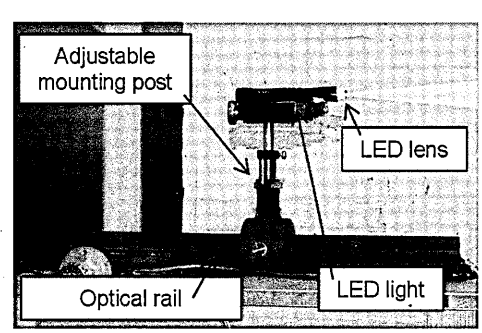

Figure 3.23 CREE Q5 LED light source used in gun tunnel rig.

3.6.3 High-speed schlieren system

The CREE Q5 LED light source was therefore used in a continuous mode and in combination with direct imaging onto a Photron APX high-speed digital camera without the need for further optical items (Fig. 3.24). By doing so, a relatively simple but efficient high-speed schlieren system was obtained (Estruch et al., 2008). Only the high-speed camera needed then to be timed with the wind tunnel facility. The trigger used was from a microphone signal which sensed the rupture of the diaphragms at the start of the run. The raw microphone signal was conditioned through a function generator (Thandar TG 503) before being sent to the camera processor box as a +5V TTL step pulse via the "General In" cable connector. The camera was then operated with the "Random Manual" function which constantly captures images and rewrites them every time the memory is full allowing the user to determine the number of images to be saved before and after the trigger is received. There was an inherent delay of 12.5ms between the trigger signal and the actual recording start time of the cameras which could be accounted for in this mode. High-speed schlieren images could thus be taken during the whole run duration.

The frame rate at which the cameras can operate is limited by the image resolution (Table 3.5). For the present study and due to the elongated shape of the field of view, schlieren images with a size of 1024px x 256px were taken for all the cases at 8000fps. In the cases where the flow was observed to be unsteady the image was also reduced and focused in the unsteady region allowing for acquisition frame rates of up to 50000 fps but with a size of 256px x 64px and same pixel resolution (refer to Appendix B).

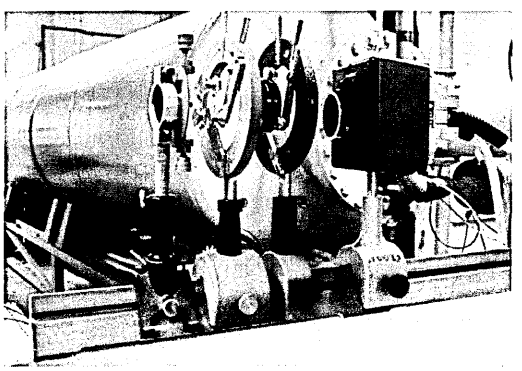

Figure 3.24 Knife-edge, convex lens, filter and high-speed camera in schlieren rig.

Frame rate (fps)	Max. Resolution (pixels)		Record time (s)
	Horizontal	Vertical	
2000	1024	1024	1
4000	1024	512	1
8000	1024	256	1
15000	256	256	1.1
50000	256	64	2.6
100000	128	32	5.2
120000	128	16	8.7

Table 3.5 Specifications of Photron APX high-speed camera.

3.6.4 Schlieren digital image processing

Apart from the qualitative schlieren videos obtained, quantitative information could be derived by reading the images as two-dimensional matrices where each cell value represents the pixel intensity on a greyscale from less intense (0) to more intense (255). This was performed with the Matlab image processing package.

Flow features in the image were quantified by looking at pixel intensity gradients. For example, the change in pixel intensity across a shock wave is shown in Fig. 3.22. Other flow features such as boundary layers or expansion regions are more gradual but are also visible. It must nevertheless be taken into account that the schlieren technique averages the density gradients across the volume and therefore the visualisations are affected by three-dimensionalities in the flow.

During the course of this investigation further digital image processing routines were developed which allowed obtaining information on the unsteadiness of the flow. A version of the Canny algorithm – which is an edge detection method of common use in machine vision applications (Gonzalez et al., 2004) - was applied to locate the shock positions. The application of this algorithm was based on the principle that the shock location is discernible in the schlieren image as distinct dark or light regions when compared with the background light intensity. In comparison with simpler edge detectors (Sobel, Prewitt, Roberts and Laplace) this was found to give enhanced

performance when locating the shock position. This was mainly due to its reduced sensitivity to noise and its edge-thinning capability, which provided a clear shock location and avoided detection of unwanted edges. Shock position was determined by applying a suitable threshold to isolate the highest intensity gradients in the image which once in binary form allowed the shocks to be distinguished as thin edges (Canny, 1986; Ding and Goshtasby, 2001). From these edges the locations of the shocks were identified for each row in the image digital matrix.

A sample case of this application performed during the schlieren system's development stages in the supersonic wind tunnel is shown in Fig. 3.25. In this case, the unsteadiness of an impinging shock-wave/boundary-layer interaction at Mach 2.4 was studied. Further information on these experiments can be found in Estruch et al. (2009c, 2009d). As expected from previous studies (Dolling, 2001), the impinging shock wave was found to be steady (Location A) and reflected shock wave was clearly unsteady (Locations B and C). At the unsteady shock locations, by processing a time series of images, the dominant frequencies in the shocks motion were obtained by means of spectral analysis using a Fourier transform based MATLAB toolbox. This provided a new method to measure shock wave unsteadiness that showed to be a reliable optical flow diagnostic for studies on shock wave unsteadiness and to be capable of yielding flow measurements in regions not accessible by intrusive methods. Further details on this method can be found in Estruch et al. (2008). However, unlike in this example, the application of this method in the present interactions did not reveal the presence of a clear dominant frequency. This is described in more detail in Chapter 7.

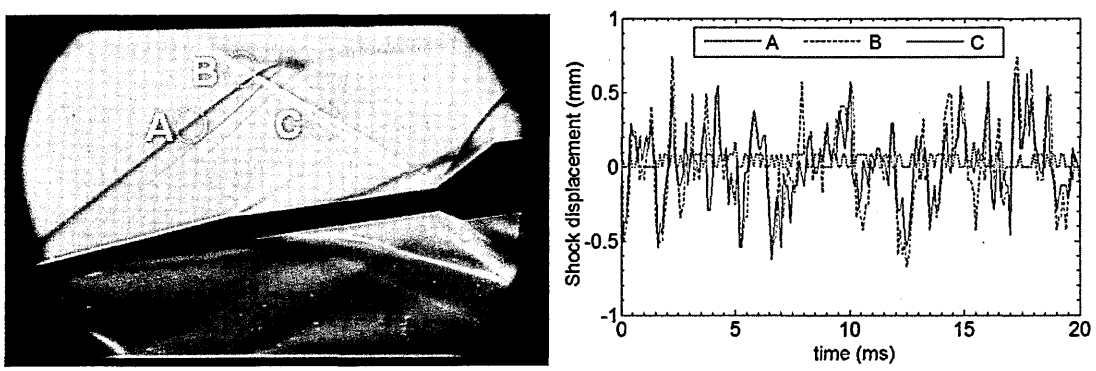

Figure 3.25 Application of the technique. Reproduced from Estruch et al. (2008). ©AIP 2008

3.7 Heat flux measurements

Highly accurate heat flux measurements were required for the present investigation in part due to the importance of this data for the reliability of a subsequent semi-empirical approach. In addition, the system needed to be sensitive to heat transfer rates as low as $0.1 W/cm^2$ given that very low heat flux values were expected at some of the test conditions as further shown in Chapters 4 and 5.

3.7.1 Thin-film gauges

Eight thin-film gauges were used for the measurement of transient temperatures during each test (Figure 3.26). These are fast response (1μs) temperature sensors which measure temperature changes of the order of 0.1K. Heat flux can be determined using the measured time-dependent temperature signal. To determine the heat flux, the theory of one-dimensional heat conduction into a semi-infinite body was assumed (refer to Appendix A). The sensors were individually pre-calibrated for both resistance temperature sensitivity and the thermodynamic property $\left(\sqrt{\rho c_p k}\right)_g$. The contact method was used to calibrate each gauge individually by the provider (SWL, RWTH). This method assumes that when the gauge is rapidly placed into contact with another element, a constant temperature is yielded for a certain time, which depends on the initial temperatures and thermodynamic properties of the thin film and contact elements.

The sensors consisted of a ceramic substrate (zirconium oxide) with a sputtered nickel thin film. A change in temperature on the surface of the thin film caused a change in its resistance as shown in Eq. 3.1, where R_0 and T_0 are the resistance and temperature of the thin film prior to the measurement, as stated in the specifications (Appendix A). The determination of heat transfer was based on the analogy between the flow of heat into a semi-infinite material and the flow of current into an R-C circuit as derived by Schultz and Jones (1973). More details on this analogy can be found in Appendix A. The final relation used to obtain the heat flux is shown in Eq. 3.2.

$$R = R_0\left(1+\alpha_R(T-T_0)\right) \qquad \text{[Eq. 3.1]}$$

$$q = \frac{\left(\sqrt{\rho c_p k}\right)_g \overline{V_2}}{\alpha_R V_1 G} \qquad \text{[Eq. 3.2]}$$

The diameter of the gauges used was 2.3mm and the length was 3.3 mm. The thin-film elements were approximately 1.2mm-long and 0.3mm-wide. Thin-films were very fragile and were only to be used in clean environmental conditions. In order to minimise changing the gauges from location, they were fixed flush to a thin-film module with dimensions shown in Fig. 3.27 which would only need to be changed to a second location on the plate. A corresponding blank module was made and placed in the redundant cavity during each test case. A sample photograph is shown in Fig. 3.28, corresponding to the side measurements on a protuberance model.

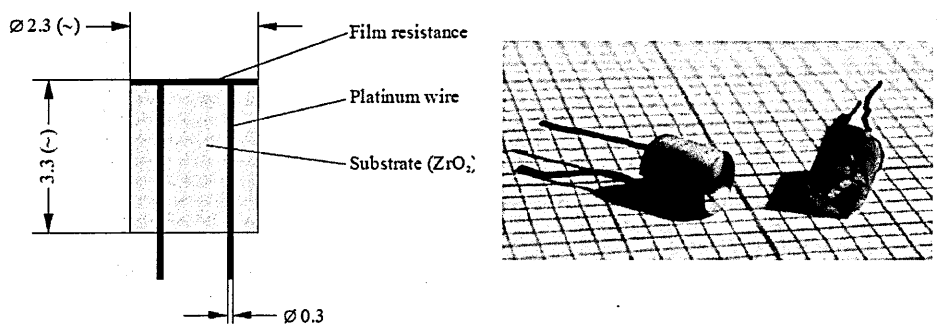

Figure 3.26 Thin-film sensor design (left) and photograph (right), reproduced from product specifications (Olivier, 2009).

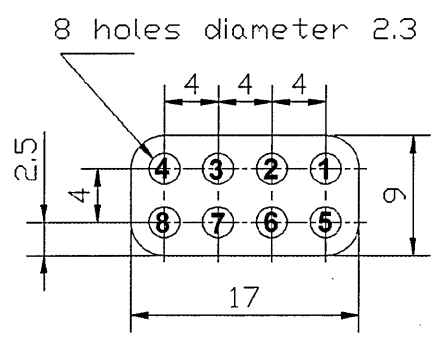

Figure 3.27 Design of 8-off thin-film module in mm and indicating gauge number (refer to Appendix A.3 for more details).

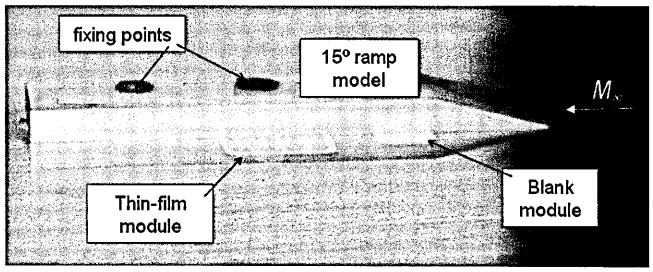

Figure 3.28 Sample protuberance model showing thin-film module and blank module on flat plate.

3.7.2 Test rig

A digital data acquisition system was commissioned in the gun tunnel to allow rapid analysis and storage of data following a run. The heat flux system was used at the same time as the high-speed schlieren system during the tests.

The gauges were inserted in the test section through the connexion cables in the bottom of the test area. The voltage change associated with the temperature rise of the gauges during each test was integrated using a resistor-capacitor (R-C) analogue integrator circuit (HTA1 5R.0185). This allowed for a direct integration of the temperature signal and avoided the uncertainties introduced by the half derivative terms in the numerical integration approach which make the calculation of heat flux particularly sensitive to experimental noise (Oldfield et al., 1978). The channels of the CONTECH analogue integrator circuits provided a constant current supply of 8.4mA to the gauges. The signal was then low-pass filtered at 50kHz (FYLDE 3018-F) and the data was acquired by a NI BNC-2110 DAQ data acquisition board without prior amplification of the signal. The sampling rate was 100kHz, and data were recorded after receiving a trigger signal from a microphone that detected the rupture of the diaphragms when the tunnel was fired. This microphone signal was also used to simultaneously trigger the high-speed schlieren system. The determination of heat transfer, as shown in Appendix A, was based on the analogy between the flow of heat into a semi-infinite material and the flow of current into an R-C circuit as described in more detail in the work of Schultz and Jones (1973). The estimated resolution in the present study was 0.1 W/cm^2. An image of the heat flux rig is shown in Fig. 3.29 and a schematic diagram of the total rig is found in Fig. 3.30.

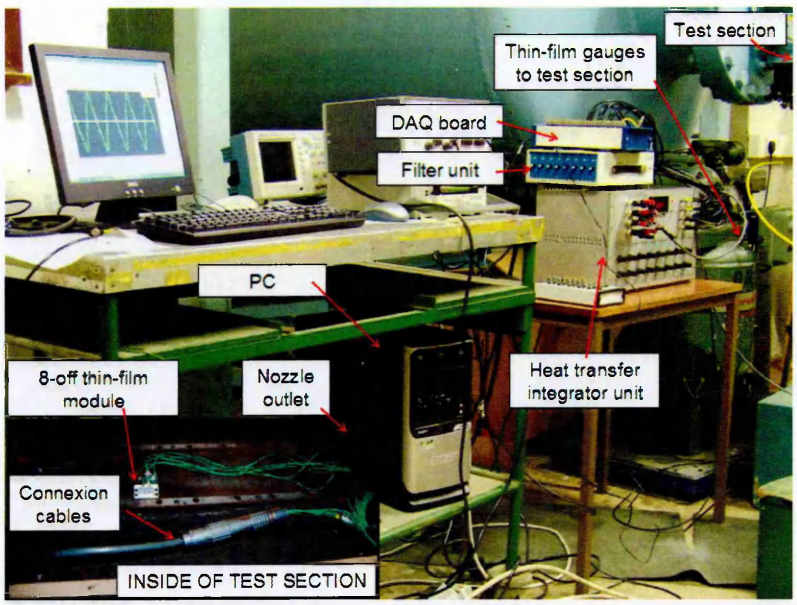

Figure 3.29 Image of heat flux rig.

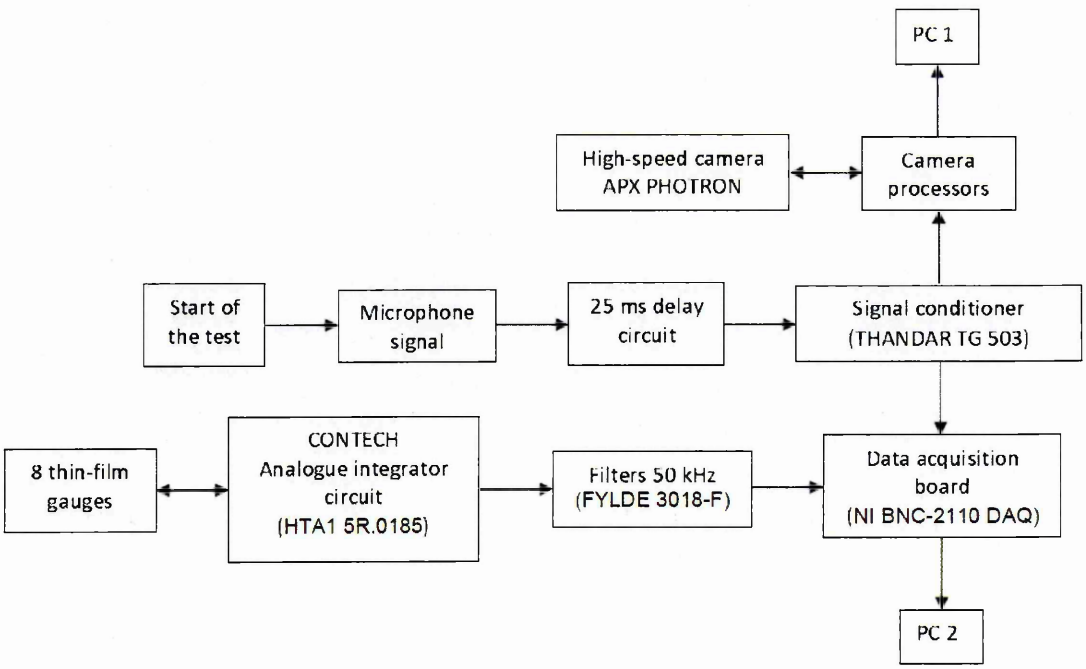

Figure 3.30 Schematic diagram of complete test rig.

3.7.3 Effective established flow

The effective duration of the flow in the gun tunnel was determined from heat flux measurements and high-speed schlieren videos. Figure 3.31 shows schlieren images corresponding to the 90° protuberance case that shows the start of the development of the boundary layer on the plate. The effect of the passage of the shock front on the boundary layer up to the end of the run is also observed.

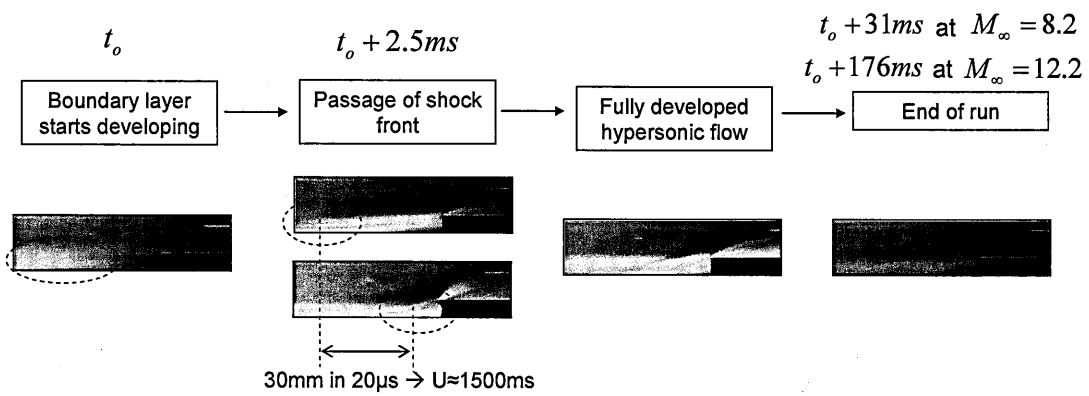

Figure 3.31 Flow establishment based on high-speed schlieren visualisations, tunnel operating at drive pressure of 2000 psig.

Measurements for the stagnation heat flux on a hemispherical forebody (as considered in Chapter 4) are shown in Fig. 3.32 and are also shown over the datum flat plate model in Fig. 3.33. The effects of the passage of a normal shock are observed 2.5ms after the start of the run, as also shown in the schlieren results. After that, the flow becomes fully established for a duration of 31ms with the Mach 8.2 nozzle and 176ms with the Mach 12.3 nozzle. As expected, the heat flux tends to decrease during the duration of the run as the temperature of the models also increases. In order to obtain an estimate of the heat flux, an average of the measurements between 10ms and 20ms with respect to the start of the run was calculated. This was selected as the established flow period based on an assessment of the high-speed schlieren videos.

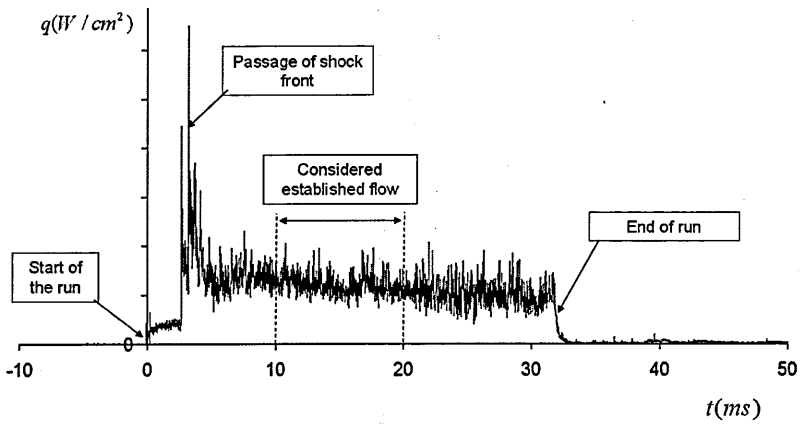

Figure 3.32 Typical measurement of heat flux with thin film gauges, stagnation measurement, $M_\infty = 8.2, \mathrm{Re}_\infty / m = 9.35x10^6$.

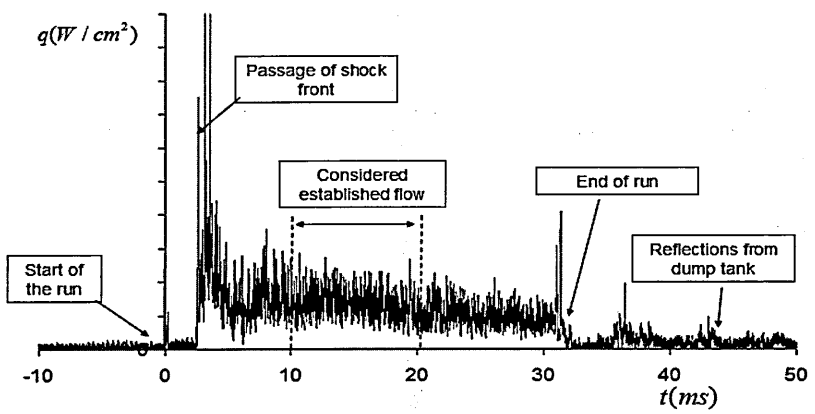

Figure 3.33 Typical measurement of heat flux with thin film gauges, flat plate. $M_\infty = 8.2, \mathrm{Re}_\infty / m = 9.35x10^6$.

3.8 Experimental uncertainty

A measure of the repeatability of the measurements is presented in the following chapter. A further uncertainty analysis is performed by considering a typical transducer error of 5% in the calibration of the thermal property of each individual gauge $\left(\sqrt{\rho c_p k}\right)_g$ and of 2% in the calibration of the thermal coefficient of resistivity α_R as quoted by the manufacturer. The error related to the input voltage of the gauges V_1(1%), the measurement resolution of the output voltage $\overline{V_2}$ (0.03%) and the calibration of the system gain G (1.6%) was also accounted for together with the uncertainties related to the freestream flow conditions (Table 3.1) and wall temperature (1.7%). With a random error of 3.5% at 99.6% confidence and a maximum systematic error in the measurement of Stanton number of 9.5% based on the uncertainties mentioned, a total combined uncertainty of ±10% is estimated, which is similar to the error range achieved in other similar experimental studies as reviewed by Simmons (1995). Further details on the uncertainty analysis can be found in Appendix C and a list of selected uncertainties is presented in Table 3.6.

Measurement	Uncertainty
q	±7%
St	±10%
δ	±16%
L	±10%

Table 3.6 Summary of uncertainty estimates

CHAPTER 4

Heat Transfer in Attached Flow

Prior to the study of aerodynamic heating in interference regions, measurements were made on configurations in which the flow remains attached and for which well-established theoretical and semi-empirical models are available. Based on these measurements, the accuracy of the system and the reliability of the main predictive approaches developed to date are assessed. The state of the boundary layer is also inferred from the schlieren images along with a comparison between measured heat transfer and the corresponding analytical estimates. An overview on the application of these methods to predict the surface heat flux on real vehicles is presented at the end of the chapter.

4.1 Introduction

The two main parameters in the design of high-speed vehicles are drag and aerodynamic heating. The latter is of especial importance at hypersonic speeds and generally drives the design characteristics of hypersonic vehicles. While this is demonstrated in the next paragraph, the definitions of heat transfer coefficient and Stanton number need to be first introduced. Although the non-dimensional heat transfer coefficient is used in part of the literature as in Eq. 4.1, the Stanton number (Eq. 4.2) is generally preferred for comparison purposes given that it provides a dimensionless ratio of the actual heating rate with respect to the potential heating rate of the local flow. An alternative coefficient is the Nusselt number (Eq. 4.3), which is related to the Stanton number, Reynolds number and Prandtl number by $Nu = St\,\mathrm{Re}\,\mathrm{Pr}$.

$$C_H = \frac{q_w}{\rho_\infty V_\infty (h_o - h_w)} \quad \text{[Eq. 4.1]}$$

$$St = \frac{q_w}{\rho_\infty V_\infty (h_{aw} - h_w)} \quad \text{[Eq. 4.2]}$$

$$Nu_x = \frac{q_w x}{k_e (T_{aw} - T_w)} \quad \text{[Eq.4.3]}$$

Departing from the definition of the heat transfer coefficient (Eq. 4.1) and noticing that at such high speeds $h_{aw} \approx h_o = h_\infty + \frac{V_\infty^2}{2}$ and $\frac{V_\infty^2}{2} >> h_\infty$, the especial importance of aerodynamic heating at hypersonic speeds is clear. Based on these approximations, heat flux is roughly proportional to the cube of the velocity as shown in Eq. 4.4. This relation can be compared with the definition of drag in Eq. 4.5, which is proportional to the square of the velocity. Aerodynamic heating therefore increases more significantly at high flow velocities and thus becomes a driving parameter in the design of hypersonic vehicles although other parameters such as drag are also important.

$$q_w \approx \frac{1}{2}\rho_\infty V_\infty^3 C_H \quad \text{[Eq. 4.4]}$$

$$D \approx \frac{1}{2}\rho_\infty V_\infty^2 C_D \quad \text{[Eq. 4.5]}$$

Different theoretical and semi-empirical models have been developed to date to obtain estimates of both the skin friction and heat transfer coefficients at hypersonic speeds. These are approximate methods which are used in engineering preliminary analysis to obtain rapid estimations of these parameters. The methods developed to date have been partly limited by the difficulty in obtaining analytical solutions based on simplifications of the governing continuity, momentum and energy equations. Whereas purely theoretical derivations are directly applicable in a limited number of cases, most approaches have relied on experimental measurements either linked with theory or in the form of data correlations. Despite their approximate nature, these are nowadays common estimation methods used in the aerothermodynamic design of vehicles such as the Space Shuttle (Hayes and Neumann, 1992). Further details on such applications are shown in Section 4.5.

The most relevant predictive approaches developed to date are considered in this chapter. The first part of the study presents measurements of the stagnation point heat transfer at the leading edge of a blunt body and compares these with estimations from the well-established method of Fay and Riddell (1958). Following this, the accuracy of the system is assessed and measurements of the heat flux from the undisturbed boundary layer to a flat plate at different operating conditions of the gun tunnel are presented. Based on the comparison of these results with the existing predictive theory and schlieren visualisations, the nature of the boundary layer is determined through consideration of the reference protuberance position in the related study on interference heating (x_{le}=175mm). Further analysis is made on the heat flux measurements over a hemisphere-cone-cylinder body with a semi-angle of 15°. An assessment of these predictive approaches is also carried out at both laminar and turbulent conditions.

4.2 Stagnation heat transfer

The stagnation point heat transfer on the forebody is one of the most critical factors in the design of hypersonic vehicles as already shown in Section 2.3.1. A comparison between existing theory and the present experimental measurements follows.

4.2.1 Established theory

The theory of stagnation heat transfer developed by Fay and Riddell (1958) is the only case for which sufficient simplifications can be made to reduce the boundary layer partial differential equations from the Navier-Stokes equations to an ordinary differential form. This is due to the unique assumptions that can be made in this point, including that the boundary layer can be considered laminar and axisymmetric. The concept of self-similar boundary layers developed by a number of aerodynamicists (Dorodnitsyn, 1942; Howarth, 1948; Lees, 1956) was used in the derivation of this method.

A schematic diagram of the flow in the stagnation region of a hemispheric body is shown in Fig. 4.1, where the freestream flow is designated by the subscript 1 and the flow behind the bow shock by the subscript 2. The portion between points A-A' in the image corresponds to the part of the detached shock which can be assumed normal respect the body's leading edge. Arrows represent the stagnation streamline, along which the flow decelerates to the stagnation conditions indicated here as point t2.

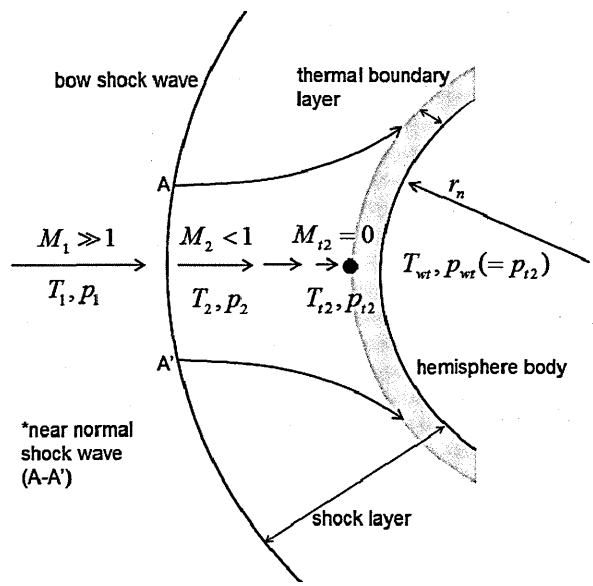

Figure 4.1 Flow field downstream of a hemisphere body at hypersonic speeds, based on Bertin (1994).

Assuming the flow to be in thermo-chemical equilibrium and the Lewis-Semenov number $Le = \left(\rho D_i c_p\right)/k$ to tend to 1, Fay and Riddell (1958) found that all their individual heat-transfer calculations could be correlated by the following expression (Eq. 4.6), where an intermediate recovery factor for a laminar boundary layer is generally assumed ($r = \sqrt{\mathrm{Pr}}$, with Pr=0.71):

$$q_{o,t} = \left(\frac{Nu_x}{\sqrt{\mathrm{Re}_x}}\right)\sqrt{\rho_{w,t}\mu_{w,t}\left(\frac{dU_e}{dx}\right)_{t2}}\left[\frac{H_{t2} - h_{w,t}}{\mathrm{Pr}_{w,t}}\right] \quad \text{[Eq. 4.6]}$$

Based on this correlation, they then derived the relation for the stagnation-point heat transfer rate for a laminar boundary layer in dissociated air and over a spherical cap as shown in Eq. 4.7. Whereas this applies for axisymmetric geometries, in two-dimensional cases the heating level is reduced by an approximate factor of $\sqrt{2}$ as noticed by Lees (1956). Fay and Riddell (1958) presented the relation in Eq. 4.8 for the case of a cylinder with its face opposed to the freestream flow to represent a two-dimensional configuration.

$$q_o = \frac{0.763}{(\mathrm{Pr})^{0.6}} (\rho_e \mu_e)^{0.4} (\rho_w \mu_w)^{0.1} (h_{oe} - h_w) \left[\frac{dU_e}{dx} \right]^{0.5} \quad \text{[Eq. 4.7]}$$

$$q_o = \frac{0.57}{(\mathrm{Pr})^{0.6}} (\rho_e \mu_e)^{0.4} (\rho_w \mu_w)^{0.1} (h_{oe} - h_w) \left[\frac{dU_e}{dx} \right]^{0.5} \quad \text{[Eq. 4.8]}$$

For the case of a sphere, the velocity gradient term can be evaluated from Newtonian theory. For an axisymmetric body, this corresponds to Eq. 4.9.

$$\frac{dU_e}{dx} = \frac{1}{R_N} \sqrt{\frac{2(p_e - p_\infty)}{\rho_e}} \quad \text{[Eq. 4.9]}$$

Three-dimensional geometries, however, do not always allow for a direct prediction of the stagnation heat flux. For example, an effective curvature radius cannot be used in many applications given the strong influence of the velocity gradients in the streamwise and crosswise directions. As shown by DeJarnette et al. (1987) a generic approximation in these cases is as in Eq. 4.10, where K is a ratio used to define the crosswise velocity gradient to the streamwise velocity gradient. In some cases, this is equal to the ratio of the two principal radii of curvature at the stagnation point. This approach is nevertheless an approximation and is prone to high errors.

$$(q_o)_{3D} = \sqrt{\frac{1+K}{2}} (q_o)_{axisym} \quad \text{[Eq. 4.10]}$$

4.2.2 Experimental measurements

Experimental measurements were performed at the leading edge of a hemispherical nose with a radius of 5mm and at freestream conditions of M_∞=8.2 and Re_∞/m =9.35x10^6. The model consisted of a hemisphere-cone-cylinder which was placed at 0° angle of attack. A thin-film gauge was located at the nose of the model to measure the stagnation heat flux as shown in the schlieren image in Fig. 4.2. Consideration of the measurements at the other locations along the forebody and further details on the model's geometry can be found in Section 4.4. A detached shock wave is observed as expected from previous studies (e.g. Miller et al., 1975). The shock stand-off distance respect the leading edge of the nose is below 0.01R as also expected.

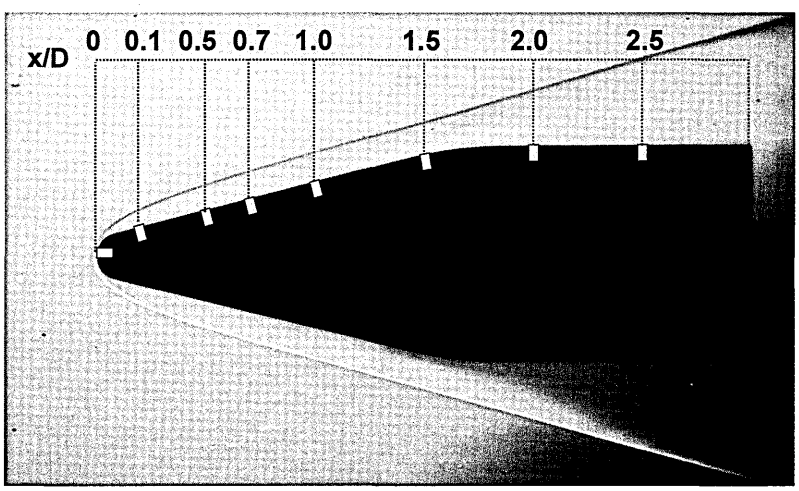

Figure 4.2 Schlieren image of forebody indicating measurement locations in axial direction respect leading edge (refer to Section 4.4).

A measure of the repeatability of the measurements is performed based on three independent tests (Table 4.1). An average stagnation heat flux value of 130.9 W/cm^2 (St_o =22.7x10^{-3}) is determined and measurements differ up to ±1.3% from the average.

Test Number	Experiments St_o (x10^{-3})	Average $St_{o,av}$ (x10^{-3})	Error $(St_o - St_{o,av})/St_{o,av}$
1	23.0	22.7	1.3%
2	22.8		0.4%
3	22.4		-1.3%

.Table 4.1 Stagnation heat transfer repeatability measurements.

Eq. 4.7 in combination with Eq. 4.9 (Fay and Ridell, 1958) are used to obtain a theoretical estimate of the stagnation point heat transfer at the given freestream conditions. Sutherland's law is used to calculate viscosity μ as shown in Eq. 4.12. The estimated heat flux at the stagnation point is q_o=132.6 W/cm^2 (St_o=23.0x10^{-3}). The average experimental value thus differs in -1.3% with respect to the theoretical estimate (Table 4.2). This gives an indication of the expected accuracy of the system for this type of flow. A further uncertainty analysis is found in Appendix C. Stanton number is used throughout the present study to provide a non-dimensional measure of heat flux with respect to the thermal capacity of the flow. Given that the recovery factor in hypersonic flow cannot be determined with accuracy this is assumed r=1 throughout the present study and therefore the presented Stanton numbers calculated as in Eq. 4.2 are effectively equivalent to the heat transfer coefficient as in Eq. 4.1. A total combined uncertainty of ±10% in the measurement of Stanton number is estimated, which is similar to the error range achieved in other similar experimental studies as reviewed by Simmons (1995). The conservative total uncertainty of ±10% - which is significantly higher than the error found in the accuracy assessment - is consistently considered.

$$\mu = 1.458\times10^{6}\frac{T^{1.5}}{T+110.4} \qquad \text{[Eq. 4.12]}$$

Experiments $St_{o,exp}$ (x10^{-3})	Theory $St_{o,th}$ (x10^{-3})	Error $(St_{o,exp} - St_{o,th})/St_{o,th}$
22.7	23.0	-1.3%

Table 4.2 Comparison between experimental and theoretical stagnation heat transfer.

Further evidence of the system's reliability is also shown by CFD simulations of the present case study using the IMPNS code by Mifsud et al. (2009). As mentioned in Section 2.5 this code is based on the solution of the Parabolised Navier Stokes equations. A continuum value of St_o=22.7x10^{-3} (St_o=27.8x10^{-3} considering $r=\sqrt{\text{Pr}}$, with Pr=0.71) was determined in the grid convergence study. This value is the same as the average stagnation Stanton number in the experiments (Table 4.1). Further details on these numerical simulations can be found in Section 4.4.

4.3 Heat transfer to a flat plate

Despite the fundamental nature of the case of a flat plate boundary layer, heat transfer estimation methods are in this case not subject to the unique simplifying assumptions considered in the stagnation point theory. Comparison is made between flat plate heat flux measurements obtained at a variety of freestream conditions in the gun tunnel and the estimated values based on different theoretical predictions.

The flat plate used in this study was the same used to represent the vehicle's fuselage in the study on aerodynamic interference heating. Given that turbulent conditions were to be reproduced for the main part of the present study, the nature of the boundary layer reproduced by the vortex generators and at the location where the protuberances were to be subsequently placed was assessed. This was based on the schlieren visualisations and on the comparison with the theoretical estimates.

4.3.1 Established theory

Relatively simple prediction methods are available to estimate the heat transfer from a boundary layer to a flat surface. Predictive approaches developed to date for laminar and turbulent boundary layers are considered.

4.3.1.1 Laminar flow

The most common approach to predict the flux of heat from a laminar compressible boundary layer to a flat plate is the reference enthalpy method. This approach was originally proposed by Chapman and Rubesin (1949) who noticed that the formulas obtained from incompressible flow theory could be evaluated at a reference temperature to describe compressible flows. This approach was further developed by Eckert (1954) and Monaghan (1955) to include the concept of reference enthalpy also. In their work, a dataset of semi-empirical correlations was approximated to the numerical solutions from van Driest (1952) for compressible boundary layers. The expression for the reference enthalpy in Eq. 4.13 was obtained from their correlations. Whereas the reference enthalpy concept can be used for variable specific heat, in most practical

applications a constant c_p is assumed, where $h = c_p T$. In this case, a reference temperature can be considered as in Eq. 4.14.

$$i^* = i_e + 0.5(i_w - i_e) + 0.22(i_{aw} - i_e) \quad \text{[Eq. 4.13]}$$

$$T^* = T_e + 0.5(T_w - T_e) + 0.22(T_{aw} - T_e) \quad \text{[Eq. 4.14]}$$

The last term in these relations can also be expressed by the Mach number of the flow outside the boundary layer as shown in Eq. 4.15. This gives a clearer indication of the great effect of Mach number, as well as freestream and wall temperatures.

$$T^* = 0.5T_e + 0.5T_w + 0.22r\frac{\gamma - 1}{2}M_e^2 T_e \quad \text{[Eq. 4.15]}$$

Eckert's (1954) expression is the classical definition of reference temperature which has been used in most of the applications to date but a modified definition of this reference temperature has been recently provided by Meador and Smart (2005). While this latter definition derives directly from solutions of the boundary layer equations, contrarily to Eckert's semi-empirical relation, the estimations obtained with Meador and Smart's relation are only slightly more accurate - depending on the freestream conditions - and generally offer little advantages in engineering applications (Anderson, 2006). For a laminar boundary layer the Meador-Smart relation is as follows (Eq. 4.16):

$$T^*/T_e = 0.45 + 0.55\frac{T_w}{T_e} + 0.16r\frac{(\gamma - 1)}{2}M_e^2 \quad \text{[Eq. 4.16]}$$

From classical incompressible theory the skin friction for a laminar boundary layer is given as a function of Reynolds number as shown in Eq. 4.17. The same expression is then evaluated at some reference conditions (Eq. 4.18) where both the skin friction coefficient (Eq. 4.19) and the Reynolds number (Eq. 4.20) are based on values derived from the reference temperature. The reference density ρ^* can be obtained by using the equation of state and assuming the same static pressure and μ^* from Sutherland's relation such that:

$$c_{fi} = 0.664\,\mathrm{Re}_x^{-0.5} \quad \text{[Eq. 4.17]}$$

$$c^*_{fi} = 0.664\,\mathrm{Re}^{*-0.5}_x \quad \text{[Eq. 4.18]}$$

$$c_f^* = \frac{\tau_w}{\frac{1}{2}\rho^* u_e^{\,2}} \quad \text{[Eq. 4.19]}$$

$$\mathrm{Re}^*_x = \frac{\rho^* u_e x}{\mu^*} \quad \text{[Eq. 4.20]}$$

Once the skin friction coefficient is obtained, the Stanton number can then be derived based on the Reynolds analogy. The relation shown in Eq. 4.21 is generally assumed in laminar flow, where Pr* is the Prandtl number evaluated at a reference temperature. For air at standard conditions, the Prandtl number can be considered 0.71 (van Driest, 1952). For more specific details on this analogy refer to White (2005) and Chi and Spalding (1966).

$$\frac{St_i}{0.5c_{fi}} = \left(\mathrm{Pr}_e\right)^{-2/3} \quad \text{[Eq. 4.21]}$$

Substituting the definition of friction coefficient in Eq. 4.18 into Eq. 4.21, an expression for Stanton number evaluated at reference conditions is obtained such that:

$$St^* = 0.332\left(\mathrm{Pr}^*_e\right)^{-2/3}\left(\mathrm{Re}^*_x\right)^{-1/2} \quad \text{[Eq. 4.22]}$$

From the reference Stanton number (St*) the heat flux can be evaluated based on the reference properties as in Eq. 4.23. This equation derives directly from the definition of Stanton number (Eq. 4.2).

$$q = \rho^* u_e c_p \left(T_{aw} - T_w\right) St^* \quad \text{[Eq. 4.23]}$$

The estimations obtained in the present case with the reference temperature method are compared with the equivalent predictions using the solutions for a laminar compressible boundary layer plotted in van Driest (1952) in terms of $St\,\mathrm{Re}_x^{0.5}$ against freestream Mach number for various wall temperature ratios T_w/T_∞ (Fig. 4.3). As it can be observed from these results, the general trend of $St\,\mathrm{Re}_x^{0.5}$ is to decrease as Mach number increases and also as T_w/T_e increases. Summarised in Table 4.4 are the estimations for laminar flow at a range of different conditions simulated in the gun tunnel. The conditions at the boundary layer edge are assumed equal to the freestream conditions. Results of the boundary layer heat flux are in this section more suitable considered in W/cm^2 units as usually done in the literature for undisturbed boundary layer heat flux. In general, good agreement among the different prediction methods is observed.

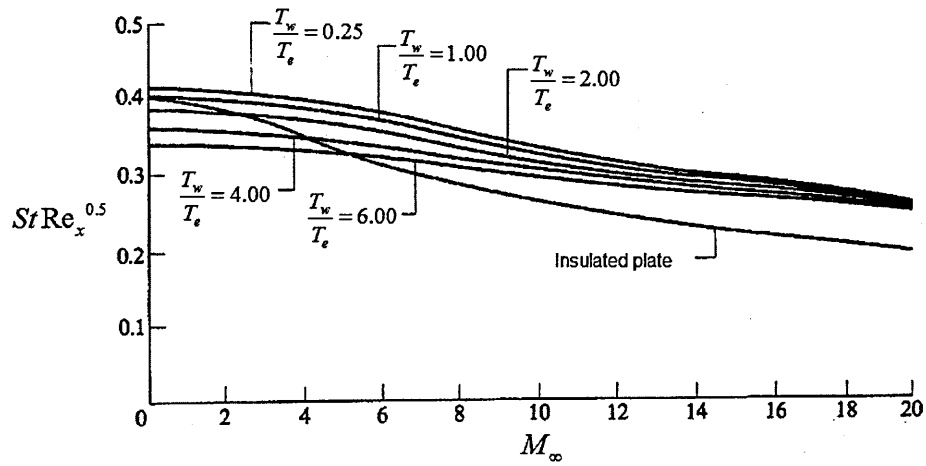

Figure 4.3 Flat plate solutions for different M_∞ and T_w/T_e based on van Driest (1952).

	Classic T* q (W/cm^2)	M-S T* q (W/cm^2)	van Driest q (W/cm^2)	Error $(q_{max}-q_{min})/q_{min}$
M_∞=8.2, Re_∞/m=9.35x10^6	1.3	1.4	1.3	8 %
M_∞=8.2, Re_∞/m=8.06x10^6	1.0	1.0	1.0	0%
M_∞=8.2, Re_∞/m=6.57x10^6	0.7	0.7	0.6	16%
M_∞=8.2, Re_∞/m=4.84x10^6	0.3	0.3	0.3	0%
M_∞=12.3, Re_∞/m=3.35x10^6	0.3	0.4	0.3	25%

Table 4.3 Theoretical predictions for laminar boundary layers at different operating conditions of gun tunnel.

4.3.1.2 Turbulent flow

For predicting the heat flux from a compressible turbulent boundary layer to a flat plate, the reference enthalpy method is also generally used. However, estimation errors in the case of turbulent boundary layers are higher than in laminar flow principally due to the difficulty in predicting the skin friction coefficient. Different definitions of skin friction coefficient can be found in the literature. This coefficient is given as a function of local Reynolds number based on semi-empirical correlations. Two independent definitions have been considered in the present study: Eq. 4.24 (taken from White, 1974) and Eq. 4.25 (taken from Schlichting, 1979). Further definitions found in the literature are shown in Eq. 4.26 (Schoenherr, 1952) and Eq. 4.27 (Crabtree et al., 1965) but are not considered here for the sake of simplicity and due to their less common use.

in White (1974): $c_{fi} = 0.0592\,\mathrm{Re}_x^{-0.2}$ [Eq. 4.24]

in Schlichting (1979): $c_{fi} = 0.02296\,\mathrm{Re}_x^{-0.139}$ [Eq. 4.25]

in Schoenherr (1952): $c_{fi} = 0.370\log(\mathrm{Re}_x)^{-2.584}$ [Eq. 4.26]

in Crabtree et al. (1965): $c_{fi} = 0.288\log(\mathrm{Re}_x)^{-2.45}$ [Eq. 4.27]

Reynolds analogy is again used to relate skin friction to Stanton number. Whereas for laminar boundary layers the ratio $St_i/\left(0.5c_{fi}\right)$ is theoretically equal to $\left(\mathrm{Pr}_e\right)^{-2/3}$, turbulent experimental data shows that a suitable ratio for turbulent boundary layers is 1.22 (Crabtree et al., 1965), Eq. 4.28. This ratio is therefore higher than the corresponding laminar value.

$$\frac{St_i}{0.5c_{fi}} = 1.22 \text{ [Eq. 4.28]}$$

By inserting the relations for skin friction in Eq. 4.24 and Eq. 4.25 into the Reynolds analogy in Eq. 4.28, the equations for Stanton number are derived. In terms of the reference conditions these are respectively as shown in Eq. 4.29 (from Eq. 4.24) and Eq. 4.30 (from Eq. 4.25).

$$St_i = 0.0142\,\mathrm{Re}_x^{-0.139} \text{ [Eq. 4.29]}$$

$$St^* = 0.0365\,\mathrm{Re}^*_x{}^{-0.2} \text{ [Eq. 4.30]}$$

The reference conditions can be evaluated at the classical reference temperature of Eckert (Eq. 4.15) or at the more recent definition of Meador and Smart (2005), which for turbulent boundary layers is:

$$T^*/T_e = 0.5\left(1+T_w/T_e\right)+0.16r\frac{(\gamma-1)}{2}M_e^2 \text{ [Eq. 4.31]}$$

Theoretical estimations considering the flow conditions reproduced in the gun tunnel are listed in Table 4.5. The three different approaches considered are:

i. Method 1: The classic definition of T* in Eq. 4.15 is used with the definition in White (1974) of skin friction coefficient, Eq. 4.24.

ii. Method 2: The classic T* (Eq. 4.15) is used with the definition in Schlichting (1979) of skin friction coefficient, Eq. 4.25.

iii. Method 3: The more recent T* definition of Meador-Smart in Eq. 4.31 is used with the definition in Schlichting (1979) of skin friction coefficient, Eq. 4.25.

	Method 1 q (W/cm^2)	Method 2 q (W/cm^2)	Method 3 q (W/cm^2)	Error $(q_{max} - q_{min})/q_{min}$
M_∞=8.2, Re_∞/m=9.35x10^6	4.3	3.0	3.5	43 %
M_∞=8.2, Re_∞/m=8.06x10^6	3.0	2.1	2.4	43%
M_∞=8.2, Re_∞/m=6.57x10^6	1.8	1.2	1.4	50%
M_∞=8.2, Re_∞/m=4.84x10^6	0.7	0.5	0.5	40%
M_∞=12.3, Re_∞/m=3.35x10^6	0.5	0.3	0.4	66%

Table 4.4 Theoretical predictions for turbulent boundary layers at different operating conditions of gun tunnel.

As shown by the large differences in some of these theoretical estimates (up to 66%), the prediction of heat transfer in turbulent flow is clearly subject to significantly higher errors than those in laminar flow. This was already shown in the work of Meador and Smart (2005), who offered a comparison of the predictions with the reference enthalpy methods using their definition of reference temperature and this of Eckert with respect to van Driest's (1952) boundary layer solutions. The percentage difference relative to the boundary layer solutions is expected to be of approximately 20%-30% at high T_w / T_e ratios and at high Mach numbers. As an example, Fig. 4.4 compares Eckert's and Meador-Smart's predictive approaches with the van Driest boundary layer solutions in the prediction of skin friction coefficient, which is considered to be proportional to the boundary layer heat flux through Reynolds analogy. The reference temperature method is found to underpredict the corresponding values from the solutions of van Driest (1952). It must therefore be remarked that despite the relative simplicity of the case of flat plate boundary layers, the available methods are of an approximate nature only. This is a good example of the great complexity involved in the prediction of heat transfer in hypersonic turbulent flows.

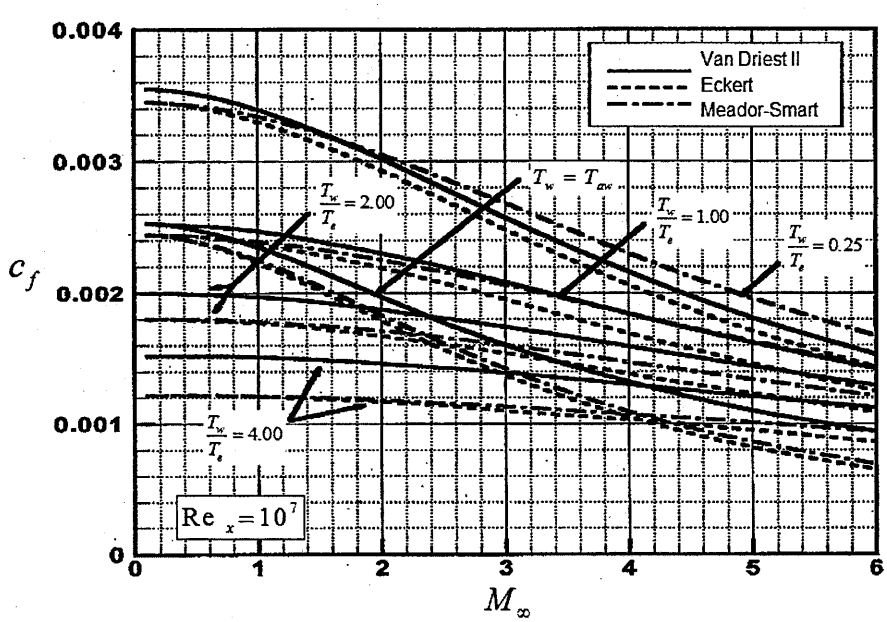

Figure 4.4 Boundary layer solutions of turbulent flat plate c_f compared with reference temperature methods based on Meador and Smart (2005).

4.3.2 Experimental measurements

At all the different freestream conditions simulated in the gun tunnel, the same vortex generators (1mm-high) were used with the purpose of obtaining a turbulent boundary layer. A fully turbulent boundary layer was not achieved in all the cases given the lower Reynolds numbers at some of the operating conditions. The state of the boundary layer was determined based on the schlieren images and the comparison between experimental heat transfer measurements and the corresponding theoretical estimations. This was then used to assess the state of the boundary layer at the reference location (x_{le}=175mm) in the experimental study of interference heating (Chapter 5). The criteria to distinguish the state of the boundary layer were the following:

i. *Criterion 1:* The appearance of the boundary layer in the schlieren images allowed discrimination between fully laminar conditions and transient/turbulent conditions. This was qualitatively observed by sampling lines of pixel data at several stations from the markedly higher intensity of the laminar boundary layer (≈255/255 pixel intensity) in comparison to this of a transitional or turbulent boundary layer (approximately 100/255 to 150/255 pixel intensity) as qualitatively shown in Fig. 4.5. Further schlieren images at different test conditions are shown in Chapter 5.

ii. *Criterion 2:* In cases where there was a doubt on whether the boundary layer was fully turbulent or transitional, comparison was made between the heat transfer measurements and the corresponding predicted estimates. Underpredictions about 20%-30% were expected in the turbulent estimations (Meador and Smart, 2005). In this way, in the cases where heating was closer to the laminar estimation - despite not appearing as a laminar boundary layer in the schlieren image - a transitional boundary layer was effectively identified.

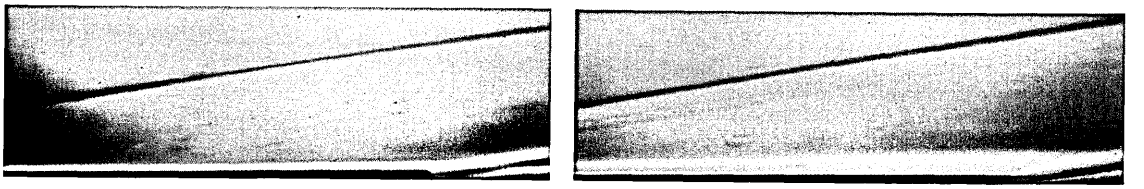

(a) Laminar flow (b) Turbulent flow

Figure 4.5 Schlieren images: M_∞=8.2, $Re_\infty/m=9.35x10^6$. Flow from left to right.

A summary of the experimental measurements and the corresponding estimates (considering a 30% underprediction in the turbulent cases) is found in Table 4.5 together with the inferred state of the boundary layer for all the different conditions. Based on this evidence, fully turbulent conditions are obtained at Mach 8.2 with drive pressures of 13.8×10^6 Pa ($Re_\infty/m=9.35 \times 10^6$) and 10.3×10^6 Pa ($Re_\infty/m=8.06 \times 10^6$) and at Mach 12.3 with 13.8×10^6 Pa ($Re_\infty/m=3.35 \times 10^6$). A transitional boundary layer is obtained at lower drive pressures of 6.9×10^6 Pa ($Re_\infty/m=6.57 \times 10^6$) at Mach 8.2 and 3.5×10^6 Pa ($Re_\infty/m=4.84 \times 10^6$). As expected, without vortex generators fully laminar conditions are obtained.

	Experiments ($x_{le} \approx 175$mm)		Estimates		Boundary layer state		
	No VG q (W/cm^2)	With VG q (W/cm^2)	Lam. q (W/cm^2)	Turb. q (W/cm^2)	Lam.	Tran.	Turb.
$M_\infty=8.2$, $Re_\infty/m=9.35 \times 10^6$	1.8	5.9	1.7	5.6	X	---	X
$M_\infty=8.2$, $Re_\infty/m=8.06 \times 10^6$	---	3.8	1.3	3.9	---	---	X
$M_\infty=8.2$, $Re_\infty/m=6.57 \times 10^6$	---	1.0	0.9	2.3	---	X	---
$M_\infty=8.2$, $Re_\infty/m=4.84 \times 10^6$	---	0.3	0.4	0.9	---	X	---
$M_\infty=12.3$, $Re_\infty/m=3.35 \times 10^6$	---	0.9	0.4	0.7	---	---	X

Table 4.5 Assessment of boundary layer state at reference location. Laminar estimates use classic T* from Eckert. Turbulent estimates use Method 1. 30% underprediction is considered.

The datum undisturbed heat flux measurement is very close (5% higher) to previous measurements by Prince (1994) performed in the same facility and test conditions ($M_\infty=8.2$ $Re_\infty/m=9.35 \times 10^6$, turbulent) and using a similar VG design. As shown in Appendix A, this value is consistently measured in the undisturbed flow regions for all the different tests. A further analysis of the heat flux measurements in the vicinity of surface protuberances in the following chapters demonstrates the validity of the measurements and confirms the inferred state of the boundary layer in Table 4.5. Further evaluation of the experimental uncertainties is found in Appendix C, which together with the agreement in the stagnation heat flux measurements proves the accuracy of the system.

4.4 Heat transfer over a hemisphere-cone-cylinder

As shown in the previous sections, the rate of stagnation heating to a hemispherical body is inversely proportional to the square root of the nose radius. It is also known that in order to reduce the drag of a hypersonic vehicle a slender afterbody is preferred. For these reasons, hemisphere-cone forebodies are a common shape in hypersonic flows.

The heat transfer over a hemisphere-cone with a semi-angle of 15° was measured at a freestream Mach number of 8.2 and $Re_\infty/m=9.35x10^6$, and at both laminar and turbulent conditions. Measurements were made at different axial locations along the surface of the test model: x/D=0.2, 0.5, 0.7, 1.0, 1.5, 2.0 and 2.5 and a comparison was made with predictive approaches. The geometry of the model is shown in Fig. 4.6. The forebody consists of a spherically blunt cone followed by a tangent-ogive with a length of 2.0D. A cylindrical portion of diameter 1.0D follows the nose with a length of 1.0D. A schlieren image is found in Fig. 4.2.

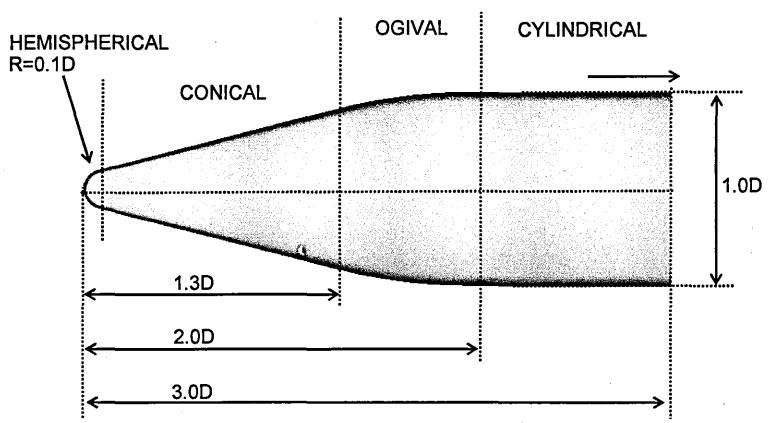

Figure 4.6 Forebody geometry.

4.4.1 Established theory

In regions far from the stagnation point, the flow properties can often be approximated by relations developed for flat plate configurations. Where reasonable predictions can be obtained by direct application of flat plate estimations over wing and cylindrical surfaces at 0° angle of attack, other geometries with more marked three-dimensionality, such as conical regions, present further complications (Hayes and Neumann, 1992).

4.4.1.1 Laminar flow

The flow around a cone is subject to a three-dimensional relieving effect that results in a thinning of the boundary layer and in turn in larger velocity and temperature gradients through it. Higher skin friction and surface heating than in an equivalent two-dimensional boundary layer over a flat plate and at the same edge conditions thus takes place. Previous studies have suggested that this effect can be accounted for by using proportionality factors applied to the flat plate boundary layer predictions. A typical approach for laminar cases consists of calculating the heat flux to a flat plate with the corresponding boundary layer edge conditions and applying the Mangler factor of $\sqrt{3}$ as shown in Eq. 4.32. To obtain the conversion between freestream conditions to local conditions over the conical surface, reference can be made to NACA report 1135 (1953). The corresponding flat plate values over the conical region in this case are: M_∞=5.26, p_∞=6800Pa, T_∞=197.4K. Although this simple approach is valid for sharp cone configurations, estimations over blunt cones can be made by assuming the flow to be far from the leading edge. Estimations in such cases can also be made by reference to the numerical solutions presented by Crabtree et al. (1965) for sharp cones. In their work, the ratio q/q_o was plotted for different cone semi-angles against the ratio x/R, where R is the nose radius of the body (Fig. 4.7). By calculating the corresponding stagnation heat transfer q_o with the theory of Fay and Riddell (Section 4.2) the heat flux at different distances over the conical surface can be estimated.

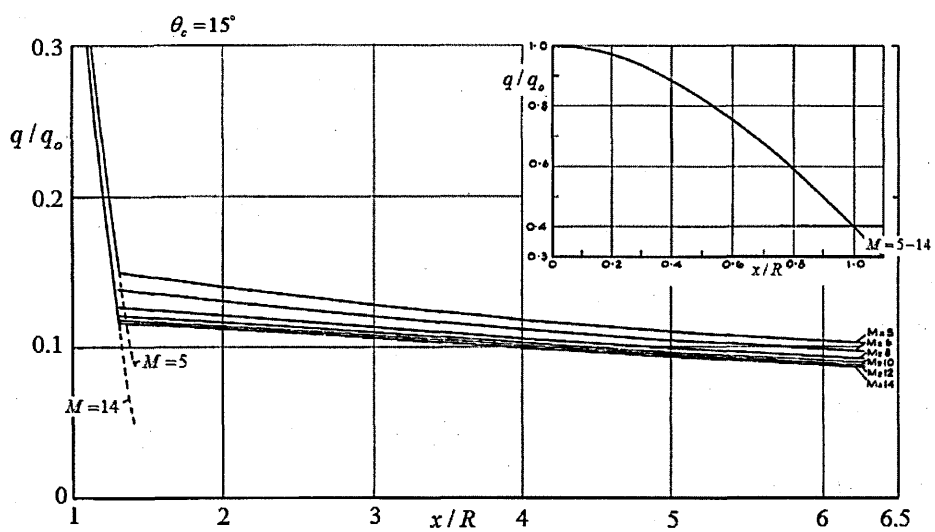

Figure 4.7 Heat flux along a 15° semi-angle sharp cone. Based on Crabtree et al. (1965).

$$q_{cone} = \sqrt{3} q_{fplate} \quad \text{[Eq. 4.32]}$$

Theoretical predictions in this case are listed in Table 4.6 using the following three different methods: the Eckert T* method considering the Mangler factor, the Meador-Smart T* method with the Mangler factor as well and Crabtree's et al. (1965) solutions. At distances close to the leading edge of the forebody, theoretical estimates differ up to 68% among them. This demonstrates that high errors are involved in the application of the Mangler factor close to the blunt leading edge as also supported by the experimental data (Section 4.4.2). Crabtree et al.'s (1965) numerical solutions are therefore expected to be more accurate. Along the cylindrical region of the forebody (Table 4.7), the reference enthalpy method is directly applied. As in Section 4.3, both the classic T* from Eckert and this of Meador-Smart are used. Reference is also made to the numerical solutions from van Driest (1952). Estimates along the cylindrical portion based on van Driest' solutions are up to 2 times higher (100% error) than the estimates using Eckert's reference enthalpy method. However, this is partly due to the low heat flux over the cylindrical region in comparison to this over the conical section. Along the conical region a reasonable agreement between the different estimates is obtained except at the locations close to the blunt leading edge.

x (mm)	Mangler & Eckert T* q (W/cm^2)	Mangler & M-S T* q (W/cm^2)	Crabtree et al. (1965) q (W/cm^2)	Error $(q_{max} - q_{min})/q_{min}$
10	26.3	26.8	15.9	68%
25	16.6	16.9	13.3	27%
35	14.1	14.3	12.6	13%
50	11.8	12.0	11.9	2%
75	9.6	9.8	10.6	10%

Table 4.6 Theoretical predictions along conical-ogival region for laminar flow.

x (mm)	Eckert T* q (W/cm^2)	M-S T* q (W/cm^2)	van Driest (1965) q (W/cm^2)	Error $(q_{max} - q_{min})/q_{min}$
100	1.3	1.4	2.6	100%
125	1.8	1.9	1.4	36%

Table 4.7 Theoretical predictions along cylindrical region for laminar flow.

4.4.1.2 Turbulent flow

A similar approach as in the previous section is used for the turbulent boundary layer cases. It is again assumed that a similarity exists between the heat flux over the conical surface (q_{cone}) with this over a flat plate (q_{fplate}). In this case, the proportionality is considered as in Eq. 4.33 (White, 1974), where q_{fplate} needs to be evaluated with the corresponding local conditions over the cone surface as described in the previous section. This factor is considerably below the laminar value of $\sqrt{3}$ (i.e. 36% lower). Estimations in Table 4.10 are presented using three different approaches, corresponding to the methods shown in Section 4.3.1.2: Method 1 (Eq. 4.15 and 4.24) and Method 2 (Eq. 4.15 and 4.25) which consider the classic T* from Eckert, and Method 3 (Eq. 4.31 and 4.25) which considers the Meador-Smart (M-S) T*. Whereas the Mangler factor is applied over the conical and ogival portion, a direct application of these methods is considered over the cylindrical region as in the previous section. Table 4.11 summarises the estimations obtained, where the highest variations in the prediction of heat flux are found along the cylindrical portion and with values up to 45%.

$$q_{cone} = 1.1 q_{fplate} \quad \text{[Eq. 4.33]}$$

x (mm)	Method 1 q (W/cm^2)	Method 2 q (W/cm^2)	Method 3 q (W/cm^2)	Error $(q_{max} - q_{min})/q_{min}$
10	33.9	24.9	27.6	36%
25	28.3	21.9	24.3	29%
35	26.4	20.9	23.2	26%
50	24.6	19.9	22.1	24%
75	22.7	18.8	20.9	21%

Table 4.8 Theoretical predictions along conical-ogival region for turbulent flow.

x (mm)	Method 1 q (W/cm^2)	Method 2 q (W/cm^2)	Method 3 q (W/cm^2)	Error $(q_{max} - q_{min})/q_{min}$
100	4.8	3.3	3.9	45%
125	4.6	3.2	3.7	44%

Table 4.9 Theoretical predictions along cylindrical region for turbulent flow.

4.4.2 Experimental measurements

The experimental measurements are listed in Table 4.10 for the laminar boundary layer cases. Measurements from the turbulent boundary layer simulations are listed in Table 4.11. The boundary layer trip in this case was carburundum grit particles placed at the start of the conical section. For both the laminar and turbulent cases, the peak heat transfer is located at the nose followed by a generally decreasing trend moving aft on the body. As expected, the turbulent configurations show a higher level of heat transfer over the body. Furthermore, for both sets of experimental data, there is a local heat transfer minimum along the conical section at approximately 0.7D which is ultimately followed by a decrease over the cylindrical section. It was ensured during the experiments that this trough was not linked to a system error and therefore there is some unidentified flow mechanism linked to this trend. Considering the theoretical estimates based on Crabtree et al. (1965) and van Driest (1952) for the laminar case along the conical and cylindrical regions respectively, and Method 2 (based on the Eckert T* method) for the turbulent case a generally good agreement is observed along the forebody, except in the dip in heat flux at x=0.7D. The laminar predictions at all the other locations are within an agreement of 13% or lower. Higher errors - of up to about 40% - are found in the turbulent predictions.

x (mm)	10	25	35	50	75	100	125
q_{exp} (W/cm^2)	16.8	12.7	9.6	12.0	9.2	2.6	1.4
St_{exp} (x10^{-3})	2.9	2.2	1.7	2.1	1.6	0.5	0.2
Error $(St_{exp}-St_{th})/S_{th}$	6%	-4%	-23%	1%	-13%	-1%	-2%

Table 4.10 Heat transfer along forebody and related uncertainty. Laminar flow.

x (mm)	10	25	35	50	75	100	125
q_{exp} (W/cm^2)	24.6	16.1	12.3	14.9	13.4	3.8	2.0
St_{exp} (x10^{-3})	4.3	2.8	2.1	2.6	2.3	0.7	0.3
Error $(St_{exp}-St_{th})/S_{th}$	-1%	-26%	-41%	-25%	-28%	16%	-39%

Table 4.11 Heat transfer along forebody and related uncertainty. Turbulent flow.

Further comparison of the present results is done with the corresponding PNS simulations by Mifsud et al. (2009). A full comparison with the present experiments and theoretical estimates is shown in Fig. 4.8. Considering the overall trend of heat flux over the forebody, the laminar predictions begin high at the stagnation point and then continuously decrease over the body length. In contrast, the turbulent predictions start high at the stagnation point, decrease over the hemisphere nose before rising over the conical region and the initial part of the ogival region to then keep falling towards the end of the model. Simulations with the algebraic turbulence model of Baldwin-Lomax (1978) predict a higher heat flux than the 1-equation turbulence model of Spalart-Allmaras (1992). In fact, the Spalart-Allmaras predictions follow the laminar heat flux level closely over the hemispherical nose before increasing with distance along the body.

In general, good agreement is shown between the empirical predictions for both laminar and turbulent assumptions and the experimental and computational results. Over the hemisphere-cone-ogive region, both analytical and experimental results with a turbulent boundary layer are close to the turbulent Baldwin-Lomax and Spalart-Allmaras predictions. In contrast, over the cylindrical portion, the turbulent Baldwin-Lomax predictions are higher than the analytical and experimental predictions, which find better agreement with the Spalart-Allmaras turbulence model.

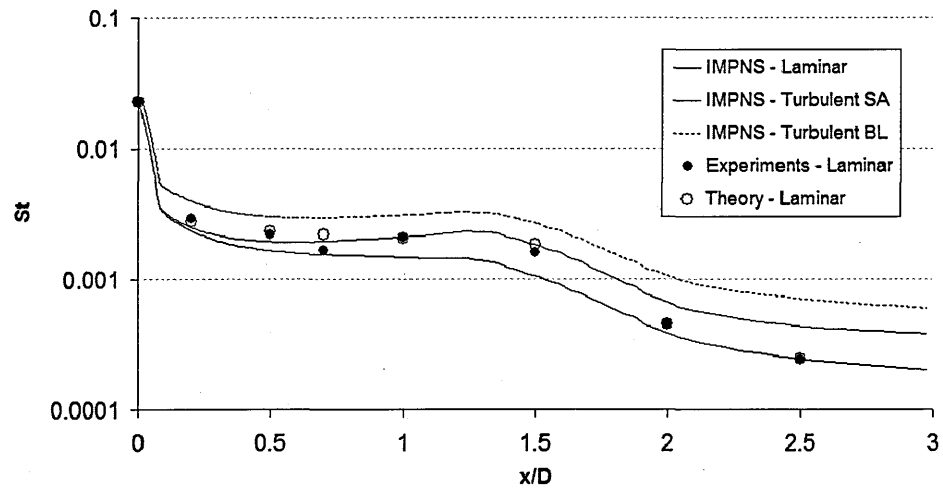

(a) Laminar flow experiments and theory compared with laminar and turbulent simulations.

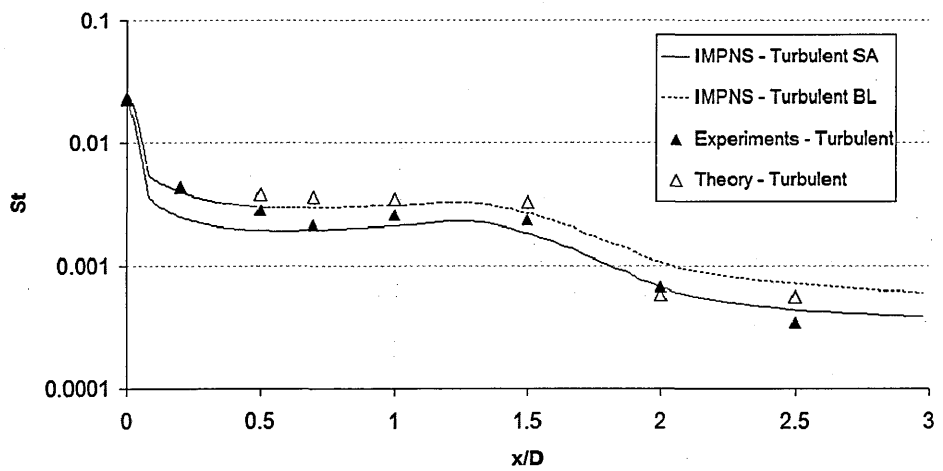

(b) Turbulent flow experiments and theory compared with turbulent simulations.

Figure 4.8 Experimental heat flux measurements along hemisphere-cone-cylinder body compared with IMPNS computations and theoretical estimates from Mifsud et al. (2009).

4.5 Application to real vehicles

The application of heat flux predictive methods in attached flow has been reviewed. The prediction of the heat flux in stagnation regions is well established but significant errors are expected in regions of undisturbed turbulent flow. Despite the approximate nature of these predictive approaches, their application has been used in the preliminary design analysis of hypersonic vehicles such as the Space Shuttle and the Apollo Command Module (Neumann and Hayes, 1992). Reasonable estimates of the actual flight environment have been obtained while real gas effects are not considerable.

As an example, the approach used for the estimations on the Space Shuttle Orbiter is shown in Fig. 4.9. As described by Haney (1983), the Space Shuttle Orbiter's TPS was designed mainly on the basis of theoretical estimations and wind tunnel data. For that, the vehicle was divided into a combination of simple shapes for which analytical solutions were available. These more tractable shapes included: cones, cylinders, flat plates, spheres and wedges. Although significant differences were noticed between the theoretical heat transfer and that measured in the wind tunnel, such variations were considered through the use of calibration factors as shown in Fig. 4.10. Based on these results, the wind tunnel data were applied directly to flight by relating them to a pertinent reference heat flux.

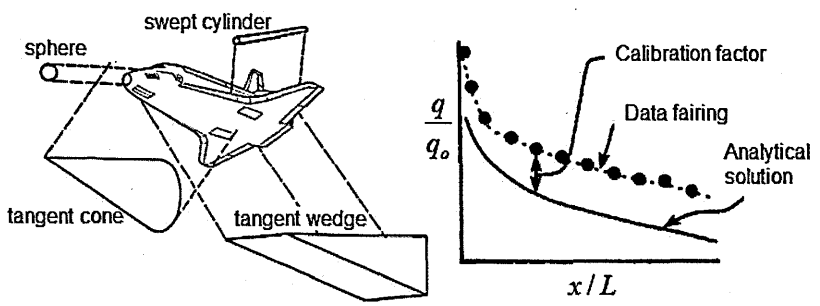

Figure 4.9 Analysis techniques applied in design of Space Shuttle and data on windward lower section. Based on Bertin (1992).

The percentage errors estimated using this approach are summarised in Fig. 4.12. These errors may seem very high but demonstrate that the prediction of the aerodynamic heating of hypersonic vehicles is one of the most challenging areas for both experimentalists and analysts. Conservative predictions are taken into account in the first development stages of any hypersonic vehicle, especially in regions of viscous interactions in which the prediction of heat flux is particularly subject to higher errors. An insight into this problem is offered in the following chapter.

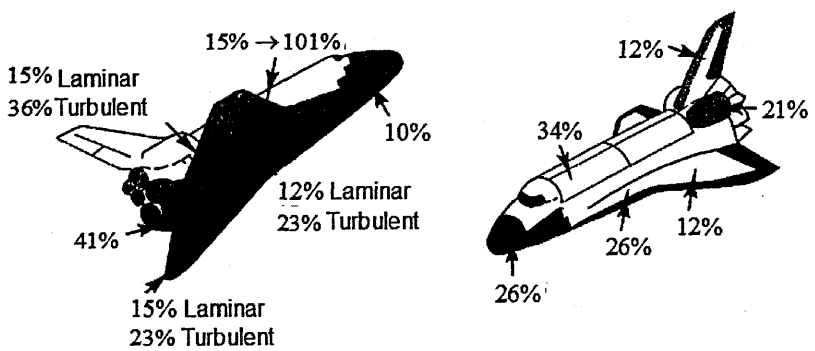

Figure 4.10 Uncertainties in pre-flight heating estimates for the Shuttle Orbiter based on empirical correlations complemented by analytical solutions (Hayes and Neumann, 1992).

CHAPTER 5

Heat Transfer in Interference Regions

In this chapter, experimental measurements are analysed to obtain an understanding of the viscous interaction induced by surface protuberances on a hypersonic vehicle. The effects of the local interference interaction on the heating of the vehicle surface are investigated in detail. Initially, the flow around the datum configuration is studied. This is followed by a brief assessment of the effects of protuberance height and width. The effect of protuberance deflection angle is also studied, together with the case of a protuberance with forward deflection. The effect of freestream conditions including boundary layer state, freestream Reynolds number and freestream Mach number is also investigated.

5.1 Datum case

The experimental investigation was centred around the datum configuration of a 30°-deflected protuberance at Mach 8.2 and with a unit Reynolds number of $Re_\infty/m=9.35x10^6$ (Table 5.1). A turbulent boundary layer with thickness δ_u=5.0mm ± 0.5mm was obtained with the vortex generator strip (Section 3.4). The h/δ_u ratio of the protuberance was thus equal to 1 and W/δ_u was 2.7.

M_∞	Re_∞ / m [m^{-1}]	T_w [K]	α [°]	h/δ_u	W/δ_u	VG h [mm]
8.2	$9.35x10^6$	295	30	1	2.7	1

Table 5.1 Freestream conditions for datum configuration.

A snapshot schlieren image of this configuration is shown in Fig. 5.1. The boundary layer just ahead of the protuberance is primarily undisturbed ($\delta_u \approx 5$mm) until it impacts on the model. An attached shock is observed in the schlieren image. The larger shock spanning from left to right in the image is the weak shock which originates at the flat plate leading edge. Its effect in the present study is insignificant.

Heat flux measurements in the vicinity of this protuberance are shown in Fig. 5.2 using the local Stanton number. As described in Chapter 4, since the recovery factor in hypersonic flow cannot be determined with accuracy this is assumed r=1 throughout the present study and therefore the Stanton number is effectively equivalent to the heat transfer coefficient (C_H) in this case.

The heat flux ahead of the protuberance is of the same order or slightly lower than the corresponding undisturbed heat flux value of St_u=1.0x10^{-3} (q_u=5.9 W/cm^2). The lower values can be explained due to the slight thickening of the boundary layer at that location which results in lower temperature gradients through it. The highest heating is located to the side of the protuberance with a value of St_{max}=2.9x10^{-3} (q_{max}=17.0W/cm^2) at $\mathrm{Re}_{x,k} = 9.8\times10^4$ ($x_k = 10.5$mm) and $\mathrm{Re}_{y,cl} = 7.5\times10^4$ ($y_{cl} = 8$mm). The increase in heating extending along the protuberance side is therefore nearly 3 times higher than the undisturbed heat flux value as plotted in Fig. 5.3 for the different axial measurement locations. The distances in the plots presented are non-dimensionalised with respect to the freestream Reynolds number and where appropriate to the original dimensions in the experiments. Although this is not common practice, the non-dimensionalisation of distance based on other parameters more commonly used (e.g. W, h, δ_u, etc.) is considered misleading in this case since it does not provide a suitable scaling in all the interactions as further shown in the following sections. Instead, the freestream Reynolds number appears to scale with the dimensions of the flow features linked with the increased heating in these interactions. It must therefore be kept in mind that the respective Reynolds numbers in the text effectively correspond to non-dimensional distances. Plan view plots of the heat flux measurements are included in Appendix A.

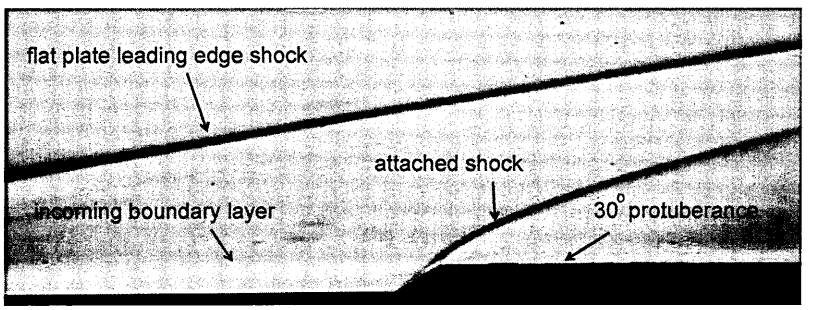

Figure 5.1 Schlieren image: turbulent, M_∞=8.2, Re_∞/m=9.35x10^6, α=30°. Flow from left to right.

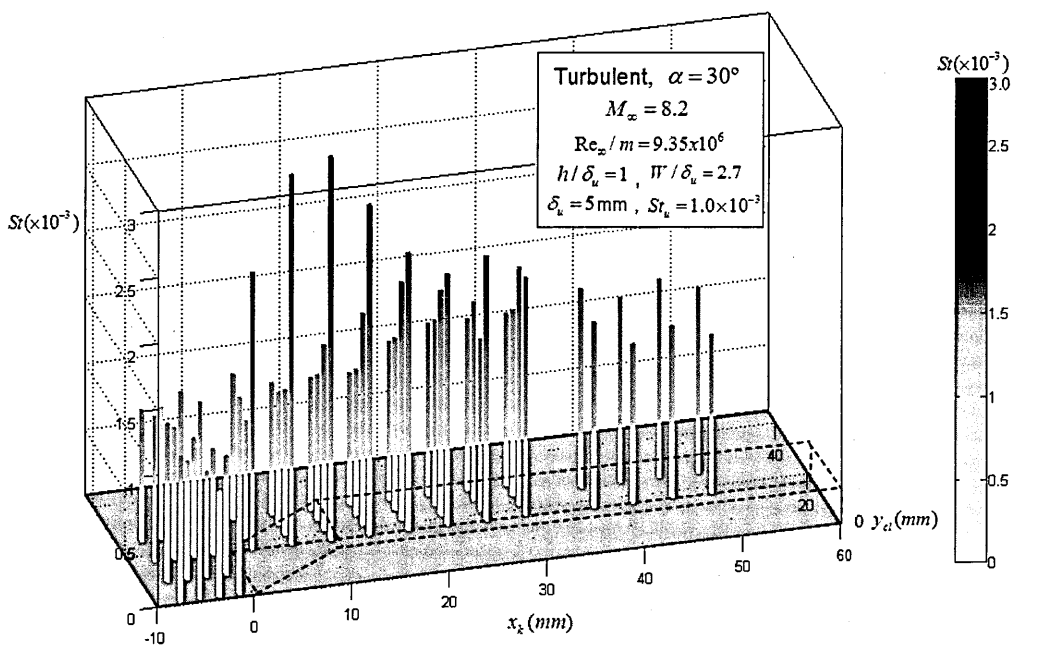

Figure 5.2 3D bar plot of heat flux measurements in the vicinity of datum protuberance.

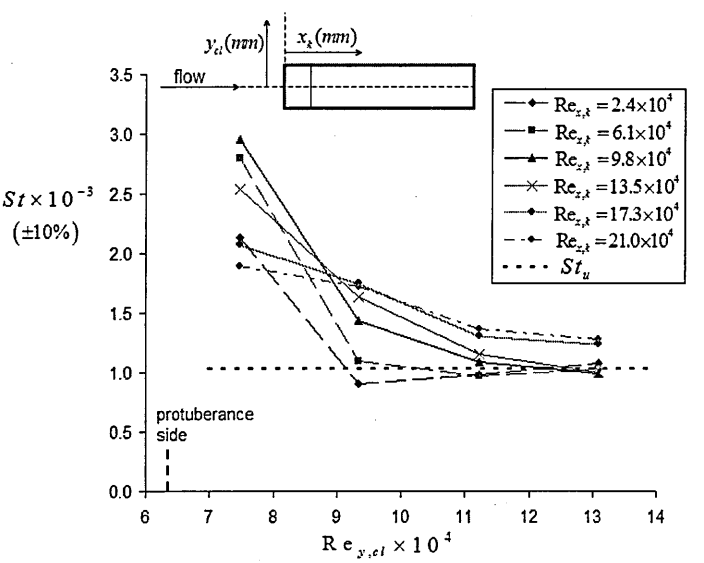

Figure 5.3 Heat flux at different cross-sectional locations to datum protuberance side.

5.2 Effect of protuberance dimensions

The effect of protuberance width and protuberance height of relevance to the present measurements was briefly studied. Due to the small working section and high-resolution requirements to which the test models were subject, a brief assessment was performed considering the cases where the h/δ_u ratio was doubled relative to the datum and another where W/δ_u was similarly doubled. The wind tunnel conditions during these tests were the same as those considered in the datum case.

5.2.1 Protuberance height

The aspect of the flow field in this case is very similar to this of the datum configuration which show two subcritical interactions in the schlieren images (Fig. 5.4). The heat flux to the side of this protuberance is qualitatively similar to that in the datum interaction also and measurements at the centreline ahead of the h/δ_u=1 and h/δ_u=2 protuberances match within 98.7% of the peak value as shown in Fig. 5.5. The behaviour of the boundary layer is therefore insensitive to the height of the protuberance for these cases.

5.2.2 Protuberance width

A W/δ_u ratio of 5.4 was considered. This is twice the W/δ_u =2.7 of the datum geometry. The schlieren results show that the aspect of the flow field is the same as with the datum protuberance model (Fig. 5.4). The local shock wave is distinguished more clearly due the increased width of the test model and given that schlieren is a spatially integrating technique. Heat flux measurements in the vicinity of this protuberance model can be found in Appendix A.

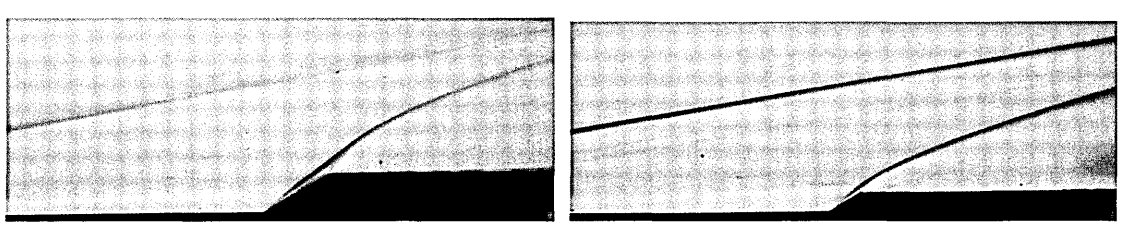

(a) h effect: h/δ_u=2, W/δ_u=2.7 (b) W effect: h/δ_u=1, W/δ_u=5.4

Figure 5.4 Schlieren image: turbulent, M_∞=8.2, $Re_\infty/m=9.35x10^6$, α=30°. Flow from left to right.

Measurements to the side of the models show that the effects of width as well as of height on the hot spot are also negligible in practice (St_{max}=2.5x10^{-3} to 2.9x10^{-3} are measured in the three cases, Fig. 5.6). These findings suggest that the maximum heating in the vicinity of surface protuberances with a subcritical interaction is independent of protuberance height, which is in contrast to equivalent supercritical studies by Hung and Clauss (1980) and Hung and Patel (1984). The present investigation, however, has not considered h/δ_u ratios lower than 1. In these cases, particularly if the protuberance is totally submerged into the subsonic portion of the boundary layer, the local heat flux augmentation is not expected to be as significant and therefore they are not of particular importance. The effect of width on the magnitude of the hot spot is negligible in subcritical interactions as in short and wide supercritical protuberances (Hung and Patel, 1984). Further understanding on the flow field is offered in Chapter 7.

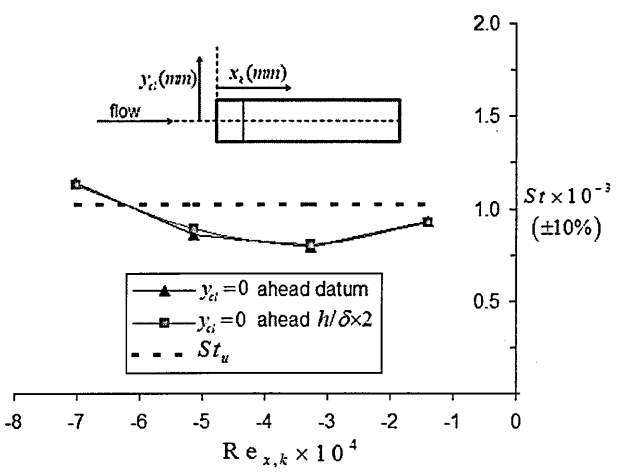

Figure 5.5 Heat flux measurements ahead of datum h/δ_u=1 and h/δ_u=2 configurations.

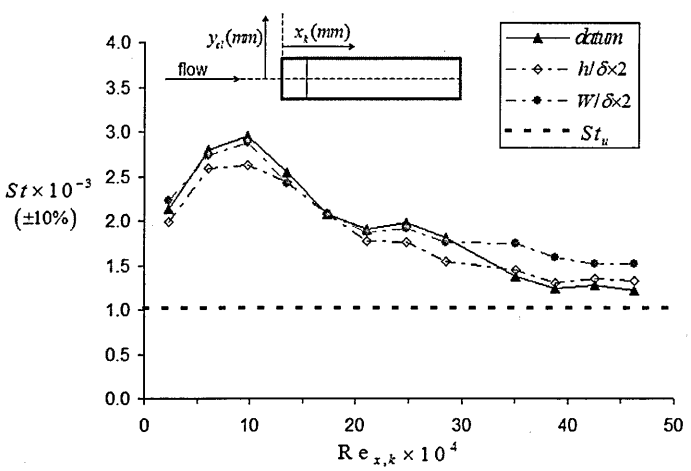

Figure 5.6 Heat flux along side of datum, h/δ_ux2 and W/δ_ux2 cases, y_{cl}=8mm.

5.3 Effect of deflection angle

A further study was performed to determine the effect of deflection angle. Protuberance models with the same height, width and length as the datum protuberance, but with leading edge angles of α=15°, α=45°, α=60° and α=90°, were used to assess the effect of protuberance deflection angle. The freestream conditions were the same as for the datum study (M_∞=8.2, $Re_\infty/m=9.35x10^6$, turbulent).

Instantaneous schlieren images for each of the leading edge deflection angle configurations are shown in Fig. 5.7. As the deflection angle increases and thus the local interaction becomes stronger, a separation region is observed ahead of the protuberance. At these freestream conditions, subcritical interactions are obtained with the α=15° protuberance and the datum case and supercritical interactions are observed for α=45°, α=60° and α=90°. This is in good agreement with previous experimental studies on two-dimensional compression ramp interactions which report incipient separation angles of approximately α_i=25°-35° at hypersonic speeds (Elfstrom, 1971) as further discussed in Chapter 6. High-speed schlieren images were recorded at frame rates of up to 50 kHz and show that the upstream flow is unsteady when the local interference interaction is supercritical. In these cases there is a clear oscillation of the boundary layer separation shock as explained in more detail in Chapter 7. For subcritical interactions, the flow appears to be pseudo-steady throughout the effective run duration.

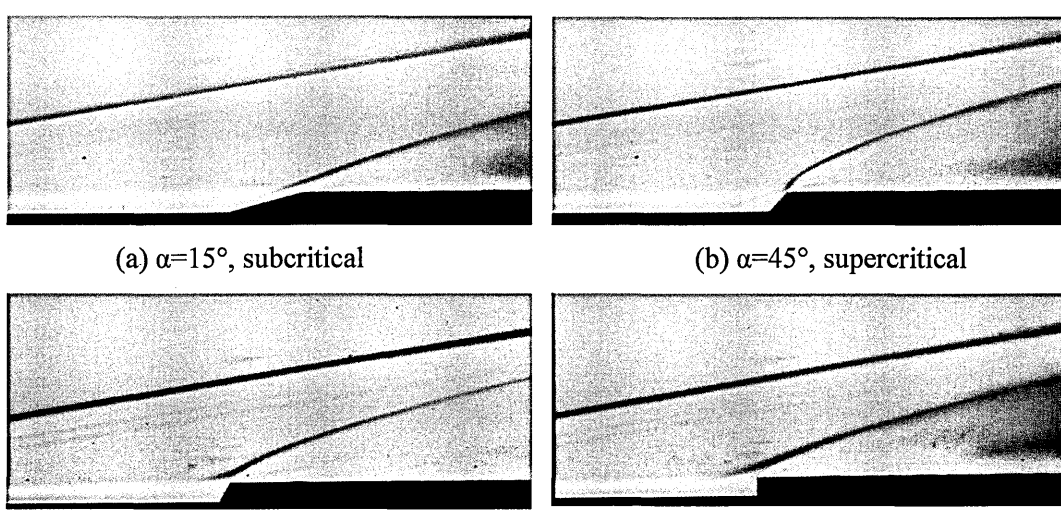

(a) α=15°, subcritical (b) α=45°, supercritical

(c) α=60°, supercritical (d) α=90°, supercritical

Fig. 5.7 Schlieren images. Turbulent, M_∞=8.2, $Re_\infty/m=9.35x10^6$. Flow from left to right.

Heat flux measurements for the different test cases can be found in Appendix A. On the α=15° protuberance, a slight decrease in heat flux ahead of the model is observed in the same way as in the α=30° case (Fig. 5.2). The reattachment of the flow to the surface on the model side results in high heat flux values of the same order as those measured in the datum configuration. Despite the lower deflection angle, the flow reattachment takes place at a slightly farther distance from the protuberance leading edge. Given that the magnitude of the hot spot is very similar to this in the α=30° case, the side heating in subcritical interactions (i.e. those in which the boundary layer remains attached ahead of the protuberance) appears independent of model height and width but also it can be considered independent of deflection angle. This is further explained in the next chapter.

For the α=45° case, similar heat flux values to those measured in the subcritical interactions were found to the protuberance side (Fig. 5.8). Due to the supercritical separation of the boundary layer ahead of the interaction, high heat flux values were also encountered just upstream of the model. The magnitudes of the high heating rates both ahead and to the side of the protuberance were similar in this case ($St_{max,side}=3.3x10^{-3}$ and $St_{max,ahead}=3.3x10^{-3}$). This is attributed to the weak supercritical nature of the interaction. As a consequence, a clear hot spot cannot be distinguished due to the mixed effects to the sides and ahead of the protuberance.

As the protuberance deflection angle is increased to α=60°, the supercritical interaction ahead of the protuberance becomes stronger and the maximum heat flux increases as well. The hot spot is in this case clearly located just ahead of the protuberance, spanning its whole width. Heating rates to the side are of the same order of magnitude but located closer to the leading edge of the model and at a further distance from its side (Fig. 5.9). At a deflection angle of α=90°, the interaction ahead of the model becomes stronger and that also results in a further increase in surface heating upstream. The heat flux to the protuberance side reaches similar values as in the previous cases (Fig. 5.10). This is further shown in the form of a 3D bar plot in Fig. 5.11. An oil flow visualisation of this protuberance can be found in Appendix B, which also indicates the presence of the highest skin friction ahead of the protuberance and with a strong upstream influence. Significant skin friction is also qualitatively shown in the surface adjacent to the protuberance but not as marked as in the front.

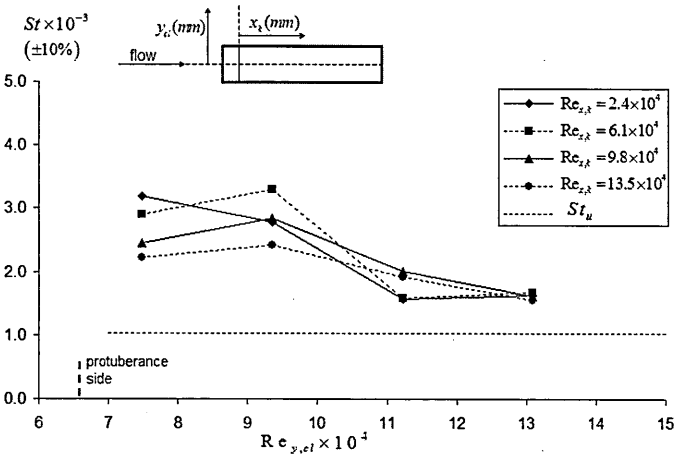

Figure 5.8 Side heat flux: turbulent, M_∞=8.2, Re_∞/m=9.35x10^6, α=45°.

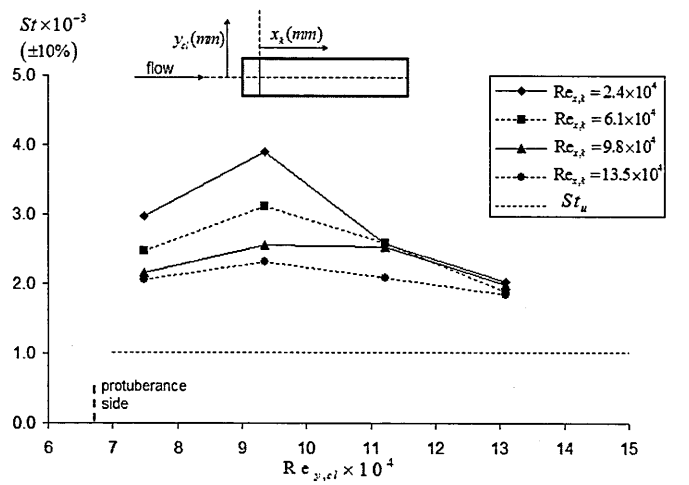

Figure 5.9 Side heat flux: turbulent, M_∞=8.2, Re_∞/m=9.35x10^6, α=60°.

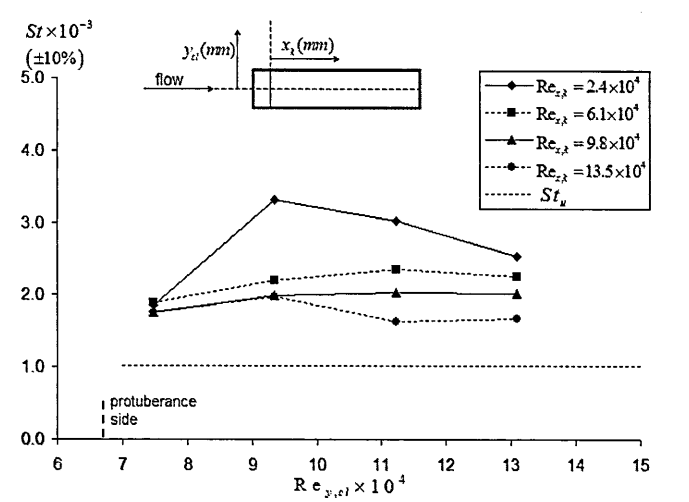

Figure 5.10 Side heat flux: turbulent, M_∞=8.2, Re_∞/m=9.35x10^6, α=90°.

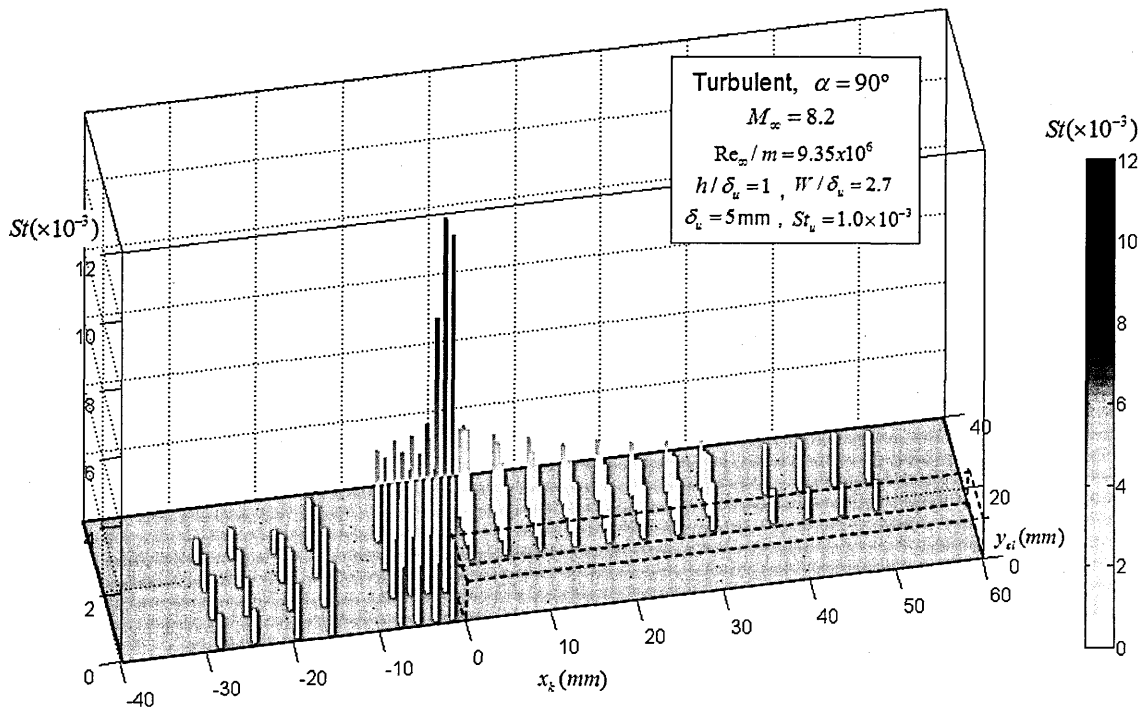

Figure 5.11 3D bar plot of heat flux measurements in the vicinity of α=90° protuberance.

Figure 5.12 plots the heat flux measurements ahead of the α=30°, α=45°, α=60° and α=90° protuberances. An almost linear relationship between protuberance deflection angle and the magnitude of the highest heat flux is observed in supercritical interactions as also shown in Fig. 5.13. The heat flux along the separated flow region increases gradually as it proceeds from the separation locus and it reaches its highest value just ahead of the protuberance. The extent of the separation region ahead of the protuberance is also longer at high deflection angles. The heat flux ahead of the subcritical interactions is equal or lower than the corresponding undisturbed value as already explained in Section 5.1.

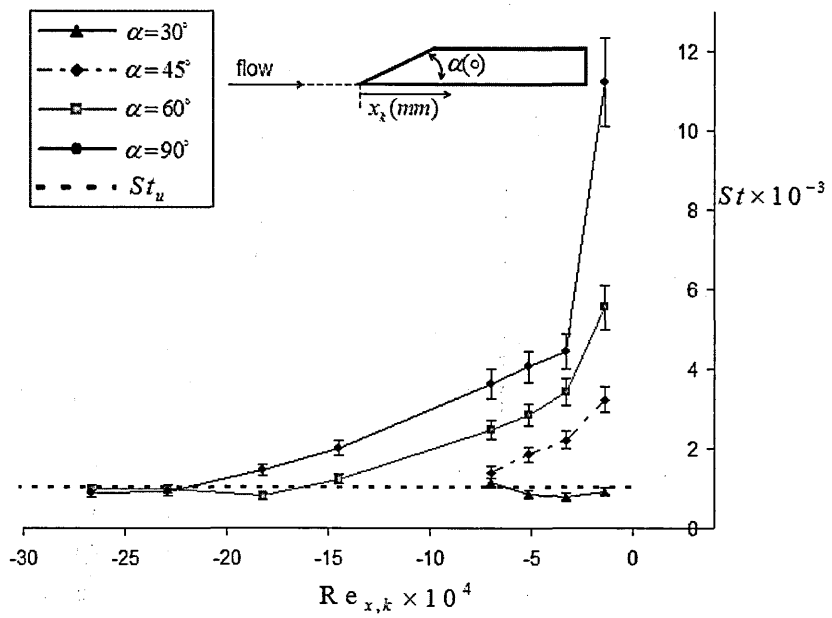

Figure 5.12 Heat flux measurements ahead of different angle protuberances: turbulent, M_∞=8.2, Re_∞/m=9.35x10^6, y_{cl}=0mm.

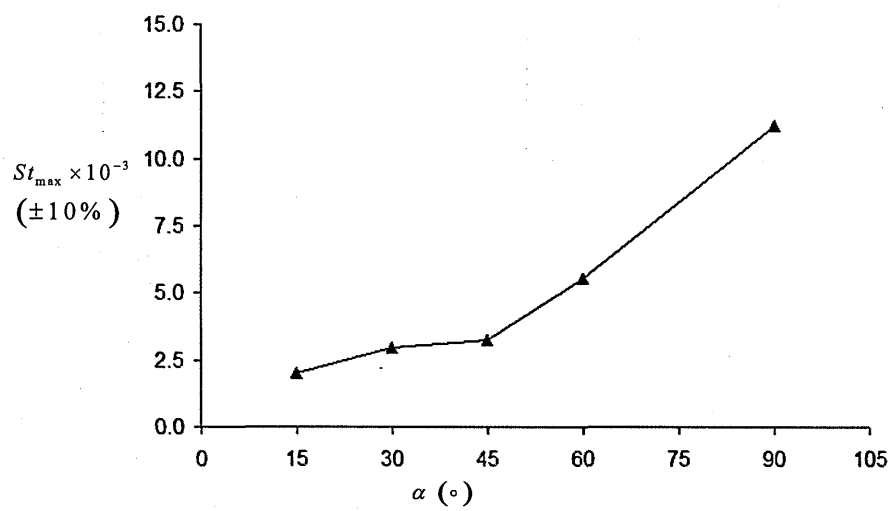

Figure 5.13 Maximum heat flux measurements for different angle protuberances: turbulent, M_∞=8.2, Re_∞/m=9.35x10^6.

The heat flux ahead of the subcritical protuberances (α=15° and α=30°) remains almost undisturbed while for supercritical cases (α=45° to α=90°) the heat flux in the separation region increases and reaches its highest value just ahead of the protuberance. An almost linear relationship between protuberance deflection angle and the magnitude and extent of the heat flux augmentation ahead of the protuberance is thus observed in supercritical interactions. As expected from previous experiments (see e.g. Kuehn, 1959; Holden, 1964) the extent of the separation region increases with deflection angle due to the higher adverse pressure gradient imposed to the incoming boundary layer. The present study of protuberance deflection angle thus shows that the local interference interaction induced by a protuberance is strongly dependent on whether the interaction is subcritical or supercritical. More details on a criterion to distinguish between these two cases is presented in Section 6.3.

As shown in Fig. 5.14, the following observations are made:

i. For subcritical interactions (α=15° and α=30° in this case) an increase in heat flux occurs to the side of the protuberance whereas heat flux rates of the same order or lower than the corresponding undisturbed value take place ahead of the protuberance.

ii. For supercritical interactions (α=45°, α=60° and α=90°) the highest heating rates are found just ahead of the protuberance where a separation bubble occurs. Increased heating is also found to the side of supercritical protuberances and with a similar magnitude to that measured to the side of subcritical protuberances. In weak supercritical interactions (α=45°) the highest heating is found both ahead of the protuberance and to its side and therefore a clear hot spot cannot be so easily identified

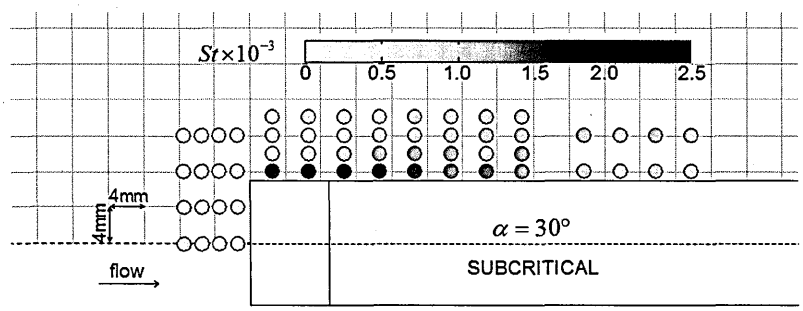

(a) Subcritical case, α=30°

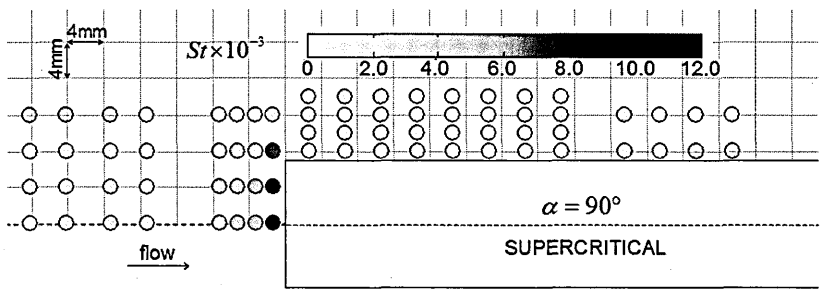

(b) Supercritical case, α=90°

Figure 5.14 Plan view of heat flux measurements on the α=30° and α=90° interactions.

5.4 Effect of forward deflection

A different case which has received little attention to date is that of a protuberance with a forward deflection angle. To simulate this, a protuberance with an effective deflection angle of α=135° was considered. A schlieren image of this configuration is shown in Fig. 5.15, where a larger separation region ahead of the model is seen with respect to the lower angle cases. The separation length is evaluated from the schlieren images with an uncertainty of ±10% based on the unsteadiness of some of the interactions and on the extrapolation of the separation shock wave to the flat plate (Appendix C). Figure 5.16 plots the extent of the separation length (L) ahead of the model (i.e. distance from boundary layer separation shock to plate-protuberance junction) which increases with protuberance angle. The high-speed schlieren results also reveal a strongly unsteady interaction in this case with a clear oscillation of the boundary layer separation shock as in the other supercritical cases.

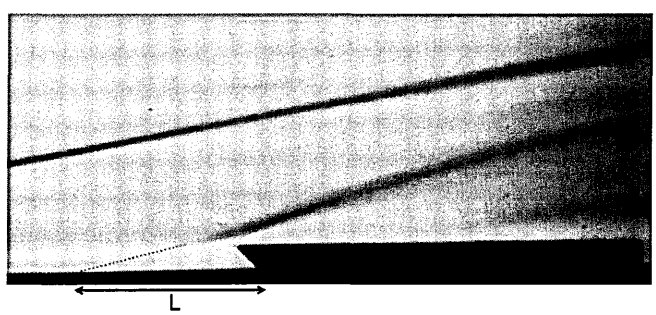

Figure 5.15 Schlieren image: turbulent, M_∞=8.2, Re_∞/m=9.35x10^6, α=135°. Flow from left to right.

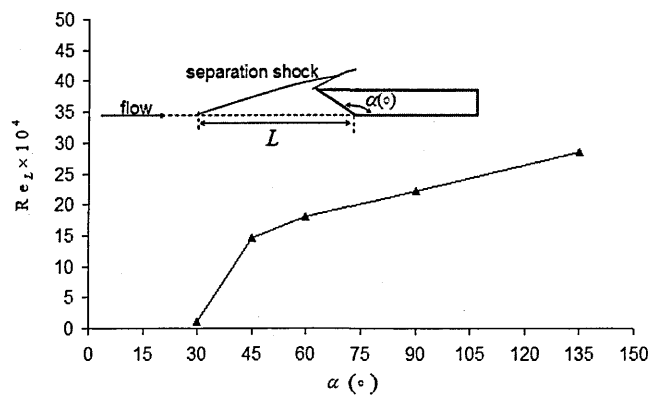

Figure 5.16 Separation length ahead of protuberance for different supercritical angles. Turbulent, M_∞=8.2, Re_∞/m=9.35x10^6, α=30° to α=135°.

Heat flux measurements in the vicinity of this protuberance can be found in Appendix A. As in the previous supercritical interactions, increased heat flux is present to the sides and upstream of the protuberance with the hot spot just ahead of the model. The magnitude of the hot spot in this case also correlates almost linearly with those at the other deflection angles as shown in Fig. 5.17. The increased heating to the sides occurs at a farther distance from the model and diminishes as it proceeds downstream. Comparing this with the measurements in Fig. 5.12, the heat flux increases progressively as the flow separates ahead of the protuberance and therefore the region of intensified heating is larger in this case due to the larger separated flow region. Heat flux measurements show that the highest heat flux occurs just ahead of the protuberance and with values of 41.2% higher than with the α=90° configuration in this case (Fig. 5.18) although high heating is also found to the side with a value of $St_{max,side}$=2.6x10^{-3} (Fig. 5.19). As shown in more detail in the following sections, it is believed that the hot spot was not captured in this configuration due to the measurement resolution and an actual increase in about 106.4% with respect to the α=90° case is expected instead. This statement is further justified by the measurements at the other freestream conditions as shown in the following sections and by the subsequent correlations presented in Chapter 6.

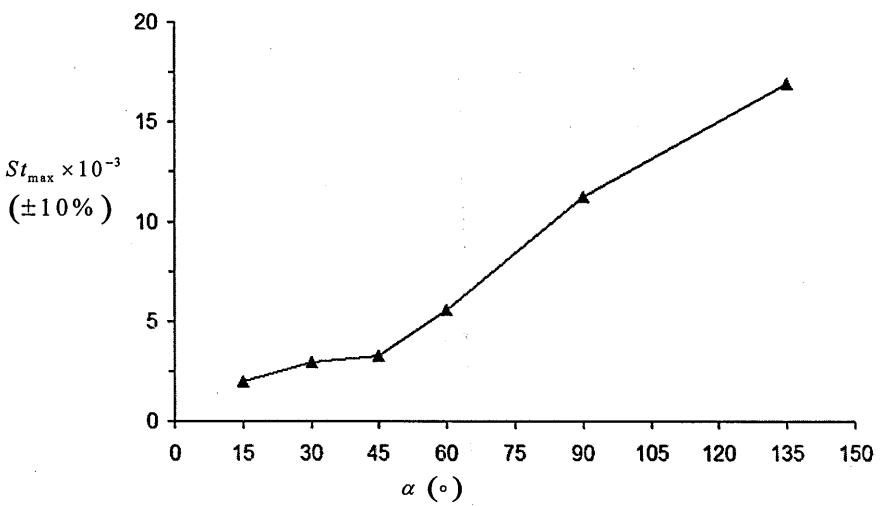

Figure 5.17 Maximum heat flux around different deflected protuberances: turbulent, M_∞=8.2, Re_∞/m=9.35x10^6, α=30° to α=135°.

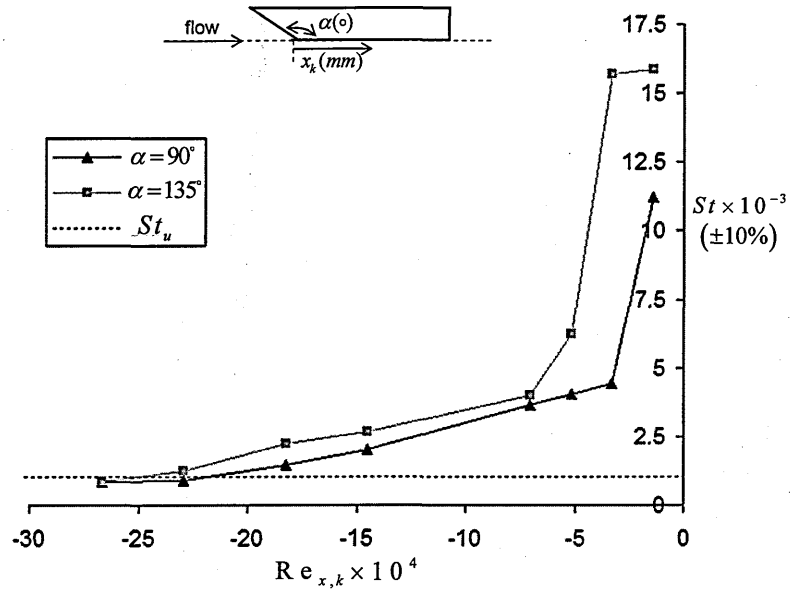

Figure 5.18 Heat flux measurements ahead of α=135° and α=90° cases. Turbulent, M_∞=8.2, Re_∞/m=9.35x10^6, y_{cl}=0mm.

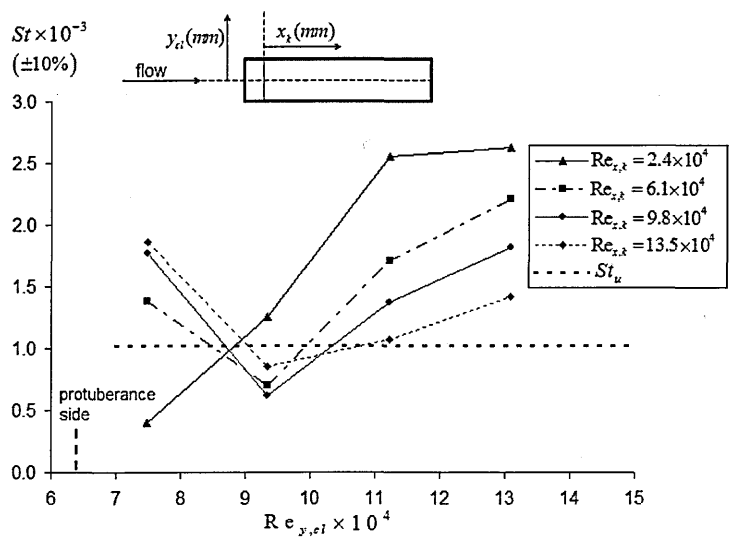

Figure 5.19 Side heat flux: turbulent, M_∞=8.2, Re_∞/m=9.35x10^6, α=135°.

5.5 Effect of freestream conditions

The effect of the freestream flow conditions was investigated. An initial study looked at the effect of incoming boundary layer state. This was then followed by an investigation into the effect of Reynolds number and subsequently into the effect of Mach number.

5.5.1 Laminar flow

To assess the influence of the incoming boundary layer on the heat flux distributions experiments were performed at the same freestream conditions used in the datum study (Table 3.2) but without the vortex generators on the flat plate. This allowed a laminar boundary layer to develop. The boundary layer thickness at the location of the protuberance was $\delta_u = 2.5\text{mm} \pm 0.25\text{mm}$. The h/δ_u ratio in this case was therefore 2. Measurements were taken in the vicinity of the datum configuration ($\alpha=30°$) and on the highest heat flux regions in the rest of the deflection angles considered.

5.5.1.1 Datum case at laminar conditions

A schlieren image of the $\alpha=30°$ case with an incoming laminar boundary layer is shown in Fig. 5.20, where the boundary layer is observed to separate ahead of the protuberance. Recall that for the datum case (turbulent, $\alpha=30°$) the boundary layer remains attached ahead of the protuberance (Fig. 5.1). This is due to the increased sensitivity of laminar boundary layers to adverse pressure gradients which results in lower incipient separation angles. At these test conditions this is estimated to be $\alpha_i<15°$ (Chapman et al., 1958; Hakkinen et al., 1959; Sterrett and Emery, 1960). Consequently, with the same protuberance geometry and operating conditions, the effect of the incoming boundary layer has a strong impact on the local interference heat transfer augmentation.

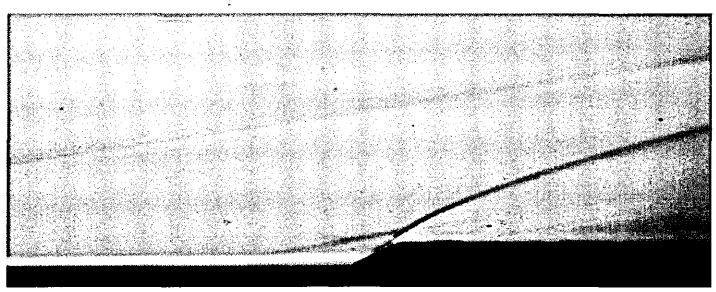

Figure 5.20 Schlieren image: laminar, M_∞=8.2, Re_∞/m=9.35x10^6, α=30°. Flow from left to right.

Heat flux measurements obtained for this configuration are presented in Appendix A. As expected, due to the upstream separation bubble the heat flux ahead is increased with respect to the corresponding undisturbed heat flux value. Although the highest heating in supercritical interactions is generally located ahead of the protuberances, in weak supercritical interactions (low-Reynolds low-deflection cases) it can take place to the side of the device, as previously suggested by the α=45° turbulent results. The hot spot takes place to the side of the protuberance but at a farther distance from its leading edge. The magnitude of the heat flux to the side of the α=30° protuberance is shown in Fig. 5.21 comparing the laminar and turbulent cases at axial locations corresponding to $Re_{x,k} = 21.0\times10^4$ (x_k=22.5mm, laminar) and $Re_{x,k} = 9.8\times10^4$ (x_k=10.5mm, turbulent) where the maximum side heating was measured for each case. The maximum side heat flux for turbulent conditions in terms of Stanton number is about 15% higher than under laminar freestream conditions. The incoming laminar boundary layer appears to become transitional or almost fully turbulent within the interaction region.

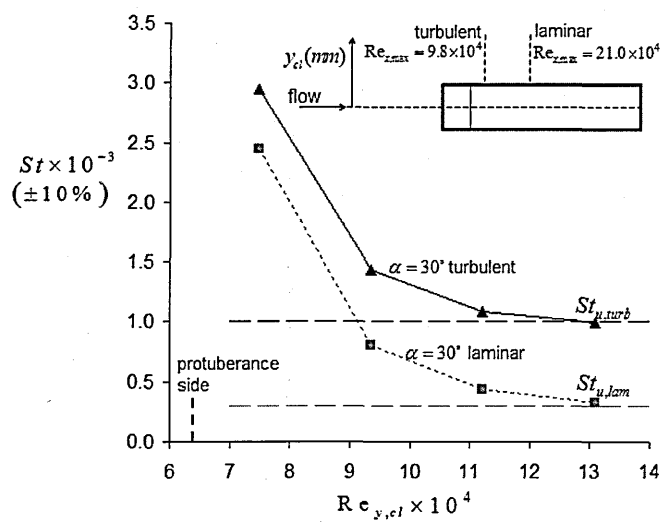

Figure 5.21 Maximum side heat flux: M_∞=8.2, Re_∞/m=9.35x10^6, α=30°. Comparison between incoming laminar and turbulent boundary layer cases.

5.5.1.2 Different deflection angles

Schlieren images for the laminar cases ranging from angles α=15° to α=135° are shown in Fig. 5.22. The boundary layer separates ahead of the protuberance in all the cases and therefore all the interactions are supercritical. At α=15°, the separation seems to be close to incipient conditions. This is in agreement with previous works by Chapman et al. (1958), Hakkinen et al. (1959) and Sterrett and Emery (1960). As also expected from these two-dimensional ramp studies, the length of the separation region for the laminar boundary layer cases is larger than in the turbulent configurations (Fig. 5.23) and increases with protuberance deflection angle in a similar way. The extent of the upstream separated region for laminar conditions is around 3 times longer than under turbulent conditions for each corresponding angle.

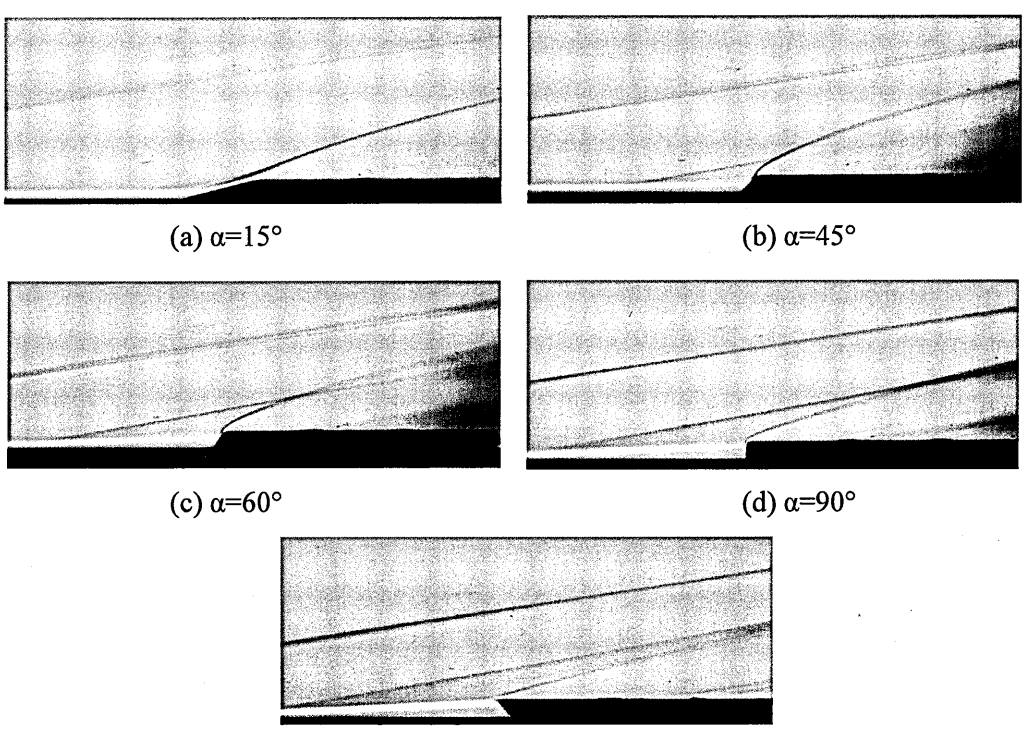

(a) α=15° (b) α=45°

(c) α=60° (d) α=90°

(e) α=135°

Fig. 5.22 Schlieren images. Laminar, M_∞=8.2, $Re_\infty/m=9.35x10^6$. Flow from left to right.

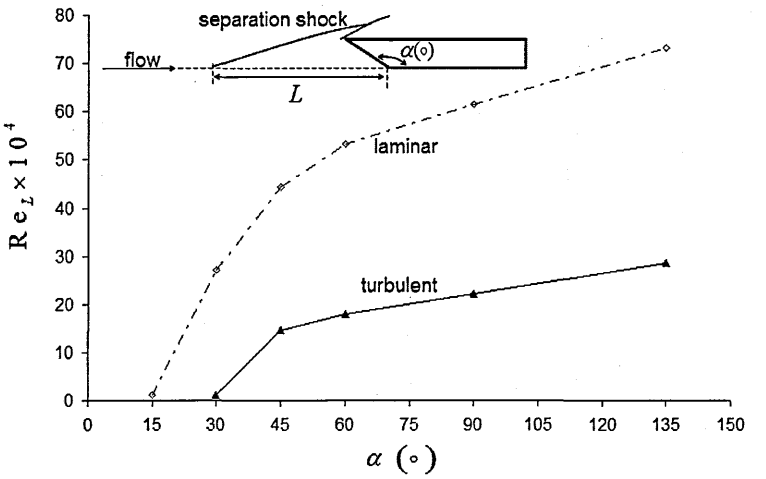

Figure 5.23 Separated region for different deflection angles: M_∞=8.2, Re_∞/m=9.35x10^6.

Heat flux measurements to the side of the α=15° and α=30° protuberances under laminar conditions are shown in Fig. 5.24, where the maximum side heat flux appears to be unaffected by deflection angle. For practical purposes and within engineering accuracy, an approximate value of the maximum heating adjacent to the protuberance can therefore be obtained by considering the heat flux to the side to be independent of boundary layer state, protuberance dimensions and deflection angle. This statement has been further demonstrated in Section 5.3 in the turbulent tests.

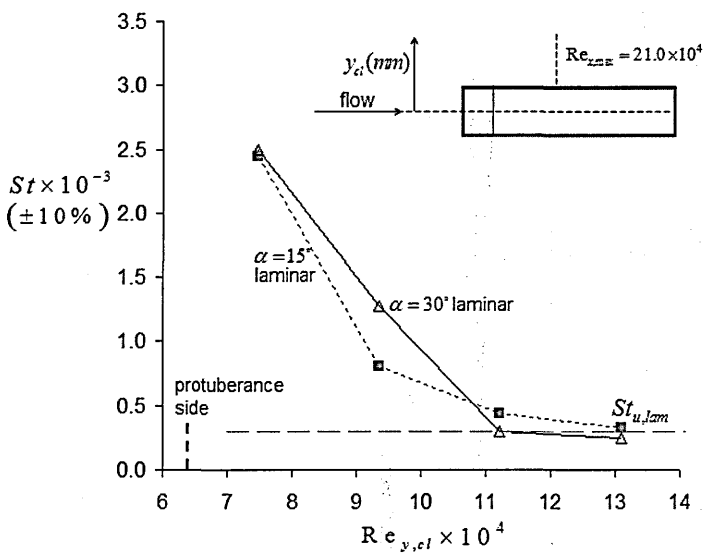

Figure 5.24 Heat flux along side of 15° and 30° protuberances: laminar, M_∞=8.2, Re_∞/m=9.35x10^6, α=135°.

At laminar conditions, heating rates higher than the undisturbed heat flux are measured ahead of the supercritical protuberances. At the low deflection angles, the heat flux amplification is small. This differs from most previous studies on two-dimensional discontinuities with laminar incoming flow (Chapter 2) in which the heat flux on the separated region ahead was found lower than the undisturbed heat flux. This is attributed to the 3-dimensionality of the present interactions causing early transition.

A comparison between the magnitude of the hot spots for different deflection angles and boundary layer state is shown in Fig. 5.25. The peak heating is found just ahead of the protuberances ($\mathrm{Re}_{x,k} = -1.4\times10^4$, x_k=-1.5mm), except for the forward deflection model (α=135°). In this case, whereas under turbulent conditions it is located at $\mathrm{Re}_{x,k} = -1.4\times10^4$ (x_k=-1.5mm), in laminar flow this is found slightly further upstream at $\mathrm{Re}_{x,k} = -3.3\times10^4$ (x_k=-3.5mm) (Fig. 5.26). For the range of angles from α=15° to α=90° the peak heat transfer magnitude is almost the same at both laminar and turbulent conditions and regardless of h/δ_u ratio with a difference of 0.5% for the α=90° interaction. Only the α=135° protuberance departs from the trend where it reaches a value of St_u=23.1x10^{-3} (q_u=132.7 W/cm^2) for a laminar boundary layer in comparison to St_u=19.1x10^{-3} (q_u=97.4 W/cm^2) for the turbulent case. This difference for the forward deflection case is attributed to the lack of measurement resolution ahead of the α=135° protuberance where a slightly more complex interaction takes place as further shown in Chapter 7. The highest heating in the M_∞=8.2, Re_∞/m=9.35x10^6, turbulent case is expected to occur at a location between ($\mathrm{Re}_{x,k} = -3.3\times10^4$) x_k=-3.5mm and $\mathrm{Re}_{x,k} = -1.4\times10^4$ (x_k=-1.5mm) based on these assumptions.

In general, based on this limited range of data, these results suggest that the maximum heat transfer rate is not strongly dependent on the state and thickness of the boundary layer for both subcritical and supercritical interactions. Although a more intensive investigation would be required to separate the effect of boundary layer thickness and boundary layer state, the consistent similitude in magnitude between the hot spot in these cases (≈0.5%) despite the very different boundary layer thickness (δ_u is 100% higher in the turbulent case than in the laminar one) provides supporting evidence to this statement.

Although the boundary layer state does not have a large influence on the magnitude of the hot spot, it does have a strong effect on the extent of the local interaction and thus on the region where heating rates are increased relative to the corresponding undisturbed value. It is worth noting that the highest heating rates in these cases are of the same order as the corresponding stagnation point heating by considering the protuberance height to be equal to an effective hemisphere radius $h = R_N = 5mm$ (Section 4.2). This approximate analogy further demonstrates that extremely high heating rates can be present in the vicinity of surface protuberances.

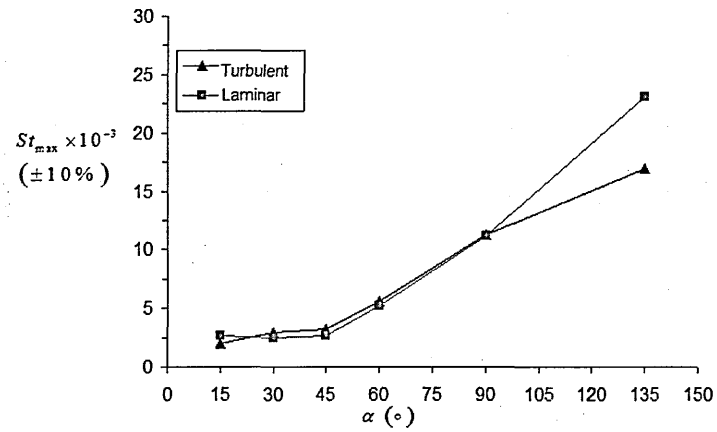

Figure 5.25 Hot spot magnitude for different deflection angles: M_∞=8.2, Re_∞/m=9.35x10^6, α=135°. Comparison between laminar and turbulent cases.

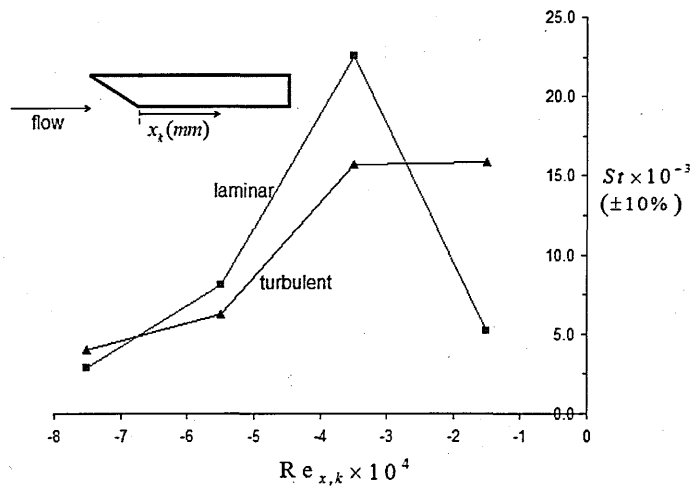

Figure 5.26 Maximum heat flux ahead of protuberance: M_∞=8.2, Re_∞/m=9.35x10^6, α=135°. Comparison between laminar and turbulent cases.

5.5.2 Reynolds number

The effect of freestream Reynolds number was studied by changing the drive pressure of the wind tunnel at Mach 8.2 conditions. Measurements were performed at a driver pressure of $13.8\text{x}10^6$Pa ($Re_\infty/m=9.35\text{x}10^6$), $10.3\text{x}10^6$Pa ($Re_\infty/m=8.06\text{x}10^6$) and $6.9\text{x}10^6$Pa ($Re_\infty/m=6.57\text{x}10^6$). As described in Chapter 3, the same vortex generators used in the datum study were employed in these cases.

5.5.2.1 Tests at $M_\infty=8.2$, $Re_\infty/m=8.06\text{x}10^6$

The incoming boundary layer at $M_\infty=8.2$, $Re_\infty/m=8.06\text{x}10^6$ test conditions is fully turbulent and has a thickness of $\delta_u = 5\text{mm} \pm 0.5\text{mm}$ (Table 4.4). Schlieren images for all different angles at these conditions are shown in Fig. 5.27. Supercritical interactions seem to be slightly larger than those at 2000psi ($Re_\infty/m=9.35\text{x}10^6$) and with a turbulent boundary layer. Similarly to the $Re_\infty/m=9.35\text{x}10^6$ tests, a subcritical interaction is obtained at a deflection angle of $\alpha=30°$, and supercritical interactions at the higher angles. Other aspects in the flow field are qualitatively the same as the corresponding interactions at the higher freestream Reynolds number conditions.

Heat flux measurements were taken in this case at the regions of highest heat transfer (refer to Appendix A). During the present tests, one of the gauges failed and reliable measurements on one of the gauge locations could not be obtained in some cases. The regions of highest interest are nevertheless considered for all the configurations. Due to the little additional information that the $\alpha=15°$ results provided, only the $\alpha=30°$ protuberance was considered. For the supercritical cases, measurements were taken ahead of the model where the hot spot is located. Further details on the heat flux measurements are presented in the following section.

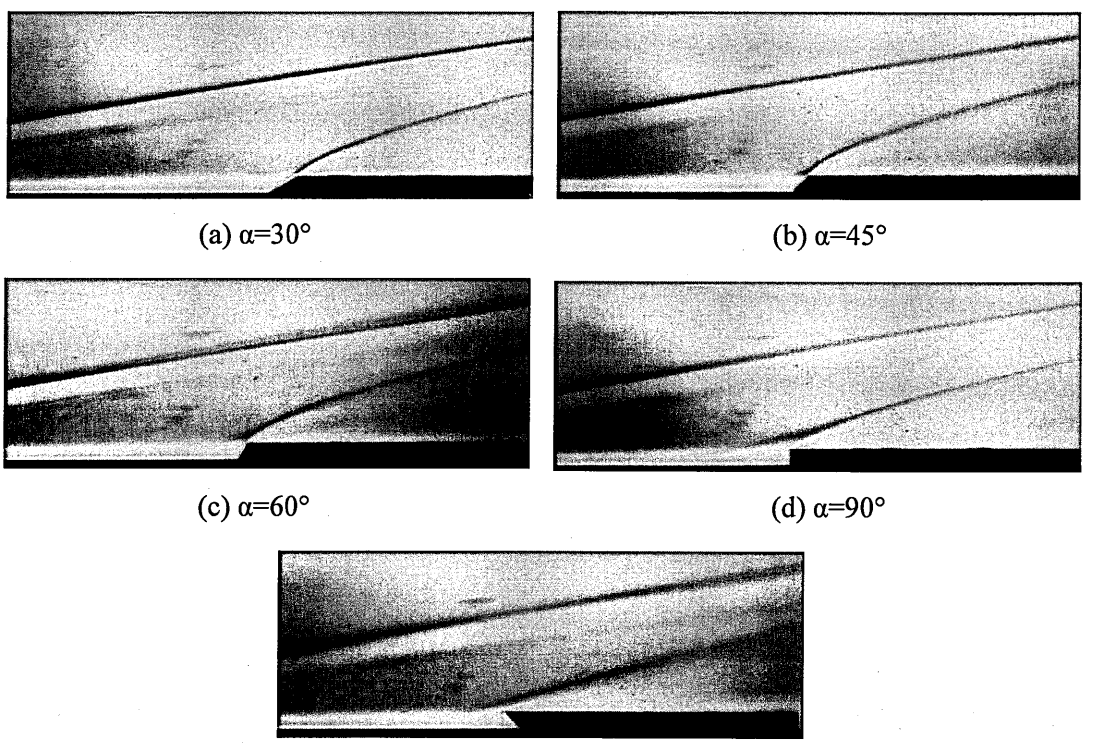

(a) α=30° (b) α=45°

(c) α=60° (d) α=90°

(e) α=135°

Fig. 5.27 Schlieren images. Turbulent, M_∞=8.2, Re_∞/m=8.06x10^6. Flow from left to right.

5.5.2.2 Tests at M_∞=8.2, Re_∞/m=6.57x10^6

At M_∞=8.2, Re_∞/m=6.57x10^6 test conditions the incoming boundary layer is transitional and has a thickness of $\delta_u = 5\text{mm} \pm 0.5\text{mm}$ as assessed in Chapter 4. Schlieren images for all different angles at these conditions are shown in Fig. 5.28. Due to the lower resistance of the boundary layer to separation, the local α=30° interaction is supercritical in this case since the boundary layer separates upstream of the protuberance.

The extent of the separation region ahead of supercritical interactions based on the high-speed schlieren images is plotted for the three different Reynolds number cases in Fig. 5.29. Supercritical interactions with a fully turbulent incoming boundary layer at Re_∞/m=8.06x10^6 are slightly larger than those at Re_∞/m=9.35x10^6 and with a fully turbulent boundary layer as well. As described by Needham and Stollery (1966a, 1966b) for two-dimensional ramp interactions, the length of the separated region is expected to increase with Reynolds numbers in fully laminar and fully turbulent flows but the opposite trend is expected in transitional flows. Although the latter trend is observed in the present case, there is a high level of confidence in the inferred state of the boundary layer as already shown in Chapter 4 – i.e. fully laminar or fully turbulent at Re_∞/m=9.35x10^6 and Re_∞/m=8.06x10^6 conditions and transitional only at Re_∞/m=6.57x10^6 - and also based on the incipient angle α_i as mentioned in Sections 5.3 and 5.5. The observed trend is attributed to the 3-dimensionality of the present interactions which results in a re-energising process of the flow through the interaction similar to this occurring in transitional flow (Needham and Stollery, 1966a, 1966b) and thus in a higher resistance to separation of the boundary layer at higher Reynolds numbers.

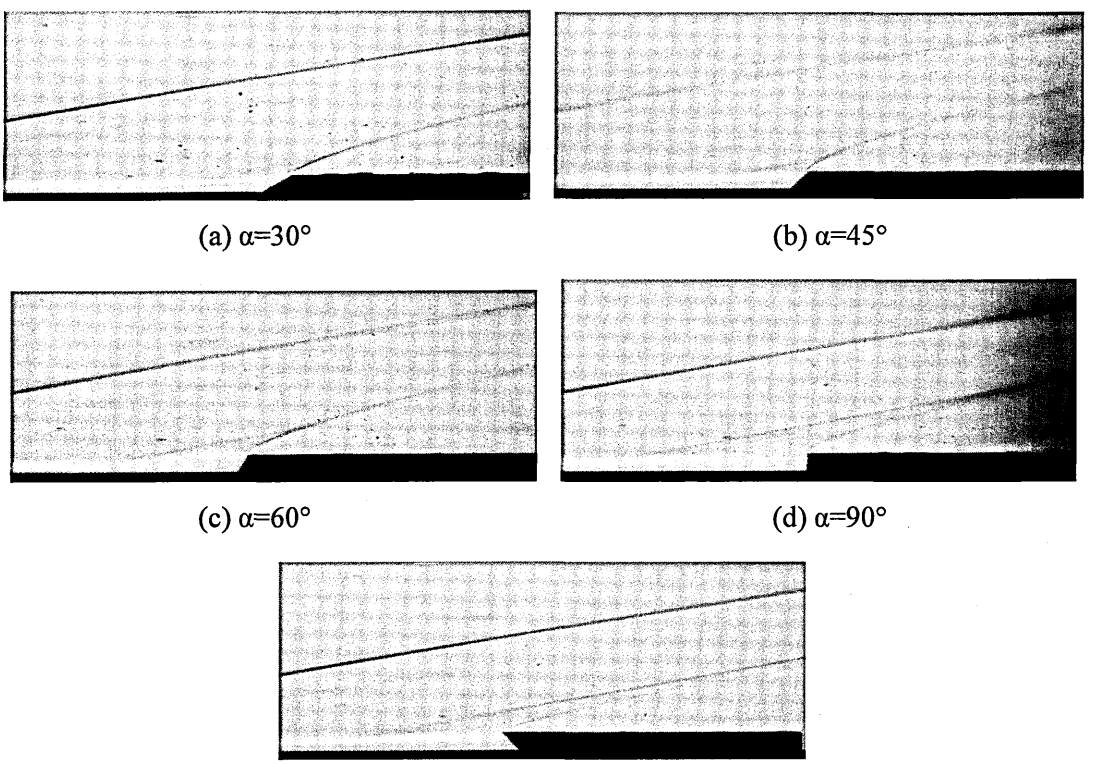

(a) α=30° (b) α=45°

(c) α=60° (d) α=90°

(e) α=135°

Fig. 5.28 Schlieren images. Transitional, M_∞=8.2, Re_∞/m=6.57x10^6. Flow from left to right.

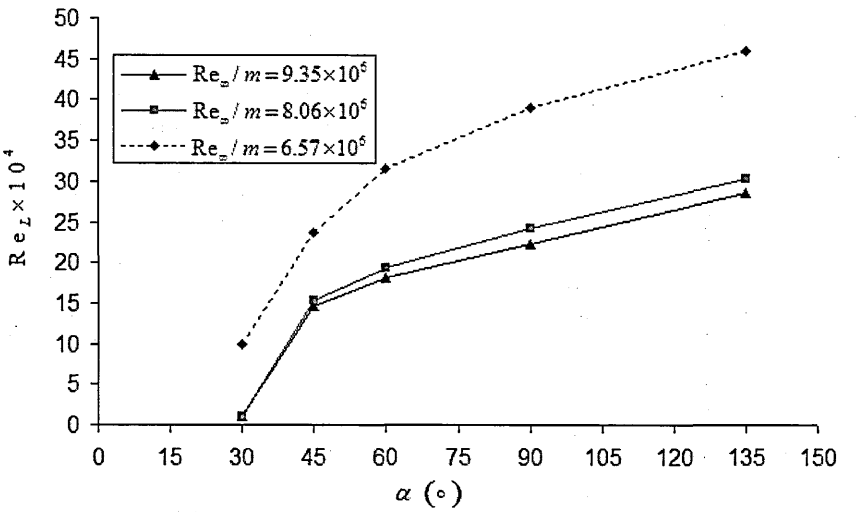

Figure 5.29 Separation length for different Reynolds number cases and different deflection angles at M_∞=8.2.

Heat flux measurements on the high heat transfer regions of these interactions can be found in Appendix A. Measurements were only taken to the side of the α=30° protuberance where the hot spot was expected. For the supercritical interactions, measurements are taken just ahead of the protuberances. As expected, at these conditions the heat flux values in dimensional form (W/cm^2 units, refer to Appendix A.2) are lower in comparison to the tests at the higher Reynolds numbers. In terms of Stanton number the non-dimensional heat flux is also found to decrease at lower Reynolds numbers as further shown in Chapter 6.

A comparison of the maximum heat flux values for the different Reynolds number cases is shown in Fig. 5.30. As before, the peak heat flux is found to the side of the protuberance in the subcritical interactions and ahead of the protuberance in the supercritical interactions. The forward deflection angle (α=135°) at Re_∞/m=9.35x10^6 is the only case which slightly deviates from this general trend. Also, the peak heating is weakly sensitive to Reynolds number. Although the location of the hot spot to the side of the subcritical protuberances is not so clear as in the supercritical protuberances where sharp gradients are present, a clear trend is noticed which shows that the reattachment of the flow to the side of the protuberance takes place at farther distances from the protuberance leading edge at lower Reynolds numbers (Fig. 5.31). This is

explained through the reduced ability of the boundary layer to reattach at low Reynolds numbers and the expectation that the highest heat flux rates at this location are caused by the flow reattachment as further shown in Chapter 7. The Reynolds number is therefore suitable to non-dimensionalise the separation length L and other distances characteristic of these interactions. A further assessment on the effect of Reynolds number is made in the following section.

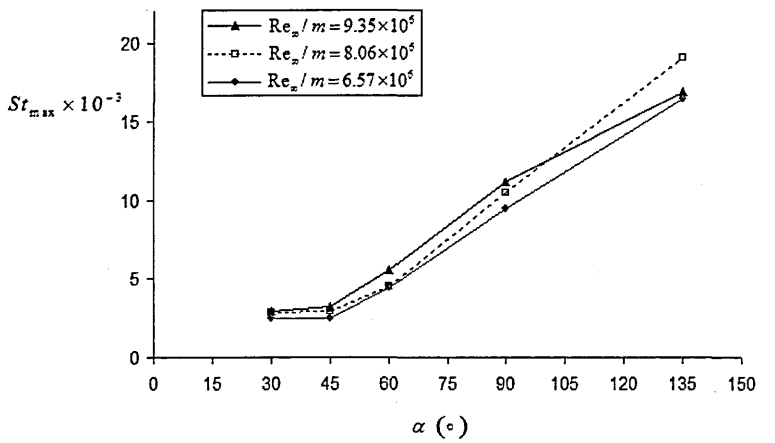

Figure 5.30 Hot spot magnitude for different Reynolds number cases and different deflection angles at M_∞=8.2.

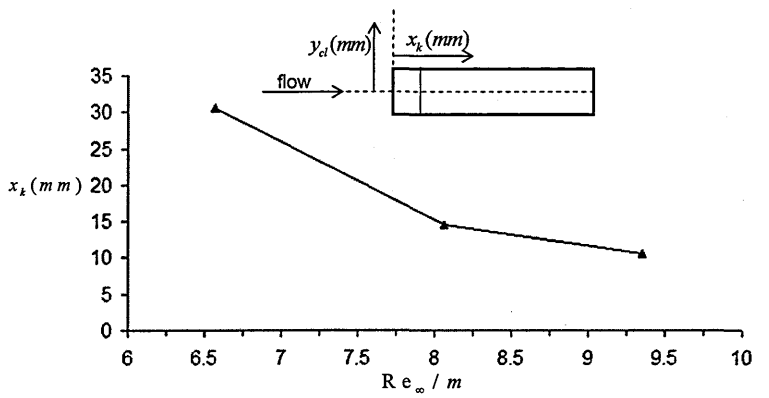

Figure 5.31 Location of highest heat flux on side of α=30° protuberances. M_∞=8.2, Re_∞/m=6.57x10^6 to Re_∞/m=9.35x10^6.

5.5.3 Mach number

Tests were performed at a freestream Mach number of 12.3. In this case, the drive pressure was 13.8x10^{6}Pa (Re_∞/m=9.35x10^6). Only turbulent conditions were reproduced since the results at the lower Mach number indicated the hot spot magnitude not to be strongly dependent on the state of the boundary layer and due to the limitation in the number of experiments that could be performed. Further details on the test conditions and on the inferred state of the boundary layer based on the schlieren images and on the undisturbed boundary layer heat flux measurements were given in Chapters 3 and 4.

5.5.3.1 Datum case at M_∞=12.3

As shown in Table 4.4, at M_∞=12.3 Re_∞/m=3.35x10^6 test conditions vortex generators were used and a fully turbulent boundary layer was obtained. The thickness of the boundary layer was δ_u=6.0mm ± 0.5mm. Schlieren visualisations in this case were not very clear due to the low density levels of the flow, which consequently resulted in low density gradients. The flow features in these interactions could still be determined in the images although the image quality is much poorer than in the previous cases. The interaction induced by the α=30° model was subcritical as shown in the schlieren image in Fig. 5.32. Heat flux measurements in the vicinity of the α=30° model can be found in Appendix A. The corresponding 3D bar plot is shown in Fig. 5.33. High heating rates are observed adjacent to the protuberance with the highest heat flux taking place far downstream from the leading edge ($Re_{x,k} = 35.1\times10^4$, x_k=37.5mm) given that the boundary layer reattaches farther at low Reynolds numbers. The highest heating to the model's side is found at $Re_{y,cl} = 3.4\times10^4$ (y_{cl}=10mm) in this case, which is farther from the model side than in the previous cases ($Re_{y,cl} = 2.7\times10^4$, y_{cl}=8mm). This is also attributed to the low Reynolds number which results in larger side recirculations.

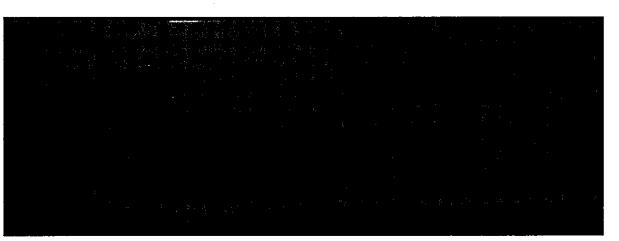

Figure 5.32 Schlieren image: turbulent, M_∞=12.3, Re_∞/m=3.35x10^6, α=30°.
Flow from left to right.

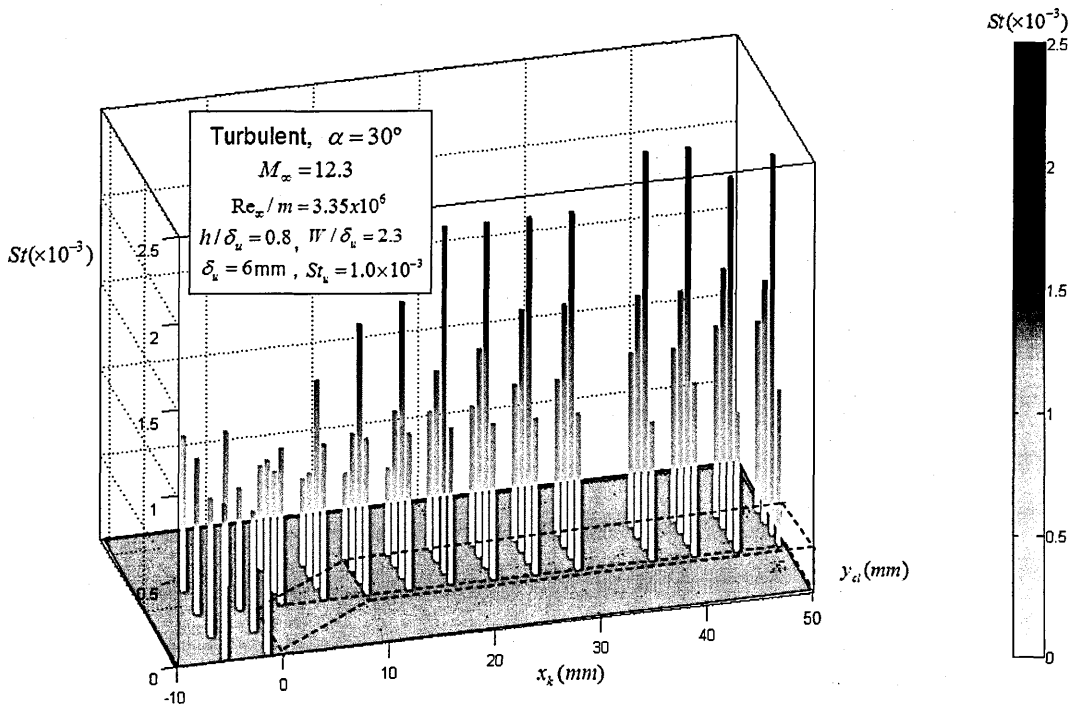

Figure 5.33 3D bar plots of heat flux measurements: turbulent, M_∞=12.3, Re_∞/m=3.35x10^6, α=30°.

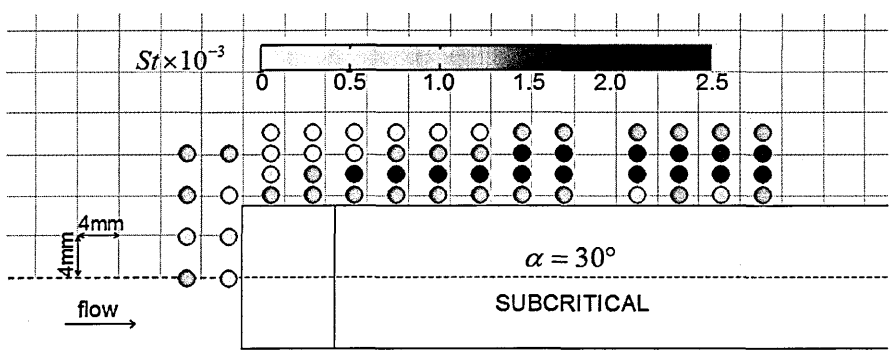

Figure 5.34 Heat flux in the vicinity of α=30° protuberance. Turbulent, M_∞=12.3, Re_∞/m=3.35x10^6.

5.5.3.2 Different deflection angles

Schlieren images of all the cases studied are presented in Fig. 5.35. An attached shock wave is found at Mach 12.3 and supercritical interactions are found at α=45°, α=60°, α=90° and α=135°. Based on the schlieren images, the length of the separation region ahead of the protuberance is smaller than in the laminar and transitional boundary layer cases ($Re_\infty/m=9.35x10^6$ without VGs and $Re_\infty/m=6.57x10^6$ with VGs) but significantly longer than in the turbulent cases at M_∞=8.2 ($Re_\infty/m=8.06x10^6$ and $Re_\infty/m=9.35x10^6$ with VGs). In non-dimensional form, as presented in Fig. 5.36, the separation region at M_∞=12.3 is smaller than in the turbulent cases at the lower Mach number of M_∞=8.2. This was expected since the resistance of boundary layers to separation increases significantly with Mach number (Kuehn, 1959).

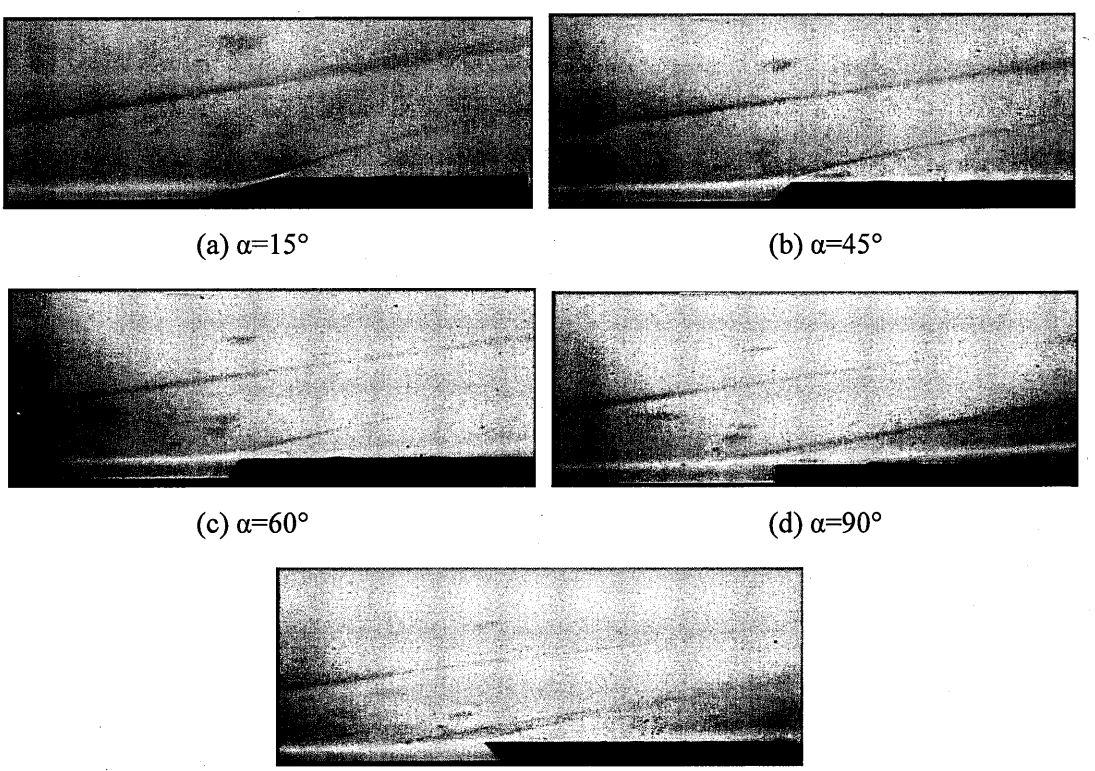

(a) α=15° (b) α=45°

(c) α=60° (d) α=90°

(e) α=135°

Figure 5.35 Schlieren images: turbulent, M_∞=12.3, $Re_\infty/m=3.35x10^6$. Flow from left to right.

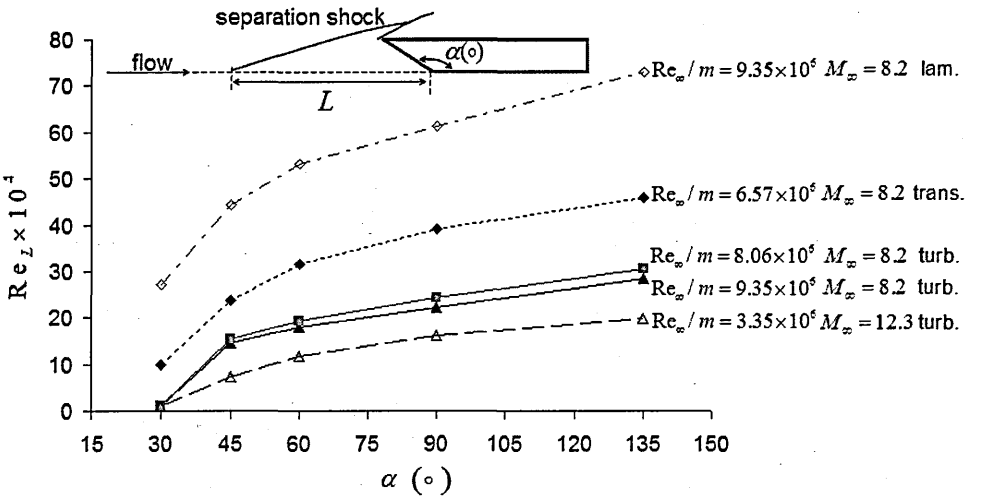

Figure 5.36 Separation length ahead of protuberance.

Heat flux measurements on these configurations are presented in Appendix A. Ahead of the α=135° case, the highest heat flux measurements are not found just close to the model but farther upstream of it ($Re_{x,k} = -3.3\times10^4$, x_k=-3.5mm) as also observed in the M_∞=8.2, $Re_\infty/m=6.57x10^6$ and in the laminar M_∞=8.2, $Re_\infty/m=9.35x10^6$ tests. In contrast, at high Reynolds number conditions the highest heating was found just ahead of the model ($Re_{x,k} = -1.4\times10^4$, x_k=-1.5mm). Consequently, the measurements can be classified in two groups:

i. Cases where the boundary layer is more robust and thus the separation region ahead of the supercritical protuberances and the distance from the leading edge to the side hot spot are shorter (M_∞=8.2 $Re_\infty/m=9.35x10^6$ turbulent, and M_∞=8.2 $Re_\infty/m=8.06x10^6$ turbulent)

ii. Cases with weaker boundary layers, longer separation regions and side hot spots farther from the protuberance leading edge (M_∞=8.2 $Re_\infty/m=6.57x10^6$ transitional, M_∞=12.3 $Re_\infty/m=3.35x10^6$ turbulent and M_∞=8.2 $Re_\infty/m=9.35x10^6$ laminar).

This is discussed further in the following chapter.

CHAPTER 6

Highest Heating in Interference Regions

One of the main concerns in practical engineering applications involving the design of hypersonic vehicles is to predict where the peak heat flux will be located during flight and how high this will be. In this chapter, the results obtained on the interference interactions investigated in the present work are considered to develop an engineering approach for the prediction of the location and magnitude of the highest heat flux in the vicinity of surface protuberances. This approach is intended as a quick and reliable tool for aerothermodynamic design applications.

6.1 Hot spot magnitude

The magnitude of the hot spot for all configurations is summarised in Fig. 6.1 in dimensional form (q_{max}, W/cm^2) and in Fig. 6.2 in non-dimensional form (St_{max}). The magnitude of the maximum heat flux generally increases with both deflection angle and Reynolds number. The measurements at Mach 8.2 group closer together and the Mach 12.3 measurements are much lower (about half the Mach 8.2 value), for which a clear effect of Mach number is also shown. The maximum heat flux in the subcritical interactions is practically the same for all the conditions simulated. These results provide further evidence that a consistent set of data has been acquired and that the measurement spatial resolution has been sufficient to capture the principal effects. As identified previously, the exception to this is the turbulent case with M_∞=8.2, Re_∞/m=9.35x10^6, α=135°.

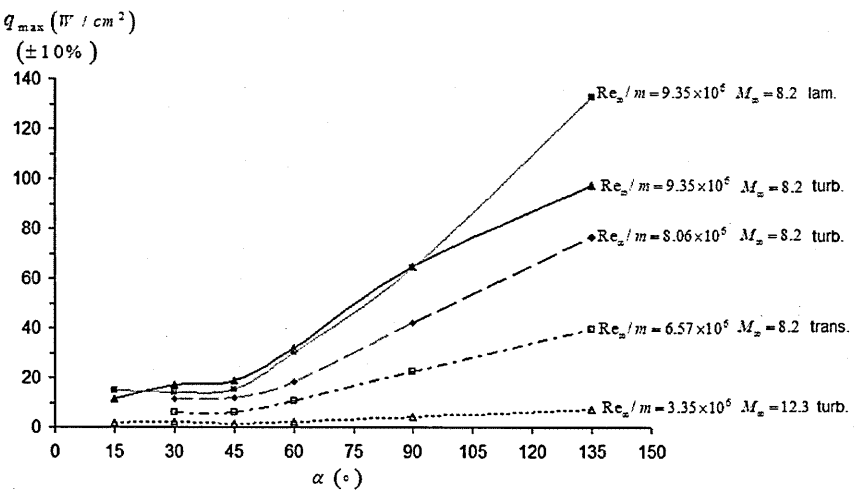

Figure 6.1 Maximum heat flux in W/cm^2 for all the different configurations.

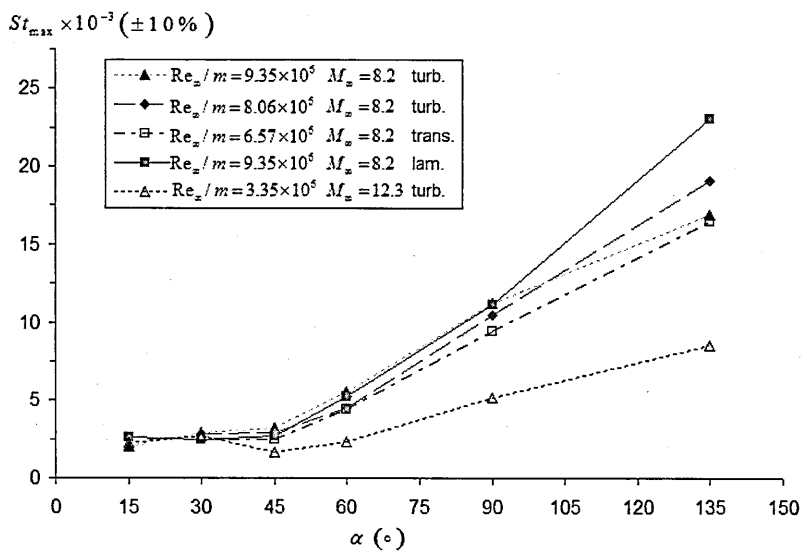

Figure 6.2 Maximum heat flux in Stanton number for all the different configurations.

6.2 Hot spot location

Based on the location of the hot spot, the Reynolds number is also observed to have a significant effect on the behaviour of the interaction. Figure 6.3 plots the cases where the boundary layer is more resistant to separation. These are the M_∞=8.2, $Re_\infty/m=9.35x10^6$ and M_∞=8.2, $Re_\infty/m=8.06x10^6$ turbulent cases. In the subcritical interactions at these freestream conditions, high heat flux is found to the side of the protuberance and relatively close to the leading edge. At the lowest deflection angle, the hot spot to the side is located slightly farther from the protuberance leading edge. In the supercritical interactions, the highest heat flux is found just in front of the model (x_k = -1.5mm). With a α=45° protuberance a weak supercritical interaction is obtained and the location of the hot spot is unclear due to high heating both ahead and to the side of the device.

The location of the hot spot in the larger interactions is summarised in Fig. 6.4. In this case, the M_∞=8.2, $Re_\infty/m=9.35x10^6$ laminar, M_∞=8.2, $Re_\infty/m=6.57x10^6$ transitional and M_∞=12.3, $Re_\infty/m=3.35x10^6$ turbulent interactions are considered. In the subcritical cases, the flow reattaches farther from the leading edge of the model given the lower strength of the boundary layer. In the supercritical cases the hot spot is also found just ahead of the model (x_k=-1.5mm) except for the forward deflection protuberances (α=135°). The highest heating in this case takes place at a farther distance upstream of the protuberance (x_k=-3.5mm) as further explained in Chapter 7.

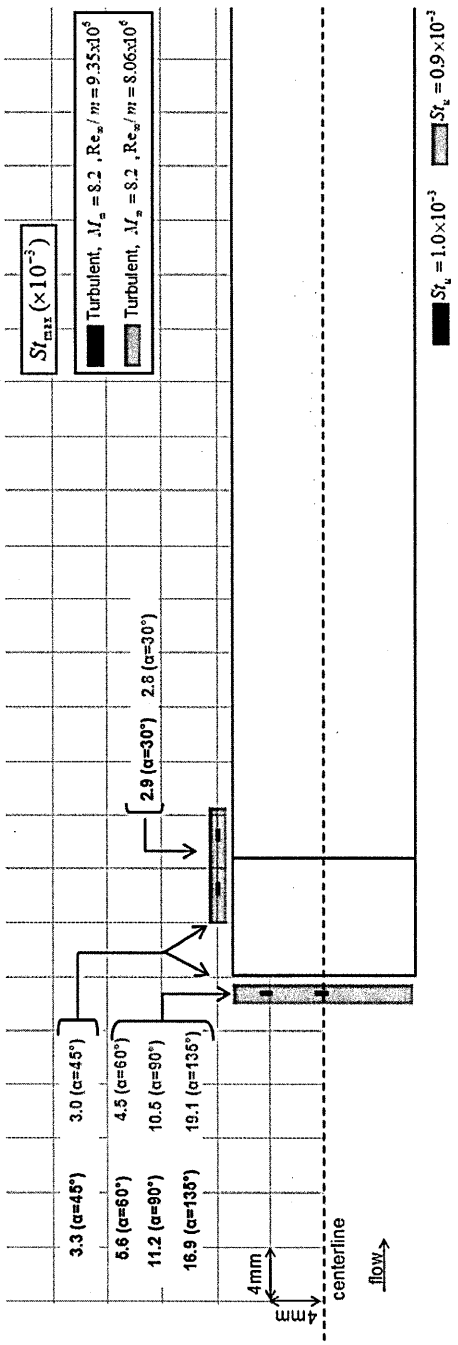

Figure 6.3 Location of maximum heat flux for resistant boundary layer configurations

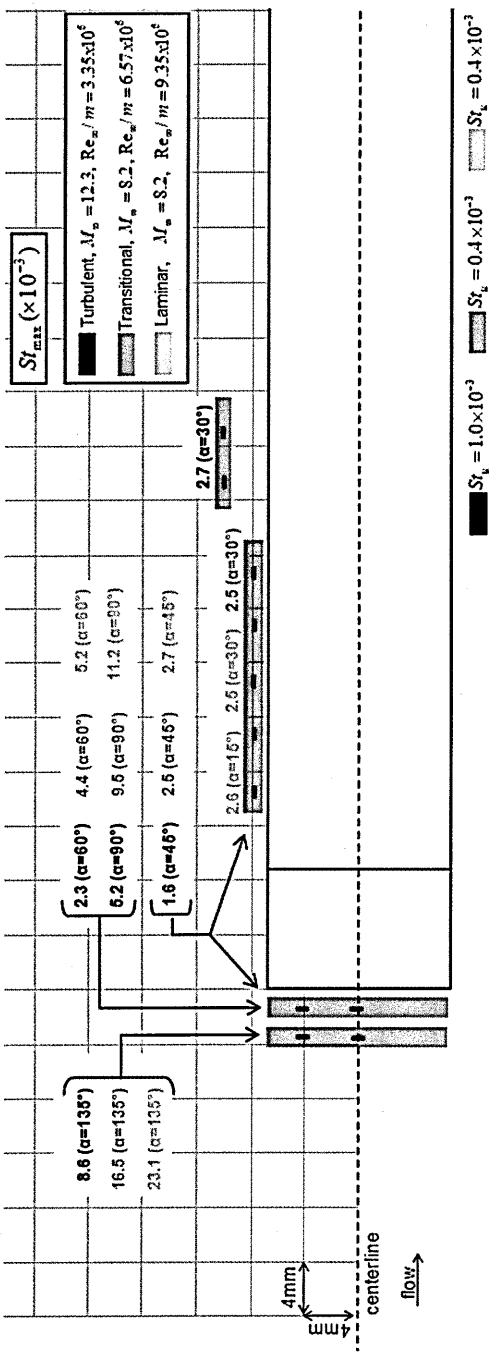

Figure 6.4 Location of maximum heat flux for weak boundary layer configurations

6.3 Incipient separation conditions

The increase in heating in the vicinity of surface protuberances is dominated by the nature of the local interference interaction. If the interaction is subcritical, and therefore the boundary layer remains attached until it meets the protuberance, high heating occurs adjacent to the protuberance. If the interaction is supercritical, and the boundary layer separates ahead of the protuberance, then the high heating occurs to the side and upstream of the protuberance but with significantly higher heating rates ahead. The exception is in the case of weak supercritical interactions, i.e. with deflection angles close to the critical angle and at low Reynolds numbers, where the small separated region results in lower heating ahead of the protuberance rather than to the side of it.

In order to predict the location and magnitude of the hot spot around a protuberance it is important to evaluate whether the local interference interaction is subcritical or supercritical. An incipient protuberance deflection angle (α_i) needs to be estimated based on the state of the incoming boundary layer (laminar, transitional or turbulent), and on the freestream Mach and Reynolds numbers. The protuberance incipient deflection angle is that where a slight increase in deflection results in an increase in the pressure gradient imposed on the incoming attached boundary layer and induces a separation. Intensive studies have been carried out on two-dimensional compression corner interactions to determine the incipient separation angle for certain freestream conditions (Chapman et al., 1958; Hakkinen et al., 1959; Sterrett and Emery, 1960; Babinsky and Edwards, 1996). A well established semi-empirical method, which can be used to predict the incipient separation of a laminar hypersonic boundary layer, was developed by Needham and Stollery (1966a, b). The relation in this case is shown in Eq. 6.1, where $\overline{\chi}_x$ is the viscous interaction parameter as defined in the notations, and thus the relation in Eq. 6.2 is obtained:

$$M_\infty \alpha_i \approx 80 \overline{\chi}_x^{0.5} \quad \text{[Eq. 6.1]}$$

$$\alpha_i \approx 80 M_\infty^{0.5} \mathrm{Re}_x^{-0.25} \left(\rho_w \mu_w\right)^{0.25} \left(\rho_e \mu_e\right)^{-0.25} \quad \text{[Eq. 6.2]}$$

In cases where the boundary layer is turbulent, prediction of the incipient separation angle is not as well established. It is necessary in this case to obtain a prediction based on empirical results such as shown in Fig. 6.5. The incipient separation angle is generally between 25° and 35° for hypersonic Mach numbers (Elfstrom, 1971). A correlation based on these turbulent data is as follows:

$$M_\infty^{-0.5}\alpha_i \approx 11 \quad \text{[Eq. 6.3]}$$

At high Mach numbers and low Reynolds numbers large protuberance deflections are possible in which the local interaction is subcritical. Although these correlations do not consider important factors such as wall temperature, they offer an approximate estimate of the incipient separation angle that may be found in real flight conditions. Once the incipient separation angle for the corresponding freestream conditions is determined, the local interaction can be predicted to be either subcritical or supercritical:

i. If $\alpha < \alpha_i$: The local interference interaction is subcritical.

ii. If $\alpha > \alpha_i$: The local interference interaction is supercritical.

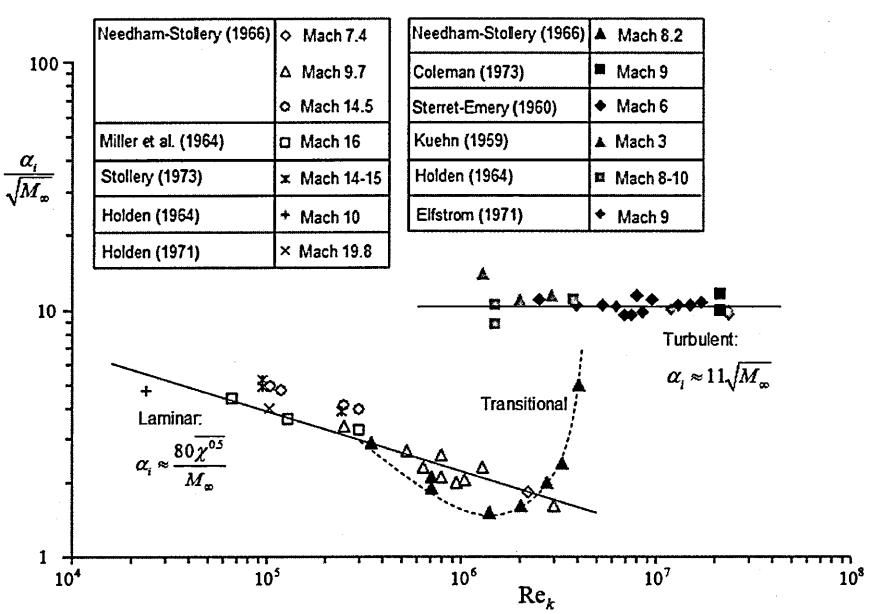

Figure 6.5 Semi-empirical prediction of incipient separation angle.

6.4 Subcritical interactions

For subcritical interactions ($\alpha < \alpha_i$) the hot spot is located to the side of the protuberance. Ahead of the protuberance the heat flux values are close to the corresponding undisturbed value or slightly lower. The ratio $St_{\max} / St_u$ is plotted for the different cases with the purpose of determining a dependence on the state of the boundary layer (Fig. 6.6). In the present case, for a fully turbulent boundary layer $St_{\max} / St_u$ is approximately 2.7 whereas for a laminar or transitional boundary layer $St_{\max} / St_u$ is around 6.5. A clearer correlation is observed in a form of Stanton number (Fig. 6.7) for all the different flow conditions considered (Eq. 6.4). The previous correlations where the undisturbed boundary layer heat flux is considered are considered misleading given that the state of the boundary layer in the region of amplified heating is believed to be transitional or even fully turbulent. Heat transfer values lower or similar to the corresponding heat transfer in undisturbed flow were measured ahead of the protuberance (Eq. 6.5). Although the exact location of the hot spot cannot be accurately predicted given its long extent to the side of the protuberance, it is convenient to consider its location from the protuberance leading edge up to a longitudinal distance of about $\mathrm{Re}_{x,k} = 0-5\times10^5$, i.e. $x_{k,\max} = 0-5\times10^5 \left(\mathrm{Re}_\infty / m\right)^{-1}$ (Eq. 6.6).

$$St_{\max,side} = 2.7\times10^{-3} \pm 20\% \quad \text{[Eq. 6.4]}$$

$$St_{\max,ahead} \approx St_u \quad \text{[Eq. 6.5]}$$

$$x_{k,\max} = 0-5\times10^5 \left(\mathrm{Re}_\infty / m\right)^{-1} \text{ to protuberance side} \quad \text{[Eq.6.6]}$$

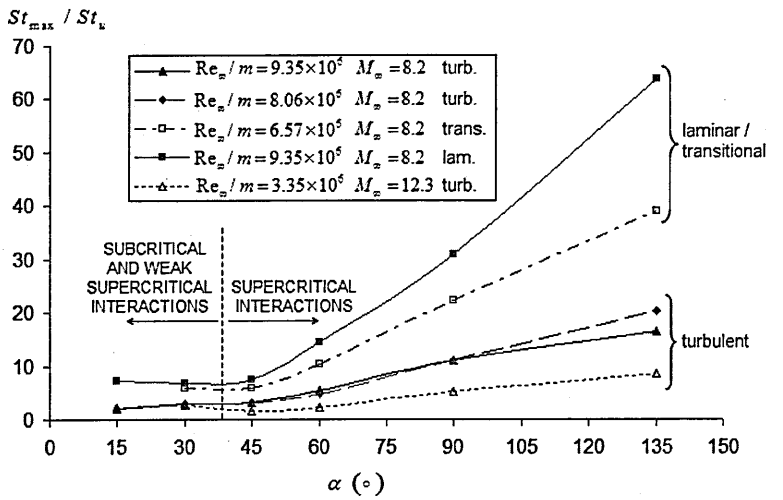

Figure 6.6 Maximum heat flux in St_{max} / St_u for all the different configurations.

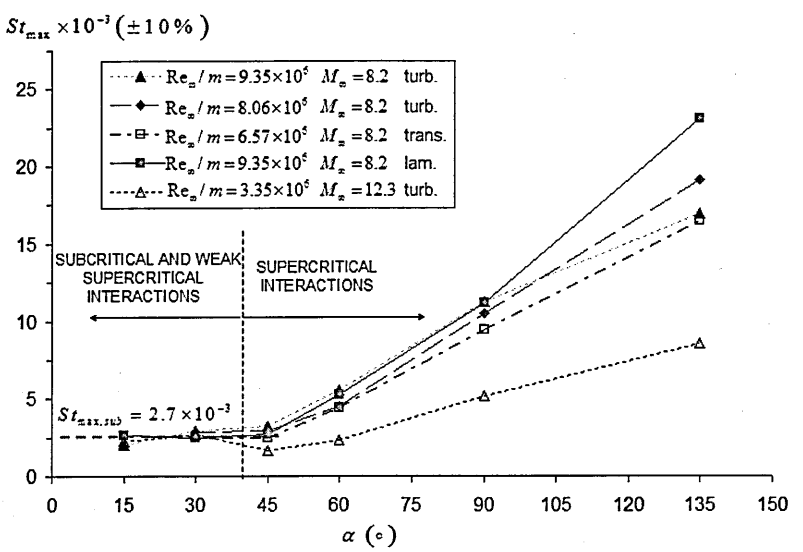

Figure 6.7 Maximum heat flux in St_{max} for all the different configurations.

6.5 Supercritical interactions

For supercritical cases the hot spot is generally found ahead of the protuberance and its magnitude is independent of the state of the incoming boundary layer. While this condition is in general related to the stagnation of the flow as hypothesised by Nestler (1985), no supporting evidence is found with the present dataset (Fig. 6.8) as the physical mechanisms that induce high heating ahead of supercritical protuberances do not directly correlate with the relevant relations considered in the classic stagnation heat transfer theory. As shown in Chapter 4, according to Lees (1956) and Fay and Riddell (1958) the following approximate relation is derived from Eqs. 4.8 and 4.9 to estimate the stagnation heat flux over a cylinder of radius equal to the height of the protuberance ($h = R_N$) and with its face opposed to the freestream flow:

$$q_{o,cyl} = \frac{0.57}{(\mathrm{Pr})^{0.6}} (\rho_e \mu_e)^{0.4} (\rho_w \mu_w)^{0.1} (h_{oe} - h_w) \frac{1}{R_N{}^{0.5}} \left(\frac{2(p_e - p_\infty)}{\rho_e} \right)^{0.25} \qquad \text{[Eq. 6.7]}$$

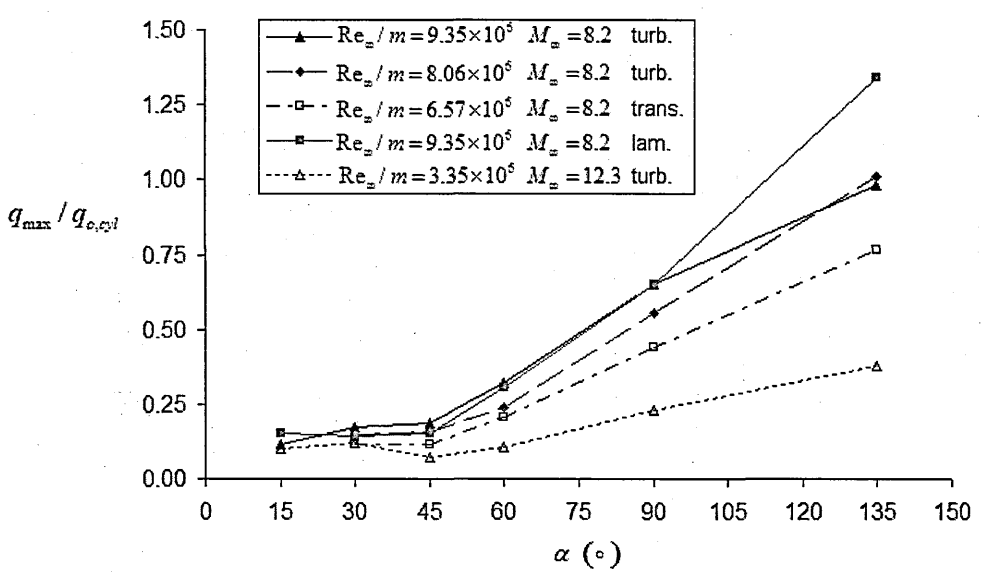

Figure. 6.8 Maximum heat flux non-dimensioned respect stagnation relation in Eq. 6.7.

Given the highest heat flux ahead of the α=135° cases is strongly dependent on the location where the separated flow reattaches to the surface and also since there is a clear increase in heat flux as the deflection angle is increased, it seems clear that the maximum heating is linked to the reattachment of the flow ahead of the protuberance also as further shown in Chapter 7.

A further assessment of the results is subsequently performed using Buckingham-Pi analysis as applied in the development of predictive methods for heat transfer in attached flows (Rogers and Mayhew, 1980). In order to derive a correlation of the data the main variables responsible for the heat flux need to be determined. It is well established that the main parameters to be considered are:

μ	viscosity
ρ	density
k	thermal conductivity
c_p	specific heat
θ	temperature (relative to wall)
U	fluid velocity
l	characteristic linear dimension

As expected from the previous literature (Chapter 2), the characteristic linear dimension l which has a dominant effect in supercritical interactions is the height of the protuberance (h) whereas the effect of width within short span protuberance configurations (about $W/\delta_u \leq 10$) is known to be negligible (e.g. see Fig. 2.15). The effect of boundary layer thickness is also considered negligible throughout the present experimental study as shown by the similitude between the peak heating at laminar and turbulent conditions (Section 5.5). Based on a dimensional analysis considering mass, length, time, thermal energy and temperature as the five fundamental units and grouping them in terms of two main non-dimensional groups (Re and Pr) the relation in Eq. 6.8 is derived, where a and b are exponents, C is a constant and Re_h is Reynolds number based on protuberance height. Since in experimental measurements of this type accurate knowledge of the Prandtl number Pr is generally not feasible, common predictive

approaches developed to date consider a constant Prandtl number. For this reason, a common simplification is to assume Pr=1 and Eq. 6.8 thus reduces to Eq. 6.9. For more details on the derivation of this relation refer to Rogers and Mayhew (1980).

$$Nu_h = C\,\mathrm{Re}_h^a\,\mathrm{Pr}^b \qquad \text{[Eq. 6.8]}$$

$$Nu_h = C\,\mathrm{Re}_h^a \qquad \text{[Eq. 6.9]}$$

The experimental results obtained at a freestream Mach number of M_∞=8.2 and at Reynolds numbers of $Re_\infty/m=6.57\times10^6$ (transitional), $Re_\infty/m=8.06\times10^6$ (turbulent) and $Re_\infty/m=9.35\times10^6$ (laminar and turbulent) are used to obtain a correlation of Nu_h with Re_h. The highest heat flux in terms of Nu_h are plotted against Re_h for the supercritical cases (α=45°, α=60°, α=90° and α=135°) showing a correlation of the measurements with a slope of a=1.6. Since Pr is considered equal to 1, $Nu_h = St_{\max}\,\mathrm{Re}_h$ and a=1.6 are introduced in Eq. 6.9 to obtain the relation in Eq. 6.10 (Fig. 6.9). Recall that the recovery factor in the calculation of Stanton number is also considered to be r=1 and that the hot spot magnitude is considered to be independent of the state of the incoming boundary layer.

$$St_{\max}\,\mathrm{Re}_h^{-0.6} = C \qquad \text{[Eq. 6.10]}$$

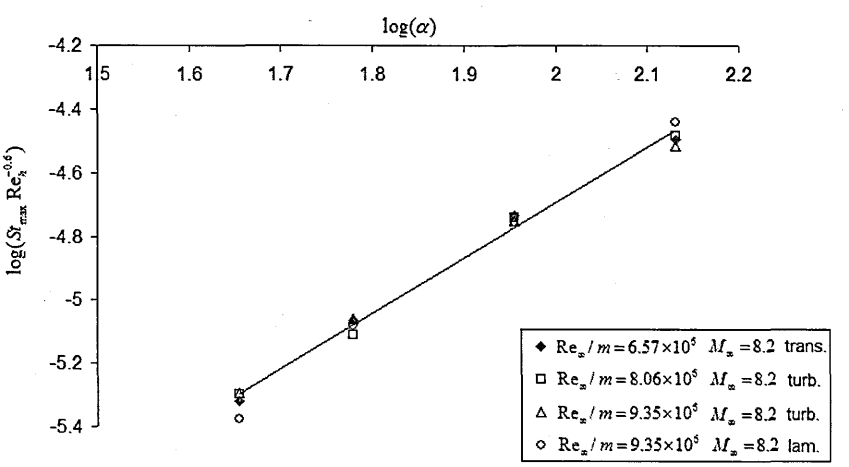

Figure 6.9 Correlation of $St_{max}Re_h^{-0.6}$ with protuberance deflection angle α at different freestream Reynolds numbers in logarithmic scale for all the Mach 8.2 cases.

The term $St_{\max}\,\mathrm{Re}_h^{-0.6}$ is constant for different Reynolds numbers but it increases with higher deflection angles (Fig. 6.10). As the protuberance deflection angle is increased, the deflection that the incoming flow experiences before reattaching to the wall is lower and so its impact energy to the surface is higher (Eq. 6.11). This is demonstrated in Fig. 6.10, which shows the constant trend obtained for the M_∞=8.2 tests at all the different conditions by non-dimensioning the relation in Eq. 6.10 with respect to $(1-\cos\alpha)$, while the same does not apply in the cases where the hot spot takes place to the side of the protuberance - i.e. in subcritical or weak supercritical interactions. The factor $(1-\cos\alpha)$ is derived through basic trigonometry from the fraction of freestream mass flow rate $\dot{m}_\infty$ which is deflected towards the surface of the vehicle by the protuberance: $\dot{m}_\infty(1-\cos\alpha)/2$. Further details on the behaviour of the flow field ahead of supercritical protuberances can be found in Chapter 7.

$$St_{\max}\,\mathrm{Re}_h^{-0.6}/(1-\cos\alpha)=C \qquad \text{[Eq. 6.11]}$$

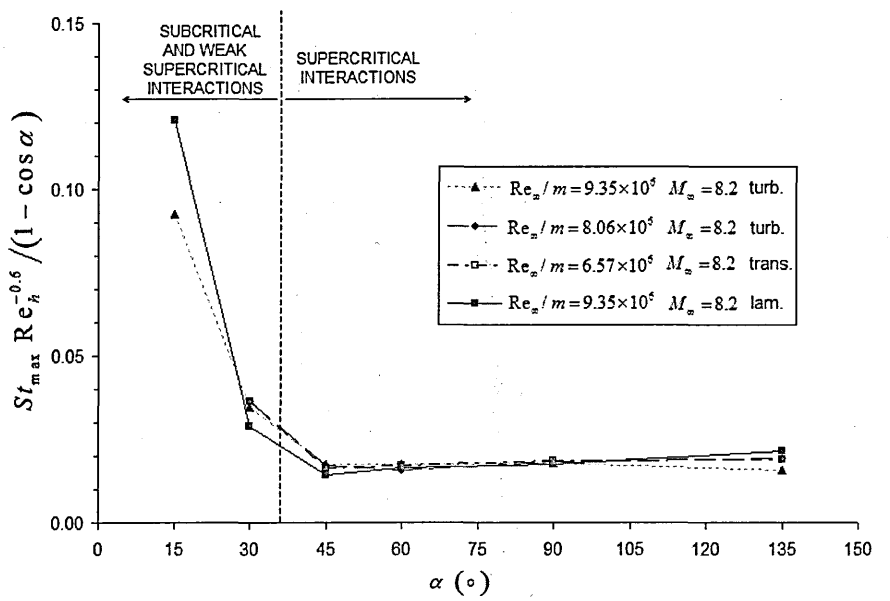

Figure 6.10 Correlation of $St_{max}Re_h^{-0.6}/(1 - \cos\alpha)$ for all the Mach 8.2 configurations.

The effect of Mach number is subsequently investigated through a similar correlation between the M_∞=8.2 and the M_∞=12.3 measurements. Its effect is found to be proportional to the square root of Mach number as shown in Eq. 6.12. Based on this analysis, Fig. 6.11 shows a correlation of the present experimental dataset in terms of the dominant parameters: Reynolds number, Mach number and protuberance deflection angle and height. A suitable constant C is found to be $C = 5.2\times10^{-5}$. The actual thermal capacity of the flow is already taken into account in the definition of Stanton number. The correlation provided is subject to a total conservative uncertainty of ±25% while also considering the ±10% uncertainty inherent to the measurements.

$$St_{\max}\,\mathrm{Re}_h^{-0.6}\,M_\infty^{0.5}/(1-\cos\alpha) = C \qquad \text{[Eq. 6.12]}$$

To conclude, the maximum heat transfer to the side of the protuberance is presented in Eq. 6.13. The hot spot will nevertheless be located ahead of the protuberance in most cases following the relation in Eq. 6.14. In these cases the hot spot will take place as shown in Eq. 6.15. Only in low-Reynolds low-deflection cases will this be located to the side of the protuberance as a subcritical interaction (Eq. 6.4).

$$St_{\max,side} = 2.7\times10^{-3} \pm 20\% \qquad \text{[Eq. 6.13]}$$

$$St_{\max,ahead} = 5.2\times10^{-5}\,\mathrm{Re}_h^{0.6}(1-\cos\alpha)M_\infty^{-0.5} \pm 25\% \qquad \text{[Eq. 6.14]}$$

$$x_{k,\max} = 0-5\times10^{4}\left(\mathrm{Re}_\infty/m\right)^{-1} \text{ ahead of protuberance} \qquad \text{[Eq. 6.15]}$$

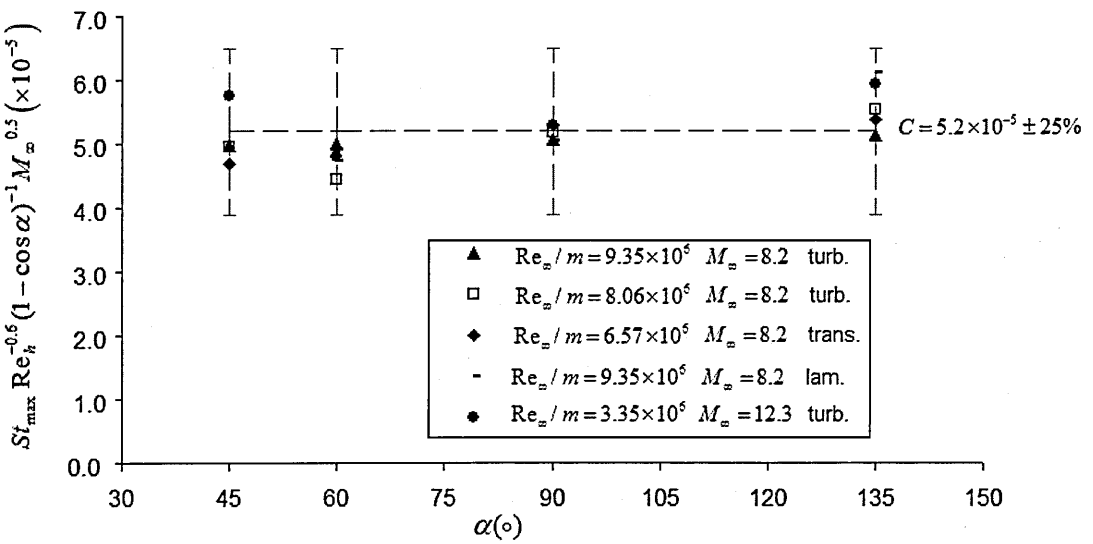

Figure 6.11 Correlation of the whole experimental dataset in the present study showing uncertainty of 25%.

6.6 Hot spot prediction

In what follows, a semi-empirical approach to predict the highest heating in the vicinity of surface protuberances is presented. Up to this point, the main findings in this investigation are summarised.

6.6.1 Summary of main findings

i. The interference interactions caused by the protuberances are expected to be strongly three-dimensional and an increase in heat transfer to the side occurs in all the cases.

ii. The impact of the local interaction on the heating of the vehicle surface is dominated by whether the interaction is subcritical or supercritical. The hot spot is found to the side of the protuberance in subcritical interactions and generally ahead of it in supercritical interactions, with the only exception being weak supercritical interactions.

iii. The state of the incoming boundary layer appears to have a negligible effect on the magnitude of the highest heat transfer in both subcritical and supercritical interactions. The boundary layer turbulence can however have a strong effect on the incipient separation angle and thus on the location of the hot spot and the region of increased heating around the protuberance.

iv. The highest heating in subcritical interactions is not affected by the height and the width of the protuberance. This is likely not to apply to protuberances with h/δ_u ratios lower than 1 and particularly if the protuberance is shorter than the subsonic portion of the boundary layer. In these cases, however, the peak heat flux is not expected to be as high. The magnitude of the hot spot in supercritical interactions increases with protuberance height.

v. The magnitude of the hot spot in supercritical interactions decreases with Mach number and increases with Reynolds number. In subcritical interactions the effect of Reynolds number and Mach number is negligible. In the later interactions, all measurements correlate at the same Stanton number.

vi. The deflection angle of the protuberance has a strong effect on the magnitude of the hot spot in supercritical interactions. At high deflection angles the magnitude of the hot spot increases and protuberances should therefore be kept as slender as possible. Forward deflection angles need to be specially avoided. In subcritical interactions, the protuberance angle does not affect the magnitude of the maximum heat flux.

vii. The extent of the interaction region and thus the area where heat transfer is increased becomes larger with higher deflection angle. Laminar and transitional boundary layers are more prone to separation than fully turbulent boundary layers and are accompanied by larger separation regions. In these cases, reattachment to the side of the model occurs at a farther distance from the leading edge. The freestream Reynolds number also has a strong effect on the extent of the separated region.

6.6.2 Hot spot estimation approach

Based on these findings and on the current semi-empirical correlations, a summary for an engineering method for hot-spot estimation is presented in Fig. 6.12. The initial step is to estimate whether the interaction is subcritical or supercritical based on two-dimensional compression corner experimental data. In this case, high heat transfer regions around the protuberance are indicated and the location and magnitude of the hot spot can be estimated by using the derived semi-empirical correlations. In particular, the highest heating ahead of the protuberances can become critical in the design of hypersonic vehicles.

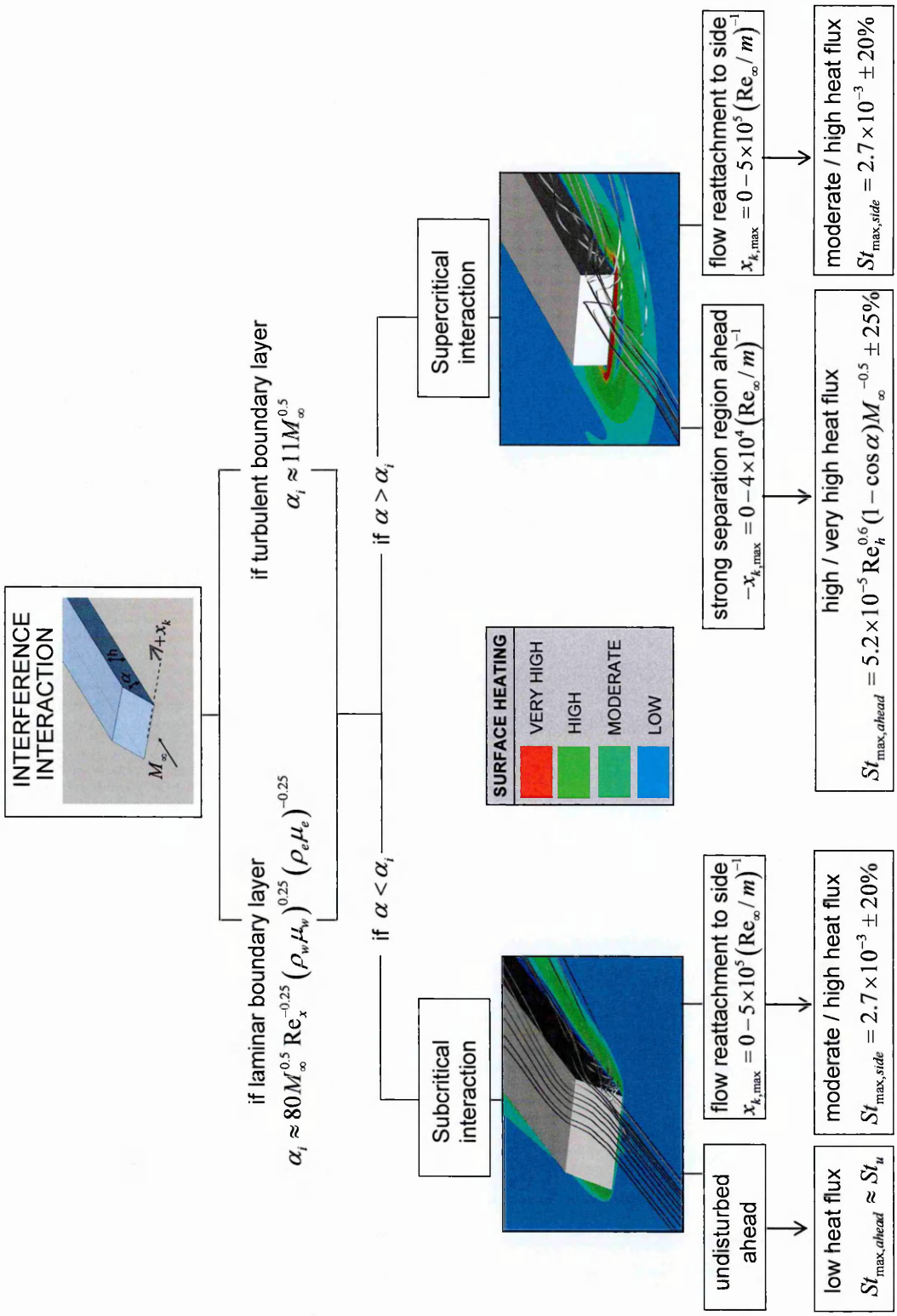

Figure 6.12 Engineering approach to predict location and magnitude of highest heating in the vicinity of surface protuberances in hypersonic flow.

More accurate estimations can be obtained in this case referring directly to Fig. 6.13 for the corresponding angle and Mach number. In this way, the uncertainty introduced by the correlations of deflection angle and Mach number is avoided and final estimates can be obtained with an uncertainty of ±15%. Particular scatter is observed at forward deflection angles (α=135°) given that the actual deflection suffered by the freestream flow before impact on the vehicle surface is also affected by the formation of secondary contrarotating vortices just ahead of the protuberance as further considered in Chapter 7.

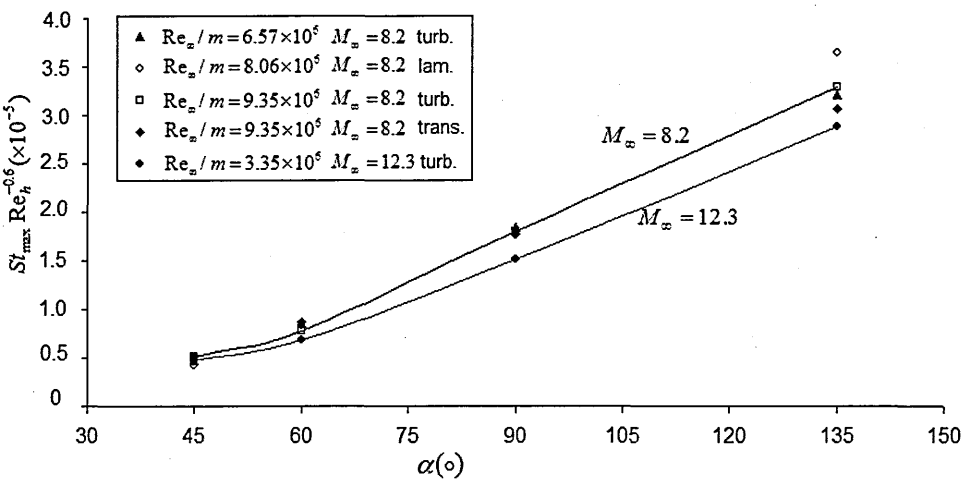

Figure 6.13 Correlation of $St_{max}Re_h^{-0.6}$ with protuberance deflection angle α at different freestream Mach numbers.

It must be noted that these semi-empirical correlations are based on well-defined forms of protuberances which do not account for other effects such as side sweep or skewness. Consideration into these effects is taken in Chapter 8, where the applicability of the method to three specific protuberances is assessed. Before, a further insight into the flow field is presented in the following chapter.

CHAPTER 7

Flow Field in Interference Regions

In this chapter, the flow structure around the protuberance and other flow characteristics are interpreted according to the experimental results. While most of the information is obtained from the high-speed schlieren videos, further details from the flow are also observed from the oil-dot visualisations and the heat flux measurements in the vicinity of the protuberances. All the interpretations are additionally supported by the computational results presented in Appendix D.

7.1 Flow visualisations

Schlieren systems capable of obtaining time-resolved visualisations from high-speed flows were first developed in the 1950s to investigate unsteady flows (Chapman et al., 1958). The application of high-speed schlieren systems to date has been limited by the high complexity in having a very intense incoherent light source in combination with a fast framing device (Settles, 2001). A digital high-speed schlieren system was developed for the present application to study the unsteadiness of the interactions induced by the protuberances. Further details about this system are found in Chapter 2 and also in Estruch et al. (2008).

7.1.1 Qualitative visualisations

Instantaneous schlieren visualisations of the different interactions investigated have been presented and described in Chapter 5 where it has also been shown that

interference interactions may sometimes result in extremely high surface heating. The time-dependent flow visualisation sequences obtained offer a qualitative idea of the unsteadiness of these interactions. It is important to determine the unsteady behaviour of the flow since in this regime this can become particularly critical in terms of fatigue and structural damage to the vehicle (Delery and Marvin, 1986; Dolling, 1993).

Examples of the interactions under study are presented in selected schlieren images taken at a frame rate of 50kHz in Fig. 7.1a – which corresponds to the subcritical interaction obtained with the datum configuration (M_∞=8.2, Re_∞/m=9.35x10^6, α=30°, turbulent) and Fig. 7.1b – which corresponds to the supercritical α=90° case at the same freestream conditions as in the datum case. Only 0.1ms out of the total run time is captured within the sequences presented due to space restrictions but the whole effective run was captured during the tests as further shown in Appendix B.

The boundary layer in the α=30° case remains attached ahead of the protuberance and the interaction is therefore subcritical (Chapter 5). As shown in Fig. 7.1a, the attached shock appears not to move during the whole steady flow duration. On the other hand, a supercritical interaction is obtained with the α=90° model. In this case a separation shock is observed ahead of the protuberance which is clearly unsteady (Fig. 7.1b). Similar results have been consistently observed for the rest of supercritical interactions, where the separation shock ahead of the protuberance has been shown to move during the established flow duration.

Further investigation on the unsteadiness of the flow to the side of the protuberance could not be performed due to measurement restrictions (see Chapter 2). However, since the increased heating to the surface to the side of a protuberance cannot reach as high values as ahead of supercritical protuberances, the unsteadiness of the flow to the side is expected not to be of particular importance. Special attention needs to be paid to supercritical interactions, ahead of which extreme high heat flux rates can take place (see Chapter 5). In this case, unsteady heat loads can generate greater hazards with the resulting interaction. Based on these findings, the present sequences of schlieren images clearly reveal the following:

i. Subcritical interactions:

The flow upstream of the protuberance appears steady. Since subcritical interactions do not induce particularly high increases in surface heat flux the unsteady behaviour of the flow is not of high importance in these cases.

ii. Supercritical interactions:

The flow upstream of supercritical protuberances is highly unsteady but no periodicity is qualitatively apparent based on the high-speed schlieren videos. The flow unsteadiness in the region of the interaction together with the high heat loads that are induced ahead of the protuberance in some cases can become a clear hazard for the integrity of the vehicle. Especial care needs to be taken in this case.

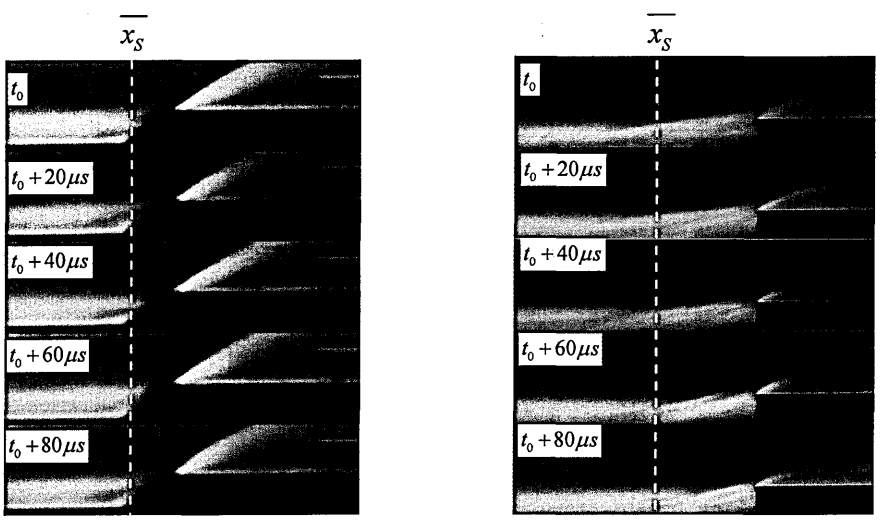

(a) α=30°, steady (b) α=90°, unsteady

Figure 7.1 Time-sequenced schlieren images: M_∞=8.2, Re_∞/m=9.35x10^6, turbulent.

7.1.2 Shock unsteadiness

Further investigation on the unsteadiness of these interactions was done based on the schlieren videos and digital image processing as described in Estruch et al. (2008). The location of the shock in the present study was determined by detecting sharp changes in pixel intensity in the digital schlieren images (Chapter 3). This thus allowed discriminating features in the images based on the pixel intensity gradients through them. The test model, the boundary layer and the shock were thus discriminated in the form of binary images as shown in Fig. 7.2 for the different protuberance deflection angles of α=15°, α=30°, α=45°, α=60°, α=90° and α=135° respectively from Fig. 7.2a to Fig. 7.2f. The shock is clearly distinguished outside of the boundary layer but detection of the separation locus on the flat plate is not possible given that the embedment of the shock into the boundary layer is not so clear in the schlieren images.

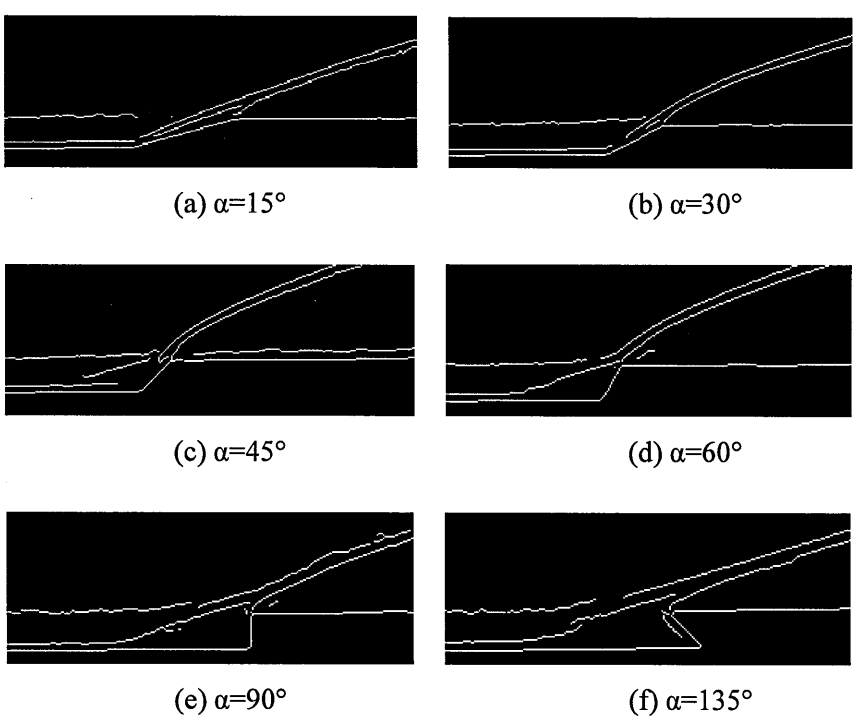

(a) α=15° (b) α=30°

(c) α=45° (d) α=60°

(e) α=90° (f) α=135°

Figure 7.2 Shock detection: M_∞=8.2, Re_∞/m=9.35x10^6, turbulent.

Figure 7.3 plots the change in the location of the shock at a distance of $y/\delta_u=2$ for the $\alpha=30°$, $\alpha=60°$ and $\alpha=90°$ protuberances at $M_\infty=8.2$, $Re_\infty/m=9.35x10^6$ and with a turbulent boundary layer to quantify the different shock locations between the subcritical and supercritical cases. This further confirms that whereas in the subcritical interaction ($\alpha=30°$) the shock appears steady, in the supercritical cases ($\alpha=60°$ and $\alpha=90°$) the separation shock wave is highly unsteady. The amplitude of the separation shock motion in the longitudinal direction is about 1.5mm in the $\alpha=60°$ case and 2mm in the $\alpha=90°$ case. Unsteadiness therefore grows with the increasing length of the separated shear layer caused by enlarging the protuberance deflection angle. As a consequence, not only the heat loads to the vehicle surface increase with high deflection supercritical protuberances, but also the flow becomes more strongly unsteady.

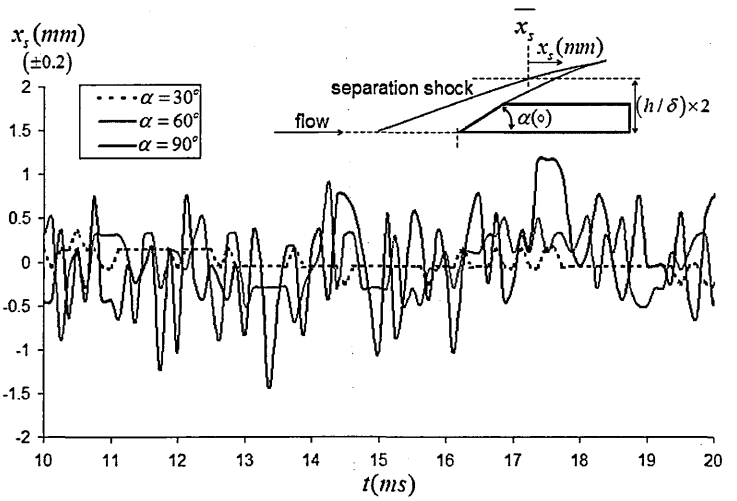

Figure 7.3 Shock wave oscillation between t=10ms and t=20ms from the start of the run. $M_\infty=8.2$, $Re_\infty/m=9.35x10^6$, turbulent.

A Fourier analysis of the shock unsteadiness for the $\alpha=90°$ interaction is shown in Fig. 7.4. Further details on this method can be found in Estruch et al. (2008). The frequency resolution in this case is limited to 100Hz by the sampling frequency (50kHz) and the duration of the effective established flow run considered (≈10ms). The power spectrum of the obtained signal is essentially broadband in nature and appears to contain no dominate frequency. This confirms what was qualitatively expected based on the schlieren videos which suggested that no clear periodic motion of the shock seems to be apparent in the supercritical interactions.

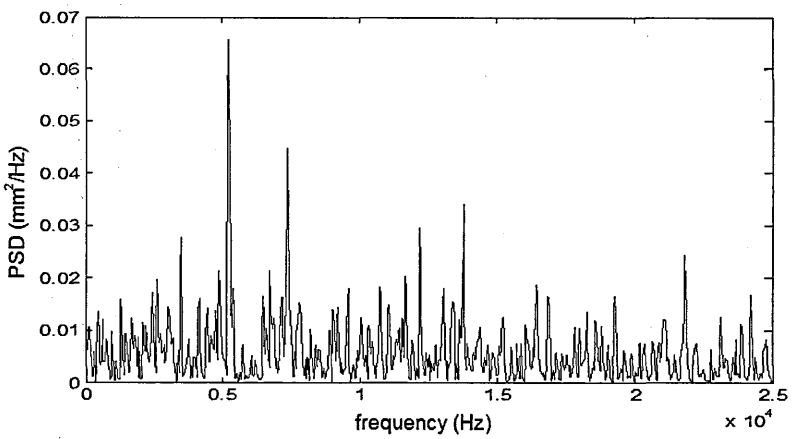

Figure 7.4 PSD showing time-dependent and broadband signal at M_∞=8.2, $Re_\infty/m=9.35x10^6$, α=90°, turbulent.

7.1.3 Supercritical hot spot unsteadiness

For a further analysis of the hot spot unsteadiness in supercritical interactions the flow ahead of the protuberance can be considered analogous to that ahead of 2-D supercritical compression ramps and 2-D steps. The physical mechanism responsible for the unsteadiness of this type of interaction is still not completely understood (Dolling, 2001; Ganapathisubramani et al., 2007). A study on supersonic interactions presented in Estruch et al. (2009d) has shown that an intermittent region takes place under the separation shock wave. In this region, lower frequency energy fluctuations are found (10^2 – 10^4 Hz) and with a larger scale than in other regions of the interaction. In the separated flow region – far from the separation locus – most of the energy is found at a similar frequency range as this characteristic of the incoming boundary layer (10^4 Hz) and at a smaller scale also. In the separated flow region the incoming turbulence levels are amplified but little low frequency influence is observed. Large-scale unsteadiness therefore takes place in the intermittent region as shown in the schematic diagrams in Fig. 7.5.

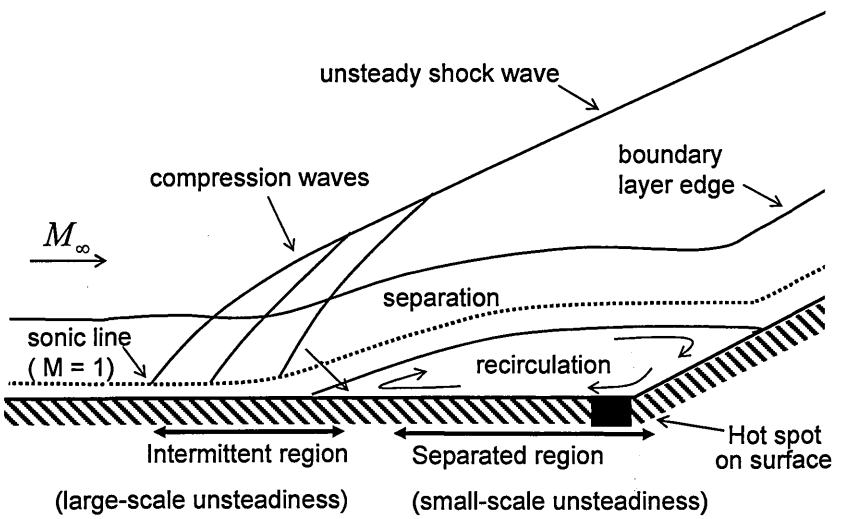

(a) 2D compression ramp

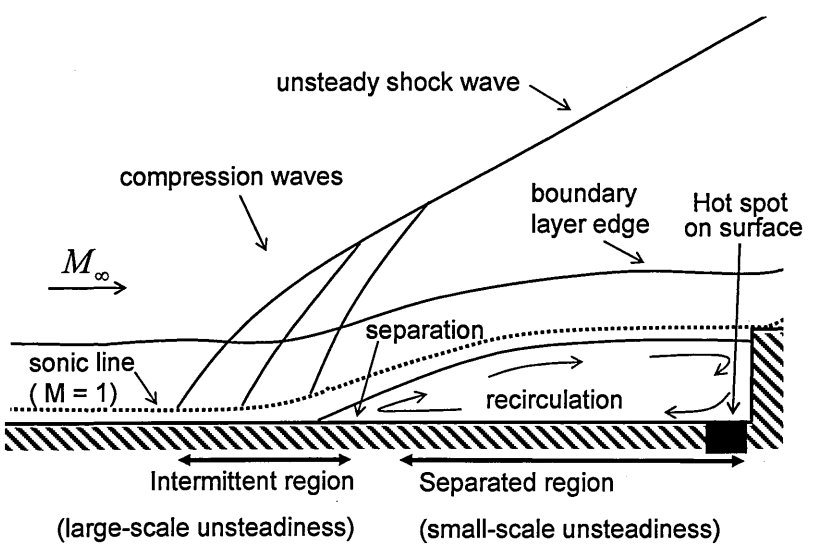

(b) Forward step

Figure 7.5 Low-frequency influence in other SWTBLIs.

Two schlieren visualisations of the α=90° interactions at M_∞=8.2, Re_∞/m=9.35x10^6 and turbulent boundary layer are shown in Fig. 7.6, where an intermittent region close to the separation shock wave is observed. It is thus expected that high-frequency small-scale fluctuations take place in the region of separated flow ahead of the protuberance. Despite the unsteady nature of these minor interactions its effect on the location of the hot spot is not expected to be significant. It is in the region where flow starts separating from the wall that large-scale unsteadiness takes place mainly due to the unsteadiness of the separation shock. As shown in Chapter 4, the heat flux augmentation in the separation region takes place gradually as the boundary layer separates from the flat plate and therefore the large-scale unsteadiness at this location does not occur in the regions of higher heat loads. Still, account needs to be taken of the intermittence of the flow and on the strong 3-dimensionality of the separation region as shown in Fig. 7.7. Further details on the concepts of large-scale low-frequency unsteadiness (in intermittent regions) and small-scale high-frequency unsteadiness (in separated regions) can be found in Estruch et al. (2009d).

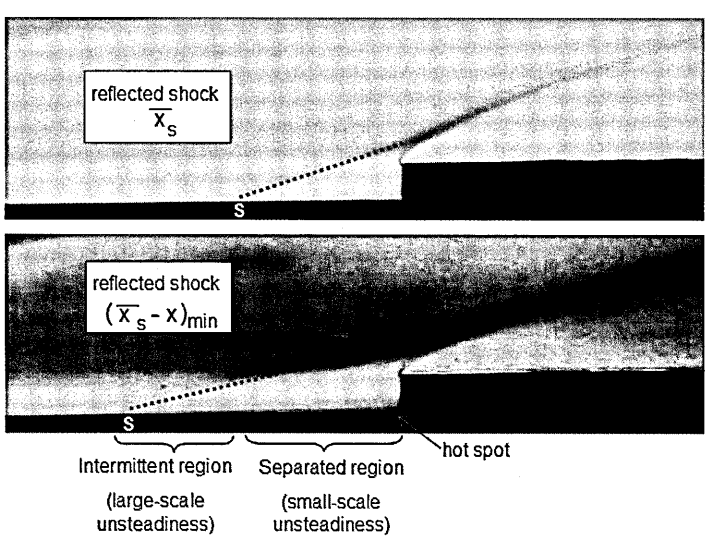

Figure 7.6 Schlieren images indicating mean position of reflected shock ($\overline{x_s}$) and maximum upstream displacement of the shock ($x_s - \overline{x_s}$). M_∞=8.2, Re_∞/m=9.35x10^6, α=90°, turbulent.

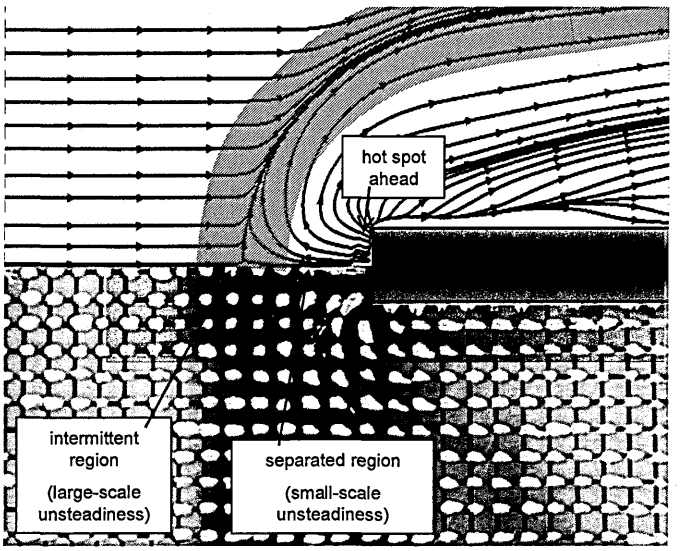

Figure 7.7 Oil flow visualisation and corresponding interpretation. M_∞=8.2, Re_∞/m=9.35x10^6, α=90°, turbulent

7.2 Flow field interpretation

A further interpretation of the flow field around a surface protuberance can be made by distinguishing between subcritical and supercritical interactions as the effects in the heat flux augmentation around the protuberance between these two types of interactions are clearly different.

7.2.1 Subcritical interactions

In the subcritical cases, the flow upstream appears undisturbed and close to the centreline of the protuberance this can be considered as quasi-two-dimensional in the y_{cl} direction. The increased heat transfer which occurs to the sides is caused by corner effects which result in the appearance of a vortex as interpreted in Fig. 7.8 and similar to the junction horseshoe vortex observed in blunt swept fin interactions (Lakshmanan et al., 1988). The high heating rates appear as a consequence of the flow reattachment to the side of the protuberance (Fig. 7.9).

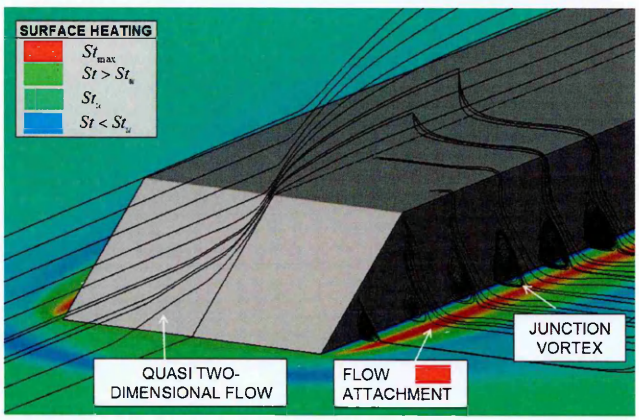

Figure 7.8 Schematic diagram of the flow field around datum protuberance based on present results.

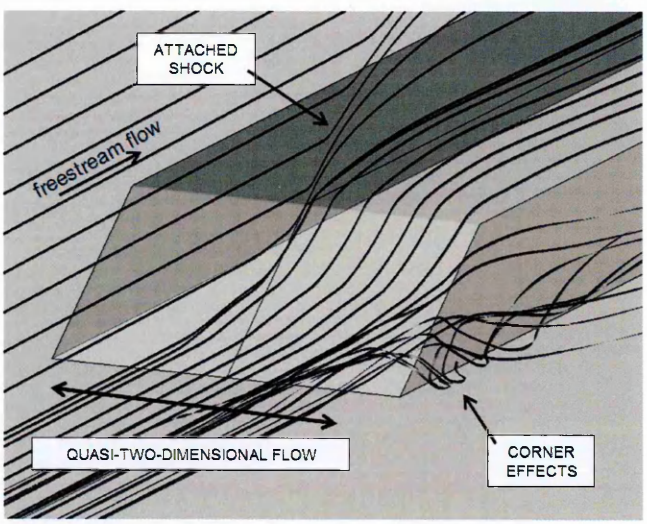

Figure 7.9 Artistic impression showing corner effects on datum case and quasi-2D flow ahead of protuberance.

7.2.2 Supercritical interactions

Whereas similar corner effects are expected to the side of supercritical interactions, the flow in this case separates ahead of the protuberance. An example is shown in Fig. 7.10 based on the case of a α=135° protuberance under turbulent flow, M_∞=8.2 and $Re_\infty/m=9.35x10^6$. Given that high heating ahead of this model is due to the reattachment of the flow and assuming the existence of a large secondary recirculation in comparison to the other supercritical cases, this may explain the minor upstream change in the location of the hot spot as shown in Chapters 5 and 6.

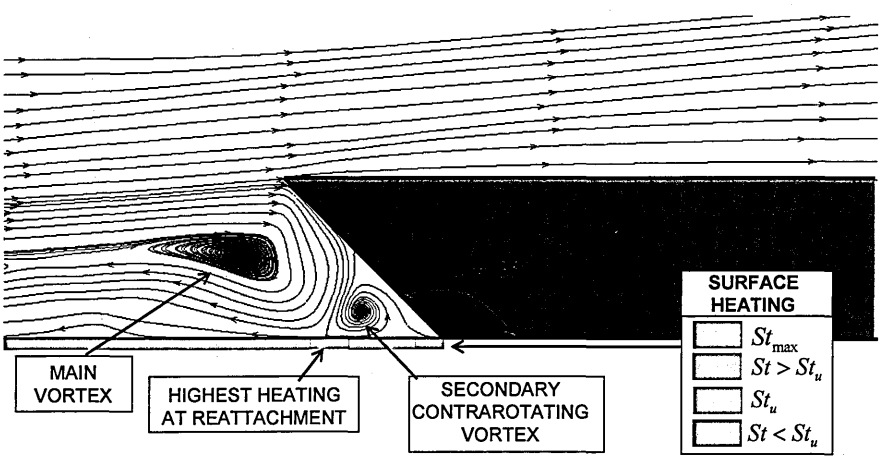

Figure 7.10 Schematic representation of flow in centreline: turbulent, M_∞=8.2, $Re_\infty/m=9.35x10^6$, α=135°. Streamlines based on qualitative CFD solution.

The same trend is also observed in the computational results by Haas (2009). Figure 7.11 shows the flow pattern predicted for the supercritical interaction induced by the α=90° protuberance at freestream conditions of M_∞=8.2 and $Re_\infty/m=9.35x10^6$. A complex skin friction pattern on the surface ahead of the protuberance is observed which is characterised by different regions of flow separation and reattachment from the surface with a strong three-dimensional aspect. As shown by a comparison with the present measurements the highest heat flux is found along the primary reattachment line. The secondary separation and reattachment regions do not result in such strong heat flux alterations with comparison to the corresponding undisturbed local heating.

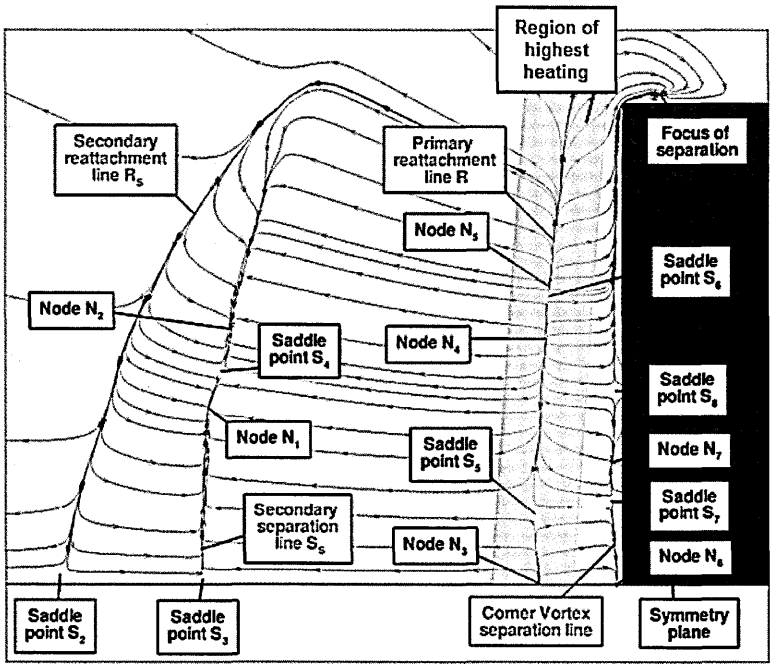

Figure 7.11 Skin friction on surface ahead of protuberance: turbulent, M_∞=8.2, $Re_\infty/m=9.35x10^6$, α=90° based on numerical simulations by Haas (2009).

The interpretation of supercritical interactions in the vicinity of the protuberances is therefore summarised in the form of two schematic diagrams in Figs. 7.12 and 7.13. The hot spot is generally found ahead of the protuberance at the location where the flow reattaches to the surface. A side vortex is also observed which induces an increase in heat flux to the side of the device as well. In weak supercritical interactions the heat flux to the side can be higher than this to the front of the protuberance. It must be taken into account that this is based on protuberances with side corners of 90° as in the present study (i.e. between protuberance side and vehicle surface). In cases where the side junction between the protuberance and the surface is found at an angle different than 90°, the consequent different reattachment of the flow to the surface is expected to result in slightly different side heat flux as estimated using the approach in Chapter 5.

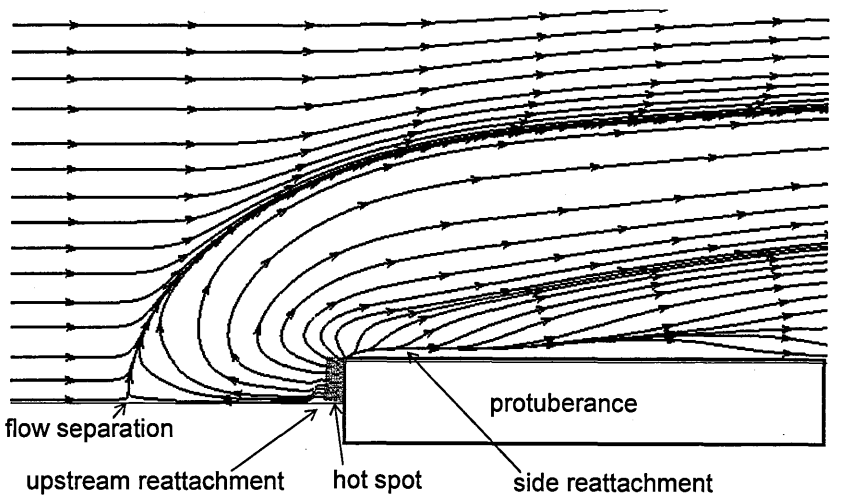

Figure 7.12 Interpretation of the flow field around supercritical protuberances. Plan view.

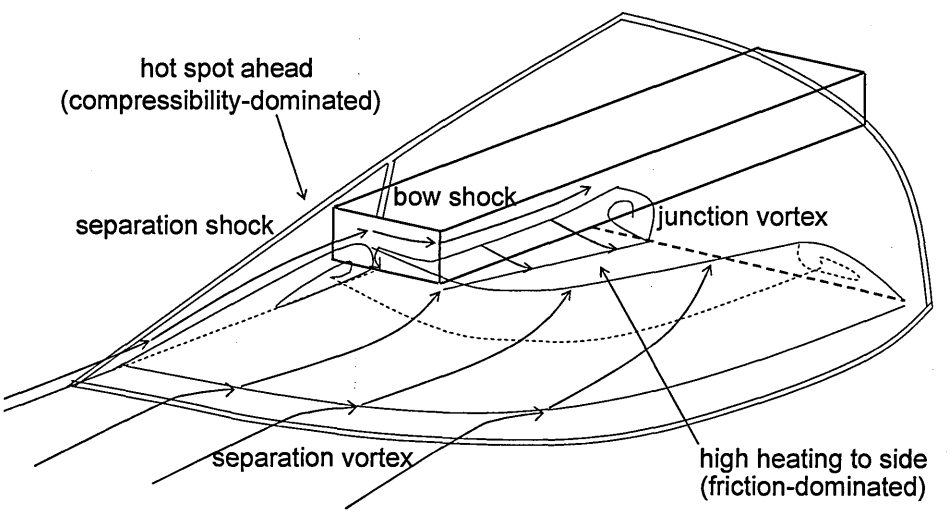

Figure 7.13 Interpretation of the flow field around supercritical protuberances.

CHAPTER 8

Application to Specific Protuberances

To further assess the results obtained from the generic interactions, an experimental investigation was also performed on three protuberances with more specific geometries. Heat flux measurements, high-speed schlieren videos and oil dot visualisations were obtained for each of these configurations. In particular, consideration is taken in the applicability of the predictive approach developed in Chapter 6 to these specific protuberances. The flow field around the protuberances is also described.

8.1 Case study

As shown in Fig. 8.1, the three protuberances that were considered in the present study were to represent the following cases:

i. A slender short protuberance which induces a subcritical interaction.

ii. A blunt short protuberance which induces a supercritical interaction.

iii. A tall protuberance which also induces a subcritical interaction.

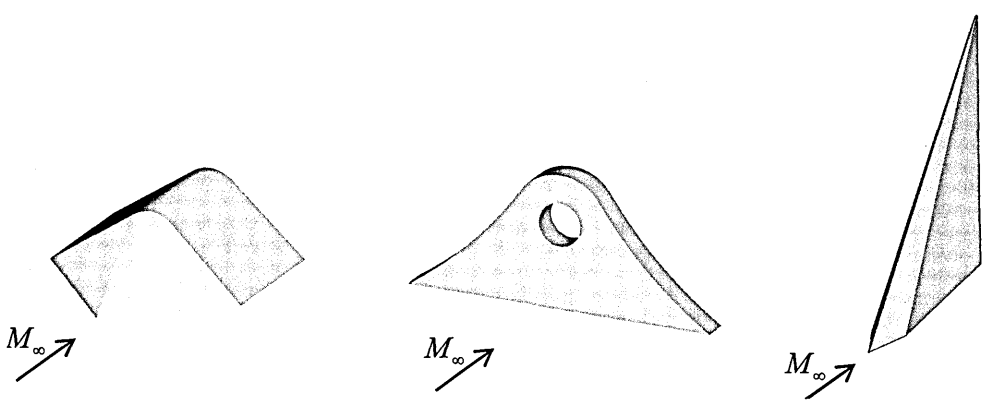

(a) Slender (b) Blunt (c) Tall

Figure 8.1 Perspective view of slender, blunt and tall protuberances.

The geometries of these protuberances are more specific than those considered in the main study. Tests were performed at M_∞=8.2 and $Re_\infty/m=9.35x10^6$ and under turbulent flow (Table 8.1). In order to provide further credibility to the validation of the predictive approach, a thicker boundary layer (δ_u=12mm) than in the datum study (δ_u=5mm) was used. This was obtained by using a set of vortex generators with a height of 4mm and with a similar design as in the main investigation (Chapter 3). The heat flux of the undisturbed boundary layer at the location of the protuberance was $St_u = 1.0x10^{-3}$ as with the δ_u=5mm boundary layer under the same freestream conditions.

M_∞	Re_∞ / m [m^{-1}]	T_w [K]	VG h (mm)	δ_u (mm)	St_u ($x10^{-3}$)
8.2	$9.35x10^6$	295	4	12	1.0

Table 8.1 Test conditions with VG design as in Fig. 3.15.

8.2 Slender case

Slender protuberances can be found on hypersonic vehicles in a number of shapes. As shown in Chapter 1, this would be for instance the case of the liquid hydrogen feedline fairing and the ullage settling motor fairings on the ARES I upper stage vehicle. The present investigation has so far shown that slender protuberances are less prone to force the separation of the boundary layer ahead of the protuberance than blunt geometries and therefore the induced interaction at some given conditions is likely to be subcritical.

8.2.1 Protuberance model

A surface protuberance in the form of a launch support or an antenna fairing has been considered to represent a slender configuration. Similar launch pins can be needed on the surface of hypersonic vehicles in order to sustain them at the moment of their launch. Other similar devices can be found on the surface of hypersonic vehicles as protection pads for different purposes (Chapter 1). The protuberance used in the present case has a width of 19.3mm and a height of 6.5mm (Fig. 8.2). The h/δ_u ratio is approximately 0.5. An extension was attached at the back of the test model in order to allow fixing it to the flat plate.

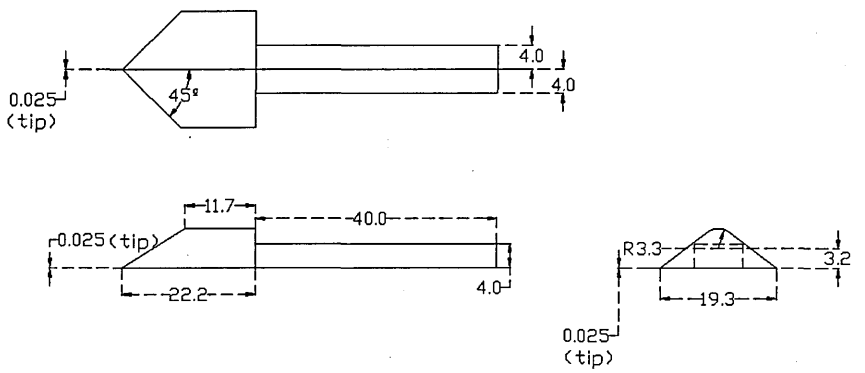

Figure 8.2 Dimensions of slender protuberance (all dimensions in millimetres)

8.2.2 Flow field

The flow field is assessed according to the schlieren and oil dot results presented respectively in Figs. 8.3 - 8.5. The subcritical nature of the present interaction is confirmed by the presence of an attached shock wave on the protuberance model. The oil dots ahead of the protuberance provide further evidence of the quasi-2-dimensional behaviour of the flow upstream of the model as interpreted in Fig. 8.5. Oil dots to the model side are the most strongly skewed. This demonstrates that the highest skin friction is located to the side of the protuberance as it is expected in subcritical protuberances.

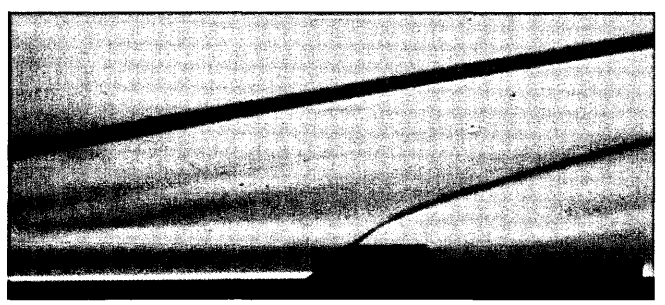

Figure 8.3 Schlieren image of slender protuberance

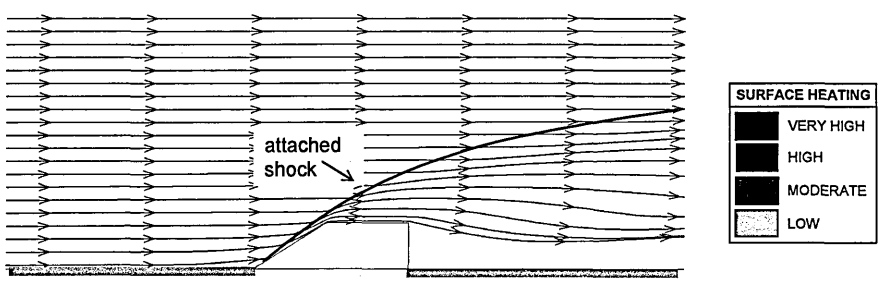

Figure 8.4 Flow field along centreline based on schlieren image.

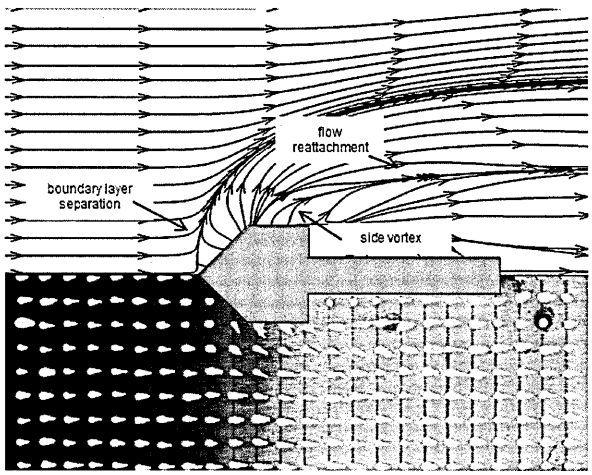

Figure 8.5 Oil flow visualisation and flow streamlines interpretation

8.2.3 Local heating

Heat flux measurements in the vicinity of this protuberance are presented in Fig. 8.6. The interference interaction induced by the protuberance results in an increase in local heating to the surface to the side of the model as expected for subcritical protuberances. It must be noticed in this case that the junction between the protuberance side and the flat plate is found at an angle of 145° and the leading edge is sharp. Thus there is a slightly different reattachment pattern of the flow to the side than with the generic protuberances considered in the main study, in which the protuberance side was perpendicular to the plate.

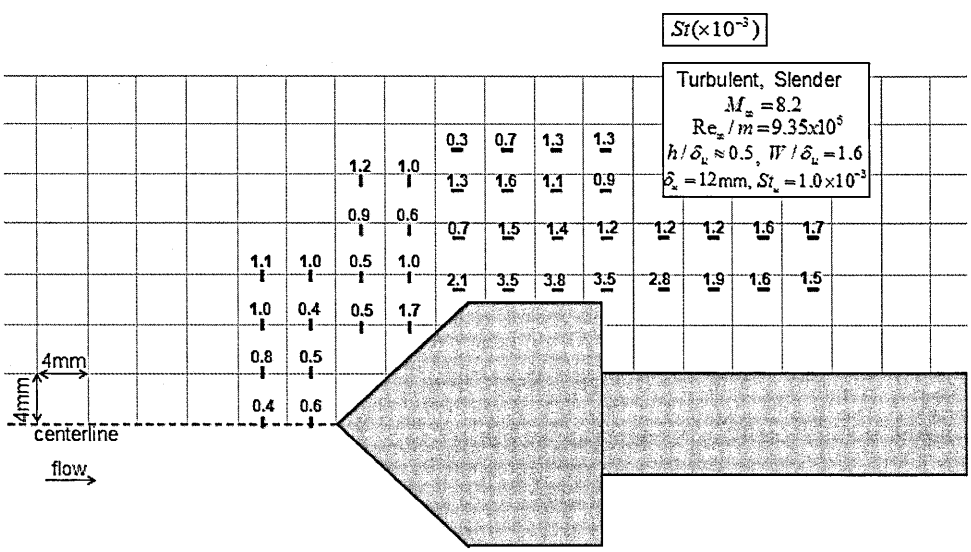

Figure 8.6 Heat flux measurements in the vicinity of slender protuberance.

The maximum heat flux measured to the side of this protuberance is $St_{max,side} = 3.8 \times 10^{-3}$, which is about 40% higher than the values found with the generic protuberances ($St_{max,side} = 2.7 \times 10^{-3} \pm 20\%$) as compared in Fig. 8.7. As expected, the different geometry of the leading edge and the protuberance side in this case result in a reduced deflection of the flow before its reattachment to the flat plate. In absolute terms, the maximum heat flux in this case is of a similar order of magnitude in comparison to the much higher heat flux augmentations ahead of supercritical interactions which reach values up to 10 times higher than the maximum heat flux to the side of the protuberance (Chapter 5). Ahead of the protuberance, the heat flux is similar to the corresponding undisturbed value or lower ($St \leq St_u$).

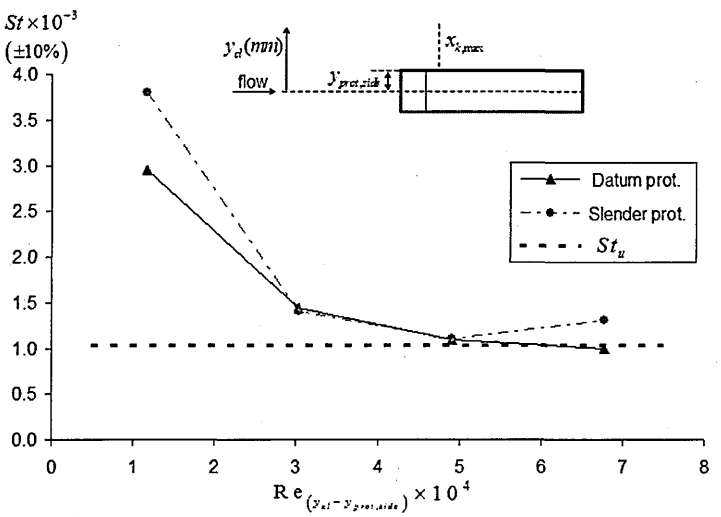

Figure 8.7 Heat flux at different lateral locations to the side of slender protuberance at location of maximum heat flux and compared with datum interaction.

It therefore appears whereas the flow field in subcritical interactions remains practically undisturbed ahead of the protuberance, the hot spot is located to the side of the device and at a distance between $\mathrm{Re}_{x,k} = 0 - 5 \times 10^5$ ($x_k = 0$mm and 50mm in this case) with respect to the protuberance leading edge. A further representation of the horseshoe vortex that induces the hot spot to the side of this protuberance is shown in Fig. 8.8. It is the slightly different reattachment pattern induced by the leading edge geometry and the protuberance side which result in slightly higher values in this case. This is further addressed in Section 8.5, where a conservative correction to account for the effects of side sweep not taken into account in the present study is considered.

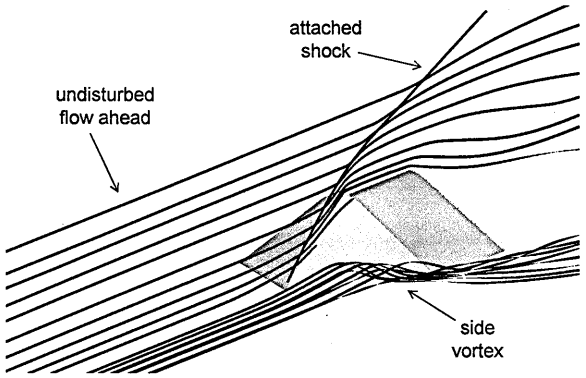

Figure 8.8 Perspective view showing formation of side vortex and quasi-2-dimensional flow at centreline: slender protuberance.

8.3 Blunt case

As shown in the previous chapters, blunt protuberances induce stronger adverse pressure gradients to the incoming boundary layer than slender protuberances and are generally more likely to cause its upstream separation from the surface. Sample blunt protuberances also found on the ARES I launch vehicle are for example the roll control system and the reaction control system module (Chapter 1). Other similar protuberances on hypersonic vehicles can also be found in a number of different shapes.

8.3.1 Protuberance model

A geometry with a deflection of α=90° and a height of h=11.9mm was chosen in this case to represent a specific blunt protuberance (Fig. 8.9). The shape of the model was representative of a ring where a hypersonic vehicle can be securely fixed before launch. The model was 27.9mm-wide and it had an extension to its back to allow fixing the protuberance at a different location on the flat plate. The h/δ_u ratio was 1.0.

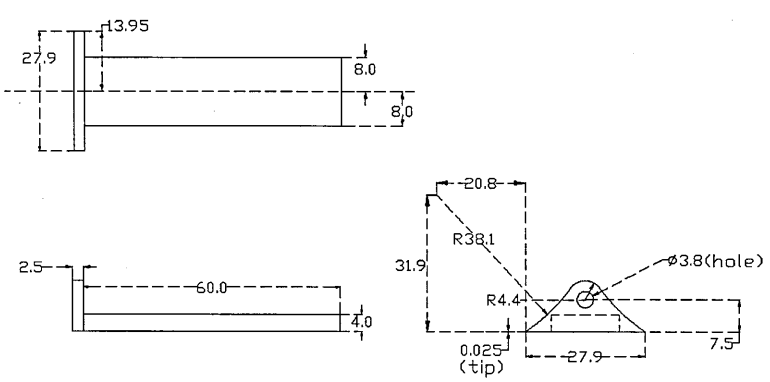

Figure 8.9 Dimensions of blunt protuberance (all dimensions in millimetres)

8.3.2 Flow field

A schlieren image of this configuration is shown in Fig. 8.10 which reveals a supercritical interaction as it was expected at this deflection angle (α=90°). An interpretation of the flow field based on the schlieren image is shown in Fig. 8.11 where a large recirculation is represented ahead of the model. The heat flux to the surface in front of the protuberance is expected to gradually increase from the location of separation and to reach its highest value just ahead of the protuberance. An oil-dot visualisation of this case is shown in Fig. 8.12 together with an interpretation of the flow streamlines. This confirms the upstream effect of the flow ahead of the model due to the large upstream recirculation. The flow around the protuberance therefore appears highly 3-dimensional.

Figure 8.10 Schlieren image of blunt protuberance

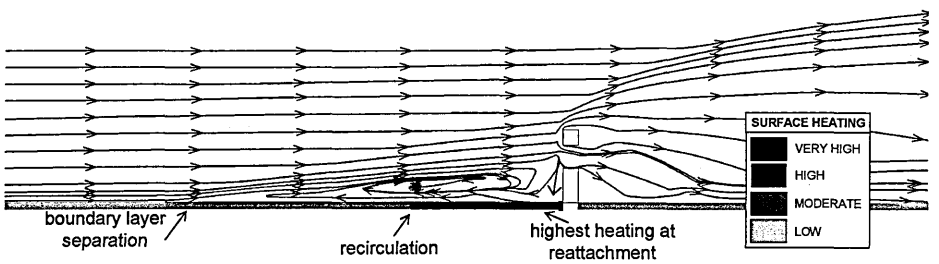

Figure 8.11 Flow field interpretation based on schlieren image

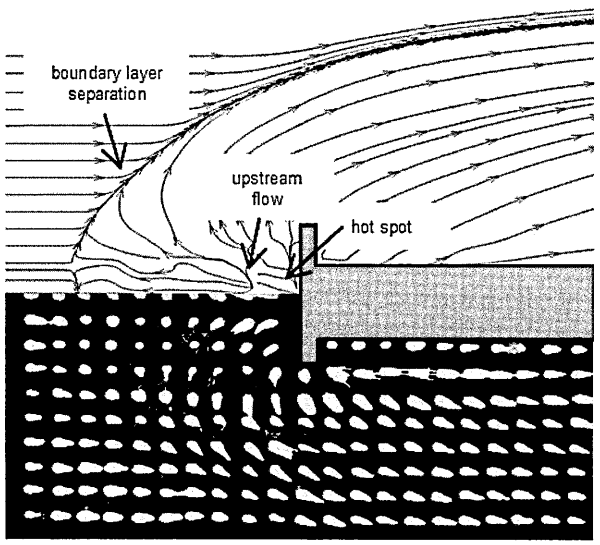

Figure 8.12 Oil flow visualisation and flow streamlines interpretation

8.3.3 Local heating

Heat flux measurements ahead of this protuberance are shown in Fig. 8.13 and the complete set of measurements around the model is presented in Fig. 8.14. The hot spot is located just ahead of the protuberance with values of $St_{\max} = 20.6\times10^{-3}$ ($q_{\max} = 118.4\text{W/cm}^2$). This is in close agreement with the estimation using the predictive approach. With the relation $St_{\max,ahead} = 5.2\times10^{-5}\,\mathrm{Re}_h^{0.6}(1-\cos\alpha)M^{-0.5}$ a heat flux rate of $St_{\max} = 19.4\times10^{-3}$ ($q_{\max} = 111.4$ W/cm^2) is estimated in this case, which is 5.9% below the actual measurement – that is taking into account that the prediction is subject to a ±25% uncertainty. By referring to the chart in Fig. 6.13, the relation $St_{\max} = 1.8\times10^{-5}\,\mathrm{Re}_h^{0.6}$ is shown to directly predict a value of $St_{\max} = 19.2\times10^{-3}$ ($q_{\max} = 110.5$ W/cm^2). This is similar to the previous prediction but is subject to a lower uncertainty of ±15%. These measurements fall within the indicated error range of the semi-empirical relation as summarised in Table 8.2. Whereas the highest heating takes place ahead of the model, the heat flux also increases on the surface to the side of the model to reach values around $St_{\max,side} = 2.7\times10^{-3}\pm20\%$ as also expected. Good agreement with the present method to predict the maximum heat transfer is thus demonstrated. It must also be noted that the induced hot spot is of the same order as the stagnation heat flux for a 5mm-radius sphere as shown in Chapter 4.

Prediction Method	Estimates		Measurements		% error (estimate measurement)
	$St_{max}(\times 10^{-3})$	$q_{max}(W/cm^2)$	$St_{max}(\times 10^{-3})$	$q_{max}(W/cm^2)$	
Fig. 6.12	19.4	111.4	20.6	118.4	5.9%
Fig. 6.13	19.2	110.5			6.7%

Table 8.2 Heat flux measurement and estimation ahead of supercritical protuberance, $y_{cl} = 0$mm.

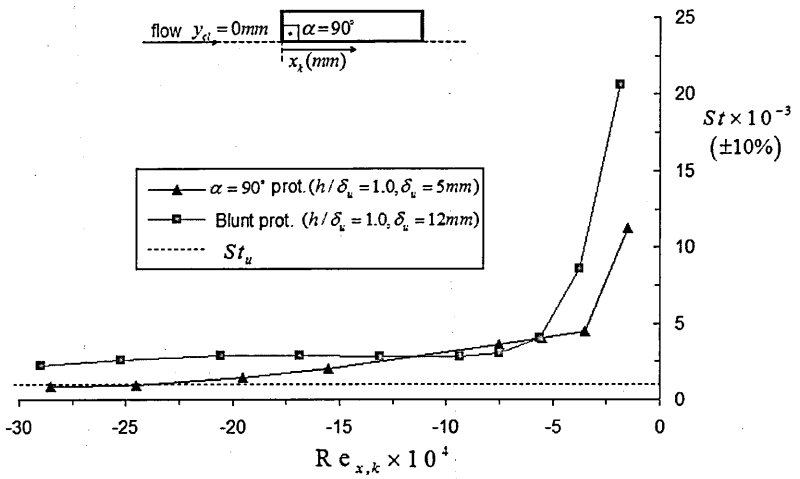

Figure 8.13 Heat flux measurements ahead of 90° generic protuberance (h/δ_u=1.0, δ_u =5mm) and ahead of specific protuberance (h/ δ_u=1.0, δ_u =12mm), y_{cl}=0mm.

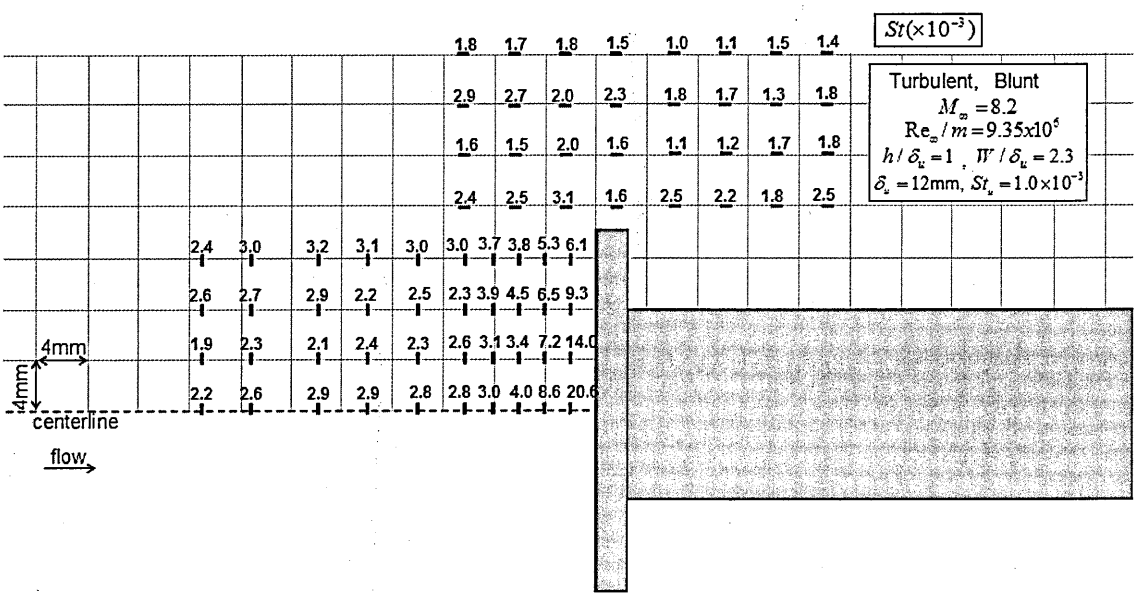

Figure 8.14 Heat flux measurements in the vicinity of blunt protuberance.

Whereas in the generic protuberances (Chapter 5) the hot spot takes place ahead of the protuberance and spanning across its whole width, the height of the present blunt protuberance is not constant in the spanwise direction (Fig. 8.15). At $y_{cl} = 4\,\text{mm}$ the height is approximately h=9mm and at $y_{cl} = 8\,\text{mm}$ this is h=5mm. The reattachment of the flow just ahead of the protuberance at these y_{cl} locations induces lower heat flux rates than at the centreline ($y_{cl} = 0\,\text{mm}$) where the height of the model is greater (h=11.9mm). At these locations, the heat flux measured is $St_{y=4mm} = 14.0\times10^{-3}$ ($q_{y=4mm} = 80.6$ W/cm^2) and $St_{y=8mm} = 9.3\times10^{-3}$ ($q_{y=8mm} = 53.5$ W/cm^2) respectively (Fig. 8.15). This falls within the error margin of ±25% considered in the relation $St_{\max,ahead} = 5.2\times10^{-5}\,\text{Re}_h^{0.6}(1-\cos\alpha)M^{-0.5}$, from which it is estimated that: $St_{y=4mm} = 16.4\times10^{-3}$ ($q_{y=4mm} = 94.2$ W/cm^2) and $St_{y=8mm} = 11.5\times10^{-3}$ ($q_{y=8mm} = 66.2$ W/cm^2). Predictions are 14.4% and 19.2% higher than the measurements at the $y_{cl} = 4\,\text{mm}$ and $y_{cl} = 8\,\text{mm}$ locations respectively. Taking into account the strong three-dimensionality of the protuberance and the difficulty in determining an effective height at these locations, the present agreement further demonstrates the validity of the predictive approach. A graphical representation of the flow field around the protuberance is shown in Fig. 8.16. The main separation region occurs upstream of the protuberance and the hot spot generally takes place just ahead of it. In addition, heating rates higher than the undisturbed heat flux also take place to the side of the protuberance, where a horseshoe vortex occurs.

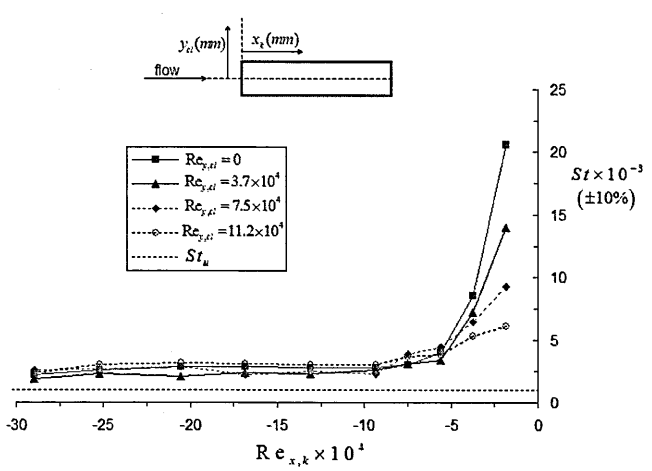

Figure 8.15 Heat flux measurements at different lateral locations (y_{cl}) ahead of blunt protuberance.

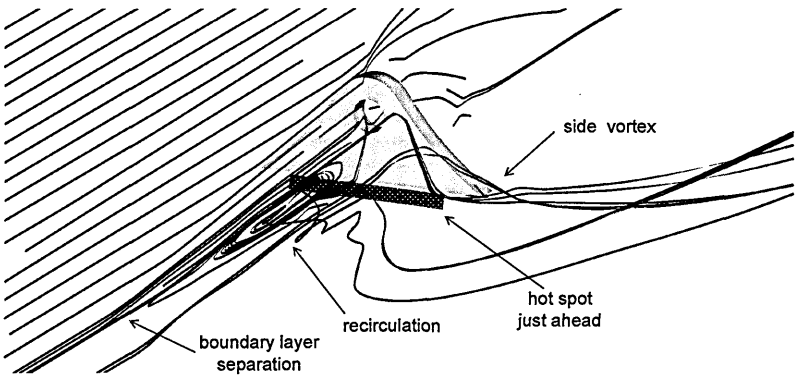

Figure 8.16 Perspective view showing highest heat flux augmentation ahead of the protuberance due to flow reattachment and side vortex: blunt protuberance.

8.4 Control fin

The most common type of protuberances in high-speed vehicles are control fins. In hypersonic vehicles, fins are usually sharp since these geometries generally provide better aerodynamic performance than blunt configurations. A sharp swept fin geometry with these characteristics is considered in this case.

8.4.1 Protuberance model

The dimensions of the fin considered in the present study are shown in Fig. 8.17. The model is significantly higher than the previous protuberances (h=63.8mm, i.e. h/δ_u=5.3). It is known that the effect of model height on the maximum heat flux is negligible with tall protuberances (Fig. 2.15). This is because the heat flux augmentation in this case is due to side effects which are independent on this parameter. The leading edge of this protuberance also has significant sweep effects as the slender case in Section 8.2.

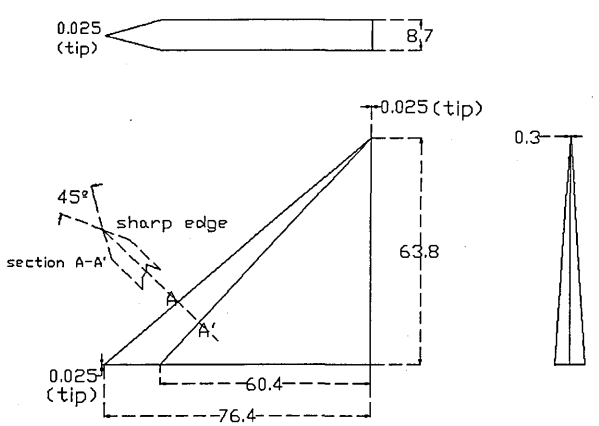

Figure 8.17 Dimensions of tall protuberance (all dimensions in millimetres)

8.4.2 Flow field

The schlieren image in Fig. 8.18 shows that the boundary layer appears undisturbed ahead of the protuberance. The subcritical nature of the interaction is thus confirmed. The three-dimensionality of the flow around the protuberance is further demonstrated by the oil-dot visualisations (Fig. 8.19). Ahead of the fin, oil dots are almost unaffected and the highest skin friction takes place to the surface to the side of the model. The local interaction is therefore expected to be similar to this characteristic of subcritical protuberances given that the increase in side heat flux is caused by corner effects independently of the height of the protuberance in this case.

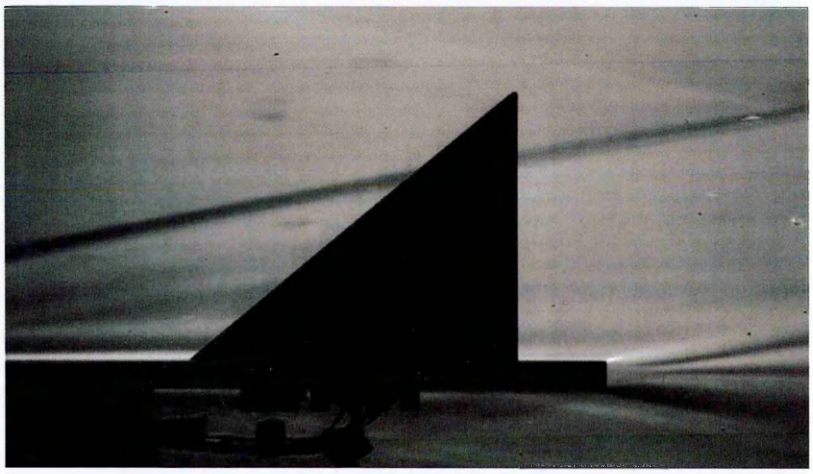

Figure 8.18 Schlieren image of tall protuberance

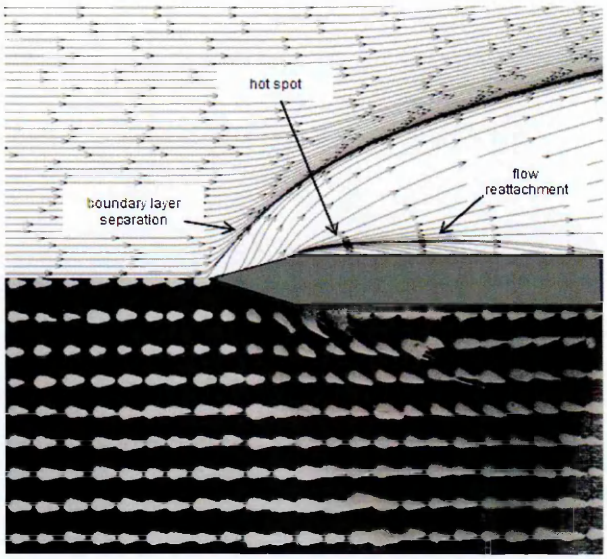

Figure 8.19 Oil flow visualisation and flow streamlines interpretation

8.4.3 Local heating

Heat flux measurements in the vicinity of the fin protuberance are presented in Fig. 8.20. The highest heat flux is found to the side of the device $St_{max} = 3.7 \times 10^{-3}$ ($q_{max} = 21 \text{W/cm}^2$). This is higher than the expected value of $St_{max} = 2.7 \times 10^{-3}$ based on the developed predictive approach (Fig. 6.12). This is attributed to the different corner effects that take place in this case although the order of magnitude is the same. The heat flux ahead St_{ahead} is of the order of the undisturbed heat flux St_u or lower as expected for subcritical interactions.

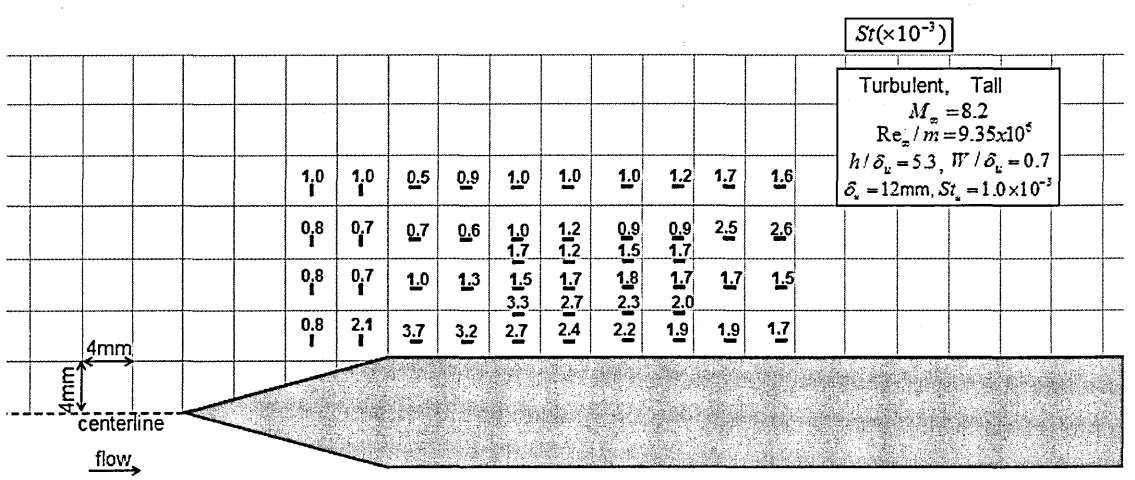

Figure 8.20 Heat flux measurements in the vicinity of tall protuberance.

The heat flux at different axial locations to the side of the protuberance is shown in Fig. 8.21. The increased heat flux in this region to the side of the fin does not take place close to the protuberance but at the second row of measurement points. This demonstrates that the specific geometry of this model results in significantly different side effects than those present in the generic protuberances. These measurements show that the method developed can also be applied to predict the maximum heat flux to the side of subcritical tall protuberances such as sharp fins, given that the side heat flux in this case is caused by the same effects. A further representation of the side vortices is shown in Fig. 8.22.

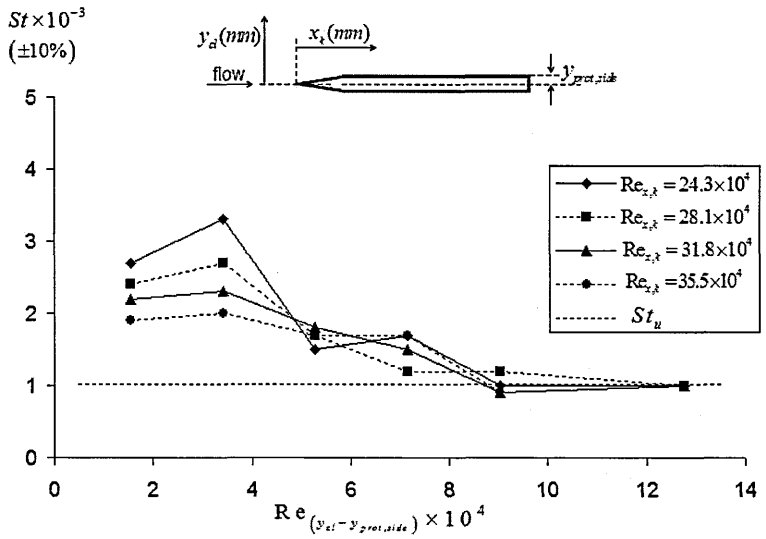

Figure 8.21 Heat flux at different axial location to the side of tall protuberance

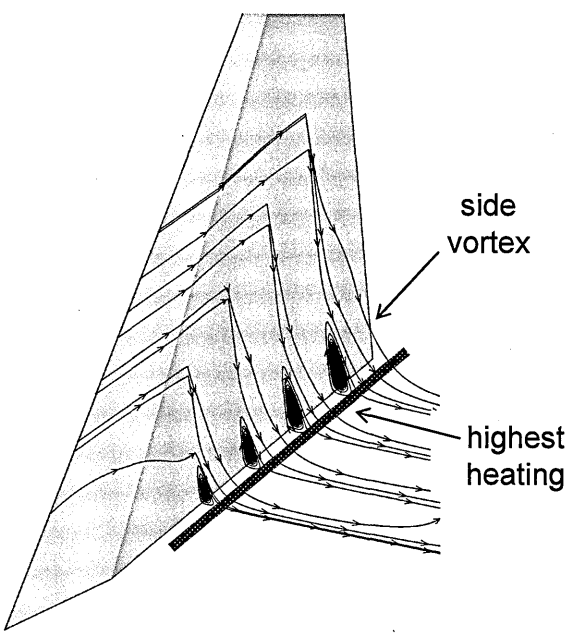

Figure 8.22 Perspective view showing hot spot at location of reattachment of the side vortex

8.5 Review of predictive approach

The predictive approach developed from the main investigation in Chapter 6 has been applied to the previous examples. The predicted results, when compared with the different specific protuberances, show good agreement. The dependence of the heat flux augmentation on whether the interaction induced by the protuberance is subcritical or supercritical has also been demonstrated. In subcritical interactions the hot spot is located to the side of the protuberance due to the junction vortex that induces an increase in heat flux. In supercritical interactions this is generally in front of the protuberance due to the reattachment of the main separation bubble at this region.

Based on the comparison of the maximum heat flux rates predicted with this method and the corresponding measurements, the main weakness of this predictive approach is found to be that the effect of sweep in the lateral and longitudinal directions is not taken into account. However, this only affects the estimation for the heat flux to the side of the protuberance which does not reach such high values as those ahead of supercritical protuberances. Furthermore, with the significantly different effects in the present protuberances the highest heat flux to the side has been found to be within 50% of $St_{\max} = 2.7\times10^{-3}$ as found with the generic protuberances (Chapter 6). Based on the present study, it is suggested that in practical applications a maximum side heat flux to the side of subcritical interactions can be considered in a conservative approach as:

$$St_{\max} = 4\times10^{-3} \qquad \text{[Eq. 8.1]}$$

The prediction of the hot spot ahead of supercritical interactions is in good agreement with the measurements on the specific blunt protuberance. However, it is confirmed that the heat flux just ahead of the protuberance is strongly dependent on its height as identified by the predictive approach. In this case, results are within 25% of $St_{\max,ahead} = 5.2\times10^{-5}\,\mathrm{Re}_h^{0.6}(1-\cos\alpha)M_\infty^{-0.5}$ and no correction is required.

CHAPTER 9

Conclusions

An extensive experimental investigation on the interference interaction induced by surface protuberances on hypersonic vehicles has been conducted. The investigation has been performed in a gun tunnel at freestream Mach numbers of 8.2 and 12.3 and Reynolds numbers ranging from $Re_\infty/m=3.35x10^6$ to $Re_\infty/m=9.35x10^6$. Generic short protuberance models in the form of 3-dimensional compression corners with finite span have been considered. The height of the models has been of a similar order of magnitude to that of the incoming boundary layer thickness as generally expected in real flight vehicles. The different protuberance models have been attached to a flat plate which replicates the surface of the vehicle.

The very high temperatures induced at the regions of the protuberances constitute one of the principal concerns regarding the safety of hypersonic vehicles. The investigation has focused on measuring the heat flux on the area surrounding the protuberance rather than on the protuberance itself given that it is the heating in this region which generally needs to be predicted in practical engineering applications. Prior to the investigation of these complex interactions, the accuracy of the experimental system and the reliability of the main predictive approaches developed to date have been assessed based on a study of heat transfer in attached flows. The heat flux at different locations around the protuberances and at a range of different freestream conditions has subsequently been measured by means of thin-film heat transfer gauges with a measuring element size of 1.2mm x 0.3mm. High-speed schlieren visualisations have been used to determine unsteady features in the flow and to further explain the flow mechanisms around the protuberances. Oil flow visualisations have also been obtained to determine the trajectory of the skin friction lines on the surface. The key findings from the investigation are summarised in the following sections.

9.1 Key findings

Surface protuberances can be found on a number of different shapes on hypersonic vehicles. The viscous interaction that results from the interference of the protuberance with the incoming undisturbed flow varies depending on protuberance geometry as well as on freestream flow conditions. The following effects have been investigated: effect of protuberance height and width, effect of protuberance deflection angle, incoming boundary layer state effect, freestream Reynolds number effect and freestream Mach number effect. Particular emphasis has been placed on the induced heat flux augmentation due to the importance of aerodynamic heating at hypersonic speeds. An outline of the key findings is presented in this section as summarised in the schematic diagram in Fig. 9.1.

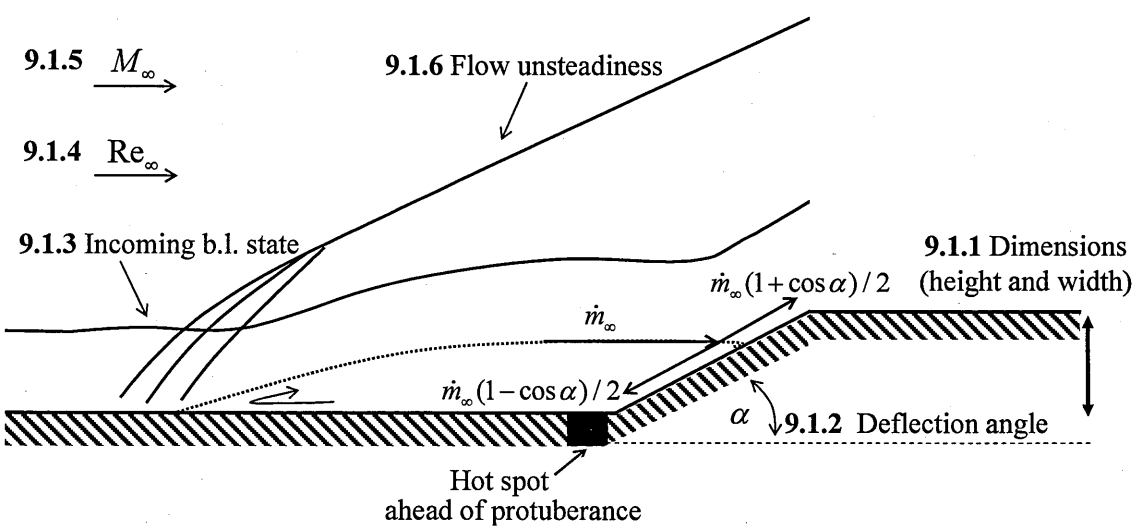

Figure 9.1 Summary of effects investigated.

9.1.1 Protuberance height and width

Results have shown that the highest heat transfer rates induced by subcritical protuberances are not affected by the height and the width of the protuberance; the local heat flux augmentation to the side is due to the appearance of a junction vortex. Protuberances shorter than the boundary layer thickness have nevertheless not been considered in the present study. It is possible that the height of subcritical protuberances has an effect on the hot spot magnitude in such cases; however, it is unlikely that the heat flux augmentation is higher than with taller protuberances and thus they are not considered important in the present study. In supercritical protuberances the peak heat flux increases with protuberance height but independently of width. In these cases the highest heat transfer rates are found ahead of the protuberance and span the whole width. It is important to distinguish between subcritical and supercritical protuberances.

9.1.2 Protuberance deflection angle

Furthermore, the peak heat flux in subcritical interactions is not affected by the protuberance deflection angle also due to the independence of corner effects from this parameter. In supercritical interactions, however, the hot spot magnitude increases significantly with deflection angle. As the protuberance deflection is increased, the deflection that the incoming flow experiences before reattaching to the wall is lower and so it results in higher mass flow rates on impact to the vehicle surface and thus in higher heat transfer rates at this location (Fig. 9.1). Higher hot spots can therefore be induced by large deflection protuberances. The hot spot can be significantly high in forward deflection cases in which the flow is deflected through a smaller angle before reaching the vehicle surface. The length of the separated flow region ahead of the protuberance is at the same time increased with higher deflection angles.

9.1.3 Incoming boundary layer state

The state of the incoming boundary layer (laminar, transitional or turbulent) has a strong effect on the incipient separation angle because laminar boundary layers are more prone to separate than turbulent boundary layers. Consequently, in cases where the boundary layer is less resistant to adverse pressure gradients the region of separated flow is larger and therefore the heat flux is influenced over a larger area. The heating over this region is higher for turbulent boundary layers than for laminar boundary layers. Nevertheless, in the present configurations there does not seem to be a large dependence of maximum heating on the incoming boundary layer state. This is most likely because the incoming laminar boundary layer becomes transitional or even fully turbulent through the interaction as suggested by the present measurements. This is believed to be directly linked to the 3-dimensionality of the interactions and is supported by the analysis of results at all the test conditions.

9.1.4 Freestream Reynolds number

The resistance of the incoming boundary layer to separate from the wall is also a function of local Reynolds number. In subcritical interactions with weak boundary layers the hot spot to the side is found farther from the protuberance leading edge than in interactions with more energetic boundary layers. In supercritical interactions, the magnitude of the hot spot increases with Reynolds number and the extent of the separation length decreases with it. Both trends are in contrast to those observed in attached fully laminar or fully turbulent flow in which the opposite behaviour occurs but they follow the same trend observed in transitional flow. This behaviour is attributed to the re-energising process that the flow suffers along the interaction, which results in higher peak heating as the inertia forces are increased with respect to the viscous forces, i.e. as Reynolds number is increased. In subcritical interactions the hot spot magnitude is independent of Reynolds number.

9.1.5 Freestream Mach number

In supercritical interactions, the non-dimensional peak heat flux is inversely proportional to the Mach number. This trend is similar to that observed in attached boundary layer cases and is due to the greater kinetic energy dissipated by viscous friction in the boundary layer at higher Mach numbers. The boundary layer also becomes more resistant to separation at higher freestream Mach numbers and therefore the interaction region is expected to be reduced. In general, the local heat flux augmentation is lower at higher Mach numbers. In subcritical interactions, however, the magnitude of the hot spot to the side of the protuberances was found to be practically independent of the freestream Mach number. These conclusions are based on turbulent experimental data and on the assumption that the hot spot magnitude at the higher Mach number is not strongly affected by the incoming boundary layer state since laminar incoming boundary layers are expected to become transitional or even fully turbulent through the interaction.

9.1.6 Flow unsteadiness

An important aspect of these interactions is the fact that they are unsteady in some cases. The high-speed schlieren visualisations have shown that the flow is essentially steady in subcritical interactions. In contrast, supercritical interactions are inherently unsteady. A region of large-scale broadband unsteadiness takes place at the location where the boundary layer separates ahead of the protuberance and high-frequency low-scale unsteadiness is expected over the region of separated flow. The hot region in supercritical interactions is therefore expected not to be subject to significant unsteady loads, which could otherwise become an additional hazard to the vehicle's structural integrity.

9.2 Hot spot prediction

It is therefore clear that the impact of the local interaction on the heating of the vehicle surface is dominated by whether the boundary layer separates ahead of the protuberance or not. The hot spot is found to the side of the protuberance in subcritical interactions, in which the boundary layer remains attached until the location of the protuberance. Whereas increased heating is also found to the side of supercritical protuberances, which induce the upstream separation of the boundary layer, the hot spot generally takes place ahead of the protuberance and can become significantly high. In this case, the value of the peak heat flux increases with freestream Reynolds number, protuberance height and deflection angle but decreases with Mach number.

Based on the present experimental dataset, a semi-empirical approach has been developed to estimate the location and magnitude of the hot spot in the vicinity of surface protuberances in hypersonic vehicles. The main limitations of this approach are related to the maximum spatial resolution of the measurements of 2mm in the longitudinal (x) and lateral (y) directions in the cases required, i.e. normal to the front and sides of the protuberance where sharper heat flux gradients take place as qualitatively shown by the CFD simulations in Appendix D. The agreement within the whole correlation study provides proof of the reliability of the measurements. Rapid estimates of the peak heat flux to the surface surrounding the protuberance can therefore be obtained within engineering accuracy. The validity of the method has been assessed based on its applicability to three specific protuberances that represent a short subcritical, a short supercritical and a tall protuberance. The effects of side sweep or skewness are not considered but a conservative correction factor is recommended to account for these effects. This approach can be used as a prediction tool in the design of hypersonic vehicles and establishes relevant design guidelines which are not currently available. This is for instance demonstrated by the clearly unfavourable modifications made to the roll control system module protuberance on the ARES I vehicle (refer back to Chapter 1, Fig. 1.4), which was made smoother by increasing slightly its deflection and its side angle with the surface. According to the present work, this results in slightly higher heat transfer rates to the side of the protuberance but significantly higher heating to the surface ahead of it.

9.3 Recommendations for future work

The viscous interaction induced by a surface protuberance on a hypersonic vehicle is a complex flow phenomenon with many future challenges. The present experimental work has provided a further understanding of these interactions and a semi-empirical approach for local hot spot prediction which facilitates engineering applications. However, there are a number of more fundamental matters which need to be understood in more detail before a full understanding of these interactions can be reached:

i. The local heat flux augmentation in the vicinity of surface protuberances has been shown to be particularly sensitive to whether the interaction is subcritical or supercritical. It is necessary to develop the current predictive capability of incipient separation conditions in hypersonic flows. While a number of ground test studies have already investigated the incipient separation of the boundary layer, there is a need for further flight test data and numerical simulations.

ii. While the prediction of the heat flux in laminar attached boundary layers is relatively well established, turbulent flows are particularly subject to large discrepancies. Wind tunnel data seem to vary significantly between different test facilities and semi-empirical methods are also sensitive to such variations. Numerical simulations are particularly restricted by the turbulence models and therefore further developments in this area are required.

iii. The present experimental investigation has been performed in a hypersonic gun tunnel. The strong real gas effects typically encountered at high Mach numbers have therefore not been taken into account. Although this allows for a conservative prediction since radiation effects are usually encountered from the vehicle to the flow, similar studies could be performed in high-enthalpy facilities or in real flight conditions in order to obtain a further understanding of such effects. However, simpler configurations should be understood first (e.g. compression corners, incident shock-wave/boundary-layer interactions).

iv. An important aspect of these interactions is the unsteadiness of the flow in separation regions. Although the implications to the surface heat transfer appear not to be so significant in that case, it is considered important to obtain a fuller understanding of these effects. As in the previous point, further understanding of the unsteadiness in simpler interactions should be first obtained.

v. Another aspect that may require future investigation is the corner flow effects that occur to the side of the protuberance. A junction vortex is known to occur at such regions but a further understanding of these aerodynamic phenomena needs to be obtained. It is therefore encouraged that further research on this type of flows is performed due to their many possible implications, e.g. in scramjets.

To conclude, the understanding of the 3-dimensional viscous interactions induced by surface protuberances on hypersonic vehicles relies on further experimental and numerical work. From the experimental side, it is expected that more detailed information from such flows will be able to be obtained as more advanced measurement diagnostics are developed. In particular optical diagnostics look promising, but these rely at the same time on technological developments regarding the instrumentation required. In general, preliminary investigations should always be performed in cold wind tunnels in which real gas effects are not reproduced. Subsequently, investigation should be performed in high-enthalpy wind tunnels. As for the numerical capability, a promising area which is expected to provide more accurate predictions of turbulent flows is Large Eddy Simulation (LES). Further developments in these areas are expected to be observed in the next coming years together with the very important data that can come from forecoming real flight tests.

References

Adrian, R. J. (1991). "Particle-imaging techniques for experimental fluid mechanics." *Annu. Rev. Fluid Mech.*, 23, 261-304.

Adrian, R. J. (2005). "Twenty years of particle image velocimetry." *Exp. Fluids*, 39(2), 159-169.

Ainsworth, R. W., Thorpe, S. J. and Manners, R. J. (1997). "A new approach to flow-field measurement: A view of Doppler global velocimetry techniques." *Int. J. of Heat and Fluid Flow*, 18(1), 116-130.

Anderson Jr., J. D. (2006). *Hypersonic and high temperature gas dynamics*, 2nd Ed., AIAA, Reston, Va., U.S.A.

Anderson Jr., J. D. (2008). *Hypersonic flight.* McGraw-Hill's Access science. Encyclopedia of Science & Technology online, available at: www.accessscience.com (last accessed 30th October 2009).

Arrington, J. P. (1968). "Heat transfer and pressure distributions due to sinusoidal distortions on a flat plate at Mach 20 in helium." NASA TN D-4907.

Atcliffe, P. A. (1995). "Effects of boundary layer separation and transition at hypersonic speeds." Ph.D. thesis, Cranfield Univ., Cranfield, U.K.

Babinsky, H. (1994). "A study of roughness in turbulent hypersonic boundary-layers." Ph.D. thesis, Cranfield Univ., Cranfield, U.K.

Babinsky, H. and Edwards, J. A. (1996). "On the incipient separation of a turbulent hypersonic boundary layer." *Aero. J.*, 100(996), 209-214.

Baldwin, B. and Lomax, H., (1978). "Thin-layer approximation and algebraic model for separated turbulent flow." AIAA paper 78-257.

Becker, J. V. (1968). "The X-15 program in retrospect." Presented in 1st Annual meeting, DLR, Germany, available at: http://www.hq.nasa.gov/pao/History/x15lect/cover.html (last accessed 30th October 2009).

Berry, S. A. and Horvath, T. J. (2007). "Discrete roughness transition for hypersonic flight vehicles." AIAA paper 2007-0307.

Bertin, J. (1994). *Hypersonic aerothermodynamics*, AIAA, Reston, Va., U.S.A.

Bertin, J. J. and Cummings, R. M. (2006). "Critical hypersonic aerothermodynamic phenomena." *Annu. Rev. Fluid Mech.*, 38, 129-157.

Bertram, M. H. and Wiggs, M. M. (1963). "Effect of surface distortions on the heat transfer on a wing at hypersonic speeds." *AIAA J.*, 1(6), 1313-1319.

Bertram, M. H., Weinstein, L. M., Cary, A. M., Jr., and Arrington, J. P. (1967). "Effect of two-dimensional multiple-wave distortions on the heat transfer to a wall in hypersonic flow." AIAA paper 67-164.

Birch, T. J., Prince, S. A., Ludlow, D. K. and Qin, N. (2001). "The application of a parabolized Navier-Stokes solver to some hypersonic flow problems." AIAA paper 2001-1753.

Boutry, A. and Vital-Durand, M. (2003). *Introduction in hypersonic. aerothermodynamics*. EPFL, Lausanne, Switzerland.

Bramlette, T. T., Smith, R. R. and Sliski, N. J. (1975). "Fin induced laminar interactions on sharp and spherically blunted cones." *J. Spacecraft and Rockets*, 10(11), 696-703.

Brenner, G., Gerhold, T., Hannemann, K. and Rues, D. (1993). "Numerical simulation of shock/shock and shock-wave/boundary-layer interactions in hypersonic flows." *Comp. and Fluids*, 22(4/5), 427-439.

Bretthauer, B., Meier, G. E. A. and Stasicki, B. (1991). "An electronic Cranz-Schardin camera." *Rev. Sci. Instrum.*, 62(2), 364-368.

Burbank, P. B. and Strass, H. K. (1958). "Heat transfer to surfaces and protuberances in a supersonic turbulent boundary layer." NACA RM L58E01a.

Burbank, P. B., Newlander, R. A. and Collins, I. K. (1962). "Heat-transfer and pressure measurements on a flat-plate surface and heat-transfer measurements on attached protuberances in a supersonic turbulent boundary layer at Mach numbers of 2.49, 3.51, and 4.44." NASA TN D-1372.

Bushnell, D. B. and Huffman, J. K. (1967). "Investigation of heat transfer to leading edge of a 76° swept fin with and without chordwise slots and correlations of swept-leading-edge transition data for Mach 2 to 8." NASA TM-X-1475.

Buttsworth, D. R. and Ahfock, T. L. (2003). "A pulsed LED system for Schlieren flow visualization." Technical Report, Univ. Southern Queensland, Toowoomba, Australia.

Canny, J. (1986). "A computational approach to edge detection." *IEEE Trans. Pattern Anal. Mach. Intell.*, 8(6), 679-698.

Cary, A. M. and Morrisette, E. L. (1968). "Effect of two-dimensional multiple sine-wave protrusions on the pressure and heat-transfer distributions for a flat plate at Mach 6." NASA TN D-4907.

Chapman, D. R. and Rubesin, M. W. (1949). "Temperature and velocity profiles in the compressible laminar boundary layer with arbitrary distribution of surface temperature." *J. Aero. Sci.*, 16(9), 547-565.

Chapman, D. R., Kuehn, D. M., and Larson, K. H. (1958). "Investigation of separated flows in supersonic and subsonic streams with emphasis on the effects of transition." NACA 1356.

Chi, S. W. and Spalding, D. B. (1966). "Influence of temperature ratio on heat transfer to a flat plate through a turbulent boundary layer in air." In Proc. of 3rd Int. Heat Transf. Conf., Vol. II, AICE, 41-49.

Childs, P. R. N., Greenwood, J. R. and Long, C. A. (1999). "Heat flux measurement techniques." *In Proc. Instit. Mech. Eng., Part C, J. Mech. Eng. Sci.*, 213(7), 655-677.

Childs, P. R. N. (2001). *Practical temperature measurement*. Butterworth-Heinemann, Oxford, U.K.

Chung, P. M. and Viegas, J. R. (1961). "Heat transfer at the reattachment zone of separated laminar boundary layers." NASA TN D-1072.

Coleman, G. T. (1972). "Tabulated heat transfer rate data for a hypersonic turbulent boundary layer over a flat plate." IC Aero Report 72-06.

Coleman, G. T. (1973a). "A study of hypersonic boundary layers over a family of axisymmetric bodies at zero incidence: preliminary report and data tabulation." IC Aero. Report 73-06.

Coleman, G. T. (1973b). "Hypersonic turbulent boundary layer studies." Ph.D. thesis, Imperial College of Science and Technology, London, U.K.

Coleman, H. W. and Lemmon, E. C. (1973). "The prediction of turbulent heat transfer and pressure on a swept leading edge near its intersection with a vehicle." AIAA paper 73-677.

Coleman, G. T. and Stollery, J. L. (1973). "A study of hypersonic boundary layers over a family of axisymmetric bodies at zero incidence: preliminary report and data

tabulation." Imperial College of Science and Technology, England, I.C. Aero. Report 73-06.

Cox, R. N. and Winter, D. F. T. (1957). "The light gas hypersonic gun tunnel at A.R.D.E." AGARD Report 139, Fort Halstead, U.K.

Crabtree, L. F., Dommett, R. L. and Woodley, J. G. (1965). "Estimation of heat transfer to flat plates, cones and blunt bodies." Royal Aircraft Establishment TR No. 65137.

Crocco, L. (1932). "Transmission of heat from a flat plate to a fluid flowing at a high velocity." NACA TM-609.

Daum, F. L. (1963). "Air condensation in a hypersonic wind tunnel." *AIAA J.*, 1(5), 1043-1046.

Davis, S. R. (2008). "Ares I-X flight test – the future begins here." AIAA paper 2008-7806.

Debes, B. (2002). "Intake study of a hypersonic research vehicle." M.Sc. thesis, Cranfield Univ., Cranfield, U.K.

DeJarnette, F. R., Hamilton, H. H., Weilmuenster, K. J. and Cheatwood, F. M. (1987). "A review of some approximate methods used in aerodynamic heating analyses." *J. Thermophys. and Heat Transf.*, 1(1), 5-12.

Delery, J. M. (2001). "Toward the elucidation of three-dimensional separation." *Annu. Rev. Fluid Mech.*, 33, 129-154.

Ding, L. and Goshtasby, A. (2001). "On the Canny edge detector." *Patt. Recog.*, 34(3), 721-725.

Dolling, D. S. (2001) "Unsteadiness of Shock-Induced Turbulent Separated Flows – Some Key Questions." AIAA Paper 2001-2708.

Dorodnitsyn, A. A. (1942). "Laminar boundary layer in compressible fluid." Doklady Akademii Nauk, SSSR 34, 213-219.

Dupont, P., Haddad, C., Ardissone, J. P. and Debieve, J. F. (2005). "Space and time organization of a shock wave/turbulent boundary layer interaction." *Aerospace Sci. Technol.*, 9(7), 561-572.

Dussauge, J. -P., Dupont, P. and Debieve, J. -F. (2006). "Unsteadiness in shock wave boundary layer interactions with separation." *Aerospace Sci. Technol.,* 10(2), 85-91.

Eckert, E. R. G. (1954). "Survey on heat transfer at high speeds." WADC TR 54-70, April.

Eckert, E. R. G. (1955). "Engineering relations for friction and heat transfer to surfaces in high velocity flow." *J. Aero. Sci.*, 22(8), 586-587.

Eckert, E. R. G. (1956). "Engineering relations for heat transfer and friction in high-velocity laminar and turbulent boundary layer flows over surfaces with constant pressure and temperature." *Trans. ASME*, 78(6), 1273-1283.

Eggers, A. J., Hansen, C. F. and Cunningham, B. E. (1955). "Theoretical and experimental investigation of the effect of yaw on heat transfer to circular cylinders in hypersonic flow." NACA RM A55E02.

Elfstrom, G. M. (1971). "Turbulent separation in hypersonic flow." I.C. Aero Report 71-16.

Estevadeordal, J., Gogineni, S., Kimmel, R. L. and Hayes, J. R. (2007). "Investigation of low-density hypersonic and plasma flows by Schlieren system using various light sources." *Exp. Thermal and Fluid Sci.*, 32(1), 98-106.

Estruch, D. and Elsari, M. (2007) "Aerodynamic pre-spinning of the wheels of aircrafts to reduce tyre wear at touchdown." *World J. Eng.*, 4(3), 58-65.

Estruch, D., Lawson, N. J., MacManus, D. G., Garry, K. P. and Stollery, J. L. (2008) "Measurement of shock wave unsteadiness using a high-speed Schlieren system and digital image processing." *Rev. Sci. Instrum.*, 79(12), 126108, 1-3.

Estruch, D., Lawson, N. J. and Garry, K. P. (2009a). "The application of optical measurement techniques to supersonic and hypersonic aerospace flows." *ASCE J. Aerospace Eng.*, 22(4), 383-395.

Estruch, D., Lawson, N. J., MacManus, D. G., Garry, K. P. and Stollery, J. L. (2009b). "Schlieren visualization of high-speed flows using a continuous LED light source." *J. Vis.*, 12(4), 289-290.

Estruch, D., Jimenez-Ortiz, A., Lawson, N. J., MacManus, D. G. and Garry, K. P. (2009c). "Particle image velocimetry study of a shock-wave/turbulent boundary-layer interaction with separation at Mach 2.4." *J. Shock Waves*. Submitted for publication.

Estruch, D., MacManus, D. G., Richardson, D. P., Lawson, N. J., Garry, K. P., and Stollery, J. L. (2009d). "Experimental study of unsteadiness in supersonic shock-wave/turbulent boundary-layer interactions with separation." *Aero. J.* Submitted for publication.

Estruch, D., Stollery, J. L., MacManus, D. G., Lawson, N. J. and Garry, K. P. (2009e). "Hypersonic interference heating: a semi-empirical hot spot predictive approach." *In Proc. AIAA/DLR/DGLR 16th Int. Space Planes and Hypersonic Systems and Technologies Conference,* Bremen, Germany, 19-22 Oct 2009. AIAA paper 2009-7444.

Estruch, D., MacManus, D. G., Stollery, J. L., Lawson, N. J. and Garry, K. P. (2009f). "Hypersonic interference heating in the vicinity of surface protuberances: a semi-empirical predictive approach." *Exp. Fluids*. Submitted for publication.

Fancett, R. K. (1968). "Boundary layer reattachment in hypersonic flow." Ph.D. thesis, Imperial College, London, U.K.

Fay, J. A. and Riddell, F. R. (1958). "Theory of stagnation point heat transfer in dissociated air." *J. Aero. Sci.*, 25(2), 73-85.

Fiala, A., Hillier, R., Mallinson, S. G. and Wijesinghe, H. S. (2006). "Heat transfer measurement of turbulent spots in a hypersonic blunt-body boundary layer." *J. Fluid Mech.*, 555, 81-111.

Fong, M. C. (1966). "Aerodynamic heating in the vicinity of surface protuberances." NASA AD-633762.

Fox, J. S., O'Byrne, S. O., Houwing, A. F. P., Papinniemi, A., Danehy, P. M. and Mudford, N. R. (2001). "Fluorescence visualization of hypersonic flow establishment over a blunt fin." *AIAA J.*, 39(7), 1329-1337.

Gadd, G. E., Cope, W. F. and Attridge, J. L. (1960). "Heat-transfer and skin-friction measurements at a Mach number of 2.44 for a turbulent boundary layer on a flat surface and in regions of separated flow." ARC TR R&M 3148.

Gaitonde, D. and Shang J. S. (1993). "Accuracy of flux-split algorithms in high speed viscous flow." *AIAA J.*, 31(7), 1215-1221.

Giles, H. L. and Thomas, J. W. (1966). "Analysis of hypersonic pressure and heat transfer tests on a flat plate with a flap and a delta wing with body, elevons, fins, and rudders." NASA CR-536.

Gnoffo, P. A., Weilmuenster, K. J., Hamilton, H. H., Olynick, D. R. and Venkathapathy, E. (1999). "Computational aerothermodynamic design issues for hypersonic vehicles." *J. Spacecrafts and Rockets*, 36, 21-43.

Gochberg, L. A. (1997). "Electron beam fluorescence methods in hypersonic aerothermodynamics." *Proc. Aerospace Sci.*, 33(7), 431-480.

Gonzalez, R. C., Woods, R. E. and Eddins, S. L. (2004). *Digital image processing using Matlab*. Prentice Hall, Upper Saddle River, N.J., U.S.A.

Grant, I. (1997). "Particle image velocimetry: a review." *In Proc. Instit. Mech. Eng., Part C, J. Mech. Eng. Sci.*, 211(1), 55-76.

Grotowsky, I. M. G. and Ballmann, J. (2000). "Numerical investigation of hypersonic step-flows." *J. Shock Waves*, 10(1), 57-72.

Guillerlain, J. D. (1975). "Experimental investigation of a fin-cone interference flowfield at Mach 5." NSWC/WOL/TR 75-63.

Guiming, T. (1994). "Surface oil flow technique and liquid crystal thermography for flow visualisation in impulse wind tunnels." *Acta Mech. Sinica*, 10(3), 220-226.

Haas, A. (2009). "Hypersonic heat transfer." M.Sc. thesis, Cranfield Univ., Cranfield, U.K.

Hakkinen R. J., Greber I., and Trilling, L. (1959). "The interaction on an oblique shock wave with a laminar boundary layer." NASA Mem 2-18-59W.

Haley, R. and Smy, P. R. (1988). "An inexpensive light source for high speed Schlieren photography." *J. Phys. E.: Sci. Instrum.*, 21, 1172-1174.

Hamel, N., deChamplain, A., Rainville, P. A., Kretschmer, D., Gaudreau, P., Bouziane, S., Farinaccio, R., and Stowe, R. A. (2001). "Supersonic PIV measurements in an open jet flow." AIAA paper 2001-3527.

Haney, J. W. (1983). "Orbiter entry heating lessons learned from development flight test program. Shuttle performance: lessons learned." NASA CP-2283, part 23.

Hayes, W. D. and Probstein, R. F. (1959). *Hypersonic flow theory.* Academic Press, New York-London.

Hayes, J. R. and Neumann, R. D. (1992). *Introduction to the aerodynamic heating analysis of supersonic missiles.* AIAA Publ., Washington D.C., U.S.A.

Hiller, W., Lent, H. -M., Meier, G. E. A. and Stasicki, B. (1987). "A pulsed light generator for high speed photography." *Exp. Fluids*, 5(2), 141-144.

Hirsch, C. (2007). *Numerical computation of internal and external flows volume 1: The fundamentals of computational fluid dynamics.* Butterworth-Heinemann, Amsterdam-London.

Hirschel, E. H. (2005). *Basics of aerothermodynamics.* Springer-Verlag in ass. with AIAA, Berlin, Germany.

Holden, M. S. (1964). *Heat transfer in separated flow.* Ph.D thesis, Imperial College, London, U.K.

Holden, M. S. (1971). "Boundary-layer displacement and leading-edge bluntness effects on attached and separated laminar boundary layers in a compression corner. Part II: Experimental study." *AIAA J.*, 9(1), 84-93.

Holden, M. S. and Moselle, J. R. (1992). "A database of aerothermal measurements in hypersonic flow for CFD validation." AIAA paper 92-4023.

Houwing, A. F. P., Smith, D. R., Fox, J. S., Danehy, P. M. and Mudford, N. R. (2001). "Laminar boundary layer separation at a fin-body junction in a hypersonic flow." *J. Shock Waves*, 11(1), 31-42.

Howarth, L. (1948). "Concerning the effect of compressibility on laminar boundary layers and their separation." Proc. Royal Soc. (London), Ser. A, 194(1036), 16-42.

Huebner, L. D., Marshall Smith, R., Campbell, J. R. and Taylor, T. L. (2009). "ARES I-X flight test vehicle similitude to the Ares I crew launch vehicle." *Acta Astron.* Submitted for publication.

Hung, F. T. and Clauss, J. M. (1980). "Three-dimensional protuberance interference heating in high-speed flow." AIAA paper 80-0289.

Hung, C. M. and MacCormack, R. W. (1976). "Numerical solutions of supersonic and hypersonic laminar compression corner flows." *AIAA J.*, 14(4), 475-481.

Hung, F. and Patel, D. (1984). "Protuberance interference heating in high-speed flow." In Proc. of 19th Thermophysics Conference. AIAA paper 84-1724.

Jaeck, C. L. (1966). "Analysis of pressure and heat-transfer tests on surface roughness elements with laminar and turbulent boundary layers." NASA CR-537.

Jones, R. A. (1964). "Heat-transfer and pressure investigation of a fin-plate interference model at a Mach number of 6." NASA TN D-2028.

Kemp, N. H., Rose, P. H. and Detra, R. W. (1959). "Laminar heat transfer around blunt bodies in dissociated air." *J. Aero. Sci.*, 26(7), 421-430.

Knight, D. D., Garrison, T. J., Settles, G. S., Zheltovodov, A. A., Maksimov, A. I., Shevchenko, A. M., Vorontsov, S. S. (1995). "Asymmetric crossing-shock-wave/turbulent-boundary-layer interaction." *AIAA J.*, 33(12), 2241-2249.

Kontis, K. (2008). "Flow control effectiveness of jets, strakes, and flares at hypersonic speeds." *Proc. Inst. Mech. Eng., G, J. Aero. Eng.*, 222(5), 585-603.

Kuehn, D. M. (1959). "Experimental investigation of the pressure rise required for the incipient separation of turbulent boundary layers in two-dimensional supersonic flow." NASA Memo 1-21-59W.

Kumar, D. (1991). "Hypersonic shockwave – boundary layer interaction." M.Sc. thesis, Cranfield Univ., Cranfield, U.K.

Kumar, D. (1995). "Hypersonic control effectiveness." Ph.D. thesis, Cranfield Univ., Cranfield, U.K.

Ledford, O. C. (1973). "Hypersonic film cooling." Ph.D. thesis, Univ. of London, London, U.K.

Lee, D. B., Bertin, J. J. and Goodrich, W. D. (1970). "Heat-transfer rate and pressure measurements obtained during Apollo orbital entries." NASA TN-6028.

Lees, L. (1956). "Laminar heat transfer over blunt-nosed bodies at hypersonic speeds." *Jet Prop.*, 26(4), 259-269.

Lemmon, E. C. and Coleman, H. W. (1973). "Turbulent heat transfer to a fin leading edge – Flight test results." *AIAA J.*, 11(4), 571-573.

Liepmann, H. W. and Roshko, A. (1957). *Elements of gasdynamics*. John Wiley & Sons Inc., London.

Lofthouse, A. J., Hughson, M. C. and Palazotto, A. N. (2002). "Hypersonic test sled external flow field investigation using computational fluid dynamics." AIAA paper 2002-0306.

Lu, F. K. and Liu, X. J. (1997). "Optical design of Cranz-Schardin cameras." *Opt. Eng.*, 36(7), 1935-1941.

Ludlow, D. K. (2001a). "IMPNS theory guide." Cranfield Univ., CoA Report NFP-0112, Cranfield, U.K.

Ludlow, D. K. (2001b). "IMPNS user's manual." Cranfield Univ., CoA Report NFP-0113, Cranfield, U.K.

Mazaheri, A. R. and Wood, W. A. (2008). "Heating augmentation for short hypersonic protuberances." AIAA paper 2008-4255.

McIntyre, T. J., Kleine, H. and Houwing, A. F. P. (2007). "Optical imaging techniques for hypersonic impulse facilities." *Aeronaut. J.*, 111(1115), 1-16.

McLaughlin, E. J. (1966). "Experimental investigation of hypersonic, turbulent flow and laminar, Lee-side flow on flat plates." AFDDL-TR-66-63, 1, Wright Patterson AFB, OH, U.S.A.

Meador, W. E. and Smart, M. K. (2005). "Reference enthalpy method developed from solutions of the boundary-layer equations." *AIAA J.*, 43(1), 135-139.

Menezes, V., Kumar, S., Maruta, K., Reddy, K. P. J. and Takayama, K. (2005). "Hypersonic flow over a multi-step afterbody." *J. Shock Waves*, 14(5/6), 421-424

Menter, F. R. (1993). "Zonal two equation k-ω turbulence models for aerodynamic flows." AIAA paper 93-2906.

Meyer, R. F., and Vail, C. F. (1967). "An experimental study of the hypersonic flow about a particular half-cone-and-delta-wing lifting configuration." NRC, NAE Aero Report LR-475, National Research Council, Ottawa, Ont., March 1967.

Mifsud, M., Estruch, D., Chaplin, R., MacManus, D. G. and Stollery, J. L. (2009). "A study of the aerodynamic heating of a hypersonic launch vehicle." Draft, to be submitted to Aero J.

Miller, D. S., Hijman, R. and Childs, M. E. (1964). "Mach 8 to 22 studies of flow separation due to deflected control surfaces." *AIAA J.*, 2(2), 312-321.

Miller, G. (1975). "A comparison of measured and predicted sphere shock shapes in hypersonic flows with density ratios from 4 to 19." NASA TN D-8076.

Mohammadian, S. (1968). "Calibration of the Mach 12 contoured nozzle." ICST Report 70-02.

Monaghan, R. J. (1955). "Formulae and approximations for aerodynamic heating rates in high speed flight." A.R.C. C.P. 360.

Murphy, E. (1965). "Heat transfer in the vicinity of a two-dimensional protuberance." NASA TM X-53257.

Naca (1953). "Equations, tables and charts for compressible flow." Naca report 1135.

Needham, D. A. (1963). "Progress report on the Imperial College hypersonic gun tunnel." I.C. Report No. 118, Univ. London, London, U.K.

Needham, D. A. (1965). "Laminar separation in hypersonic flow." Ph.D. thesis, Univ. London, London, U.K.

Needham, D. A. and Stollery, J. L. (1966a). "Hypersonic studies of incipient separation and separated flows." Aeronautical Res. Council paper ARC 27752, U.K.

Needham, D. A. and Stollery, J. L. (1966b). "Boundary layer separation hypersonic flow." AIAA paper 66-455.

Nestler, D. E. (1982). "Heat transfer non-uniformities downstream of three-dimensional boundary layer trips." Proc. 7th Int. Heat Transfer Conference, 3, 195-200.

Nestler, D. E. (1985). "The effects of surface discontinuities on convective heat transfer in hypersonic flow." AIAA paper 85-0971.

Neumann, R. D. and Hayes, J. R. (1981). "Protuberance heating at high Mach numbers, a critical review and extension of the database." AIAA paper 81-0420.

Nikuradse, J. (1942). *Turbulence Reibungsschichten and der Platte.* ZWB, R. Oldenbourg, Munich, Germany.

O'Byrne, S., Doolan, M., Olsen, S. R. and Houwing, A. F. P. (1999) "Measurement and imaging of supersonic combustion in a model scramjet engine." *J. Shock Waves*, 9(4), 221-226.

Oldfield, M. L. G., Jones, T. V. and Schultz, D. L. (1978). "On-line computer for transient turbine cascade instrumentation." *IEEE Trans. Aerospace and Electronic Syst.*, AES-14(5), 738-749.

Oldfield, M. L. G., Burd, H. J. and Doe, N. G. (1984). "Design of wide-bandwidth analogue circuits for heat transfer instrumentation in transient tunnels." *In: Heat and mass transfer in rotating machinery* (A86-24451 09-34), Washington, U.S.A.

Olivier, H. (2009). "Thin film gauges and coaxial thermocouples for measuring transient temperatures." SWL, RWTH, Aachen, Germany.

Opatowski, T. P. S. (1967). "An experimental study of the flow around and the forces developed by hypersonic lifting vehicles." Ph.D. thesis, Univ. of London, London, U.K.

Opatowski, T. P. S. (1969). "A three-component gun tunnel balance designed for testing thin delta wings." ARC TR 31278.

Pai, S. (1978). "Supersonic turbulent boundary layer flow over a protuberance." *J. Aero. Sci. India*, 30(3-4), 167-171.

Papuccuoglu, H. (1993). "Experimental investigation of hypersonic three-dimensional corner flow." *AIAA J.*, 31(4), 652-656.

Pawliszyn, J. (1987). "LEDs and laser diodes as light sources for the Schlieren optics." *Rev. Sci. Instrum.*, 58, 245-248.

Peaker, A. (2005). "Transition on a conical centre body for a hypersonic ramjet." M.Sc. thesis, Cranfield Univ., Cranfield, U.K.

Pianthong, K., Zakrzewski, S., Behnia, M. and Milton, B. E. (2003). "Characteristics of impact driven supersonic liquid jets." *Exp. Thermal Fluid Sci.*, 27(5), 589–598.

Polak, A. (1974). "A numerical study of supersonic turbulent boundary layer over a small protuberance." *AIAA J.*, 12(10), 1409-1411.

Polezhaev, Y. V. (2000). "Will there or will there not be a hypersonic airplane?" *J. Eng. Phys. Therm.*, 73(1), 3-8.

Porcar, R. and Prenel, J. P. (1982). "A partially, incoherent, periodic, pulsed light source for optical flow studies." *Opt. Las. Tech.*, 14(6), 320-324.

Price, E. A. and Stallings, R. L. (1967). "Investigation of turbulent separated flows in the vicinity of fin-type protuberances at supersonic Mach numbers." NASA TN D-3804.

Prince, S. A. (1994). "Hypersonic turbulent interaction phenomena and control flap effectiveness." M.Sc. thesis, Cranfield Univ., Cranfield, U.K.

Raffel, M. and Kost, F. (1998). "Investigation of aerodynamic effects of coolant ejection at the trailing edge of a turbine blade model by PIV and pressure measurements." *Exp. Fluids*, 24(5-6), 447-461.

Raffel, M., Willert, C. E., Wereley, S. T. and Kompenhans, J. (2007). *Particle Image Velocimetry: A Practical Guide.* 2nd ed., Springer-Verlag Berlin and Heidelberg.

Rao, D. M. and Whitehead, A. H. (1972). "Lee-side vortices on delta wings at hypersonic speeds". *AIAA J.*, 10(11), 1458-1465.

Rogers, G. F. C. and Mayhew, Y. R. (1980). *Engineering thermodynamics Work and Heat Transfer*. Longman Scientific & Technical. John Wiley & Sons, New York.

Rumsey, C. L. (2009). "Compressibility considerations for k-omega turbulence models in hypersonic boundary layer applications." NASA/TM-2009-215705.

Savino, R. and Paterna, D. (2005). "Blunted cone-flare in hypersonic flow." *Comp. and Fluids,* 34(7), 859-875.

Schlichting, H. (1979). *Boundary layer theory.* 7th Ed. McGraw-Hill, N.Y., U.S.A.

Schneider, S. P. (2001). "Effects of high-speed tunnel noise on laminar-turbulent transition." *J. Spacecrafts and Rockets*, 38(3), 1106-1116.

Schoenherr, K. E. (1932). "Resistance of flat surfaces moving through a fluid." *Trans. Soc. Nav. Arch. Mar. Eng.,* 40, 279–313.

Schrijer, F. F. J. (2003). "Transient heat transfer measurements in a short duration hypersonic facility on a blunted cone-flare using QIRT." M.Sc. thesis, TU Delft, Delft, The Netherlands.

Schrijer, F. F. J., Scarano, F. and van Oudheusden, B. (2004). "Roughness induced BL transition measurements in hypersonic flow using infrared thermography." QIRT 2004-090, TU Delft, Delft, The Netherlands.

Schultz, D. L. and Jones, T. V. (1973). "Heat-transfer measurements in short-duration hypersonic facilities." AGARD-AG-165, Fort Halstead, U.K.

Sedney, R. (1973). "A survey of the effect of small protuberances on boundary layer flows." *AIAA J.*, 11(6), 782-792.

Sedney, R. and Kitchens, C.W. Jr. (1977). "Separation ahead of protuberances in supersonic turbulent boundary layers." *AIAA J.*, 15(4), 546-552.

Settles, G. S. (1985). "Colour-coding Schlieren techniques for the optical study of heat and fluid flow." *Int. J. Heat and Fluid Flow,* 6(1), 3-15.

Settles, G. S. (2001). *Schlieren and shadowgraph techniques*. Springer-Verlag Berlin Heidelberg New York.

Shapiro, A. H. (1953). *The dynamics and thermodynamics of compressible fluid flow.* Ronald Press Co., New York, U.S.A.

Shifen, W. and Qingquan, L. (1990). "Nature of the surface heat transfer fluctuation in a hypersonic separated turbulent flow." *Acta Mech. Sinica*, 6(4), 296-302.

Shoesmith, B., Birch, T., Mifsud, M., Meunier, M. and Shaw, S. (2006). "CFD analysis of a supersonic projectile with deflectable nose control." AIAA paper 2006-3200.

Shore, C. P., Dixon, S. C. and Griffith, G. E. (1963). "Experimental pressures and turbulent heat-transfer coefficients associated with sinusoidal protuberances on a flat plate at a mach number of 3." NASA TN D-1626.

Simmons J. M. (1995). "Measurement techniques in high-enthalpy hypersonic facilities." *Exp. Therm. Fluid Sci.*, 10(4), 454-469.

Singh, A. (1996). "Experimental study of slender vehicles at hypersonic speeds." Ph.D. thesis, Cranfield Univ., London, U.K.

Smart, M. K. and Suraweera, M. V. (2009). "HIFiRE 7 - Development of a 3-D scramjet for flight testing". AIAA paper 2009-7259.

Smith, L. G. (1994). "Pulsed-laser Schlieren visualization of hypersonic boundary-layer instability waves." In 18th AIAA Aerospace Ground Testing Conf. AIAA paper 94-2639.

Spalart, P. R. and Allmaras, S. R., (1992). "A one-equation turbulence model for aerodynamic flow." AIAA paper 92-0439.

Sperinck, N. P. B. (1989). "The simulation of rocket plume effects on a blunted conical body." M.Sc. thesis, Cranfield Univ., Cranfield, U.K.

Srinivasan, R., and Bowersox, R. D. W. (2004). "Role of the barrel shock as control element for hypersonic transverse jet injection flows." AIAA paper 2004-2698.

Stainback, P. C. (1969). "Effect of unit Reynolds number, nose bluntness, angle of attack, and roughness on transition on a 5° half-angle cone at Mach 8." NASA TN D-4961.

Stainback, P. C. and Weinstein, L. M. (1967). "Aerodynamic heating in the vicinity of corners at hypersonic speeds." NASA TN D-4130.

Stasicki, B., Hiller, W. J. and Meier, G. E. A. (1990). "Light pulse generator for high speed photography using semiconductor devices as a light source." *Opt. Eng.*, 29(7), 821-827.

Sterret, J. R. and Emery, J. C. (1960). "Extension of boundary layer separation criteria to a Mach number of 6.5 by utilizing flat plates with forward facing steps." NASA TN D-618.

Sterret, J. R. and Emery, J. C. (1962). "Experimental separation studies for two-dimensional wedges and curved surfaces at M = 4.8 to 6.2." NASA TN D-1014.

Sterret, J. R., Morrissete, E. L., Whitehead, A. H., Jr., and Hicks, R. M. (1967). "Transition fixing for hypersonic flow." NASA TN D-4129.

Stetson, K. F. (1992). "Hypersonic boundary-layer transition", 324-417, in: "Advances in Hypersonics, Volume 1: Defining the Hypersonic Environment", Bertin, J. J., Glowinski, R., and Periaux, J., Birkhauser, Boston, MA.

Stine, H. A. and Wanlass, K. (1954). "Theoretical and experimental investigation of aerodynamic-heating and isothermal heat-transfer parameters on a hemi-spherical nose with laminar boundary layer at supersonic Mach numbers." NACA TN 3344.

Stollery, J. L., Maull, D. J. and Belcher, B. J. (1960). "The Imperial College hypersonic gun tunnel." *J. Aero. Soc.*, 64, 24-32.

Stollery, J. L. (1972). "Viscous interaction effects on re-entry aerothermodynamics: theory and experimental results. Aerodynamic problems associated with hypersonic vehicles." AGARD-LS-42-vol 1, Lecture 10.

Stollery, J. L. (1973). "Turbulent boundary layer at hypersonic speeds." Imperial College Aero Report 73-04, London, U.K.

Stollery, J.L. and Coleman, G.T. (1975). "A correlation between pressure and heat transfer distributions at supersonic and hypersonic speeds." *Aero. Quart.*, Nov, 304-312.

Stollery, J. L. (1987). "Some aspects of shock-wave boundary-layer interaction relevant to intake flows." Aerodynamics of hypersonic lifting vehicles, CP-428, AGARD.

Stollery, J. L., MacManus, D. G., and Estruch, D. (2008) *Hypersonic research and its application to a real vehicle*. Seminar presentation, University of Manchester, November 2008.

Surber, T.E. (1965). "Heat transfer in the vicinity of surface protuberances." *J. Spacecraft and Rockets,* 2(6), 978-980.

Taylor, J. R. (1992). *An introduction to error analysis: the study of uncertainties in physical measurements.* 2nd Ed. University Science Books, California, U.S.A.

Thompson, M. O. (1992). *At the Edge of Space: The X-15 Flight Program.* Smithsonian Institution Press, Washington, U.S.A.

Thyson, N., Todisco, A., Reeves, F. and McCauley, W. (1978). "Active and passive tripping of frustum transition at Mach numbers of 8 and 10." AIAA paper 78-1128.

Tobin, D. (2005). "Transition of the nose cone of a hypersonic test vehicle." M.Sc. thesis, Cranfield Univ., Cranfield, U.K.

Truitt, R. W. (1965). "Hypersonic turbulent boundary-layer interference heat transfer in vicinity of protuberances." *AIAA J.*, 3(9), 1754-1755.

Tsai, C. -Y. and Bakos, R. J. (1998). "Shock-tunnel flow visualization with a high-speed Schlieren and laser holographic interferometry system." AIAA paper 1998-2700.

van Driest, E. R. (1952a). Investigation of laminar boundary layers in compressible fluids using the Crocco method. NACA TN 2597.

van Driest, E. R. (1952b). "Turbulent boundary layer in compressible fluids." *J Aero. Sci.*, 18(3), 145-160.

van Driest, E. R. (1956). "The problem of aerodynamic heating." *Aeronautical Eng. Review*, 15(10), 26-41.

Vannahme, M. (1994). "Roughness effects on flap control effectiveness at hypersonic speeds." M.Sc. thesis, Cranfield Univ., Cranfield, U.K.

Vermuelen, J. P. and Simeonides, G. (1992). "Parametric studies of shock wave/boundary layer interactions over 2D compression corners at Mach 6." von Karman Institute for Fluid Dynamics VKI TN 181, Rhode-St-Genese, Belgium.

Wang, S. F., Ren, Z. Y. and Wang, Y. (1998). "Effects of Mach number on turbulent separation behaviours induced by blunt fin." *Exp. Fluids*, 25(4), 347-351.

Watts, J. D. (1968). "Flight experience with shock impingement and interference heating on the X-15-2 research airplane." NASA TM X-1669.

Watts, J. D. and Olinger, F. V. (1968). "Heat-transfer effects of surface protuberances on the X-15 airplane." NASA TM X-1566.

Weinberg, F. J. (1963). *Optics of flames*. London Butterworths, London, U.K.

Weinstein, L. M. (1970). "Effects of two-dimensional sinusoidal waves on heat transfer and pressure over a flat plate at Mach 8." NASA TN D-5937.

Weinstein, L. M. (2000). "Large-field Schlieren visualization from wind tunnel to flight." *J. Vis.*, 2 (3/4), 321-329.

White, F. (2005). *Viscous fluid flow,* 3rd Edition, McGraw Hill, N.Y., U.S.A.

Wilcox, D. C. (1992). "The remarkable ability of turbulence model equations to describe transition." DCW Industries, CA., U.S.A.

Winkelmann, A. E. (1972). "Experimental investigations of a fin protuberance partially immersed in a turbulent boundary layer at Mach 5." NOLTR 72-33, MA., U.S.A.

Wood, C. F., Leach, D. H., Zhang, J. Z., Chang, R. K. and Barber, P. W. (1988). "Time-resolved shadowgraphs of large individual water and ethanol droplets vaporized by a pulsed CO2 laser." *Applied Opt.*, 27(11), 2279-2286.

Zakkay, V., and Wang, C. R. (1973) "Applications of active cooling to nose cones." ARL 73-0143.

APPENDIX A

Heat Flux Measurements

In this appendix, further information on the heat flux measurements is provided. Initially, the fundamentals of the measurements are reviewed and details on the calibration of the experimental rig are shown. Subsequently the heat flux measurements in the vicinity of the protuberances are presented in the form of plan view plots. Measurements are additionally provided in tabulated form as W/cm^2, Stanton number (St) and also as the ratio St / St_u to facilitate future reference to the present work.

A.1 Measurement approach

The present heat flux measurements are based on the theory of one-dimensional heat conduction. Consideration was taken between using a numerical or an analogical approach. Eventually the latter was employed as already discussed in Chapter 3.

A.1.1 Theory of one-dimensional heat conduction

A temperature difference between at least two systems results in the transfer of energy from hot to cold systems until equilibrium is reached. This flow of energy or heat flux (q) is generally expressed per unit cross-sectional area and in a direction normal to the flow of heat (Fig. A.1). Given that a measure of energy cannot be directly obtained, heat flux measurements generally rely on its effects on temperature or spectral emissions to estimate the flow of energy. Four principal methodologies to measure heat flux are generally used: differential temperature, calorimetric, energy supply or removal and mass transfer analogy methods. Further details on these methods can be found in Childs (2001).

The theory of one-dimensional heat conduction considers the conduction of heat between a conductive slab (thin-film in the present case) placed onto a semi-infinite insulating substrate. The temperature at the rear of the sensor is assumed not to be affected by the heat during the recording period. The direction of the deduced heat flux is perpendicular to the surface of the gauge and the variation of temperature in time and depth into a semi-infinite surface is thus modelled as in Eq. A.1, where α is the thermal diffusivity, $\alpha = k/(\rho c)$. The same principle is also used in heat flux measurements performed with other instruments such as plug gauges, null point calorimeters, coaxial thermocouple gauges, thermo-chromic liquid crystals and radiometers, amongst others (Childs et al., 1999).

$$\frac{\partial^2 T}{\partial x^2} = \frac{1}{\alpha}\frac{\partial T}{\partial t} \quad \text{[Eq. A.1]}$$

A.1.2 Thin-film gauges

The gauges in the present study were used to monitor a time-dependent surface temperature. Thin-film sensors were specifically developed for shock-tunnel and gun-tunnel applications. Their very thin element (a few μm thick) allows for very fast speed of response (about 1μs) to the highly transient surface temperatures typical of these facilities. The specified maximum recording time for the measurement of heat flux with the thin-film gauges used was 100ms. These makes the Cranfield University gun tunnel an ideal facility for the measurement of heat transfer by means of this approach.

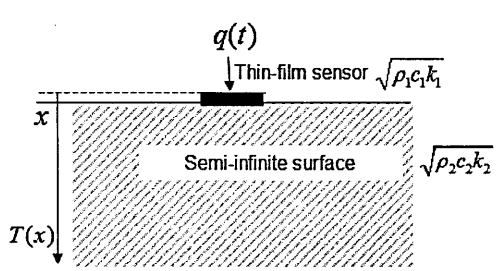

Figure A.1 Principle of theory of one-dimensional heat conduction.

A.1.3 Calculation of heat flux

The transient temperature signal yielded by the thin-film gauges was used to obtain a measure of heat flux rate. This could be done numerically from mathematical models that integrate the time-dependent temperature signal (Atcliffe, 1995), or by using an analogue electrical circuit that serves the same function (Schultz and Jones, 1983; Sperinck, 1989).

A.1.3.1 Numerical technique

Assuming that $\Delta(T_0)=0$ at t_0=0s and $0<x<\infty$, the original one-dimensional heat conduction equation can be developed to offer a relationship between heat flux to the surface and time-dependent surface temperature measurements, which for a step surface temperature change T_1-T_0 is as shown in Eq. A.2. From superposition, and considering a number of step surface temperature changes, the previous expression can be derived to Eq. A.3, which for a semi-infinite geometry can then be represented as in Eq. A.4.

$$q(t)=\frac{\sqrt{\rho c_p k}}{\sqrt{\pi}}\frac{T_1-T_0}{\sqrt{t-t_0}} \quad \text{[Eq. A.2]}$$

$$q(t)=\frac{\sqrt{\rho c_p k}}{\sqrt{\pi}}\sum_{i=1}^{n}\frac{T_i-T_{i-1}}{\sqrt{t_n-t_{i-1}}} \quad \text{[Eq. A.3]}$$

$$q(t)=\frac{2\sqrt{\rho c_p k}}{\sqrt{\pi}}\sum_{i=1}^{n}\frac{T(t_i)-T(t_{i-1})}{\sqrt{t_n-t_i}+\sqrt{t_n-t_{i-1}}} \quad \text{[Eq. A.4]}$$

This derivation is based on the conditions that $\Delta(T_0)=0$ at t_0=0s and thus the recorded temperatures are relative to the initial temperature. It must also be noticed that the square root of time is considered and thus it behaves as a half derivative, which makes it very sensitive to experimental noise as noticed by Oldfield et al. (1978).

A.1.3.2 Electrical analogy

An alternative approach consists in using electrical analogue integrator circuits that incorporate the integration of the transient temperature signal (Schultz and Jones, 1973). This method is based on the analogy between the flow of heat into a semi-infinite material and the flow of current into an R-C circuit as shown in Figure A.2.

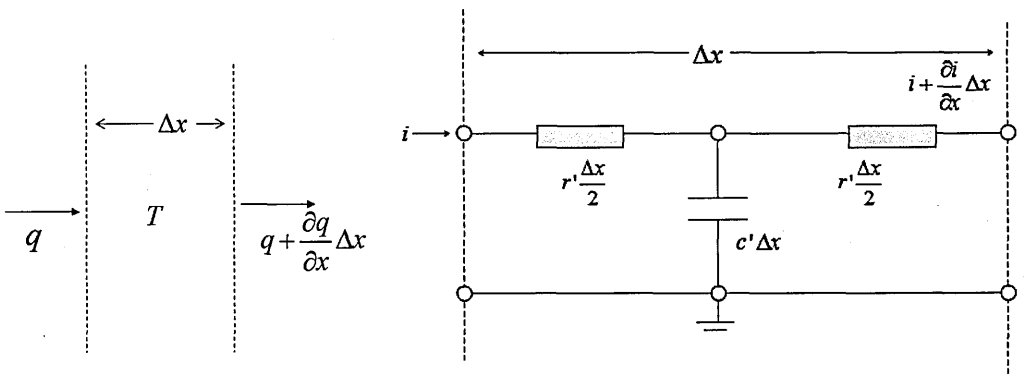

(a) Flow of heat into semi-infinite material (b) Flow of current into R-C circuit

Figure A.2 Electrical analogy.

The rate of absorption of heat through a semi-infinite material with thickness Δx is considered to be $-\frac{\partial q}{\partial x}\Delta x$ by conservation of energy, this is also equal to $\rho c_p \frac{\partial T}{\partial t}\Delta x$. The corresponding governing equation for a semi-infinite material can thus be obtained by equalling both terms (Eq. A.5):

$$\frac{\partial q}{\partial x} = -\rho c_p \frac{\partial T}{\partial t} \qquad \text{[Eq. A.5]}$$

In a similar way, the rate of current through an R-C circuit is $-\frac{\partial i}{\partial x}\Delta x$, or also $c'\frac{\partial V}{\partial t}\Delta x$, where c' and r' are the capacity and resistance per unit length, yielding the following governing equation in this case (Eq. A.6):

$$\frac{\partial i}{\partial x} = -c'\frac{\partial V}{\partial t} \qquad \text{[Eq. A.6]}$$

Observing the analogy between the two governing equations, the conduction equation and Ohm's law are also compared in Eqs. A.7 and A.8, where k is the thermal conductivity.

$$q = -k\frac{\partial T}{\partial x} \quad \text{(Conduction equation)} \quad \text{[Eq. A.7]}$$

$$-i = \frac{1}{r'}\frac{\partial V}{\partial x} \quad \text{(Ohm's law)} \quad \text{[Eq. A.8]}$$

Based on the equations above, the following analogies can thus be drawn (Eqs. A.9-A.12).

$$q \equiv i \quad \text{[Eq. A.9]}$$

$$T \equiv V \quad \text{[Eq. A.10]}$$

$$\rho c_p \equiv c' \quad \text{[Eq. A.11]}$$

$$k \equiv \frac{1}{r'} \quad \text{[Eq. A.12]}$$

Both the conduction equation and Ohm's law can be solved by means of Laplace transforms to obtain the following relations, with the conditions that $T(t_0) = V(t_0) = 0$ at t_0 =0, (Eqs. A.13 and A.14), s being the Laplace variable.

$$\overline{q}(s) = \sqrt{\rho c_p k}\sqrt{s}\overline{T}(s) \quad \text{(Conduction equation)} \quad \text{[Eq. A.13]}$$

$$\overline{i}(s) = \sqrt{\frac{c'}{r'}}\sqrt{s}\overline{V}(s) \quad \text{(Ohm's law)} \quad \text{[Eq. A.14]}$$

The change in voltage across the film is known to depend on temperature following this relation (Eq. A.15), where α_R is the temperature sensitivity, V_o the output voltage and V_{in} is the voltage prior to the run.

$$V_0 = \frac{V_{in}}{\alpha_R T} \qquad \text{[Eq. A.15]}$$

Substituting Eq. A.15 into the solution of the Ohm's equation in the Laplace domain (Eq. A.14), Eq. A.16 is obtained.

$$\bar{i}_{in} = \sqrt{\frac{c'}{r'}}\sqrt{s}\alpha_R V_0 T \qquad \text{[Eq. A.16]}$$

This expression can then be substituted into the solution of the conduction equation in the Laplace domain (Eq. A.13) to obtain a relation between heat transfer and current through the resistor (Eq. A.17). The equivalent of this equation in the temporal domain is shown in Eq. A.18, where the current i_{in} through the resistor R_1 is subject to the voltage as $V_{out} = R_1 i_{in}$, and thus Eq. A.19 can be derived.

$$\bar{q} = \sqrt{\rho c_p k}\sqrt{\frac{r'}{c'}}\frac{1}{\alpha_R V_0}\bar{i}_{in} \qquad \text{[Eq. A.17]}$$

$$q = \sqrt{\rho c_p k}\sqrt{\frac{r'}{c'}}\frac{1}{\alpha_R V_0} i_{in} \qquad \text{[Eq. A.18]}$$

$$q = \sqrt{\rho c_p k}\sqrt{\frac{r'}{c'}}\frac{1}{\alpha_R V_0}\frac{V_{out}}{R_1} \qquad \text{[Eq. A.19]}$$

Considering also that at large times $r'/c' = R/C$ the following relation for the gain through the analogue circuit can be derived in the Laplace domain as in Eq. A.20. In the time domain this is as in Eq. A.21.

$$G = \frac{V_{out}}{V_{in}\sqrt{\omega}} = R_i\sqrt{\frac{C}{R}}\sqrt{s}\frac{1}{\sqrt{\omega}} \qquad \text{[Eq. A.20]}$$

$$G = R_i\sqrt{\frac{C}{R}} \qquad \text{[Eq. A.21]}$$

Substituting this into Eq. A.19, the final relationship is obtained (Eq. A.22).

$$q = \left(\sqrt{\rho c_p k}\right)_g \frac{1}{\alpha_R V_0}\frac{V_{out}}{G} \qquad \text{[Eq. A.22]}$$

Knowing the gain of the system (G), the thermal property of the gauges $\left(\sqrt{\rho c_p k}\right)_g$, the thermal coefficient of resistivity α_R, the voltage across the gauges V_o and by measuring the output voltage V_{out}, this relation can be used to calculate the heat flux. Information on the measurement of V_o and V_{out} can be found in Section 3.6.5 in a description of the experimental rig. Further details on the calibration of the other variables ($\left(\sqrt{\rho c_p k}\right)_g$, α_R and G) are provided in the following section.

A.2 Calibration factors

While the thermal property $\left(\sqrt{\rho c_p k}\right)_g$ of the substrate and thin-film and the thermal coefficient α_R (or α_o in the calibration sheets) were provided by the manufacturer of the gauges, a calibration of the system gain (G) was specifically performed for each of the 8 channels for a range of different signal frequencies. As shown in the calibration curve in Fig. A.3, the gain G was 2.06 ±1.6%, at frequencies 0.1 kHz ≤ freq ≤ 5 kHz. Details on the other calibration factors of the gauges are summarised in Table A.1. The full calibration sheets for the 8 gauges are shown in Figs. A.4 to A.11.

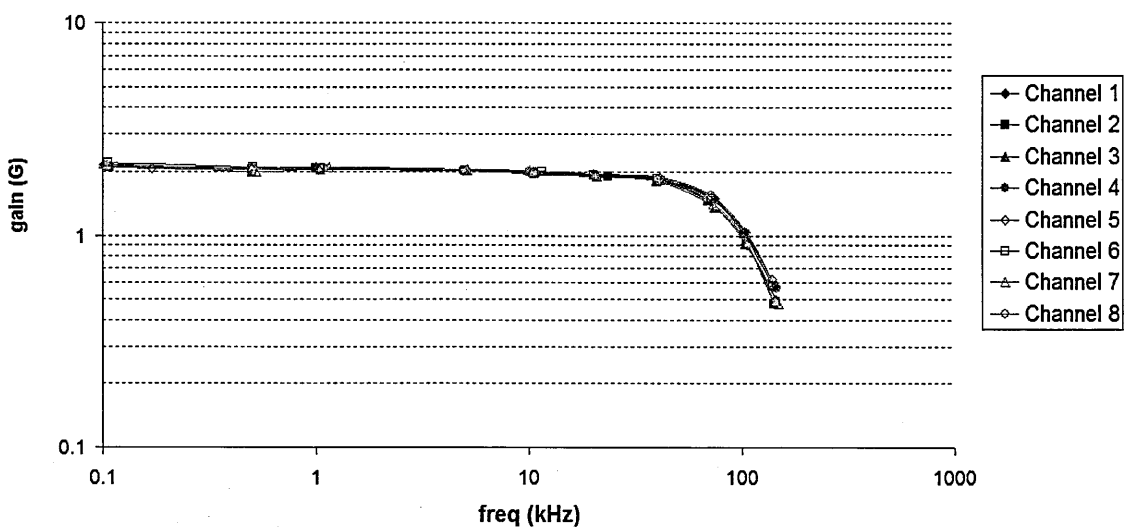

Figure A.3 Gain calibration plot across 8 channels.

Gauge	$\left(\sqrt{\rho c_p k}\right)_g$ (W cm^{-2} K^{-1} s$^{0.5}$)	α_R (K^{-1})	V_o (V)
1	0.3299	2.533	0.280
2	0.3317	2.074	0.363
3	0.3362	2.567	0.268
4	0.3377	2.495	0.340
5	0.3418	2.411	0.287
6	0.3336	2.450	0.386
7	0.3208	2.448	0.275
8	0.3394	2.661	0.286

Table A.1 Calibration properties.

Gauge No.: P-767 Date: 19.06.2006

R(A) = 29.5 Ω R(B) = 0000 Ω at T = 298 K

Static calibration

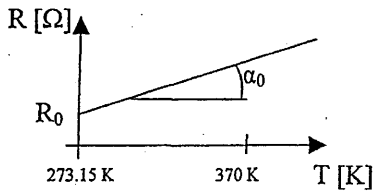

(A)
R_0 = 27.67 Ω
α_0 = 2.533 10^{-3} K^{-1}
(B)
R_0 = 00000 Ω
α_0 = 00000 10^{-3} K^{-1}

Dynamic calibration

Double pulse technique in air and glycerine.

Voltage Pulse in air: U_{air} = 13.344 V
Voltage Pulse in glycerine: U_{glyc} = 13.344 V

The data from Fig.2 is approximated by linear regression.

Fig.1 gauge response

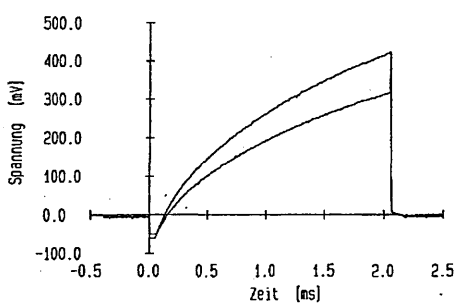

Fig.2: $\sqrt{time}$ - transformation

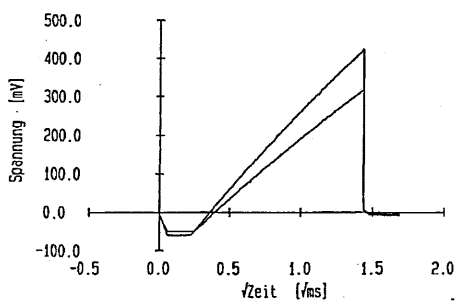

	gradient $\left[\frac{mV}{\sqrt{s}}\right]$	correlation coefficient
air (A+B)	385,129	0,9996
glycerine (A+B)	300,910	0,9997

$$\sqrt{\rho c k} = 0.3299 \frac{J}{K \cdot cm^2 \cdot \sqrt{s}}$$

Figure A.4 Specifications of thin-film gauge 1

Gauge No.: P-780 Date: 15.09.2006

R(A) = 39.2 Ω R(B) = 0000 Ω at T = 298 K

Static calibration

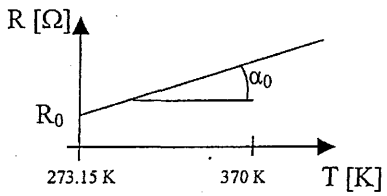

(A)
R_0 = 37.26 Ω
α_0 = 2.074 10^{-3} K^{-1}
(B)
R_0 = 00000 Ω
α_0 = 00000 10^{-3} K^{-1}

Dynamic calibration

Double pulse technique in air and glycerine.

Voltage Pulse in air: U_{air} = 13.056 V
Voltage Pulse in glycerine: U_{glyc} = 13.056 V

The data from Fig.2 is approximated by linear regression.

Fig.1 gauge response

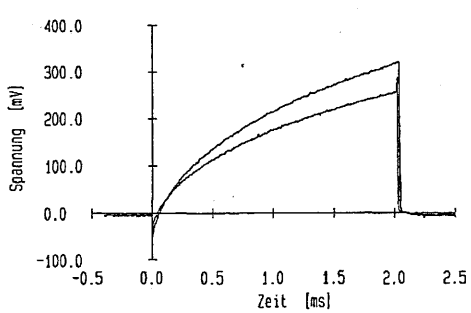

Fig.2: $\sqrt{\text{time}}$ - transformation

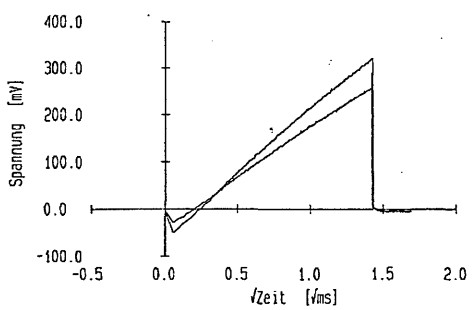

	gradient $\left[\text{mV}/\sqrt{\text{s}}\right]$	correlation coefficient
air (A+B)	260,325	0,9995
glycerine (A+B)	203,632	0,9994

$$\sqrt{\rho c k} = 0.3317 \frac{J}{K \cdot cm^2 \cdot \sqrt{s}}$$

Figure A.5 Specifications of thin-film gauge 2

Gauge No.: P-765 Date: 19.06.2006

R(A) = 28.1 Ω R(B) = 0000 Ω at T = 298 K

Static calibration

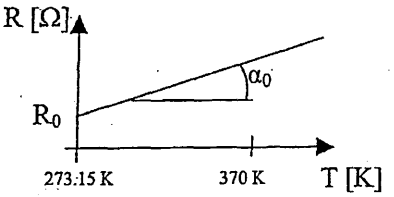

(A)
R_0 = 26.34 Ω
α_0 = 2.567 10^{-3} K^{-1}
(B)
R_0 = 00000 Ω
α_0 = 00000 10^{-3} K^{-1}

Dynamic calibration

Double pulse technique in air and glycerine.

Voltage Pulse in air: U_{air} = 13.312 V
Voltage Pulse in glycerine: U_{glyc} = 13.312 V

The data from Fig.2 is approximated by linear regression.

Fig.1 gauge response

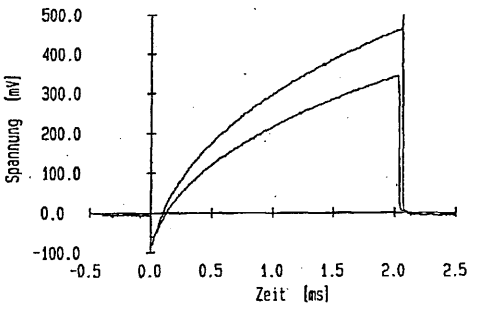

Fig.2: $\sqrt{time}$ - transformation

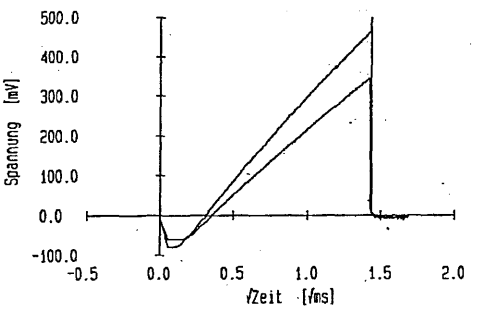

	gradient $\left[\frac{mV}{\sqrt{s}}\right]$	correlation coefficient
air (A+B)	402,190	0,9996
glycerine (A+B)	315,536	0,9996

$$\sqrt{\rho c k} = 0.3362 \frac{J}{K \cdot cm^2 \cdot \sqrt{s}}$$

Figure A.6 Specifications of thin-film gauge 3

Gauge No.: P-778 Date: 15.09.2006

R(A) = 36.6 Ω R(B) = 0000 Ω at T = 298 K

Static calibration

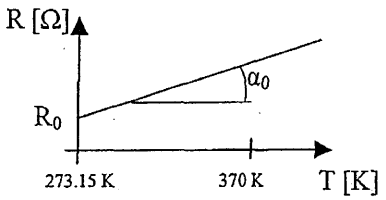

(A)
R_0 = 34.44 Ω
α_0 = 2.495 10^{-3} K^{-1}
(B)
R_0 = 00000 Ω
α_0 = 00000 10^{-3} K^{-1}

Dynamic calibration

Double pulse technique in air and glycerine.

Voltage Pulse in air: U_{air} = 13.184 V
Voltage Pulse in glycerine: U_{glyc} = 13.184 V

The data from Fig.2 is approximated by linear regression.

Fig.1 gauge response

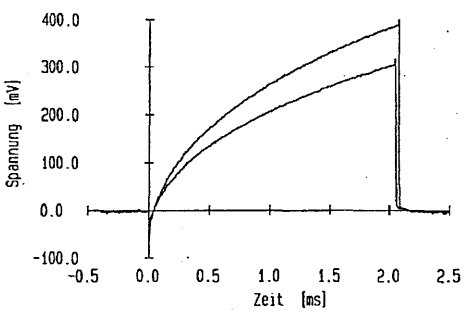

Fig.2: $\sqrt{time}$ - transformation

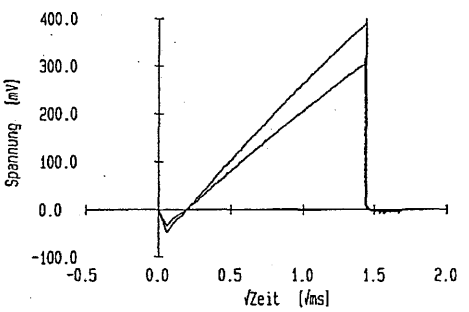

	gradient $\left[\mathrm{mV}/\sqrt{\mathrm{s}}\right]$	correlation coefficient
air (A+B)	302,805	0,9995
glycerine (A+B)	237,783	0,9996

$$\sqrt{\rho c k} = 0.3377 \frac{J}{K \cdot cm^2 \cdot \sqrt{s}}$$

Figure A.7 Specifications of thin-film gauge 4

Gauge No.: P-766 Date: 19.06.2006

R(A) = 30.3 Ω R(B) = 0000 Ω at T = 298 K

Static calibration

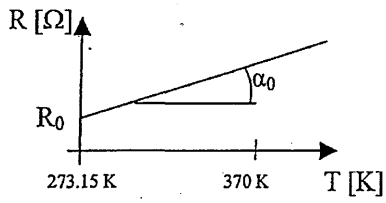

(A)
R_0 = 28.50 Ω
α_0 = 2.411 10^{-3} K^{-1}
(B)
R_0 = 00000 Ω
α_0 = 00000 10^{-3} K^{-1}

Dynamic calibration

Double pulse technique in air and glycerine.

Voltage Pulse in air: U_{air} = 13.312 V
Voltage Pulse in glycerine: U_{glyc} = 13.312 V

The data from Fig.2 is approximated by linear regression.

Fig.1 gauge response

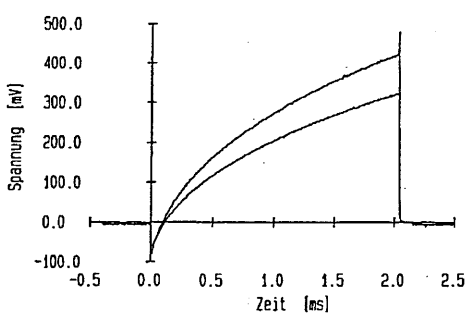

Fig.2: $\sqrt{time}$ - transformation

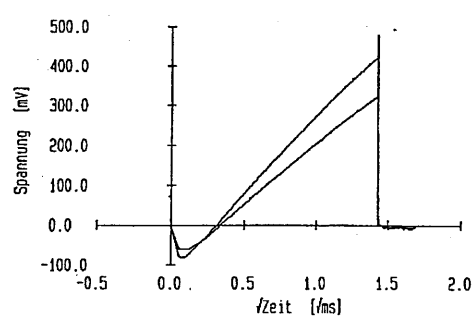

	gradient $\left[\mathrm{mV}/\sqrt{\mathrm{s}}\right]$	correlation coefficient
air (A+B)	367,890	0,9996
glycerine (A+B)	289,635	0,9996

$$\sqrt{\rho c k} = 0.3418 \frac{J}{K \cdot cm^2 \cdot \sqrt{s}}$$

Figure A.8 Specifications of thin-film gauge 5

Gauge No.: P-777 Date: 15.09.2006

R(A) = 42.0 Ω R(B) = 0000 Ω at T = 298 K

Static calibration

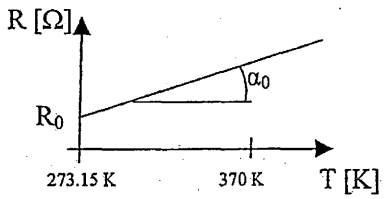

(A)
R_0 = 39.55 Ω
α_0 = 2.450 10^{-3} K^{-1}
(B)
R_0 = 00000 Ω
α_0 = 00000 10^{-3} K^{-1}

Dynamic calibration

Double pulse technique in air and glycerine.

Voltage Pulse in air: U_{air} = 13.120 V
Voltage Pulse in glycerine: U_{glyc} = 13.120 V

The data from Fig.2 is approximated by linear regression.

Fig.1 gauge response

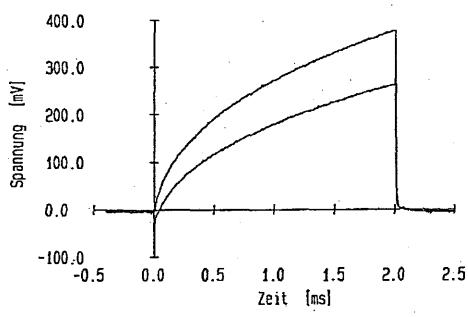

Fig.2: $\sqrt{\text{time}}$ - transformation

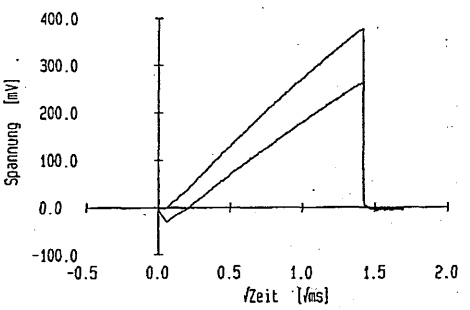

	gradient $\left[\frac{mV}{\sqrt{s}}\right]$	correlation coefficient
air (A+B)	268,831	0,9996
glycerine (A+B)	210,557	0,9996

$$\sqrt{\rho c k} = 0.3336 \frac{J}{K \cdot cm^2 \cdot \sqrt{s}}$$

Figure A.9 Specifications of thin-film gauge 6

Gauge No.: P-768 Date: 19.06.2006

R(A) = 28.6 Ω R(B) = 0000 Ω at T = 298 K

Static calibration

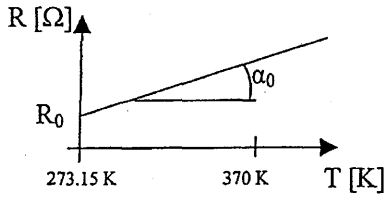

(A)
R_0 = 26.89 Ω
α_0 = 2.448 10^{-3} K^{-1}
(B)
R_0 = 00000 Ω
α_0 = 00000 10^{-3} K^{-1}

Dynamic calibration

Double pulse technique in air and glycerine.

Voltage Pulse in air: U_{air} = 13.312 V
Voltage Pulse in glycerine: U_{glyc} = 13.312 V

The data from Fig.2 is approximated by linear regression.

Fig.1 gauge response

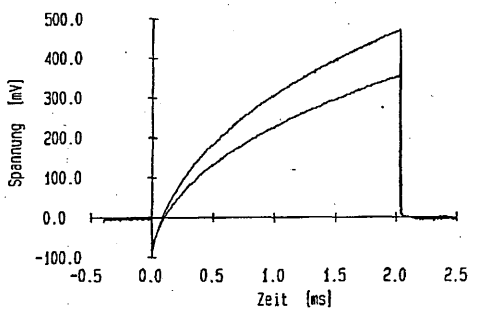

Fig.2: $\sqrt{time}$ - transformation

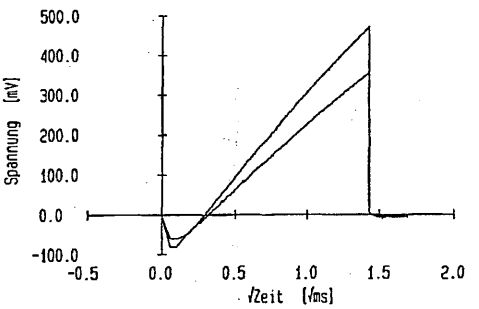

	gradient $\left[\frac{mV}{\sqrt{s}}\right]$	correlation coefficient
air (A+B)	403,709	0,9996
glycerine (A+B)	313,487	0,9996

$$\sqrt{\rho c k} = 0.3208 \frac{J}{K \cdot cm^2 \cdot \sqrt{s}}$$

Figure A.10 Specifications of thin-film gauge 7

Gauge No.: P-779 Date: 11.07.2006

R(A) = 30.0 Ω R(B) = 0000 Ω at T = 297 K

Static calibration

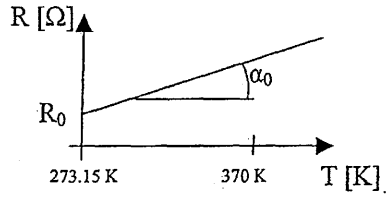

(A)
R_0 = 28.14 Ω
α_0 = 2.661 10^{-3} K^{-1}
(B)
R_0 = 00000 Ω
α_0 = 00000 10^{-3} K^{-1}

Dynamic calibration

Double pulse technique in air and glycerine.

Voltage Pulse in air: U_{air} = 13.248 V
Voltage Pulse in glycerine: U_{glyc} = 13.248 V

The data from Fig.2 is approximated by linear regression.

Fig.1 gauge response

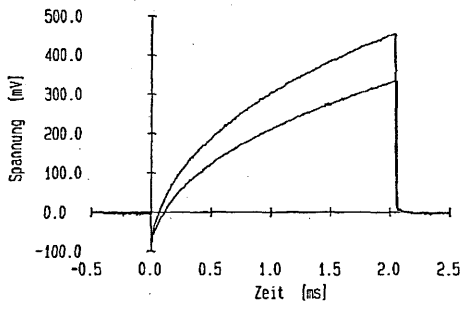

Fig.2: $\sqrt{time}$ - transformation

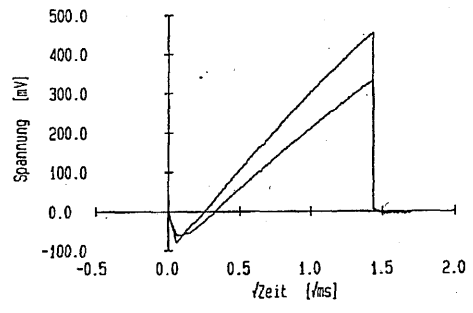

	gradient $\left[\mathrm{mV}/\sqrt{\mathrm{s}}\right]$	correlation coefficient
air (A+B)	373,963	0,9996
glycerine (A+B)	293,986	0,9996

$$\sqrt{\rho c k} = 0.3394 \frac{J}{K \cdot cm^2 \cdot \sqrt{s}}$$

Figure A.11 Specifications of thin-film gauge 8

A.3 Heat flux in the vicinity of the protuberances

In this section, the plots of heat flux measurements obtained in the vicinity of the different protuberance-plate configurations are presented in the form of Stanton number for all the conditions reproduced. Special care was taken in the selection of the measurement points so that enough resolution would be obtained in the vicinity of the model to capture the hot spot. The thin film elements were also oriented perpendicular to the direction of the highest heat flux gradients - which take place normal to the front and side of the model - to improve discretisation of the hot spot. Care was taken to ensure that the gauges, mounting block and the blanking piece were flush with the surface. Further details on the uncertainty of the measurements can be found in Appendix C. It must be remarked that each measurement was performed over a rectangular region of 1.2mm x 0.3mm which corresponds to the dimensions of the thin film element of the gauges.

A.3.1 Turbulent flow, α=15°, δ_u=5mm, M_∞=8.2, Re_∞/m=9.35x10^6

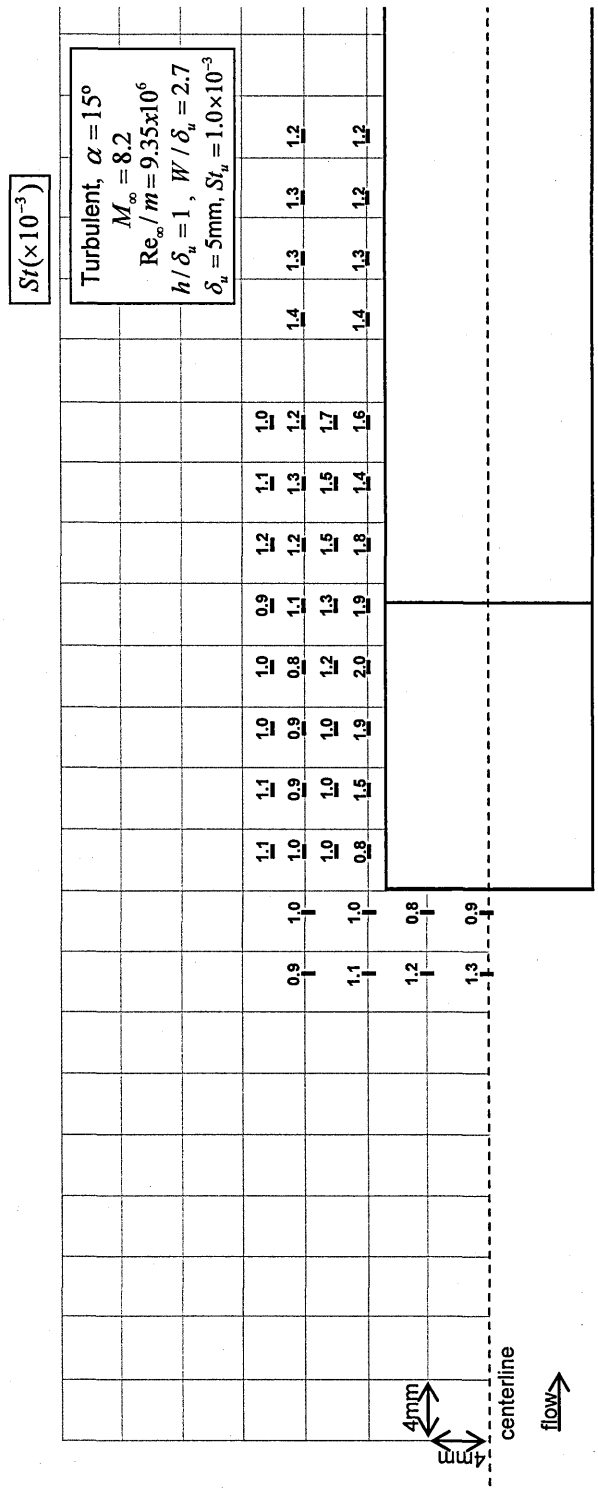

Figure A.12 Heat flux measurements: turbulent flow, α=15°, δ_u=5mm, M_∞=8.2, Re_∞/m=9.35x10^6.

A.3.2 Turbulent flow, α=30°, δ_u=5mm, M_∞=8.2, Re_∞/m=9.35x10^6

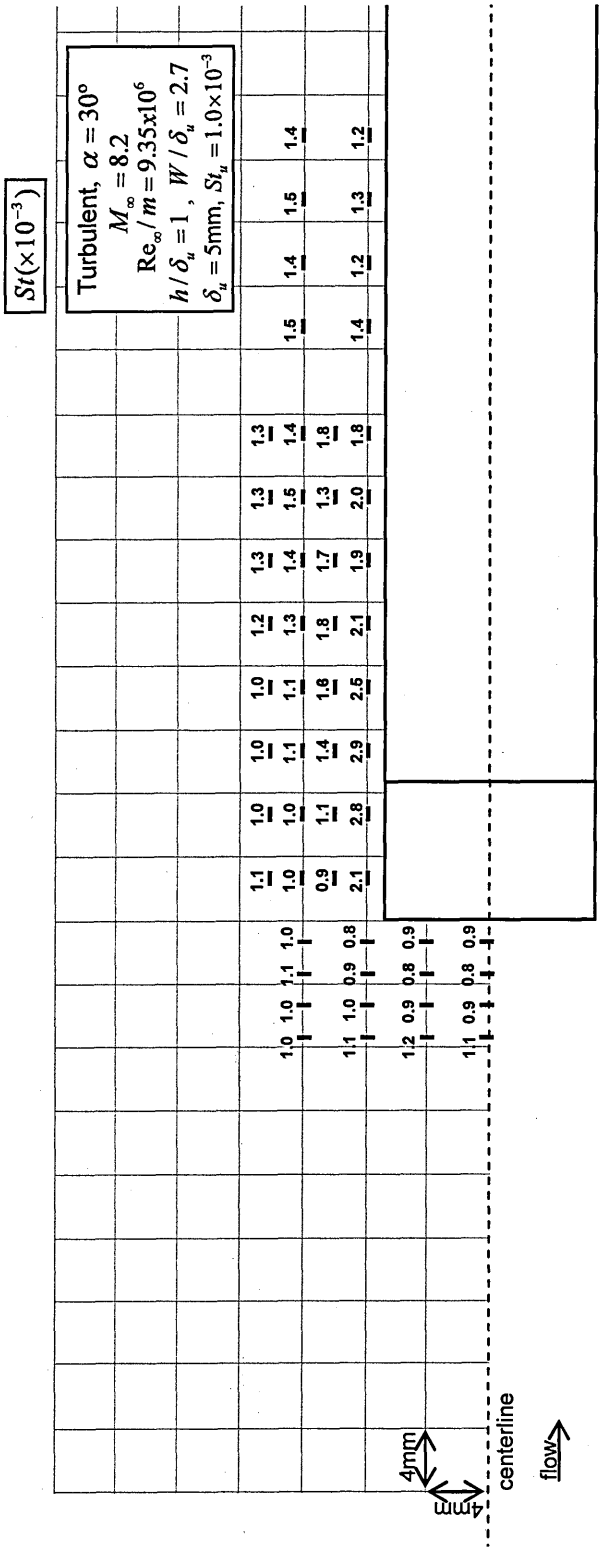

Figure A.13 Heat flux measurements: turbulent flow, α=30°, δ_u=5mm, M_∞=8.2, Re_∞/m=9.35x10^6.

A.3.3 Turbulent flow, α=45°, δ_u=5mm, M_∞=8.2, Re_∞/m=9.35x10^6

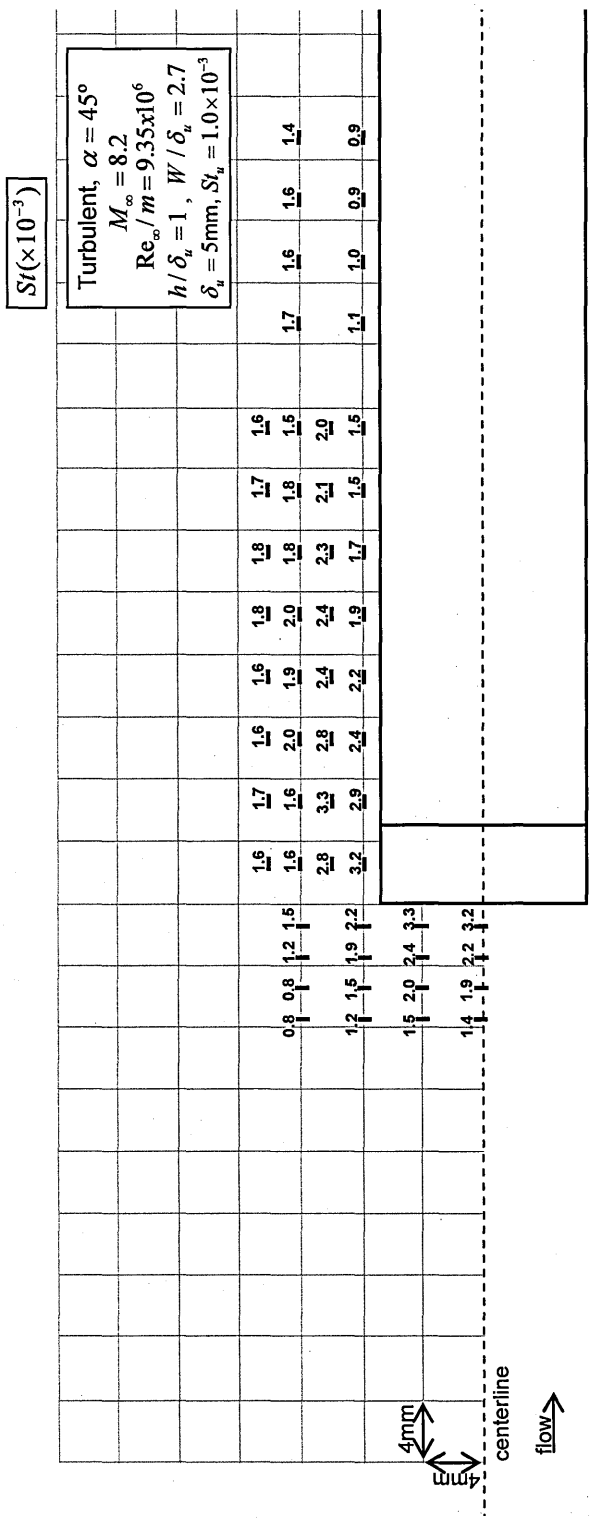

Figure A.14 Heat flux measurements: turbulent flow, α=45°, δ_u=5mm, M_∞=8.2, Re_∞/m=9.35x10^6.

A.3.4 Turbulent flow, α=60°, δ_u=5mm, M_∞=8.2, Re_∞/m=9.35x10^6

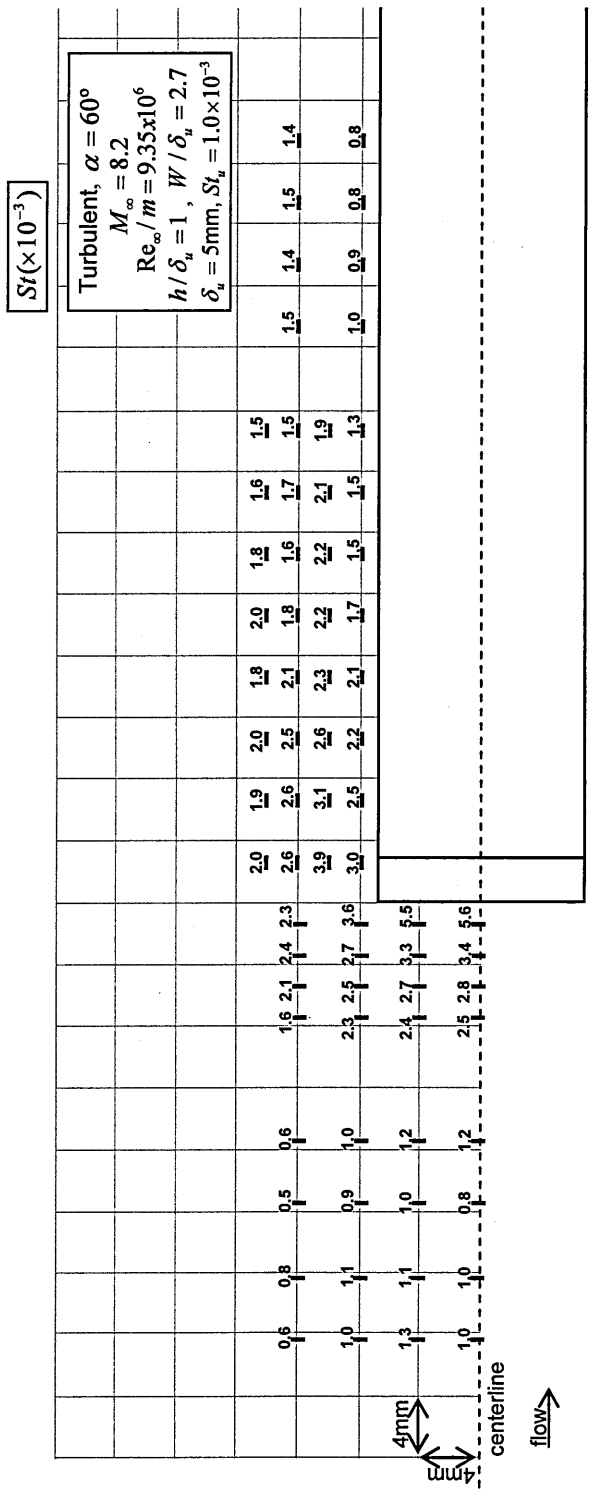

Figure A.15 Heat flux measurements: turbulent flow, α=60°, δ_u=5mm, M_∞=8.2, Re_∞/m=9.35x10^6.

A.3.5 Turbulent flow, α=90°, δ_u=5mm, M_∞=8.2, Re_∞/m=9.35x10^6

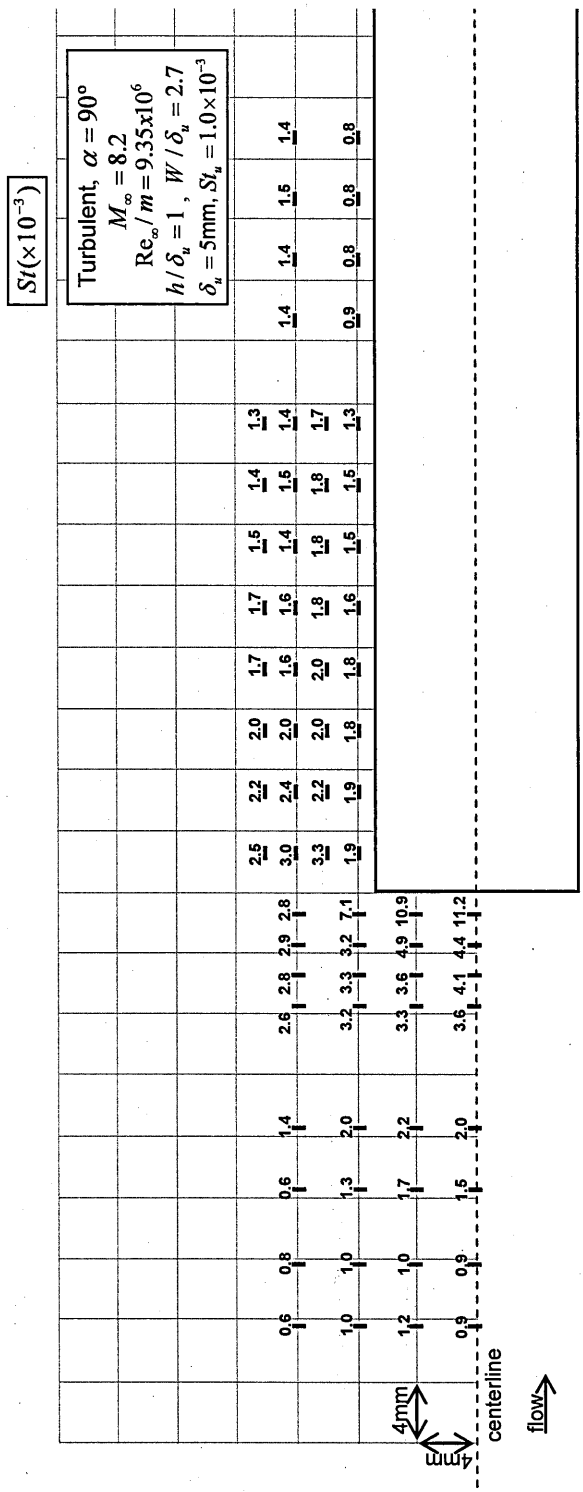

Figure A.16 Heat flux measurements: turbulent flow, α=90°, δ_u=5mm, M_∞=8.2, Re_∞/m=9.35x10^6.

A.3.6 Turbulent flow, α=135°, δ_u=5mm, M_∞=8.2, Re_∞/m=9.35x10^6

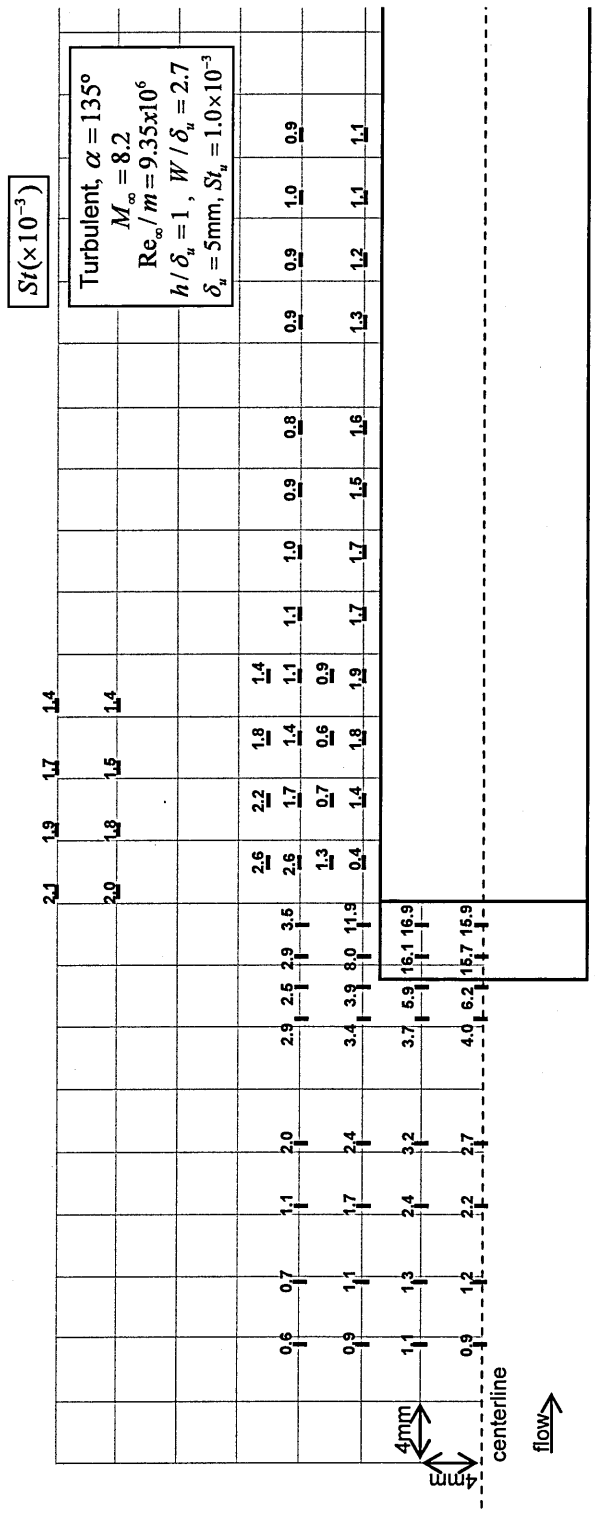

Figure A.17 Heat flux measurements: turbulent flow, α=135°, δ_u=5mm, M_∞=8.2, Re_∞/m=9.35x10^6.

A.3.7 Turbulent flow, α=30°, δ_u=5mm, h/δ_ux2, M_∞=8.2, Re_∞/m=9.35x10^6

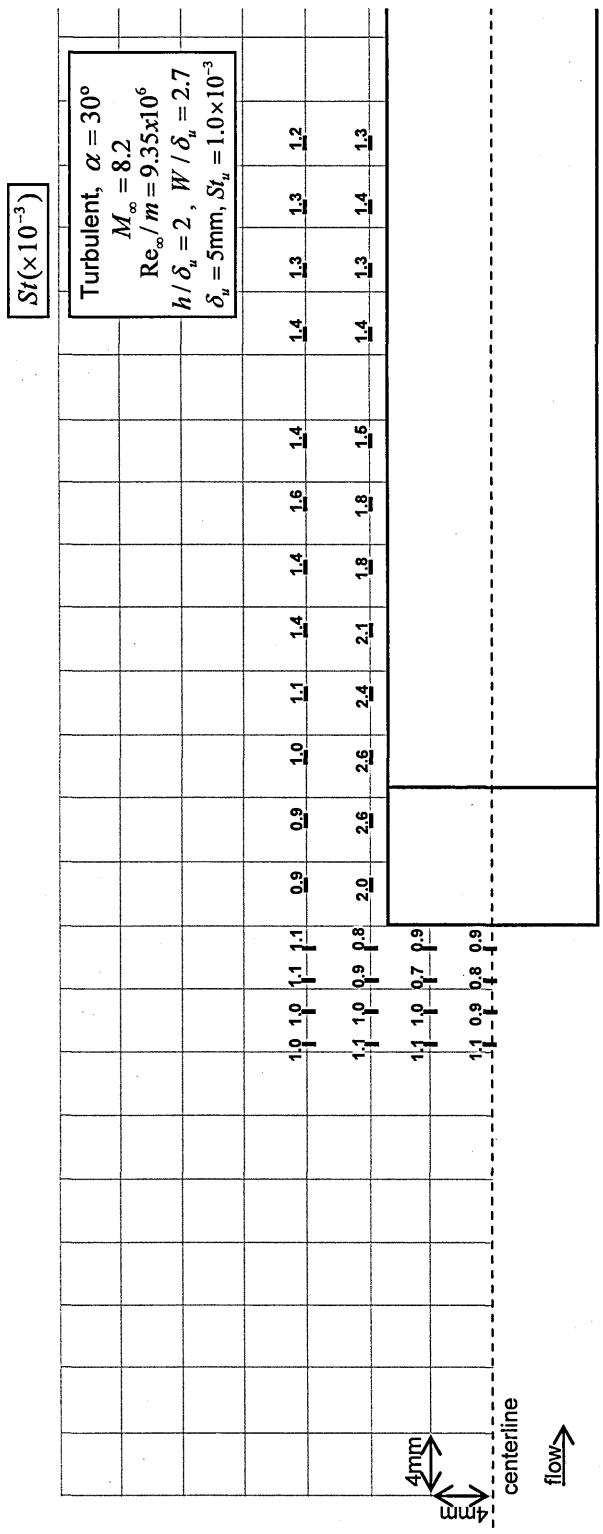

Figure A.18 Heat flux measurements: turbulent flow, α=30°, δ_u=5mm, h/δ_ux2, M_∞=8.2, Re_∞/m=9.35x10^6.

A.3.8 Turbulent flow, α=30°, δ_u=5mm, W/δ_ux2, M_∞=8.2, Re_∞/m=9.35x10^6

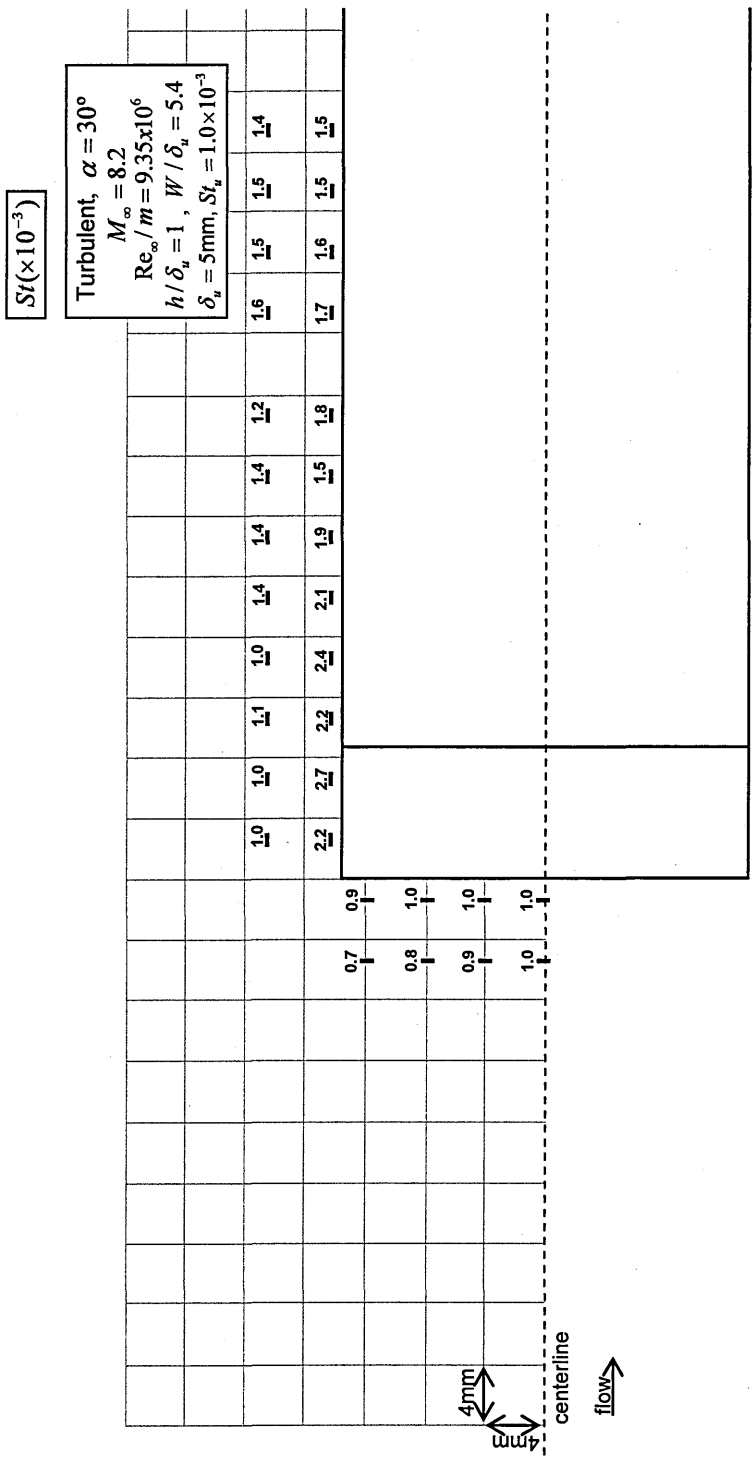

Figure A.19 Heat flux measurements: turbulent flow, α=30°, δ_u=5mm, W/δ_ux2, M_∞=8.2, Re_∞/m=9.35x10^6.

A.3.9 Laminar flow, α=30°, δ_u=2.5mm, M_∞=8.2, Re_∞/m=9.35x10^6

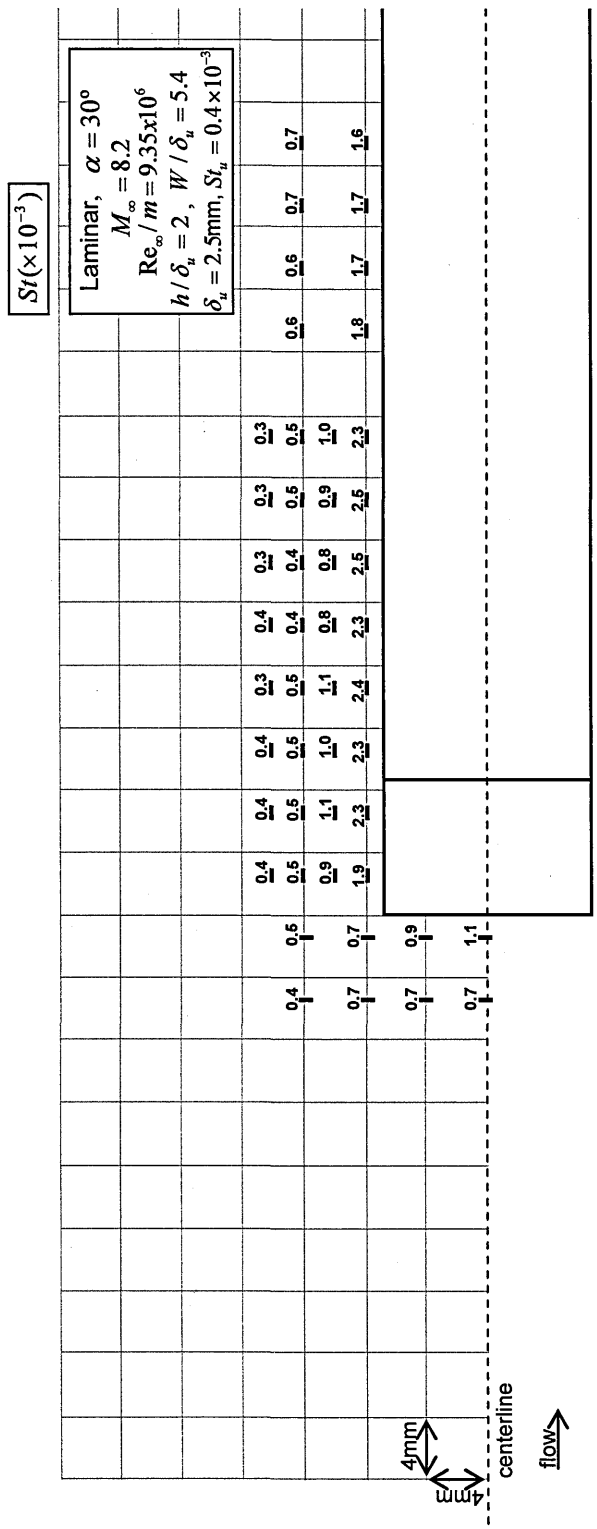

Figure A.20 Heat flux measurements: laminar flow, α=30°, δ_u=2.5mm, M_∞=8.2, Re_∞/m=9.35x10^6.

A.3.10 Laminar flow, α=15°, δ_u=2.5mm, M_∞=8.2, Re_∞/m=9.35x10^6

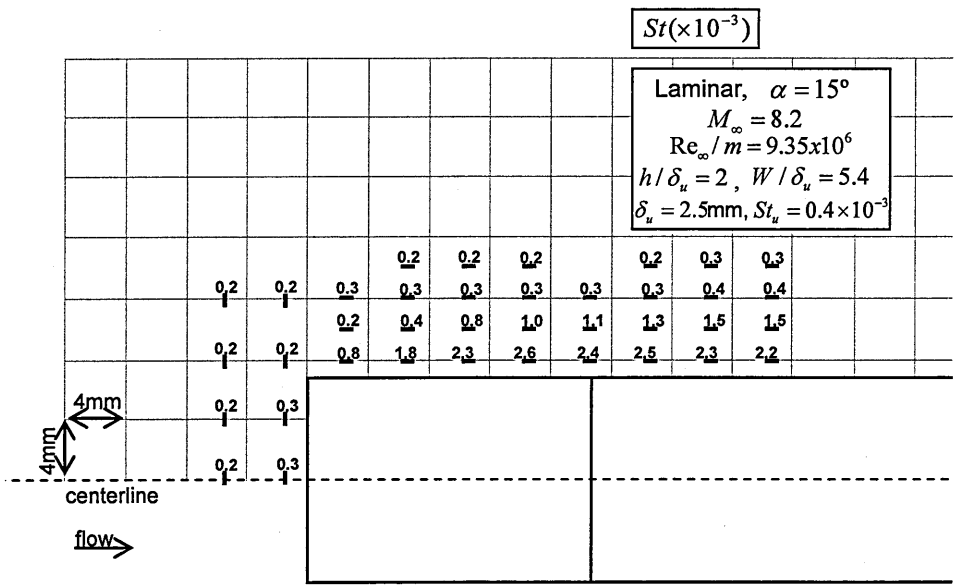

Figure A.21 Heat flux measurements: laminar flow, α=15°, δ_u=2.5mm, M_∞=8.2, Re_∞/m=9.35x10^6.

A.3.11 Laminar flow, α=45°, δ_u=2.5mm, M_∞=8.2, Re_∞/m=9.35x10^6

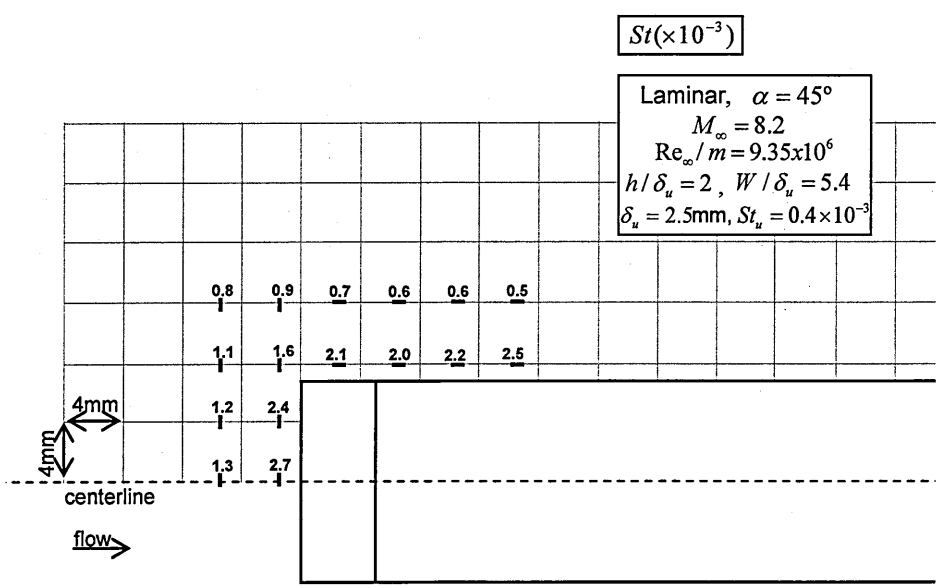

Figure A.22 Heat flux measurements: laminar flow, α=45°, δ_u=2.5mm, M_∞=8.2, Re_∞/m=9.35x10^6.

A.3.12 Laminar flow, $\alpha=60°$, $\delta_u=2.5mm$, $M_\infty=8.2$, $Re_\infty/m=9.35x10^6$

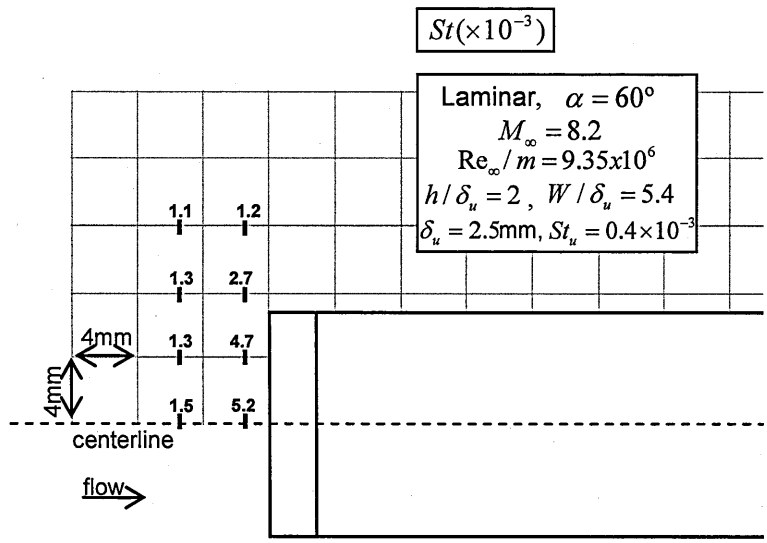

Figure A.23 Heat flux measurements: laminar flow, $\alpha=60°$, $\delta_u=2.5mm$, $M_\infty=8.2$, $Re_\infty/m=9.35x10^6$.

A.3.13 Laminar flow, $\alpha=90°$, $\delta_u=2.5mm$, $M_\infty=8.2$, $Re_\infty/m=9.35x10^6$

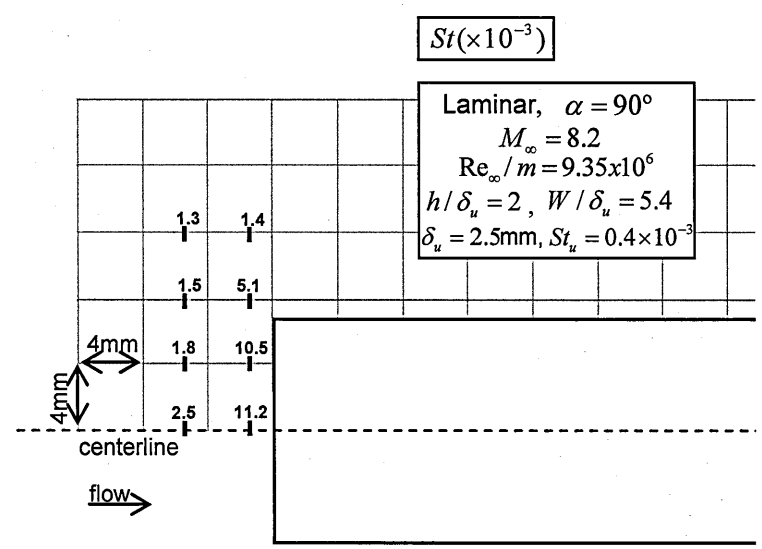

Figure A.24 Heat flux measurements: laminar flow, $\alpha=90°$, $\delta_u=2.5mm$, $M_\infty=8.2$, $Re_\infty/m=9.35x10^6$.

A.3.14 Laminar flow, α=135°, δ_u=2.5mm, M_∞=8.2, Re_∞/m=9.35x10^6

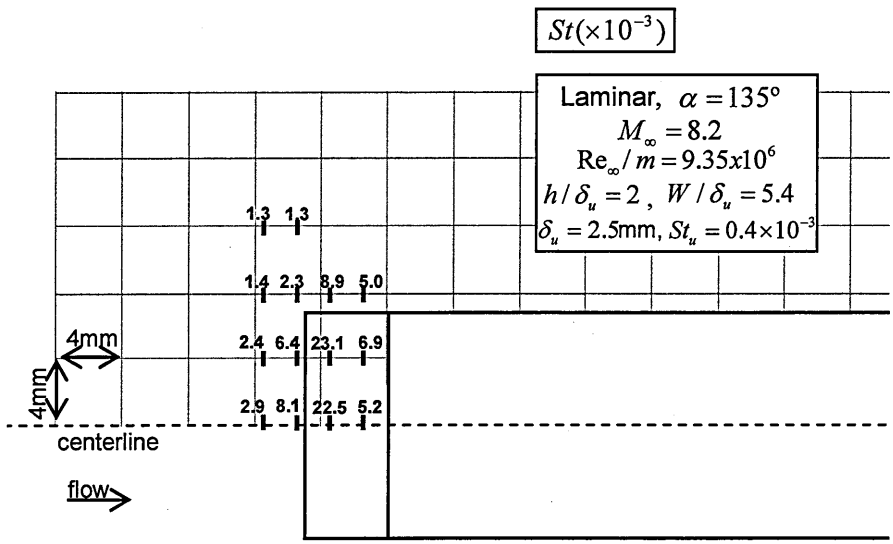

Figure A.25 Heat flux measurements: laminar flow, α=135°, δ_u=2.5mm, M_∞=8.2, Re_∞/m=9.35x10^6.

A.3.15 Turbulent flow, α=30°, δ_u=5mm, M_∞=8.2, Re_∞/m=8.06x10^6

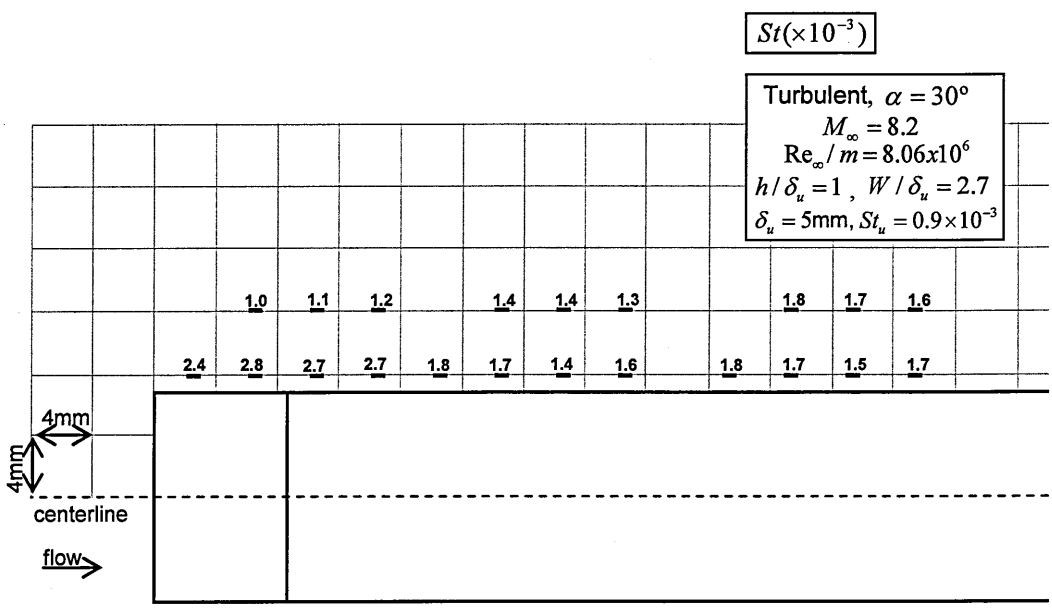

Figure A.26 Heat flux measurements: turbulent flow, α=30°, δ_u=5mm, M_∞=8.2, Re_∞/m=8.06x10^6.

A.3.16 Turbulent flow, α=45°, δ_u=5mm, M_∞=8.2, Re_∞/m=8.06x10^6

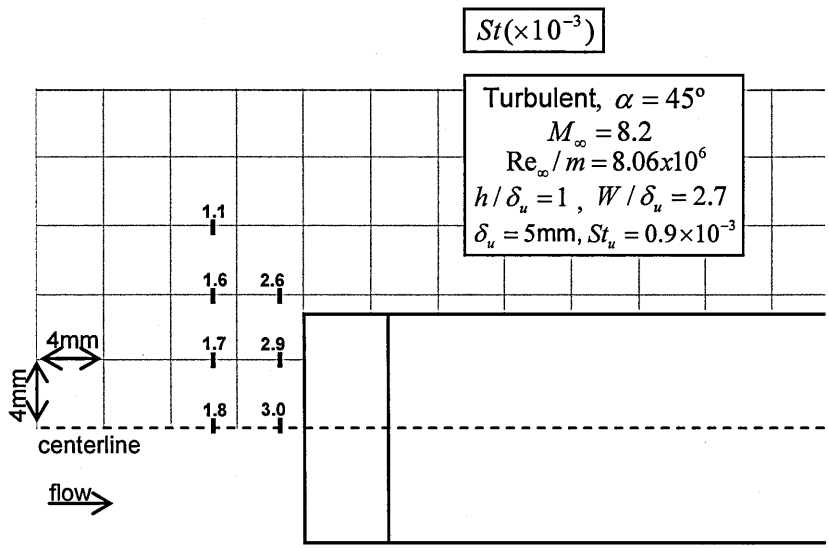

Figure A.27 Heat flux measurements: turbulent flow, α=45°, δ_u=5mm, M_∞=8.2, Re_∞/m=8.06x10^6.

A.3.17 Turbulent flow, α=60°, δ_u=5mm, M_∞=8.2, Re_∞/m=8.06x10^6

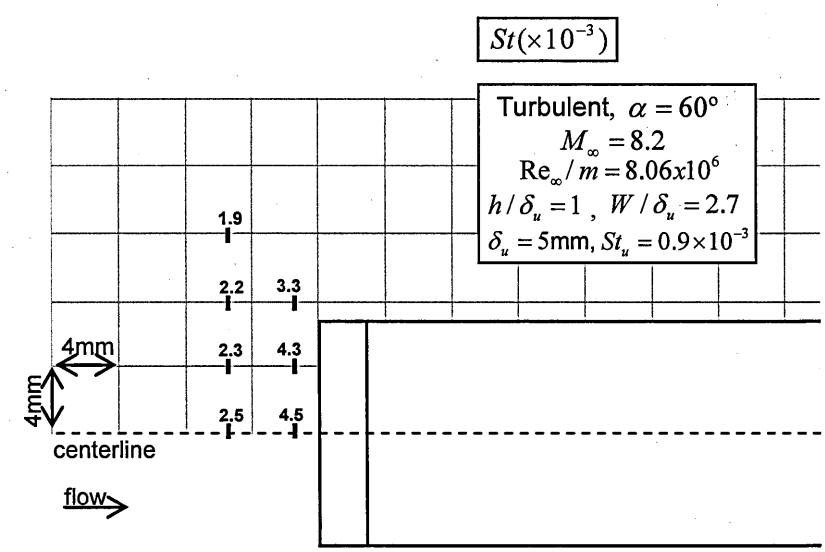

Figure A.28 Heat flux measurements: turbulent flow, α=60°, δ_u=5mm, M_∞=8.2, Re_∞/m=8.06x10^6.

A.3.18 Turbulent flow, α=90°, δ_u=5mm, M_∞=8.2, Re_∞/m=8.06x10^6

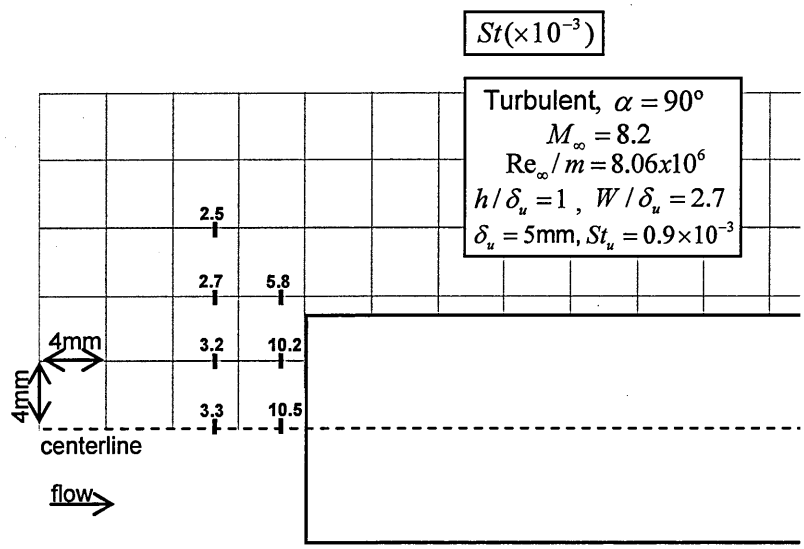

Figure A.29 Heat flux measurements: turbulent flow, α=90°, δ_u=5mm, M_∞=8.2, Re_∞/m=8.06x10^6.

A.3.19 Turbulent flow, α=135°, δ_u=5mm, M_∞=8.2, Re_∞/m=8.06x10^6

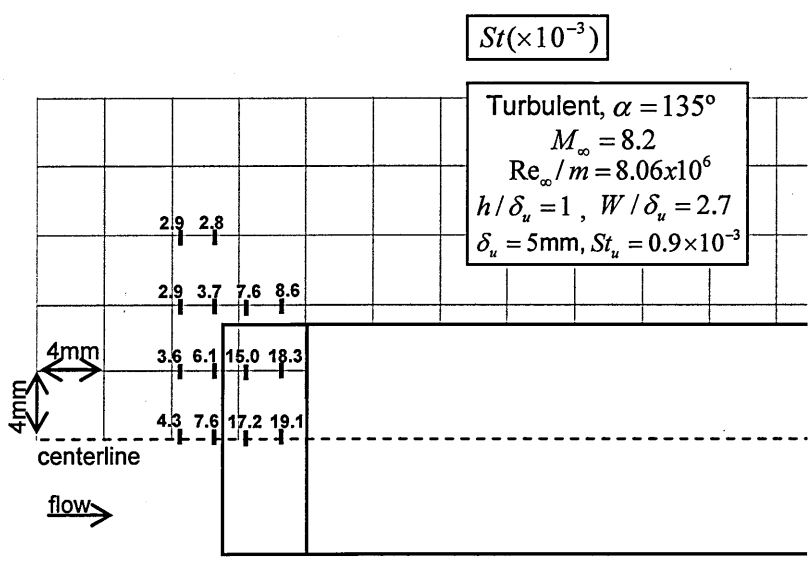

Figure A.30 Heat flux measurements: turbulent flow, α=135°, δ_u=5mm, M_∞=8.2, Re_∞/m=8.06x10^6.

A.3.20 Transitional flow, α=30°, δ_u=5mm, M_∞=8.2, Re_∞/m=6.57x10^6

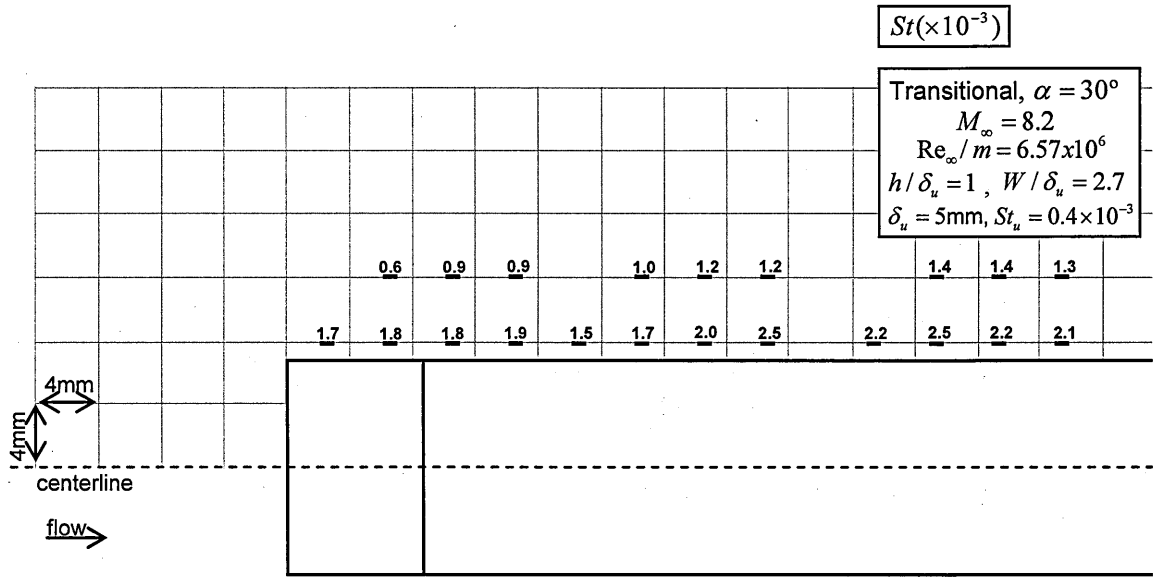

Figure A.31 Heat flux measurements: transitional flow, α=30°, δ_u=5mm, M_∞=8.2, Re_∞/m=6.57x10^6.

A.3.21 Transitional flow, α=45°, δ_u=5mm, M_∞=8.2, Re_∞/m=6.57x10^6

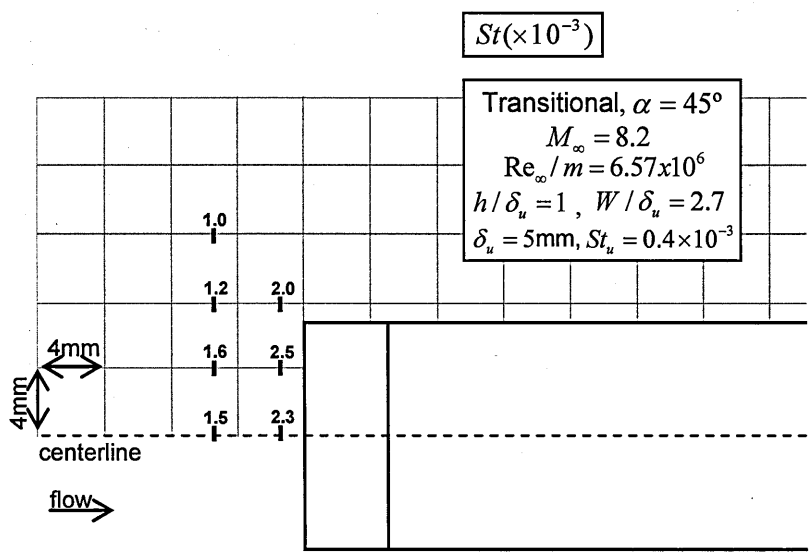

Figure A.32 Heat flux measurements: transitional flow, α=45°, δ_u=5mm, M_∞=8.2, Re_∞/m=6.57x10^6.

A.3.22 Transitional flow, α=60°, δ_u=5mm, M_∞=8.2, Re_∞/m=6.57x10^6

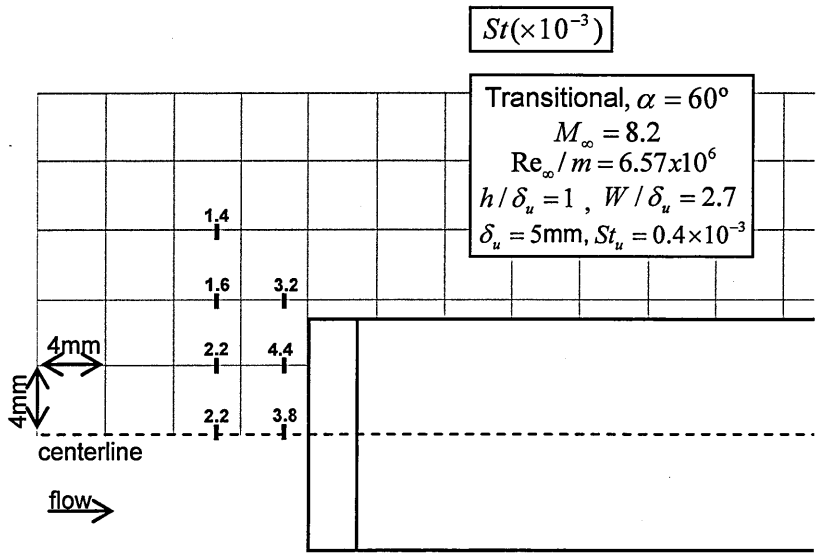

Figure A.33 Heat flux measurements: transitional flow, α=60°, δ_u=5mm, M_∞=8.2, Re_∞/m=6.57x10^6.

A.3.23 Transitional flow, α=90°, δ_u=5mm, M_∞=8.2, Re_∞/m=6.57x10^6

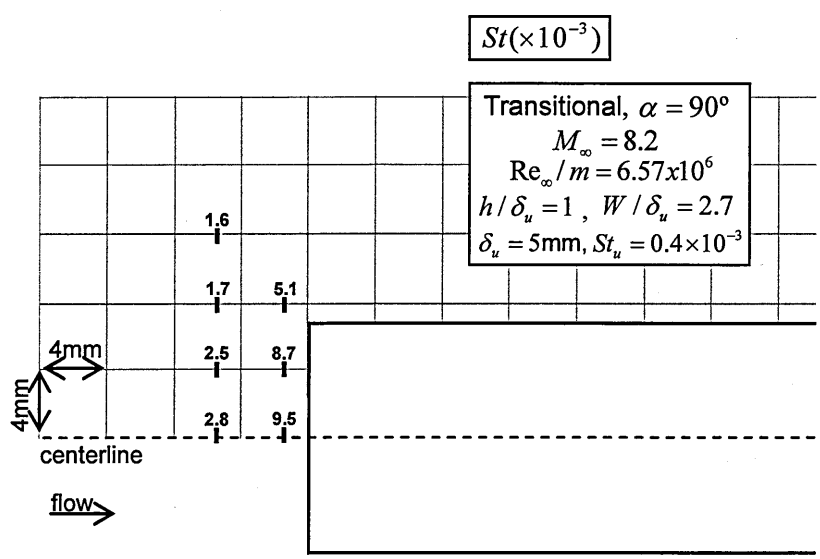

Figure A.34 Heat flux measurements: transitional flow, α=90°, δ_u=5mm, M_∞=8.2, Re_∞/m=6.57x10^6.

A.3.24 Transitional flow, α=135°, δ_u=5mm, M_∞=8.2, Re_∞/m=6.57x10^6

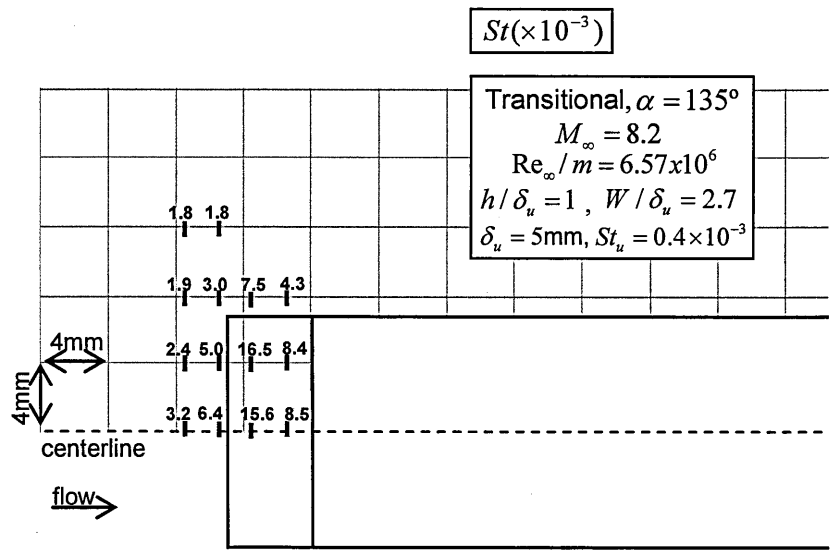

Figure A.35 Heat flux measurements: transitional flow, α=135°, δ_u=5mm, M_∞=8.2, Re_∞/m=6.57x10^6.

A.3.25 Turbulent flow, α=15°, δ_u=6mm, M_∞=12.3, Re_∞/m=3.35x10^6

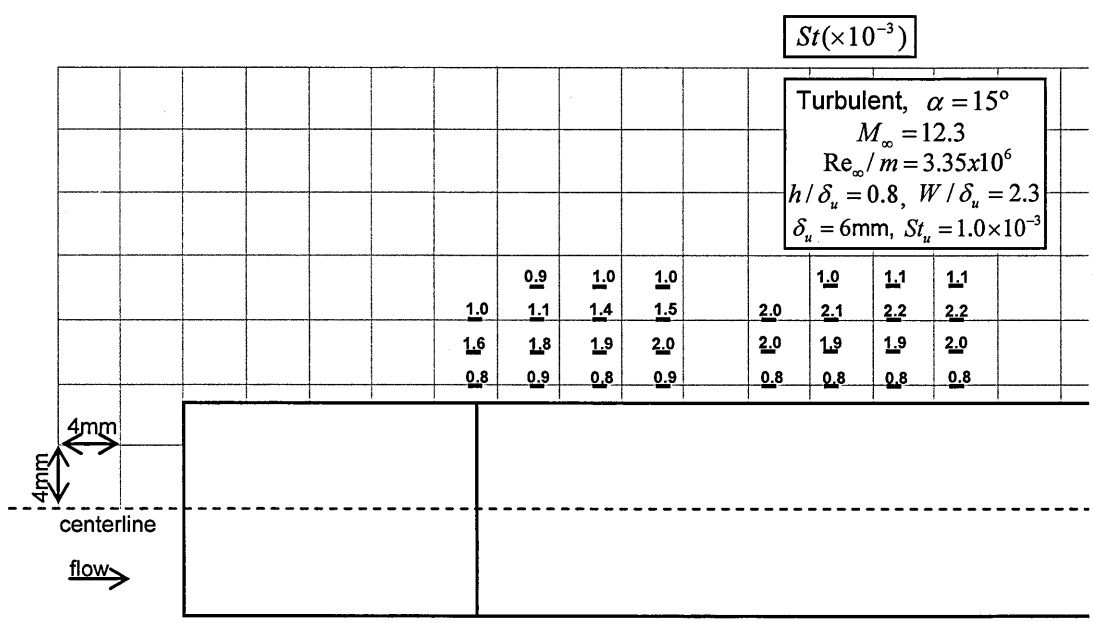

Figure A.36 Heat flux measurements: turbulent flow, α=15°, δ_u=6mm, M_∞=12.3, Re_∞/m=3.35x10^6.

A.3.26 Turbulent flow, α=30°, δ_u=6mm, M_∞=12.3, Re_∞/m=3.35x10^6

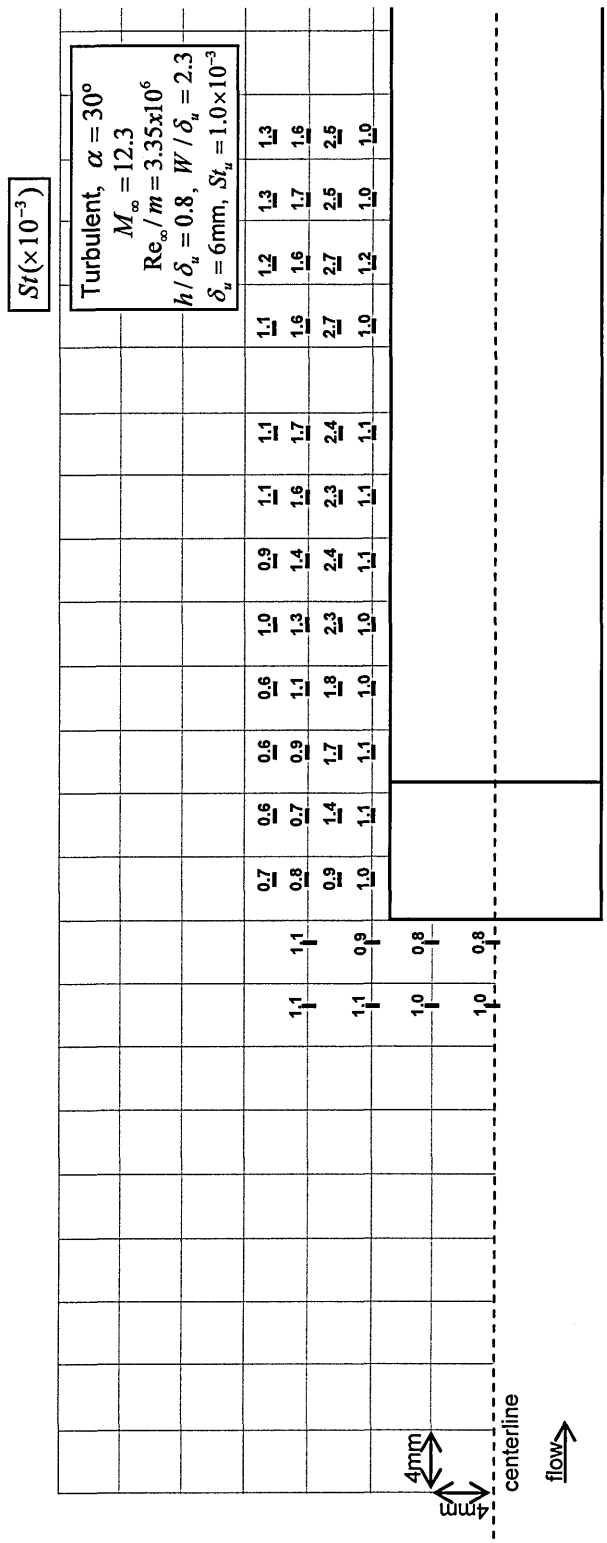

Figure A.37 Heat flux measurements: turbulent flow, α=30°, δ_u=6mm, M_∞=12.3, Re_∞/m=3.35x10^6.

A.3.27 Turbulent flow, α=45°, δ_u=6mm, M_∞=12.3, Re_∞/m=3.35x10^6

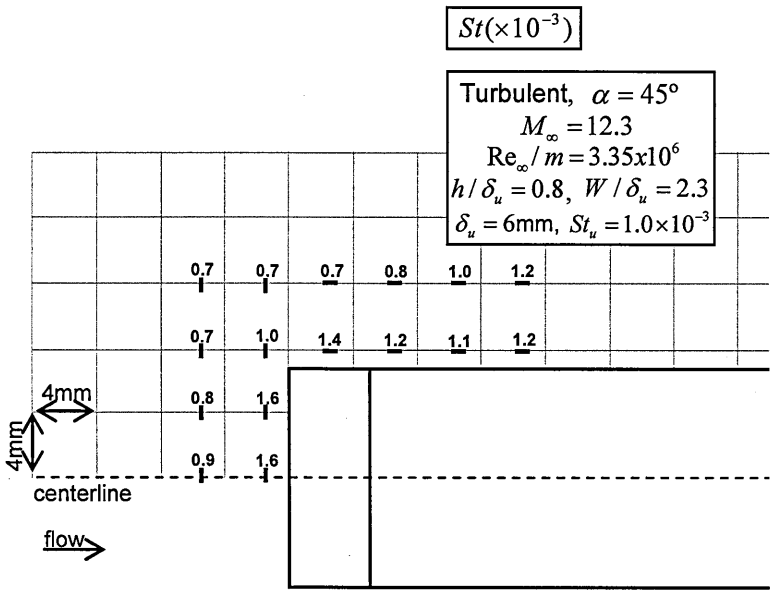

Figure A.38 Heat flux measurements: turbulent flow, α=45°, δ_u=6mm, M_∞=12.3, Re_∞/m=3.35x10^6.

A.3.28 Turbulent flow, α=60°, δ_u=6mm, M_∞=12.3, Re_∞/m=3.35x10^6

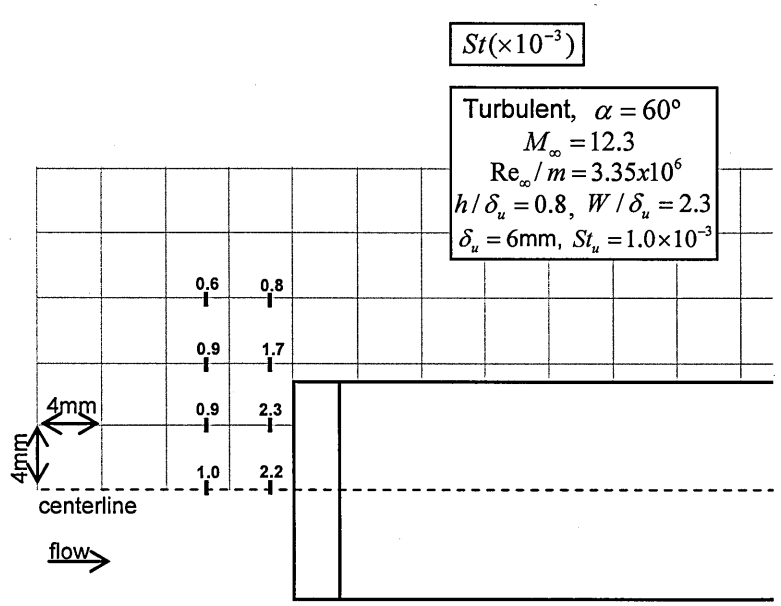

Figure A.39 Heat flux measurements: turbulent flow, α=60°, δ_u=6mm, M_∞=12.3, Re_∞/m=3.35x10^6.

A.3.29 Turbulent flow, α=90°, δ_u=6mm, M_∞=12.3, Re_∞/m=3.35x10^6

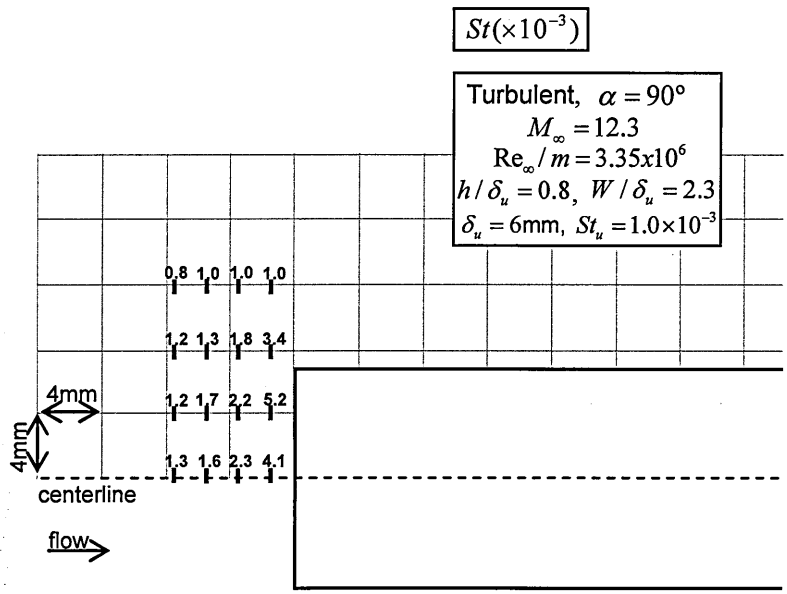

Figure A.40 Heat flux measurements: turbulent flow, α=90°, δ_u=6mm, M_∞=12.3, Re_∞/m=3.35x10^6.

A.3.30 Turbulent flow, α=135°, δ_u=6mm, M_∞=12.3, Re_∞/m=3.35x10^6

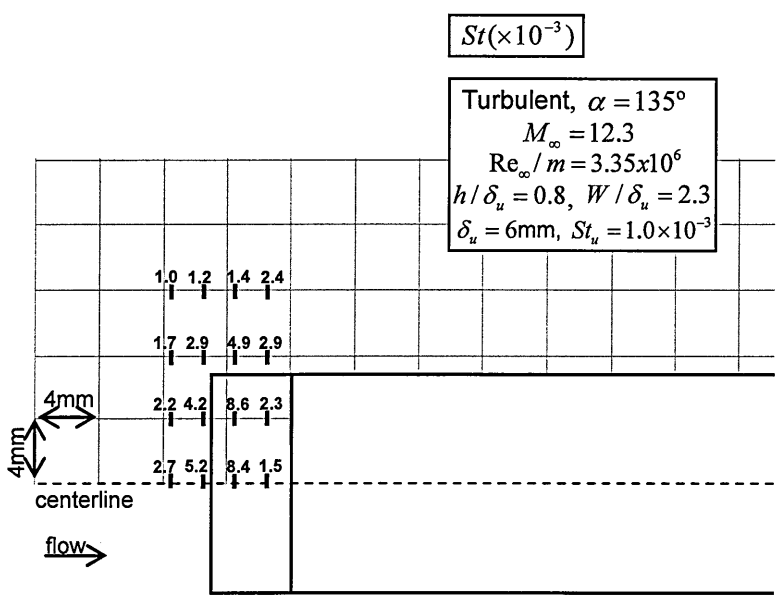

Figure A.41 Heat flux measurements: turbulent flow, α=135°, δ_u=6mm, M_∞=12.3, Re_∞/m=3.35x10^6.

A.4 Tables of heat flux measurements

The heat flux measurements obtained in the vicinity of the generic surface protuberances are listed. The longitudinal and lateral location of the measurements with respect to the protuberance are based on the coordinate system in Fig. A.42. The heat transfer rate is provided in dimensional form (W/cm^2) and as Stanton number. The heat flux augmentation with respect to the undisturbed heating is also indicated as St/St_u. The height and width of the protuberance was h=5mm and W=13.5mm for all the tests except in the study of h/δ_u and W/δ_u effects as further shown in Chapter 3. The reference location (x_k, y_{cl}) is based on the centre of the rectangular measurement area, which as previously explained corresponds to the thin film element of the gauges with dimensions 1.2mm x 0.3mm.

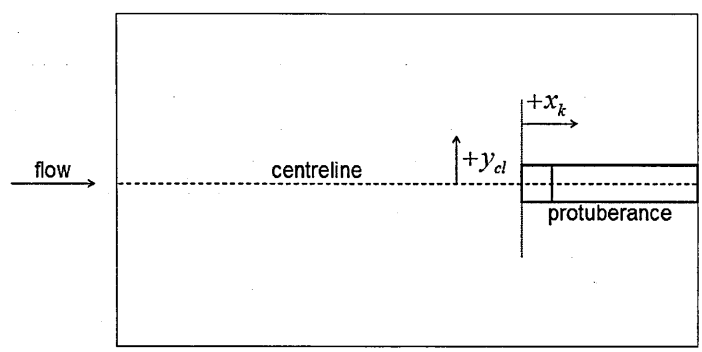

Fig. A.42 Coordinate system.

A.4.1 Turbulent flow, $\alpha=15^o$, $\delta_u=5mm$, $M_\infty=8.2$, $Re_\infty/m=9.35x10^6$

x_k (mm)	y_{cl} (mm)	q (W/cm^2)	St ($x10^3$)	St/St_u
-5.5	0	7.3	1.3	1.3
-1.5	0	5.1	0.9	0.9
-5.5	4	6.7	1.2	1.2
-1.5	4	4.8	0.8	0.8
-5.5	8	6.3	1.1	1.1
-1.5	8	5.9	1.0	1.0
2.5	8	4.7	0.8	0.8
6.5	8	8.7	1.5	1.5
10.5	8	10.9	1.9	1.9
14.5	8	14.6	2.5	2.5
18.5	8	10.9	1.9	1.9
22.5	8	10.2	1.8	1.8
26.5	8	7.8	1.4	1.4
30.5	8	9.0	1.6	1.6

37.5	8	8.3	1.4	1.4
41.5	8	7.4	1.3	1.3
45.5	8	6.8	1.2	1.2
49.5	8	6.7	1.2	1.2
2.5	10	5.5	1.0	1.0
6.5	10	5.6	1.0	1.0
10.5	10	6.0	1.0	1.0
14.5	10	6.7	1.2	1.2
18.5	10	7.6	1.3	1.3
22.5	10	8.5	1.5	1.5
26.5	10	8.7	1.5	1.5
30.5	10	9.5	1.7	1.7
-5.5	12	4.9	0.9	0.9
-1.5	12	5.9	1.0	1.0
2.5	12	5.7	1.0	1.0
6.5	12	5.2	0.9	0.9
10.5	12	5.3	0.9	0.9
14.5	12	4.9	0.8	0.8
18.5	12	6.4	1.1	1.1
22.5	12	6.9	1.2	1.2
26.5	12	7.5	1.3	1.3
30.5	12	7.1	1.2	1.2
37.5	12	8.2	1.4	1.4
41.5	12	7.6	1.3	1.3
45.5	12	7.5	1.3	1.3
49.5	12	6.7	1.2	1.2
2.5	14	6.6	1.1	1.1
6.5	14	6.4	1.1	1.1
10.5	14	6.0	1.0	1.0
14.5	14	5.7	1.0	1.0
18.5	14	5.0	0.9	0.9
22.5	14	6.6	1.2	1.2
26.5	14	6.2	1.1	1.1
30.5	14	6.0	1.0	1.0

Table A.2 Heat flux measurements: turbulent flow, α=15°, δ_u=5mm, M_∞=8.2, $Re_\infty/m=9.35x10^6$.

A.4.2 Turbulent flow, α=30°, δ_u=5mm, M_∞=8.2, $Re_\infty/m=9.35x10^6$

x_k (mm)	y_{cl} (mm)	q (W/cm^2)	St (x10^3)	St/St$_u$
-7.5	0	6.6	1.1	1.1
-5.5	0	4.9	0.9	0.9
-3.5	0	4.6	0.8	0.8
-1.5	0	5.4	0.9	0.9
-7.5	4	6.7	1.2	1.2
-5.5	4	5.0	0.9	0.9
-3.5	4	4.4	0.8	0.8
-1.5	4	5.1	0.9	0.9
-7.5	8	6.5	1.1	1.1
-5.5	8	5.6	1.0	1.0
-3.5	8	5.2	0.9	0.9
-1.5	8	4.5	0.8	0.8
2.5	8	12.3	2.1	2.1

6.5	8	16.1	2.8	2.8
10.5	8	17.0	2.9	2.9
14.5	8	14.6	2.5	2.5
18.5	8	12.0	2.1	2.1
22.5	8	10.9	1.9	1.9
26.5	8	11.3	2.0	2.0
30.5	8	10.4	1.8	1.8
37.5	8	7.9	1.4	1.4
41.5	8	7.1	1.2	1.2
45.5	8	7.4	1.3	1.3
49.5	8	7.0	1.2	1.2
2.5	10	5.2	0.9	0.9
6.5	10	6.3	1.1	1.1
10.5	10	8.2	1.4	1.4
14.5	10	9.4	1.6	1.6
18.5	10	10.1	1.8	1.8
22.5	10	9.9	1.7	1.7
26.5	10	7.3	1.3	1.3
30.5	10	10.1	1.8	1.8
-7.5	12	5.8	1.0	1.0
-5.5	12	5.6	1.0	1.0
-3.5	12	6.4	1.1	1.1
-1.5	12	5.8	1.0	1.0
2.5	12	5.7	1.0	1.0
6.5	12	5.6	1.0	1.0
10.5	12	6.3	1.1	1.1
14.5	12	6.6	1.1	1.1
18.5	12	7.5	1.3	1.3
22.5	12	7.9	1.4	1.4
26.5	12	8.7	1.5	1.5
30.5	12	8.3	1.4	1.4
37.5	12	8.4	1.5	1.5
41.5	12	8.1	1.4	1.4
45.5	12	8.7	1.5	1.5
49.5	12	8.0	1.4	1.4
2.5	14	6.2	1.1	1.1
6.5	14	5.9	1.0	1.0
10.5	14	5.7	1.0	1.0
14.5	14	5.7	1.0	1.0
18.5	14	7.2	1.2	1.2
22.5	14	7.3	1.3	1.3
26.5	14	7.6	1.3	1.3
30.5	14	7.3	1.3	1.3

Table A.3 Heat flux measurements: turbulent flow, $\alpha=30°$, $\delta_u=5mm$, $M_\infty=8.2$, $Re_\infty/m=9.35x10^6$.

A.4.3 Turbulent flow, $\alpha=45°$, $\delta_u=5mm$, $M_\infty=8.2$, $Re_\infty/m=9.35x10^6$

x_k (mm)	y_{cl} (mm)	q (W/cm^2)	St (x10^3)	St/St$_u$
-7.5	0	8.1	1.4	1.4
-5.5	0	10.7	1.9	1.9
-3.5	0	12.7	2.2	2.2
-1.5	0	18.6	3.2	3.2

-7.5	4	8.6	1.5	1.5
-5.5	4	11.3	2.0	2.0
-3.5	4	14.1	2.4	2.4
-1.5	4	19.2	3.3	3.3
-7.5	8	7.0	1.2	1.2
-5.5	8	8.9	1.5	1.5
-3.5	8	10.7	1.9	1.9
-1.5	8	12.6	2.2	2.2
2.5	8	18.3	3.2	3.2
6.5	8	16.7	2.9	2.9
10.5	8	14.1	2.4	2.4
14.5	8	12.8	2.2	2.2
18.5	8	10.7	1.9	1.9
22.5	8	9.6	1.7	1.7
26.5	8	8.7	1.5	1.5
30.5	8	8.7	1.5	1.5
37.5	8	6.2	1.1	1.1
41.5	8	5.7	1.0	1.0
45.5	8	5.0	0.9	0.9
49.5	8	5.1	0.9	0.9
2.5	10	16.0	2.8	2.8
6.5	10	19.0	3.3	3.3
10.5	10	16.3	2.8	2.8
14.5	10	13.9	2.4	2.4
18.5	10	13.8	2.4	2.4
22.5	10	13.5	2.3	2.3
26.5	10	12.1	2.1	2.1
30.5	10	11.2	2.0	2.0
-7.5	12	4.3	0.8	0.8
-5.5	12	4.7	0.8	0.8
-3.5	12	7.0	1.2	1.2
-1.5	12	8.6	1.5	1.5
2.5	12	9.1	1.6	1.6
6.5	12	9.1	1.6	1.6
10.5	12	11.6	2.0	2.0
14.5	12	11.0	1.9	1.9
18.5	12	11.7	2.0	2.0
22.5	12	10.6	1.8	1.8
26.5	12	10.1	1.8	1.8
30.5	12	8.8	1.5	1.5
37.5	12	9.8	1.7	1.7
41.5	12	9.1	1.6	1.6
45.5	12	9.1	1.6	1.6
49.5	12	8.1	1.4	1.4
2.5	14	9.4	1.6	1.6
6.5	14	9.6	1.7	1.7
10.5	14	9.3	1.6	1.6
14.5	14	8.9	1.6	1.6
18.5	14	10.5	1.8	1.8
22.5	14	10.1	1.8	1.8
26.5	14	9.9	1.7	1.7
30.5	14	9.3	1.6	1.6

Table A.4 Heat flux measurements: turbulent flow, $\alpha=45°$, $\delta_u=5mm$, $M_\infty=8.2$, $Re_\infty/m=9.35x10^6$.

A.4.4 Turbulent flow, $\alpha=60°$, $\delta_u=5mm$, $M_\infty=8.2$, $Re_\infty/m=9.35x10^6$

x_k (mm)	y_{cl} (mm)	q (W/cm^2)	St ($x10^3$)	St/St_u
-28.5	0	5.6	1.0	1.0
-24.5	0	5.6	1.0	1.0
-19.5	0	4.6	0.8	0.8
-15.5	0	7.1	1.2	1.2
-7.5	0	14.2	2.5	2.5
-5.5	0	16.4	2.8	2.8
-3.5	0	19.7	3.4	3.4
-1.5	0	31.9	5.6	5.6
-28.5	4	7.2	1.3	1.3
-24.5	4	6.2	1.1	1.1
-19.5	4	6.0	1.0	1.0
-15.5	4	7.2	1.2	1.2
-7.5	4	13.6	2.4	2.4
-5.5	4	15.7	2.7	2.7
-3.5	4	19.2	3.3	3.3
-1.5	4	31.4	5.5	5.5
-28.5	8	5.6	1.0	1.0
-24.5	8	6.2	1.1	1.1
-19.5	8	5.1	0.9	0.9
-15.5	8	5.9	1.0	1.0
-7.5	8	13.2	2.3	2.3
-5.5	8	14.5	2.5	2.5
-3.5	8	15.5	2.7	2.7
-1.5	8	21.0	3.6	3.6
2.5	8	17.1	3.0	3.0
6.5	8	14.2	2.5	2.5
10.5	8	12.4	2.2	2.2
14.5	8	11.8	2.1	2.1
18.5	8	9.5	1.7	1.7
22.5	8	8.7	1.5	1.5
26.5	8	8.4	1.5	1.5
30.5	8	7.4	1.3	1.3
37.5	8	6.0	1.0	1.0
41.5	8	5.0	0.9	0.9
45.5	8	4.8	0.8	0.8
49.5	8	4.5	0.8	0.8
2.5	10	22.5	3.9	3.9
6.5	10	17.9	3.1	3.1
10.5	10	14.7	2.6	2.6
14.5	10	13.3	2.3	2.3
18.5	10	12.8	2.2	2.2
22.5	10	12.7	2.2	2.2
26.5	10	11.8	2.1	2.1
30.5	10	11.1	1.9	1.9
-28.5	12	3.2	0.6	0.6
-24.5	12	4.5	0.8	0.8
-19.5	12	2.7	0.5	0.5
-15.5	12	3.5	0.6	0.6
-7.5	12	9.4	1.6	1.6
-5.5	12	11.8	2.1	2.1
-3.5	12	13.7	2.4	2.4
-1.5	12	13.4	2.3	2.3

2.5	12	14.8	2.6	2.6
6.5	12	14.9	2.6	2.6
10.5	12	14.6	2.5	2.5
14.5	12	12.0	2.1	2.1
18.5	12	10.6	1.8	1.8
22.5	12	9.5	1.6	1.6
26.5	12	9.6	1.7	1.7
30.5	12	8.6	1.5	1.5
37.5	12	8.8	1.5	1.5
41.5	12	8.3	1.4	1.4
45.5	12	8.8	1.5	1.5
49.5	12	7.9	1.4	1.4
2.5	14	11.7	2.0	2.0
6.5	14	10.8	1.9	1.9
10.5	14	11.5	2.0	2.0
14.5	14	10.6	1.8	1.8
18.5	14	11.3	2.0	2.0
22.5	14	10.2	1.8	1.8
26.5	14	9.5	1.6	1.6
30.5	14	8.7	1.5	1.5

Table A.5 Heat flux measurements: turbulent flow, $\alpha=60°$, $\delta_u=5mm$, $M_\infty=8.2$, $Re_\infty/m=9.35x10^6$.

A.4.5 Turbulent flow, $\alpha=90°$, $\delta_u=5mm$, $M_\infty=8.2$, $Re_\infty/m=9.35x10^6$

x_k (mm)	y_{cl} (mm)	q (W/cm^2)	St (x10^3)	St/St$_u$
-28.5	0	5.0	0.9	0.9
-24.5	0	5.2	0.9	0.9
-19.5	0	8.4	1.5	1.5
-15.5	0	11.6	2.0	2.0
-7.5	0	20.9	3.6	3.6
-5.5	0	23.3	4.1	4.1
-3.5	0	25.6	4.4	4.4
-1.5	0	64.6	11.2	11.2
-28.5	4	6.9	1.2	1.2
-24.5	4	5.6	1.0	1.0
-19.5	4	9.5	1.7	1.7
-15.5	4	12.8	2.2	2.2
-7.5	4	19.3	3.3	3.3
-5.5	4	20.8	3.6	3.6
-3.5	4	28.2	4.9	4.9
-1.5	4	62.8	10.9	10.9
-28.5	8	5.7	1.0	1.0
-24.5	8	5.6	1.0	1.0
-19.5	8	7.2	1.3	1.3
-15.5	8	11.6	2.0	2.0
-7.5	8	18.3	3.2	3.2
-5.5	8	18.8	3.3	3.3
-3.5	8	18.4	3.2	3.2
-1.5	8	40.9	7.1	7.1
2.5	8	10.7	1.9	1.9

6.5	8	10.9	1.9	1.9
10.5	8	10.1	1.8	1.8
14.5	8	10.1	1.8	1.8
18.5	8	9.0	1.6	1.6
22.5	8	8.4	1.5	1.5
26.5	8	8.4	1.5	1.5
30.5	8	7.6	1.3	1.3
37.5	8	5.4	0.9	0.9
41.5	8	4.6	0.8	0.8
45.5	8	4.5	0.8	0.8
49.5	8	4.4	0.8	0.8
2.5	10	19.0	3.3	3.3
6.5	10	12.7	2.2	2.2
10.5	10	11.4	2.0	2.0
14.5	10	11.4	2.0	2.0
18.5	10	10.3	1.8	1.8
22.5	10	10.6	1.8	1.8
26.5	10	10.4	1.8	1.8
30.5	10	9.8	1.7	1.7
-28.5	12	3.4	0.6	0.6
-24.5	12	4.3	0.8	0.8
-19.5	12	3.7	0.6	0.6
-15.5	12	7.8	1.4	1.4
-7.5	12	15.3	2.6	2.6
-5.5	12	16.2	2.8	2.8
-3.5	12	16.5	2.9	2.9
-1.5	12	16.0	2.8	2.8
2.5	12	17.4	3.0	3.0
6.5	12	13.5	2.4	2.4
10.5	12	11.7	2.0	2.0
14.5	12	9.4	1.6	1.6
18.5	12	9.0	1.6	1.6
22.5	12	8.3	1.4	1.4
26.5	12	8.7	1.5	1.5
30.5	12	8.0	1.4	1.4
37.5	12	8.3	1.4	1.4
41.5	12	7.9	1.4	1.4
45.5	12	8.4	1.5	1.5
49.5	12	7.8	1.4	1.4
2.5	14	14.6	2.5	2.5
6.5	14	12.9	2.2	2.2
10.5	14	11.7	2.0	2.0
14.5	14	9.6	1.7	1.7
18.5	14	9.6	1.7	1.7
22.5	14	8.7	1.5	1.5
26.5	14	8.1	1.4	1.4
30.5	14	7.4	1.3	1.3

Table A.6 Heat flux measurements: turbulent flow, $\alpha=90°$, $\delta_u=5mm$, $M_\infty=8.2$, $Re_\infty/m=9.35x10^{6.}$

A.4.6 Turbulent flow, $\alpha=135^{o}$, $\delta_u=5mm$, $M_\infty=8.2$, $Re_\infty/m=9.35x10^6$

x_k (mm)	y_{cl} (mm)	q (W/cm^2)	St (x10^3)	St/St$_u$
-28.5	0	5.1	0.9	0.9
-24.5	0	7.1	1.2	1.2
-19.5	0	12.8	2.2	2.2
-15.5	0	15.4	2.7	2.7
-7.5	0	23.0	4.0	4.0
-5.5	0	35.9	6.2	6.2
-3.5	0	90.4	15.7	15.7
-1.5	0	91.3	15.9	15.9
-28.5	4	6.3	1.1	1.1
-24.5	4	7.3	1.3	1.3
-19.5	4	13.9	2.4	2.4
-15.5	4	18.3	3.2	3.2
-7.5	4	21.1	3.7	3.7
-5.5	4	34.1	5.9	5.9
-3.5	4	92.4	16.1	16.1
-1.5	4	97.4	16.9	16.9
-28.5	8	5.2	0.9	0.9
-24.5	8	6.2	1.1	1.1
-19.5	8	9.9	1.7	1.7
-15.5	8	13.8	2.4	2.4
-7.5	8	19.5	3.4	3.4
-5.5	8	22.6	3.9	3.9
-3.5	8	46.0	8.0	8.0
-1.5	8	68.4	11.9	11.9
2.5	8	2.3	0.4	0.4
6.5	8	8.0	1.4	1.4
10.5	8	10.2	1.8	1.8
14.5	8	10.7	1.9	1.9
18.5	8	9.6	1.7	1.7
22.5	8	9.6	1.7	1.7
26.5	8	8.9	1.5	1.5
30.5	8	9.1	1.6	1.6
37.5	8	7.3	1.3	1.3
41.5	8	7.0	1.2	1.2
45.5	8	6.2	1.1	1.1
49.5	8	6.3	1.1	1.1
2.5	10	7.2	1.3	1.3
6.5	10	4.0	0.7	0.7
10.5	10	3.5	0.6	0.6
14.5	10	4.9	0.9	0.9
-28.5	12	3.2	0.6	0.6
-24.5	12	4.2	0.7	0.7
-19.5	12	6.1	1.1	1.1
-15.5	12	11.4	2.0	2.0
-7.5	12	16.6	2.9	2.9
-5.5	12	14.3	2.5	2.5
-3.5	12	16.8	2.9	2.9
-1.5	12	20.0	3.5	3.5
2.5	12	14.7	2.6	2.6
6.5	12	9.8	1.7	1.7
10.5	12	7.9	1.4	1.4
14.5	12	6.2	1.1	1.1

18.5	12	6.4	1.1	1.1
22.5	12	5.7	1.0	1.0
26.5	12	5.4	0.9	0.9
30.5	12	4.7	0.8	0.8
37.5	12	5.0	0.9	0.9
41.5	12	5.1	0.9	0.9
45.5	12	5.5	1.0	1.0
49.5	12	5.1	0.9	0.9
2.5	14	15.1	2.6	2.6
6.5	14	12.7	2.2	2.2
10.5	14	10.5	1.8	1.8
14.5	14	8.1	1.4	1.4
1	24	11.7	2.0	2.0
5	24	10.4	1.8	1.8
9	24	8.9	1.5	1.5
13	24	8.2	1.4	1.4
1	28	11.9	2.1	2.1
5	28	10.7	1.9	1.9
9	28	10.0	1.7	1.7
13	28	8.3	1.4	1.4

Table A.7 Heat flux measurements: turbulent flow, $\alpha=135°$, $\delta_u=5mm$, $M_\infty=8.2$, $Re_\infty/m=9.35x10^6$.

A.4.7 Turbulent flow, $\alpha=30°$, $\delta_u=5mm$, $h/\delta_u x2$, $M_\infty=8.2$, $Re_\infty/m=9.35x10^6$

x_k (mm)	y_{cl} (mm)	q (W/cm^2)	St (x10^3)	St/St$_u$
-7.5	0	6.5	1.1	1.1
-5.5	0	5.1	0.9	0.9
-3.5	0	4.6	0.8	0.8
-1.5	0	5.3	0.9	0.9
-7.5	4	6.4	1.1	1.1
-5.5	4	5.6	1.0	1.0
-3.5	4	4.3	0.7	0.7
-1.5	4	5.4	0.9	0.9
-7.5	8	6.4	1.1	1.1
-5.5	8	6.0	1.0	1.0
-3.5	8	5.1	0.9	0.9
-1.5	8	4.5	0.8	0.8
2.5	8	11.4	2.0	2.0
6.5	8	14.9	2.6	2.6
10.5	8	15.1	2.6	2.6
14.5	8	14.0	2.4	2.4
18.5	8	11.9	2.1	2.1
22.5	8	10.2	1.8	1.8
26.5	8	10.1	1.8	1.8
30.5	8	8.9	1.5	1.5
37.5	8	8.3	1.4	1.4
41.5	8	7.5	1.3	1.3
45.5	8	7.8	1.4	1.4
49.5	8	7.6	1.3	1.3
-7.5	12	5.9	1.0	1.0
-5.5	12	5.7	1.0	1.0
-3.5	12	6.4	1.1	1.1

-1.5	12	6.1	1.1	1.1
2.5	12	5.1	0.9	0.9
6.5	12	5.2	0.9	0.9
10.5	12	6.0	1.0	1.0
14.5	12	6.4	1.1	1.1
18.5	12	7.8	1.4	1.4
22.5	12	8.2	1.4	1.4
26.5	12	9.0	1.6	1.6
30.5	12	8.1	1.4	1.4
37.5	12	7.8	1.4	1.4
41.5	12	7.4	1.3	1.3
45.5	12	7.8	1.3	1.3
49.5	12	7.1	1.2	1.2

Table A.8 Heat flux measurements: turbulent flow, $\alpha=30°$, $\delta_u=5mm$, $h/\delta_u x2$, $M_\infty=8.2$, $Re_\infty/m=9.35x10^6$.

A.4.8 Turbulent flow, $\alpha=30°$, $\delta_u=5mm$, $W/\delta_u x2$, $M_\infty=8.2$, $Re_\infty/m=9.35x10^6$

x_k (mm)	y_{cl} (mm)	q (W/cm^2)	St ($x10^3$)	St/St_u
-5.5	0	5.5	1.0	1.0
-1.5	0	5.5	1.0	1.0
-5.5	4	5.0	0.9	0.9
-1.5	4	5.8	1.0	1.0
-5.5	8	4.9	0.8	0.8
-1.5	8	5.9	1.0	1.0
-5.5	12	4.2	0.7	0.7
-1.5	12	5.3	0.9	0.9
2.5	14.75	12.8	2.2	2.2
6.5	14.75	15.8	2.7	2.7
10.5	14.75	12.9	2.2	2.2
14.5	14.75	14.0	2.4	2.4
18.5	14.75	12.0	2.1	2.1
22.5	14.75	10.7	1.9	1.9
26.5	14.75	8.7	1.5	1.5
30.5	14.75	10.1	1.8	1.8
37.5	14.75	10.0	1.7	1.7
41.5	14.75	9.2	1.6	1.6
45.5	14.75	8.8	1.5	1.5
49.5	14.75	8.7	1.5	1.5
2.5	18.75	5.6	1.0	1.0
6.5	18.75	5.5	1.0	1.0
10.5	18.75	6.2	1.1	1.1
14.5	18.75	5.9	1.0	1.0
18.5	18.75	7.8	1.4	1.4
22.5	18.75	7.8	1.4	1.4
26.5	18.75	8.1	1.4	1.4
30.5	18.75	7.1	1.2	1.2
37.5	18.75	9.1	1.6	1.6
41.5	18.75	8.5	1.5	1.5
45.5	18.75	8.7	1.5	1.5
49.5	18.75	7.8	1.4	1.4

Table A.9 Heat flux measurements: turbulent flow, $\alpha=30°$, $\delta_u=5mm$, $W/\delta_u x2$, $M_\infty=8.2$, $Re_\infty/m=9.35x10^6$.

A.4.9 Laminar flow, $\alpha=30°$, $\delta_u=2.5mm$, $M_\infty=8.2$, $Re_\infty/m=9.35x10^6$

x_k (mm)	y_{cl} (mm)	q (W/cm^2)	St ($x10^3$)	St/St_u
-5.5	0	4.1	0.7	1.8
-1.5	0	6.2	1.1	2.7
-5.5	4	3.8	0.7	1.7
-1.5	4	5.3	0.9	2.3
-5.5	8	3.8	0.7	1.6
-1.5	8	4.3	0.7	1.8
2.5	8	11.1	1.9	4.8
6.5	8	13.0	2.3	5.7
10.5	8	13.5	2.3	5.9
14.5	8	13.8	2.4	6.0
18.5	8	13.4	2.3	5.8
22.5	8	14.1	2.5	6.1
26.5	8	14.2	2.5	6.2
30.5	8	13.4	2.3	5.8
37.5	8	10.1	1.8	4.4
41.5	8	9.7	1.7	4.2
45.5	8	9.9	1.7	4.3
49.5	8	9.3	1.6	4.0
2.5	10	4.9	0.9	2.1
6.5	10	6.3	1.1	2.7
10.5	10	6.0	1.0	2.6
14.5	10	6.4	1.1	2.8
18.5	10	4.8	0.8	2.1
22.5	10	4.6	0.8	2.0
26.5	10	5.3	0.9	2.3
30.5	10	5.8	1.0	2.5
-5.5	12	2.4	0.4	1.0
-1.5	12	3.0	0.5	1.3
2.5	12	3.0	0.5	1.3
6.5	12	2.7	0.5	1.2
10.5	12	2.9	0.5	1.3
14.5	12	2.8	0.5	1.2
18.5	12	2.6	0.4	1.1
22.5	12	2.5	0.4	1.1
26.5	12	2.8	0.5	1.2
30.5	12	3.0	0.5	1.3
37.5	12	3.2	0.6	1.4
41.5	12	3.3	0.6	1.4
45.5	12	3.9	0.7	1.7
49.5	12	3.9	0.7	1.7
2.5	14	2.4	0.4	1.0
6.5	14	2.2	0.4	1.0
10.5	14	2.2	0.4	1.0
14.5	14	2.0	0.3	0.9
18.5	14	2.1	0.4	0.9
22.5	14	1.9	0.3	0.8
26.5	14	2.0	0.3	0.8
30.5	14	1.8	0.3	0.8

Table A.10 Heat flux measurements: laminar flow, $\alpha=30°$, $\delta_u=2.5mm$, $M_\infty=8.2$, $Re_\infty/m=9.35x10^6$.

A.4.10 Laminar flow, $\alpha=15^{o}$, $\delta_u=2.5mm$, $M_\infty=8.2$, $Re_\infty/m=9.35x10^6$

x_k (mm)	y_{cl} (mm)	q (W/cm^2)	St (x10^3)	St/St$_u$
-5.5	0	1.2	0.2	0.5
-1.5	0	1.5	0.3	0.7
-5.5	4	1.2	0.2	0.5
-1.5	4	1.5	0.3	0.6
-5.5	8	1.1	0.2	0.5
-1.5	8	1.3	0.2	0.6
2.5	8	4.7	0.8	2.1
6.5	8	10.3	1.8	4.5
10.5	8	13.4	2.3	5.8
14.5	8	15.0	2.6	6.5
18.5	8	14.0	2.4	6.1
22.5	8	14.4	2.5	6.2
26.5	8	13.5	2.3	5.9
30.5	8	12.7	2.2	5.5
2.5	10	1.2	0.2	0.5
6.5	10	2.4	0.4	1.0
10.5	10	4.3	0.8	1.9
14.5	10	5.6	1.0	2.4
18.5	10	6.6	1.1	2.9
22.5	10	7.3	1.3	3.2
26.5	10	8.4	1.5	3.6
30.5	10	8.4	1.5	3.6
-5.5	12	1.1	0.2	0.5
-1.5	12	1.1	0.2	0.5
2.5	12	1.6	0.3	0.7
6.5	12	1.6	0.3	0.7
10.5	12	1.7	0.3	0.8
14.5	12	1.6	0.3	0.7
18.5	12	1.6	0.3	0.7
22.5	12	1.7	0.3	0.7
26.5	12	2.2	0.4	1.0
30.5	12	2.4	0.4	1.0
6.5	14	1.2	0.2	0.5
10.5	14	1.2	0.2	0.5
14.5	14	1.3	0.2	0.6
22.5	14	1.4	0.2	0.6
26.5	14	1.5	0.3	0.7
30.5	14	1.5	0.3	0.6

Table A.11 Heat flux measurements: laminar flow, $\alpha=15^{o}$, $\delta_u=2.5mm$, $M_\infty=8.2$, $Re_\infty/m=9.35x10^6$.

A.4.11 Laminar flow, $\alpha=45^{o}$, $\delta_u=2.5mm$, $M_\infty=8.2$, $Re_\infty/m=9.35x10^6$

x_k (mm)	y_{cl} (mm)	q (W/cm^2)	St (x10^3)	St/St$_u$
-5.5	0	7.3	1.3	3.2
-1.5	0	15.4	2.7	6.7
-5.5	4	6.6	1.2	2.9
-1.5	4	13.6	2.4	5.9
-5.5	8	6.4	1.1	2.8
-1.5	8	9.0	1.6	3.9

2.5	8	12.0	2.1	5.2
6.5	8	11.3	2.0	4.9
10.5	8	12.5	2.2	5.4
14.5	8	14.3	2.5	6.2
-5.5	12	4.7	0.8	2.0
-1.5	12	5.1	0.9	2.2
2.5	12	4.0	0.7	1.7
6.5	12	3.4	0.6	1.5
10.5	12	3.2	0.6	1.4
14.5	12	2.7	0.5	1.2

Table A.12 Heat flux measurements: laminar flow, $\alpha=45°$, $\delta_u=2.5$mm, $M_\infty=8.2$, $Re_\infty/m=9.35x10^6$.

A.4.12 Laminar flow, $\alpha=60°$, $\delta_u=2.5$mm, $M_\infty=8.2$, $Re_\infty/m=9.35x10^6$

x_k (mm)	y_{cl} (mm)	q (W/cm^2)	St (x10^3)	St/St_u
-5.5	0	8.6	1.5	3.7
-1.5	0	30.2	5.2	13.1
-5.5	4	7.5	1.3	3.3
-1.5	4	26.9	4.7	11.7
-5.5	8	7.5	1.3	3.2
-1.5	8	15.7	2.7	6.8
-5.5	12	6.5	1.1	2.8
-1.5	12	6.7	1.2	2.9

Table A.13 Heat flux measurements: laminar flow, $\alpha=60°$, $\delta_u=2.5$mm, $M_\infty=8.2$, $Re_\infty/m=9.35x10^6$.

A.4.13 Laminar flow, $\alpha=90°$, $\delta_u=2.5$mm, $M_\infty=8.2$, $Re_\infty/m=9.35x10^6$

x_k (mm)	y_{cl} (mm)	q (W/cm^2)	St (x10^3)	St/St_u
-5.5	0	14.5	2.5	6.3
-1.5	0	64.3	11.2	27.9
-5.5	4	10.6	1.8	4.6
-1.5	4	60.2	10.5	26.2
-5.5	8	8.6	1.5	3.7
-1.5	8	29.1	5.1	12.6
-5.5	12	7.6	1.3	3.3
-1.5	12	7.8	1.4	3.4

Table A.14 Heat flux measurements: laminar flow, $\alpha=90°$, $\delta_u=2.5$mm, $M_\infty=8.2$, $Re_\infty/m=9.35x10^6$.

A.4.14 Laminar flow, $\alpha=135°$, $\delta_u=2.5$mm, $M_\infty=8.2$, $Re_\infty/m=9.35x10^6$

x_k (mm)	y_{cl} (mm)	q (W/cm^2)	St (x10^3)	St/St_u
-7.5	0	16.6	2.9	7.2
-5.5	0	46.8	8.1	20.3
-3.5	0	129.8	22.5	56.4
-1.5	0	30.2	5.2	13.1
-7.5	4	13.6	2.4	5.9
-5.5	4	36.8	6.4	16.0

-3.5	4	132.7	23.1	57.6
-1.5	4	39.4	6.9	17.1
-7.5	8	7.8	1.4	3.4
-5.5	8	13.2	2.3	5.7
-3.5	8	51.0	8.9	22.2
-1.5	8	28.7	5.0	12.5
-7.5	12	7.2	1.3	3.1
-5.5	12	7.6	1.3	3.3

Table A.15 Heat flux measurements: laminar flow, α=135°, δ_u=2.5mm, M_∞=8.2, $Re_\infty/m=9.35x10^6$.

A.4.15 Turbulent flow, α=30°, δ_u=5mm, M_∞=8.2, $Re_\infty/m=8.06x10^6$

x_k (mm)	y_{cl} (mm)	q (W/cm^2)	St (x10^3)	St/St$_u$
2.5	8	9.7	2.4	2.7
6.5	8	11.4	2.8	3.2
10.5	8	10.6	2.7	2.9
14.5	8	10.7	2.7	3.0
18.5	8	7.4	1.8	2.0
22.5	8	6.8	1.7	1.9
26.5	8	5.8	1.4	1.6
30.5	8	6.5	1.6	1.8
37.5	8	7.1	1.8	2.0
41.5	8	6.9	1.7	1.9
45.5	8	6.0	1.5	1.7
49.5	8	6.9	1.7	1.9
6.5	12	3.8	1.0	1.1
10.5	12	4.4	1.1	1.2
14.5	12	4.9	1.2	1.3
22.5	12	5.7	1.4	1.6
26.5	12	5.8	1.4	1.6
30.5	12	5.4	1.3	1.5
41.5	12	7.0	1.8	1.9
45.5	12	6.9	1.7	1.9
49.5	12	6.3	1.6	1.7

Table A.16 Heat flux measurements: turbulent flow, α=30°, δ_u=5mm, M_∞=8.2, $Re_\infty/m=8.06x10^6$.

A.4.16 Turbulent flow, α=45°, δ_u=5mm, M_∞=8.2, $Re_\infty/m=8.06x10^6$

x_k (mm)	y_{cl} (mm)	q (W/cm^2)	St (x10^3)	St/St$_u$
-5.5	0	7.1	1.8	2.0
-1.5	0	11.8	3.0	3.3
-5.5	4	6.9	1.7	1.9
-1.5	4	11.7	2.9	3.2
-5.5	8	6.4	1.6	1.8
-1.5	8	10.4	2.6	2.9
-5.5	12	4.5	1.1	1.2

Table A.17 Heat flux measurements: turbulent flow, α=45°, δ_u=5mm, M_∞=8.2, $Re_\infty/m=8.06x10^6$.

A.4.17 Turbulent flow, $\alpha=60°$, $\delta_u=5mm$, $M_\infty=8.2$, $Re_\infty/m=8.06x10^6$

x_k (mm)	y_{cl} (mm)	q (W/cm^2)	St (x10^3)	St/St$_u$
-5.5	0	9.9	2.5	2.7
-1.5	0	18.1	4.5	5.0
-5.5	4	9.2	2.3	2.6
-1.5	4	17.3	4.3	4.8
-5.5	8	8.7	2.2	2.4
-1.5	8	13.4	3.3	3.7
-5.5	12	7.6	1.9	2.1

Table A.18 Heat flux measurements: turbulent flow, $\alpha=60°$, $\delta_u=5mm$, $M_\infty=8.2$, $Re_\infty/m=8.06x10^6$.

A.4.18 Turbulent flow, $\alpha=90°$, $\delta_u=5mm$, $M_\infty=8.2$, $Re_\infty/m=8.06x10^6$

x_k (mm)	y_{cl} (mm)	q (W/cm^2)	St (x10^3)	St/St$_u$
-5.5	0	13.3	3.3	3.7
-1.5	0	42.1	10.5	11.6
-5.5	4	12.7	3.2	3.5
-1.5	4	40.9	10.2	11.3
-5.5	8	11.0	2.7	3.1
-1.5	8	23.5	5.8	6.5
-5.5	12	10.2	2.5	2.8

Table A.19 Heat flux measurements: turbulent flow, $\alpha=90°$, $\delta_u=5mm$, $M_\infty=8.2$, $Re_\infty/m=8.06x10^6$.

A.4.19 Turbulent flow, $\alpha=135°$, $\delta_u=5mm$, $M_\infty=8.2$, $Re_\infty/m=8.06x10^6$

x_k (mm)	y_{cl} (mm)	q (W/cm^2)	St (x10^3)	St/St$_u$
-7.5	0	17.3	4.3	4.8
-5.5	0	30.5	7.6	8.5
-3.5	0	69.0	17.2	19.1
-1.5	0	76.7	19.1	21.2
-7.5	4	14.5	3.6	4.0
-5.5	4	24.5	6.1	6.8
-3.5	4	60.3	15.0	16.7
-1.5	4	73.3	18.3	20.3
-7.5	8	11.8	2.9	3.3
-5.5	8	14.7	3.7	4.1
-3.5	8	30.5	7.6	8.4
-1.5	8	34.3	8.6	9.5
-7.5	12	11.5	2.9	3.2
-5.5	12	11.4	2.8	3.2

Table A.20 Heat flux measurements: turbulent flow, $\alpha=135°$, $\delta_u=5mm$, $M_\infty=8.2$, $Re_\infty/m=8.06x10^6$.

A.4.20 Transitional flow, $\alpha=30°$, $\delta_u=5mm$, $M_\infty=8.2$, $Re_\infty/m=6.57x10^6$

x_k (mm)	y_{cl} (mm)	q (W/cm^2)	St (x10^3)	St/St$_u$
2.5	8	4.1	1.7	4.3
6.5	8	4.2	1.8	4.4
10.5	8	4.4	1.8	4.6
14.5	8	4.6	1.9	4.8
18.5	8	3.6	1.5	3.7
22.5	8	4.1	1.7	4.3
26.5	8	4.7	2.0	4.9
30.5	8	6.0	2.5	6.3
37.5	8	5.3	2.2	5.6
41.5	8	5.9	2.5	6.1
45.5	8	5.4	2.2	5.6
49.5	8	5.0	2.1	5.2
6.5	12	1.5	0.6	1.5
10.5	12	2.1	0.9	2.1
14.5	12	2.3	0.9	2.4
22.5	12	2.5	1.0	2.6
26.5	12	2.8	1.2	2.9
30.5	12	2.8	1.2	2.9
41.5	12	3.3	1.4	3.5
45.5	12	3.4	1.4	3.5
49.5	12	3.2	1.3	3.4

Table A.21 Heat flux measurements: transitional flow, $\alpha=30°$, $\delta_u=5mm$, $M_\infty=8.2$, $Re_\infty/m=6.57x10^6$.

A.4.21 Transitional flow, $\alpha=45°$, $\delta_u=5mm$, $M_\infty=8.2$, $Re_\infty/m=6.57x10^6$

x_k (mm)	y_{cl} (mm)	q (W/cm^2)	St (x10^3)	St/St$_u$
-5.5	0	3.7	1.5	3.8
-1.5	0	5.6	2.3	5.8
-5.5	4	3.8	1.6	4.0
-1.5	4	5.9	2.5	6.2
-5.5	8	2.8	1.2	2.9
-1.5	8	4.7	2.0	4.9
-5.5	12	2.4	1.0	2.5

Table A.22 Heat flux measurements: transitional flow, $\alpha=45°$, $\delta_u=5mm$, $M_\infty=8.2$, $Re_\infty/m=6.57x10^6$.

A.4.22 Transitional flow, $\alpha=60°$, $\delta_u=5mm$, $M_\infty=8.2$, $Re_\infty/m=6.57x10^6$

x_k (mm)	y_{cl} (mm)	q (W/cm^2)	St (x10^3)	St/St$_u$
-5.5	0	5.2	2.2	5.4
-1.5	0	9.0	3.8	9.4
-5.5	4	5.3	2.2	5.5
-1.5	4	10.6	4.4	11.0

-5.5	8	3.9	1.6	4.1
-1.5	8	7.6	3.2	7.9
-5.5	12	3.4	1.4	3.6

Table A.23 Heat flux measurements: transitional flow, $\alpha=60°$, $\delta_u=5mm$, $M_\infty=8.2$, $Re_\infty/m=6.57x10^6$.

A.4.23 Transitional flow, $\alpha=90°$, $\delta_u=5mm$, $M_\infty=8.2$, $Re_\infty/m=6.57x10^6$

x_k (mm)	y_{cl} (mm)	q (W/cm^2)	St (x10^3)	St/St$_u$
-5.5	0	6.8	2.8	7.1
-1.5	0	22.7	9.5	23.6
-5.5	4	6.0	2.5	6.3
-1.5	4	20.9	8.7	21.8
-5.5	8	4.2	1.7	4.4
-1.5	8	12.3	5.1	12.8
-5.5	12	3.8	1.6	3.9

Table A.24 Heat flux measurements: transitional flow, $\alpha=90°$, $\delta_u=5mm$, $M_\infty=8.2$, $Re_\infty/m=6.57x10^6$.

A.4.24 Transitional flow, $\alpha=135°$, $\delta_u=5mm$, $M_\infty=8.2$, $Re_\infty/m=6.57x10^6$

x_k (mm)	y_{cl} (mm)	q (W/cm^2)	St (x10^3)	St/St$_u$
-7.5	0	7.7	3.2	8.0
-5.5	0	15.3	6.4	16.0
-3.5	0	37.4	15.6	39.0
-1.5	0	20.5	8.5	21.3
-7.5	4	5.8	2.4	6.1
-5.5	4	12.1	5.0	12.6
-3.5	4	39.5	16.5	41.2
-1.5	4	20.2	8.4	21.0
-7.5	8	4.6	1.9	4.8
-5.5	8	7.1	3.0	7.4
-3.5	8	18.0	7.5	18.8
-1.5	8	10.4	4.3	10.9
-7.5	12	4.3	1.8	4.5
-5.5	12	4.4	1.8	4.6

Table A.25 Heat flux measurements: transitional flow, $\alpha=135°$, $\delta_u=5mm$, $M_\infty=8.2$, $Re_\infty/m=6.57x10^6$.

A.4.25 Turbulent flow, $\alpha=15°$, $\delta_u=6mm$, $M_\infty=12.3$, $Re_\infty/m=3.35x10^6$

x_k (mm)	y_{cl} (mm)	q (W/cm^2)	St (x10^3)	St/St$_u$
18.5	8	0.7	0.8	0.8
22.5	8	0.7	0.9	0.9
26.5	8	0.7	0.8	0.8

30.5	8	0.8	0.9	0.9
37.5	8	0.7	0.8	0.8
41.5	8	0.7	0.8	0.8
45.5	8	0.7	0.8	0.8
49.5	8	0.7	0.8	0.8
18.5	10	1.4	1.6	1.6
22.5	10	1.5	1.8	1.8
26.5	10	1.6	1.9	1.9
30.5	10	1.7	2.0	2.0
37.5	10	1.7	2.0	2.0
41.5	10	1.6	1.9	1.9
45.5	10	1.6	1.9	1.9
49.5	10	1.7	2.0	2.0
18.5	12	0.9	1.0	1.0
22.5	12	0.9	1.1	1.1
26.5	12	1.2	1.4	1.4
30.5	12	1.3	1.5	1.5
37.5	12	1.7	2.0	2.0
41.5	12	1.8	2.1	2.1
45.5	12	1.9	2.2	2.2
49.5	12	1.9	2.2	2.2
22.5	14	0.8	0.9	0.9
26.5	14	0.8	1.0	1.0
30.5	14	0.8	1.0	1.0
41.5	14	0.8	1.0	1.0
45.5	14	1.0	1.1	1.1
49.5	14	0.9	1.1	1.1

Table A.26 Heat flux measurements: turbulent flow, α=15°, δ_u=6mm, M_∞=12.3, $Re_\infty/m=3.35x10^6$.

A.4.26 Turbulent flow, α=30°, δ_u=6mm, M_∞=12.3, $Re_\infty/m=3.35x10^6$

x_k (mm)	y_{cl} (mm)	q (W/cm^2)	St (x10^3)	St/St$_u$
-5.5	0	0.9	1.0	1.0
-1.5	0	0.7	0.8	0.8
-5.5	4	0.8	1.0	1.0
-1.5	4	0.7	0.8	0.8
-5.5	8	0.9	1.1	1.1
-1.5	8	0.7	0.9	0.9
2.5	8	0.9	1.0	1.0
6.5	8	0.9	1.1	1.1
10.5	8	0.9	1.1	1.1
14.5	8	0.9	1.0	1.0
18.5	8	0.9	1.0	1.0
22.5	8	0.9	1.1	1.1
26.5	8	0.9	1.1	1.1
30.5	8	1.0	1.1	1.1
37.5	8	0.8	1.0	1.0
41.5	8	1.0	1.2	1.2
45.5	8	0.8	1.0	1.0
49.5	8	0.9	1.0	1.0
2.5	10	0.7	0.9	0.9
6.5	10	1.2	1.4	1.4

10.5	10	1.5	1.7	1.7
14.5	10	1.6	1.8	1.8
18.5	10	2.0	2.3	2.3
22.5	10	2.0	2.4	2.4
26.5	10	2.0	2.3	2.3
30.5	10	2.0	2.4	2.4
37.5	10	2.3	2.7	2.7
41.5	10	2.3	2.7	2.7
45.5	10	2.1	2.5	2.5
49.5	10	2.2	2.5	2.5
-5.5	12	0.9	1.1	1.1
-1.5	12	0.9	1.1	1.1
2.5	12	0.7	0.8	0.8
6.5	12	0.6	0.7	0.7
10.5	12	0.8	0.9	0.9
14.5	12	0.9	1.1	1.1
18.5	12	1.1	1.3	1.3
22.5	12	1.2	1.4	1.4
26.5	12	1.4	1.6	1.6
30.5	12	1.4	1.7	1.7
37.5	12	1.4	1.6	1.6
41.5	12	1.4	1.6	1.6
45.5	12	1.5	1.7	1.7
49.5	12	1.4	1.6	1.6
2.5	14	0.6	0.7	0.7
6.5	14	0.5	0.6	0.6
10.5	14	0.5	0.6	0.6
14.5	14	0.5	0.6	0.6
18.5	14	0.8	1.0	1.0
22.5	14	0.8	0.9	0.9
26.5	14	0.9	1.1	1.1
30.5	14	0.9	1.1	1.1
37.5	14	0.9	1.1	1.1
41.5	14	1.0	1.2	1.2
45.5	14	1.1	1.3	1.3
49.5	14	1.1	1.3	1.3

Table A.27 Heat flux measurements: turbulent flow, $\alpha=30°$, $\delta_u=6mm$, $M_\infty=12.3$, $Re_\infty/m=3.35x10^6$.

A.4.27 Turbulent flow, $\alpha=45°$, $\delta_u=6mm$, $M_\infty=12.3$, $Re_\infty/m=3.35x10^6$

x_k (mm)	y_{cl} (mm)	q (W/cm^2)	St ($x10^3$)	St/St_u
-5.5	0	0.8	0.9	0.9
-1.5	0	1.4	1.6	1.6
-5.5	4	0.7	0.8	0.8
-1.5	4	1.4	1.6	1.6
-5.5	8	0.6	0.7	0.7
-1.5	8	0.9	1.0	1.0
2.5	8	1.2	1.4	1.4
6.5	8	1.0	1.2	1.2
10.5	8	1.0	1.1	1.1

14.5	8	1.0	1.2	1.2
-5.5	12	0.6	0.7	0.7
-1.5	12	0.6	0.7	0.7
2.5	12	0.6	0.7	0.7
6.5	12	0.7	0.8	0.8
10.5	12	0.9	1.0	1.0
14.5	12	1.0	1.2	1.2

Table A.28 Heat flux measurements: turbulent flow, $\alpha=45°$, $\delta_u=6mm$, $M_\infty=12.3$, $Re_\infty/m=3.35x10^6$.

A.4.28 Turbulent flow, $\alpha=60°$, $\delta_u=6mm$, $M_\infty=12.3$, $Re_\infty/m=3.35x10^6$

x_k (mm)	y_{cl} (mm)	q (W/cm^2)	St (x10^3)	St/St$_u$
-5.5	0	0.9	1.0	1.0
-1.5	0	1.9	2.2	2.2
-5.5	4	0.8	0.9	0.9
-1.5	4	2.0	2.3	2.3
-5.5	8	0.8	0.9	0.9
-1.5	8	1.5	1.7	1.7
-5.5	12	0.5	0.6	0.6
-1.5	12	0.7	0.8	0.8

Table A.29 Heat flux measurements: turbulent flow, $\alpha=60°$, $\delta_u=6mm$, $M_\infty=12.3$, $Re_\infty/m=3.35x10^6$.

A.4.29 Turbulent flow, $\alpha=90°$, $\delta_u=6mm$, $M_\infty=12.3$, $Re_\infty/m=3.35x10^6$

x_k (mm)	y_{cl} (mm)	q (W/cm^2)	St (x10^3)	St/St$_u$
-7.5	0	1.1	1.3	1.3
-5.5	0	1.4	1.6	1.6
-3.5	0	2.0	2.3	2.3
-1.5	0	3.5	4.1	4.1
-7.5	4	1.0	1.2	1.2
-5.5	4	1.4	1.7	1.7
-3.5	4	1.8	2.2	2.2
-1.5	4	4.4	5.2	5.2
-7.5	8	1.1	1.2	1.2
-5.5	8	1.1	1.3	1.3
-3.5	8	1.6	1.8	1.8
-1.5	8	2.9	3.4	3.4
-7.5	12	0.7	0.8	0.8
-5.5	12	0.8	1.0	1.0
-3.5	12	0.9	1.0	1.0
-1.5	12	0.8	1.0	1.0

Table A.30 Heat flux measurements: turbulent flow, $\alpha=90°$, $\delta_u=6mm$, $M_\infty=12.3$, $Re_\infty/m=3.35x10^6$.

A.4.30 Turbulent flow, α=135°, δ_u=6mm, M_∞=12.3, Re_∞/m=3.35x10^6

x_k (mm)	y_{cl} (mm)	q (W/cm^2)	St (x10^3)	St/St$_u$
-7.5	0	2.3	2.7	2.7
-5.5	0	4.4	5.2	5.2
-3.5	0	7.2	8.4	8.4
-1.5	0	1.2	1.5	1.5
-7.5	4	1.9	2.2	2.2
-5.5	4	3.6	4.2	4.2
-3.5	4	7.3	8.6	8.6
-1.5	4	1.9	2.3	2.3
-7.5	8	1.4	1.7	1.7
-5.5	8	2.5	2.9	2.9
-3.5	8	4.2	4.9	4.9
-1.5	8	2.5	2.9	2.9
-7.5	12	0.9	1.0	1.0
-5.5	12	1.0	1.2	1.2
-3.5	12	1.2	1.4	1.4
-1.5	12	2.0	2.4	2.4

Table A.31 Heat flux measurements: turbulent flow, α=135°, δ_u=6mm, M_∞=12.3, Re_∞/m=3.35x10^6.

APPENDIX B

Flow Visualisations

This appendix presents flow visualisations obtained during the investigation on the interference interaction induced by surface protuberances. Both surface oil visualisations and high-speed schlieren visualisations are shown. Although these techniques are not inherently 3-dimensional, their combined results provide qualitative evidence of the flow's 3-dimensionality.

B.1 Surface oil visualisations

Oil-dot surface visualisations were obtained to qualitatively determine the regions where the highest skin friction is present. Oil dots were placed on a 5mm x 5mm grid around the protuberance. Further details on the application of this technique in the present study can be found in Chapter 3.

B.1.1 Turbulent flow, $\alpha=30^{o}$, $\delta_u=5mm$, $M_\infty=8.2$, $Re_\infty/m=9.35x10^6$

Figure B.1 presents an oil-dot visualisation taken for the datum protuberance. The flow upstream of the protuberance remains practically undisturbed while most of the dots are slightly moved in the direction of the freestream flow therefore indicating the flow's two-dimensionality in this region. Oil dots are more markedly streaked to the side of the protuberance rather than ahead of it as expected from the higher heat flux measurements in this region. This provides qualitative evidence of the strong relation between skin friction and heat flux.

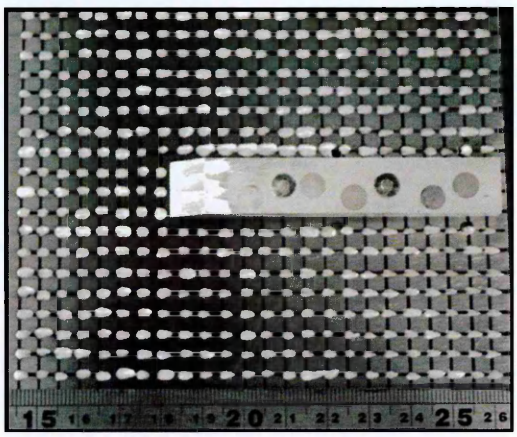

Figure B.1 Oil dot visualisation of datum configuration. Flow from left to right.

B.1.2 Turbulent flow, $\alpha=90°$, $\delta_u=5mm$, $M_\infty=8.2$, $Re_\infty/m=9.35x10^6$

An oil dot visualisation corresponding to the $\alpha=90°$ interaction is presented in Fig. B.2. In this case the interaction is supercritical and therefore the boundary layer separates ahead of the protuberance. There is a strong upstream influence which results in highly streaked oil dots especially close ahead of the model. These results, together with the corresponding schlieren images, provide further evidence of the particularly strong 3-dimensionality of these interactions. The location of boundary layer separation is not clear in the oil pattern due to the lower skin friction in the region of separating flow.

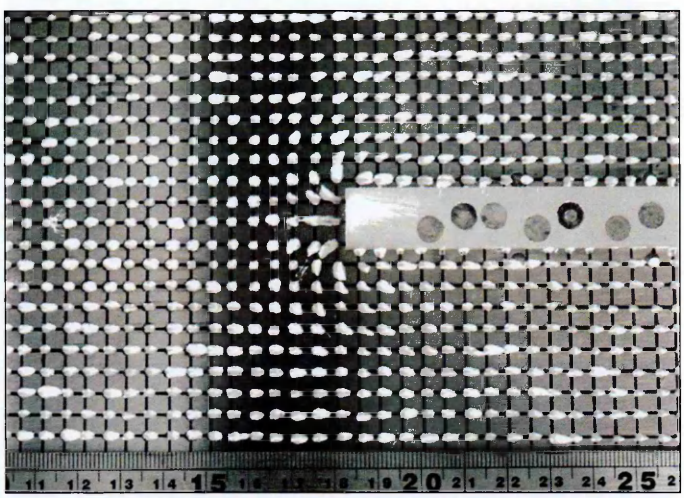

Figure B.2 Oil dot visualisation: turbulent, $M_\infty=8.2$, $Re_\infty/m=9.35x10^6$, $\alpha=90°$. Flow from left to right.

B.1.3 Turbulent flow, α=135°, δ_u=5mm, M_∞=8.2, $Re_\infty/m=9.35x10^6$

An oil-dot visualisation of the α=135° protuberance is presented in Fig. B.3. A strong upstream influence is observed in a similar way as in the α=90° interaction, with highly streaked dots ahead of the model as well. A close-up view of the oil dots below the leading edge of the protuberance shows the departure of the flow in two directions in this case: downstream and upstream (Fig. B.4). In order to image this effect, the protuberance was removed to obtain the close-up photograph and the 90° model was placed instead in order to be able to observe the oil dots under the forward leading edge. Two contra-rotating recirculations are expected ahead of the protuberance as shown in Chapter 7.

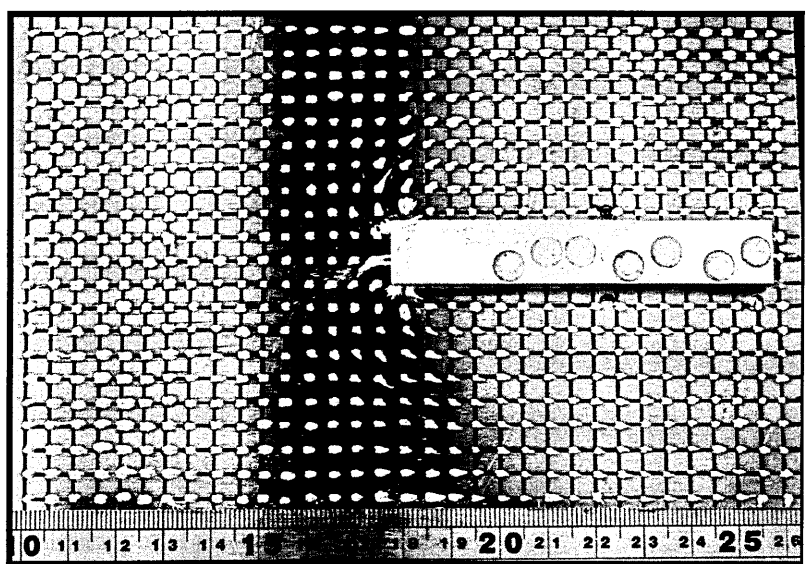

Figure B.3 Oil dot visualisation: turbulent, M_∞=8.2, $Re_\infty/m=9.35x10^6$, α=135°. Flow from left to right.

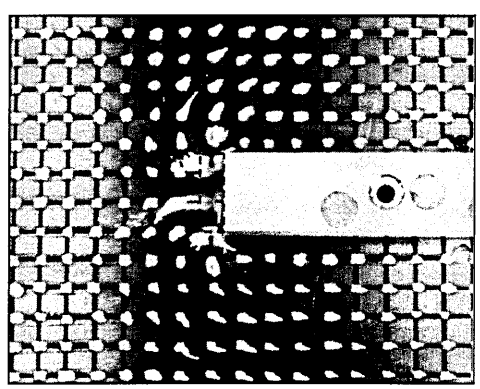

Figure B.4 Oil dot visualisation close-up view: turbulent, M_∞=8.2, $Re_\infty/m=9.35x10^6$, α=135°. Flow from left to right.

B.2 Schlieren image sequence

A complete sequence of schlieren visualisations is presented in this appendix in order to demonstrate the flow establishment during a typical gun tunnel run and also as a raw proof of the unsteady behaviour of the flow in supercritical interactions (Figs. B.5 to B.15). The configuration presented is the α=90° protuberance under turbulent flow with M_∞=8.2, $Re_\infty/m=9.35x10^6$. The images in this case were obtained at a frame rate of 8000fps and with a resolution of 1024px x 256px.

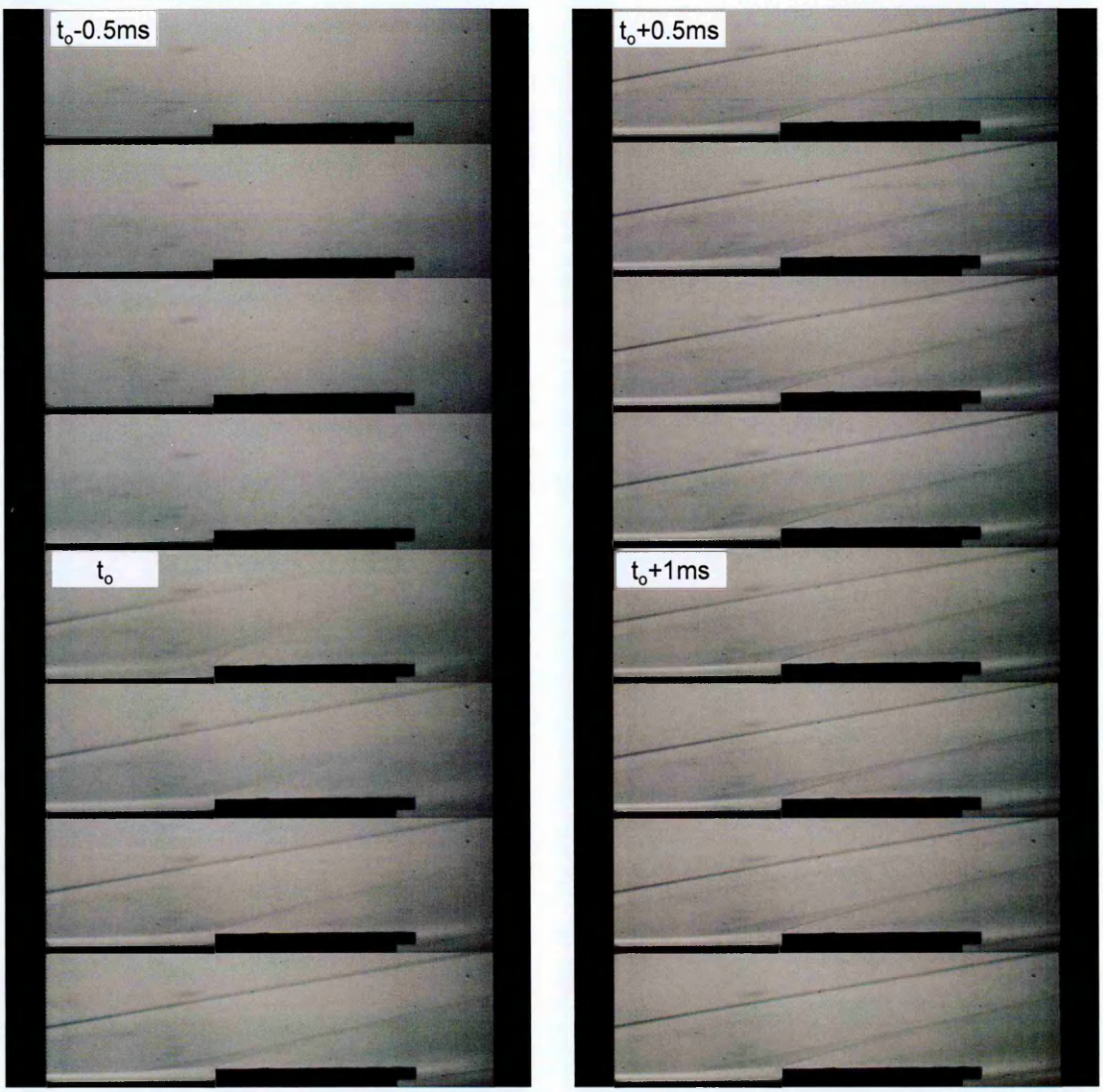

Figure B.5 Schlieren image sequence from t_o–0.5ms to t_o+1.375ms.

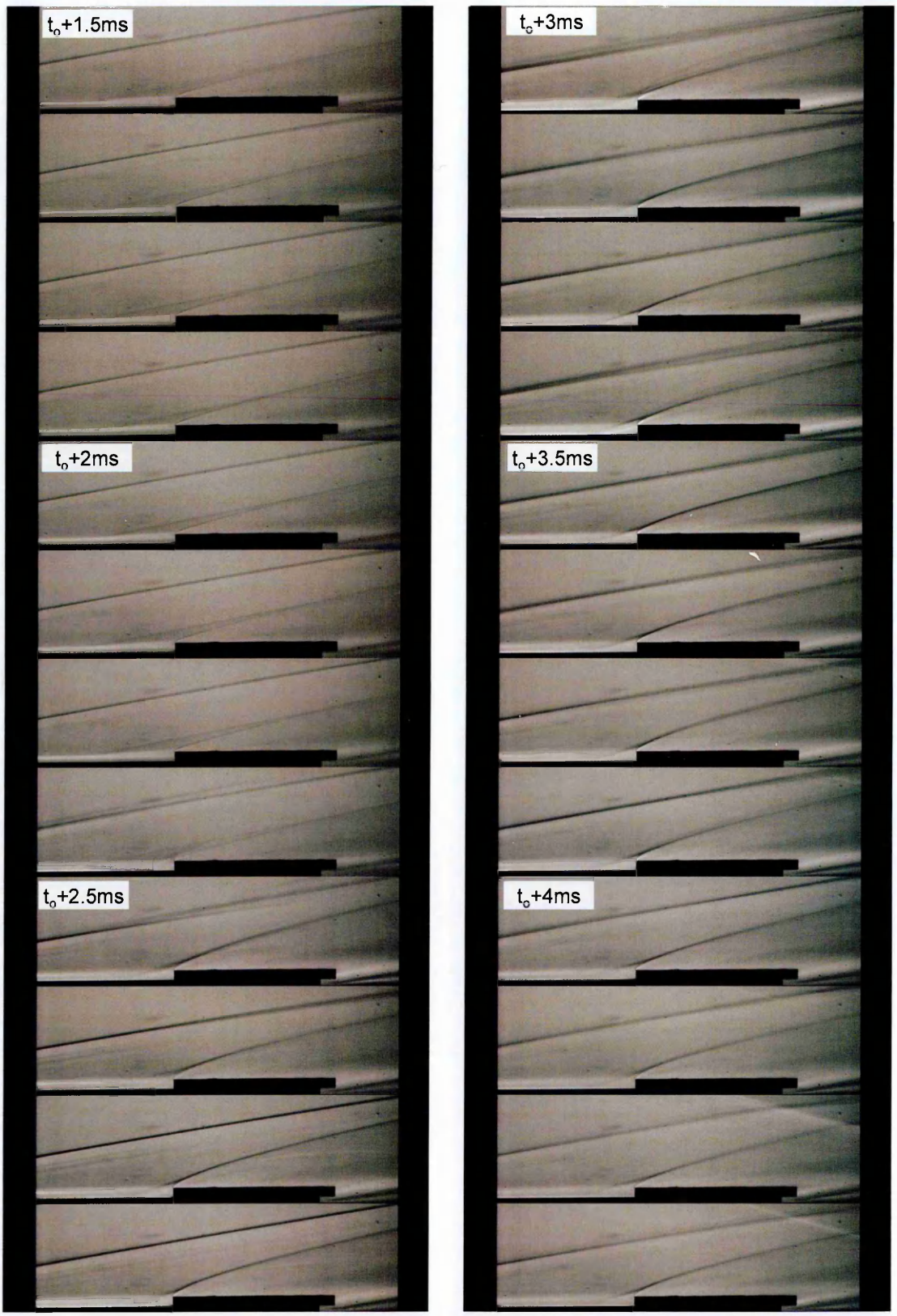

Figure B.6 Schlieren image sequence from t_o+1.5ms to t_o+4.375ms.

Figure B.7 Schlieren image sequence from t_o+4.5ms to t_o+7.375ms.

Figure B.8 Schlieren image sequence from t_o+7.5ms to t_o+10.375ms.

Figure B.9 Schlieren image sequence from t_o+10.5ms to t_o+13.375ms.

Figure B.10 Schlieren image sequence from t_o+13.5ms to t_o+16.375ms.

Figure B.11 Schlieren image sequence from t_o+16.5ms to t_o+19.375ms.

Figure B.12 Schlieren image sequence from t_o+19.5ms to t_o+22.375ms.

Figure B.13 Schlieren image sequence from t_o+22.5ms to t_o+25.375ms.

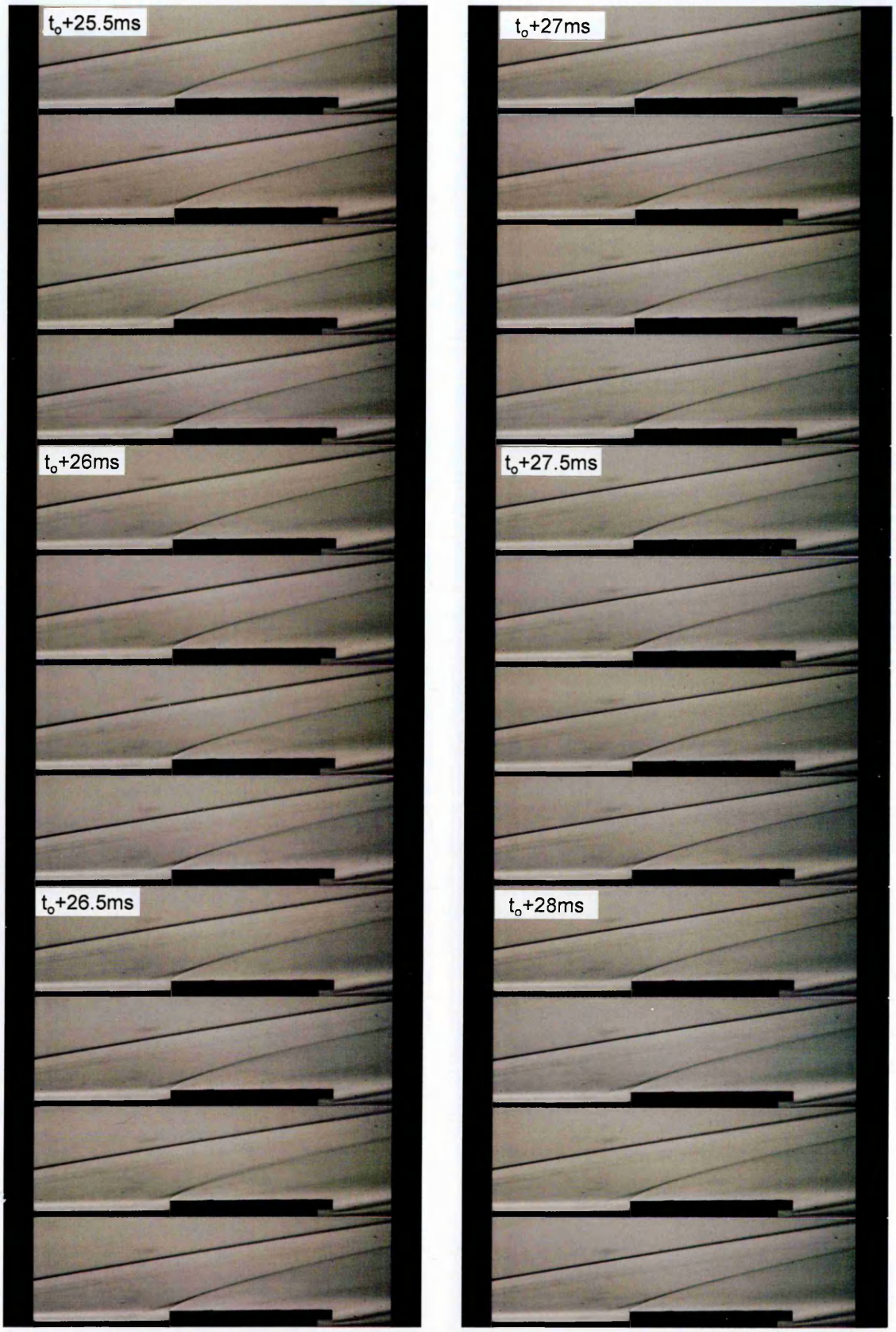

Figure B.14 Schlieren image sequence from t_o+25.5ms to t_o+28.375ms.

Figure B.15 Schlieren image sequence from t_o+28.5ms to t_o+31.375ms.

APPENDIX C

Uncertainty Analysis

An assessment of the uncertainties related to the present experimental work is presented in this appendix. The uncertainties are associated to the freestream wind tunnel conditions and to the location and magnitude of the measured heat transfer rates. The errors associated with the determined boundary layer thickness and separation length ahead of the supercritical protuberances are also briefly assessed. Further details on the methodology used to evaluate the present experimental uncertainties can be found in the book by Taylor (1992).

C.1 Freestream flow conditions

The freestream conditions of the working section flow in the Cranfield University gun tunnel are dominated by the following three parameters:

i. The tunnel drive pressure (P_D).

ii. The total temperature of the air in the reservoir (T_o).

iii. The Mach contoured nozzle being used (either Mach 8.2 or Mach 12.3).

As shown in Chapter 3, the drive pressure of the gun tunnel is changed in order to obtain different freestream Reynolds number conditions. This is regulated manually by the gun tunnel operator and there is therefore the possibility of human error. At the same time small air leaks can be expected in between the moment when the high-pressure pumps are stopped and until the tunnel blowdown is started. Based on past experience, the characteristics of the regulator system and the typically low decrease in the drive pressure observed during the operation of the tunnel result in an error estimate of ±20psig at a typical drive pressure of 2000psig, giving:

$$\frac{\delta(P_o)}{P_o} = \pm 1\% \quad \text{[Eq. C.1]}$$

The reservoir temperature of the facility was calculated by Needham (1965) and Opatowski (1967) at a range of driver pressure to barrel pressure ratios P_D/P_1 from 50 to 137. The total temperature during their tests was inferred from stagnation point heat transfer measurements on a hemispherical body using the stagnation point theory from Fay and Riddell (1959). Estimates were also based on the duration of the run and assuming chocked nozzle conditions. From their results, an uncertainty of 3% in the total temperature is considered:

$$\frac{\delta(T_o)}{T_o} = \pm 3\% \quad \text{[Eq. C.2]}$$

The two nozzles used in the present case were designed to provide nominal Mach numbers of 8.2 and 12.3. Calibrations of these nozzles were performed by Opatowski (1967, 1969) and by Ledford (1973) for the Mach 8.2 nozzle and by Mohammadian (1968) for the Mach 12.3 nozzle. Their calibrations showed a maximum uncertainty of 4%, however, this does not isolate the uncertainty in the nozzle but it also accounts for errors induced by the drive pressure (1%) and the total temperature (3%). In the more recent work by Fiala et al. (2006) in the Imperial College gun tunnel an estimate on the uncertainty of the Mach number was ±0.05 with respect to the nominal Mach number (Mach 8.9). It seems reasonable to estimate the same value in our case:

$$\delta(M_\infty) = \pm 0.05 \quad \text{[Eq. C.3]}$$

Based on the uncertainties associated with the drive pressure, temperature and Mach number (P_D, T_o and M_∞) the uncertainties in the freestream density, velocity and Reynolds number are assessed. The larger uncertainty margins are found at the minimum estimated Mach number (M_∞-0.05), minimum total temperature (T_o - 3%) and maximum drive pressure (P_D + 1%). The flow properties are derived from the corresponding compressible flow relations as shown in equations C.4 to C.7 and the freestream viscosity is evaluated from Sutherland's relation. The corresponding uncertainty margins are considered as listed in Table C.1. These estimates are clearly of a conservative nature.

$$T_\infty = \frac{T_o}{(1+\frac{\gamma-1}{2}M_\infty^2)} \qquad \text{[Eq. C.4]}$$

$$p_\infty = P_o(1+\frac{\gamma-1}{2}M_\infty^2)^{-3.5} \qquad \text{[Eq. C.5]}$$

$$\rho_\infty = p_\infty (RT_\infty)^{-1} \qquad \text{[Eq. C.6]}$$

$$U_\infty = M_\infty (\gamma RT_\infty)^{0.5} \qquad \text{[Eq. C.7]}$$

$$\mu_\infty = 1.458\times10^6 \frac{T_\infty^{1.5}}{T_\infty + 110.4} \qquad \text{[Eq. C.8]}$$

M_∞	P_D [MPa]	$T_{0,\infty}$ [K]	ρ_∞ [kg·m^{-3}]	U_∞ [m·s^{-1}]	Re_∞ / m [m^{-1}]
8.2±0.05	13.8 ± 1%	1290 ± 3%	0.0371 ± 7.1%	1553 ± 1.6%	9.35x10^6 ± 7.6%
8.2±0.05	10.3 ± 1%	1180 ± 3%	0.0304 ± 7.1%	1486 ± 1.6%	8.06x10^6 ± 7.7%
8.2±0.05	6.9 ± 1%	1040 ± 3%	0.0230 ± 7.1%	1395 ± 1.6%	6.57x10^6 ± 7.7%
12.3±0.05	13.8 ± 1%	1290 ± 3%	0.0054 ± 6.2%	1584 ± 1.5%	3.35x10^6 ± 7.5%

Table C.1 Experimental test conditions indicating conservative uncertainty margin.

C.2 Heat flux measurements

In the measurement of the heat flux in the vicinity of the protuberances distinction is made between the error related to the measurement location respect the protuberance and this related to the measured heat flux value.

C.2.1 Measurement location

Two main sources of error could be mainly related to the measurement location with respect to the protuberance: the machining accuracy in the manufacture of the test models and the possible human error in the placement of the models on the plate for all the different protuberance-plate arrangements. However, the human error in placing the models at the different flat plate positions is considered negligible since special care was at all times taken in ensuring the correct position of the flat plate and protuberance arrangements. The total error in measurement location is therefore attributed to machining accuracy only.

Models were made by means of a computer numerical controlled (CNC) machine with an expected accuracy of ±0.005mm. An image of a sample flat plate is shown in Fig. C.1 and a sample test model is shown in Fig. C.2 which corresponds to the datum protuberance (refer to Chapter 3). As shown in these technical drawings the protuberances had a number of holes in them which allowed placing them at different locations on the flat plate. A set of holes was also made on the plate which allowed for the different protuberance/flat plate arrangements. Considering an uncertainty of ±0.005mm in the drilling of the flat plate fixing points, model fixing points, and on the sharpening of the protuberance leading edge, the maximum location error is estimated:

$$\delta(d_T) = \sqrt{\left(\frac{\delta(d_{fp,holes})}{d_{fp,holes}}\right)^2 + \left(\frac{\delta(d_{prot,holes})}{d_{prot,holes}}\right)^2 + \left(\frac{\delta(d_{prot,le})}{d_{prot,le}}\right)^2} = \sqrt{3\times 0.005^2}\,mm \qquad \text{[Eq. C.9]}$$

$$\delta(d_T) = \pm 0.009mm \qquad \text{[Eq. C.10]}$$

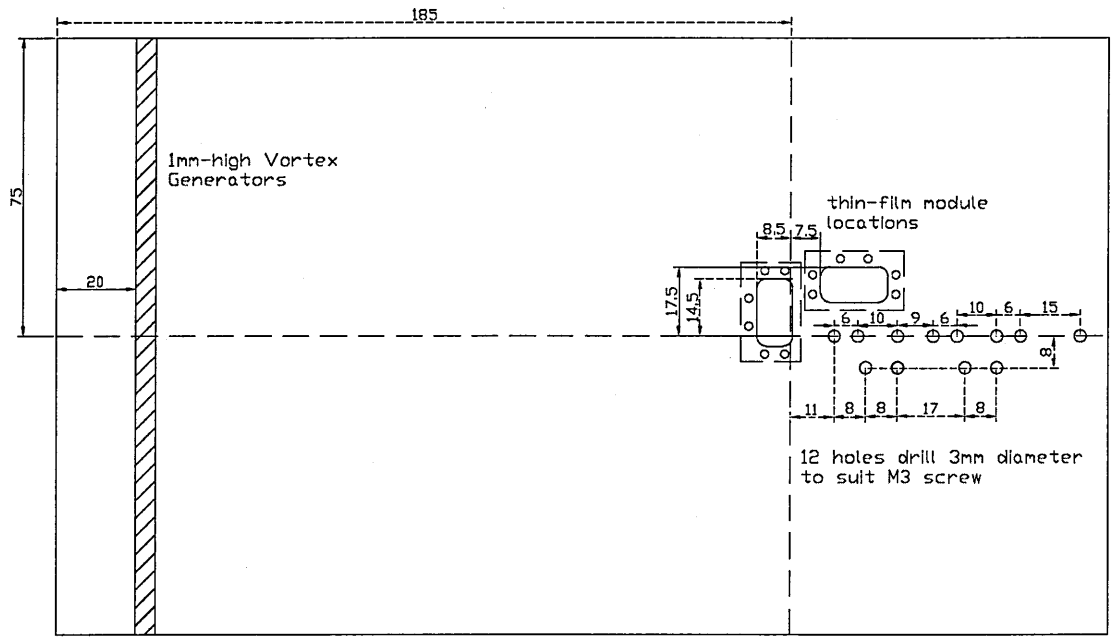

Figure C.1 Design of flat plate with vortex generators on.

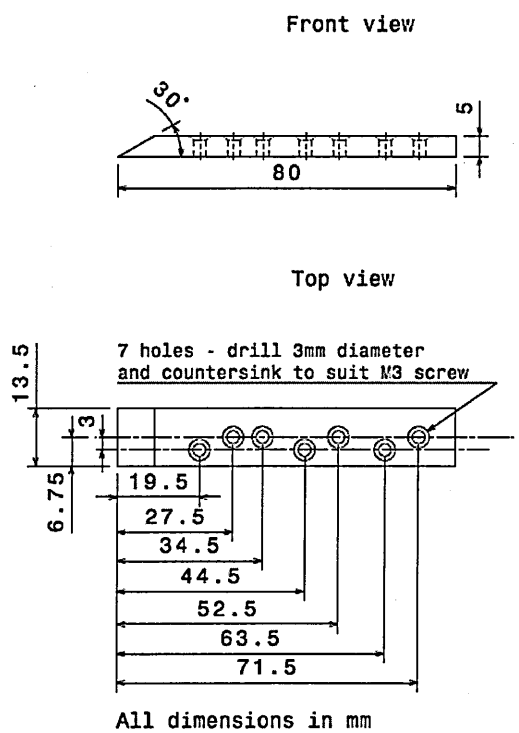

Figure C.2 Design of datum protuberance model.

C.2.2 Measured value

An evaluation of the systematic, statistical and repeatability errors follows.

C.2.2.1 Systematic error

The present measurement approach consisted in placing the protuberance models at different locations on the flat plate so that its relative distance to the gauges would provide a final distributed pattern of measurement points around the protuberance. While the change with respect to the centreline (y_{cl}) is not assumed to affect the local undisturbed heat flux due to the expected two-dimensionality of the flat plate in the lateral direction, the change of the protuberance between different longitudinal locations respect the flat plate leading edge (x_{le}) is expected to have an effect on the reference undisturbed heat flux. Along this direction, the protuberance was placed at different locations between x_{le}=157.5mm and x_{le}=192.5mm, i.e. x_{le}=175mm ±10%. As listed in Table C.2, based on the theory and on the computational results by Haas (2009), a maximum variation of ±2% is expected along this region:

$$\frac{\delta(q_u)}{q_u} = \pm 2\% \quad \text{[Eq. C.11]}$$

Arrangement case	Fixing points on plate x_{le} (mm)	Fixing points on model x_{le} (mm)	Model l.e. from plate l.e. (mm)
Protuberance closest to plate leading edge	202 & 221	44.5 & 63.5	157.5
Protuberance farthest from plate leading edge	212 & 237	19.5 & 44.5	192.5

Table C.2 Closest and farthest positions of the protuberance models respect the flat plate leading edge (l.e.).

		x_{le}=157.7mm	x_{le}=175mm	x_{le}=192.5mm	Error respect x_{le}=175mm
q (W/cm^2)	Cobalt	3.57	3.50	3.45	2%
	Fluent	3.64	3.60	3.56	1.1%
	Eckert	2.98	2.93	2.89	1.7%

Table C.3 Computational and theoretical estimates at these locations. Turbulent flow.

The heat flux was calculated based on the relation shown in Eq. C.12. This is therefore a function of the product or quotient of the following independent variables: $\left(\sqrt{\rho c_p k}\right)_g$, α_R, G, V_{out} and V_0 (Eq. C.13).

$$q = \left(\sqrt{\rho c_p k}\right)_g \frac{1}{\alpha_R V_0} \frac{V_{out}}{G} \quad \text{[Eq. C.12]}$$

.

$$q = f(\left(\sqrt{\rho c k}\right)_g, \alpha_R, G, V_{out} V_0) \quad \text{[Eq. C.13]}$$

Assuming that the measured heat flux is restricted by the uncertainties involved in the derivation of each of these variables - $\delta\left(\sqrt{\rho c_p k}\right)$, $\delta(\alpha_R)$, $\delta(G)$, $\delta(V_{out})$ and $\delta(V_0)$ - the uncertainty in percentage error in the measurement of q is given as:

$$\frac{\delta(q)}{q} = \pm\sqrt{\left(\frac{\delta(q_u)}{q_u}\right)^2 + \left(\frac{\delta\left(\sqrt{\rho c_p k}\right)}{\sqrt{\rho c_p k}}\right)^2 + \left(\frac{\delta(\alpha_R)}{\alpha_R}\right)^2 + \left(\frac{\delta(G)}{G}\right)^2 + \left(\frac{\delta(V_{out})}{V_{out}}\right)^2 + \left(\frac{\delta(V_o)}{V_o}\right)^2} \quad \text{[Eq.C.14]}$$

Hence, the corresponding individual uncertainties are analysed:

i. The calibration of the gauges was performed by the provider. The respective errors in the thermal product $\left(\sqrt{\rho c_p k}\right)_g$ and the thermal coefficient of resistivity α_T are the following:

$$\frac{\delta\left(\left(\sqrt{\rho c_p k}\right)_g\right)}{\left(\sqrt{\rho c_p k}\right)_g} = \pm 5\% \quad \text{[Eq. C.15]}$$

$$\frac{\delta(\alpha_T)}{\alpha_T} = \pm 2\% \quad \text{[Eq. C.16]}$$

ii. The systematic error on the gain G was evaluated during the calibration of the system:

$$\frac{\delta(G)}{G} = \pm 1.6\% \quad \text{[Eq. C.17]}$$

iii. The initial voltage V_o was monitored on the CONTECH analogue integrator and kept within 1% from the reference voltage:

$$\frac{\delta(V_o)}{V_o} = \pm 1\% \quad \text{[Eq. C.18]}$$

iv. As described in Chapter 3, the output voltage of the thin-film gauges goes through the analogue integrator circuit, the filter and the data acquisition board before being read in the computer (PC2). The errors relative to the analogue integrator and the filter were taken into account during the calibration of the system and are therefore included in the 1.6% error on the gain G. Hence the only error affecting V_{out} is the discretisation error that occurs when the signal is digitalised by the data acquisition board (DAQ) NI BNC-2110. Considering that the DAQ was set to read an output voltage in the range from -10V to 10V and the number of levels for a 16-bit discretisation, the error associated to the output voltage is:

$$\frac{\delta(V_{out})}{V_{out}} = \pm\frac{Range(V_{out})}{2^{16}} \times 100 = \pm\frac{20}{2^{16}} \times 100 = \pm 0.03\% \quad \text{[Eq. C.19]}$$

Following Eq. C.14 and based on these individual uncertainties, the systematic error associated to the measurement of the heat flux is as follows:

$$\frac{\delta(q)}{q} = \pm\sqrt{2^2 + 5^2 + 2^2 + 1.6^2 + 1^2 + 0.03^2} \approx \pm 6\% \quad \text{[Eq. C.20]}$$

In this work, the Stanton number is consistently used as a non-dimensional measure of heat flux. The uncertainties related to the freestream density, velocity and the drive temperature also need to be considered as shown in Section C.1. While the uncertainties related to the total temperature are already included within the freestream density and velocity uncertainties, the wall temperature variation during the tests needs to be accounted for (Eq. C.22). The atmospheric temperature during the tests was within 295±5K. Considering the wall temperature (T_w) equal to this, an uncertainty of 1.7% is calculated. The uncertainty in the Stanton number is therefore as follows:

$$\frac{\delta(St)}{St} = \pm\sqrt{\left(\frac{\delta(q)}{q}\right)^2 + \left(\frac{\delta(\rho_\infty)}{\rho_\infty}\right)^2 + \left(\frac{\delta(U_\infty)}{U_\infty}\right)^2 + \left(\frac{\delta(T_w)}{T_w}\right)^2} \qquad \text{[Eq. C.22]}$$

$$\frac{\delta(St)}{St} = \pm\sqrt{6^2 + 7.1^2 + 1.6^2 + 1.7^2} \approx \pm 9.5\% \qquad \text{[Eq. C.23]}$$

C.2.2.2 Statistical error

To calculate the heat flux a mean output voltage was measured during the effective run duration between 10ms and 20ms from the tunnel start as shown in Chapter 3. Hence it is also necessary to calculate the statistical error on V_{out}.

The statistical error was evaluated for the maximum and minimum experimental mean heat fluxes. The maximum heat flux in the present experiments was 132.73 W/cm^2 ahead of the turbulent α=135° protuberance at Mach 8.2 and $Re_\infty/m=9.35x10^6$. The minimum heat flux corresponded to the undisturbed boundary layer during the Mach 12.3 tests, which was 0.68 W/cm^2. The mean output voltage, standard deviation and standard deviation of the mean relative to these two cases are listed in Table C.4.

	$V_{out,m}[V]$	$\sigma_d[V]$	$\sigma_m[V]$
$q_{\max,m}$	0.61979	0.23822	0.00753
$q_{\min,m}$	0.00217	0.00326	0.00007

Table C.4 Statistical parameters for the maximum and minimum experimental turbulent heat fluxes.

The uncertainty on the mean values is thus estimated from the standard deviation of the mean. For the gauge the maximum heat flux measurement, 99.6% of the mean readings are expected to be within:

$V_{out,m} \pm 3\sigma_m$ that is 0.61979 ± 3 x 0.00753 at 99.6% confidence [Eq. C.24]

Similarly for the minimum heat flux measurement, 99.6% of the mean readings are included in:

$V_{out,m} \pm 3\sigma_m$ that is 0.00217 ± 3 x 0.00007 at 99.6% confidence [Eq. C.25]

In terms of heat transfer this is equivalent to:

$q_m \pm 3\sigma_m$ that is 132.73 ± 4.83 W/cm^2 at 99.6% confidence [Eq. C.26]

$q_m \pm 3\sigma_m$ that is 0.68 ± 0.02 W/cm^2 at 99.6% confidence [Eq. C.27]

Hence for a maximum and minimum heat fluxes the statistical errors are:

$$\left(\frac{\delta(q)}{q}\right)_{max} = \frac{4.83}{132.73} \times 100 \approx 3.5\% \text{ at 99.6\% confidence} \qquad \text{[Eq. C.28]}$$

$$\left(\frac{\delta(q)}{q}\right)_{min} = \frac{0.02}{0.68} \times 100 \approx 2.9\% \text{ at 99.6\% confidence} \qquad \text{[Eq. C.29]}$$

The error in both cases is very similar. For the following developments, the largest value is considered:

$$\left(\frac{\delta(q)}{q}\right)_{max} = \pm 3.5\% \quad \text{[Eq. C.30]}$$

C.2.2.3 Repeatability error

As shown in Section 4.3, a measure of the repeatability error was performed based on the heat flux measurements at the stagnation point of a hemisphere-cylinder forebody. Based on these three measurements, the system's repeatability was assessed to be within ±1.3%. That is in agreement with previous repeatability assessments performed in the same facility, which indicated a repeatability of 1.2% (Opatowski, 1967). The slightly higher error in the present study is considered:

$$\frac{\delta(R)}{R} = \pm 1.3\% \qquad \text{[Eq. C.31]}$$

C.2.2.4 Combined error

The total combined error accounts for the systematic, statistical and repeatability errors. The maximum uncertainty in the measurement of heat flux is thus considered as follows:

$$\frac{\delta(q)}{q} = \pm\sqrt{6^2 + 3.5^2 + 1.3^2} \approx \pm 7\% \text{ at 99.6\% confidence} \qquad \text{[Eq. C.32]}$$

In terms of Stanton number this is:

$$\frac{\delta(St)}{St} = \pm\sqrt{9.5^2 + 3.5^2 + 1.3^2} \approx \pm 10\% \text{ at 99.6\% confidence} \qquad \text{[Eq. C.33]}$$

As shown throughout the present investigation these measures are of a conservative nature.

C.3 Schlieren visualisations

A brief analysis of the uncertainties related to the calculation of the boundary layer thickness and the separation length upstream of supercritical interactions is also performed. As shown in Chapter 3, these features were extracted from the digital schlieren visualisations by means of digital image processing using the Matlab image processing toolbox.

C.3.1 Measurement of boundary layer thickness

The measured boundary layer thickness in the schlieren visualisations is affected by a number of factors. The principal factors include image resolution and the discrimination of the flat plate and boundary layer edges.

The image focus is very sensitive to small changes in the schlieren optical arrangement, including changes in the angle of the light source, camera, mirrors and other schlieren optics. The best possible focus was maintained throughout the experimental programme. As shown in Fig. C.3, where the protuberance height (h=5mm) and length (l=80mm) are taken as a reference, the image resolution was 5px/mm.

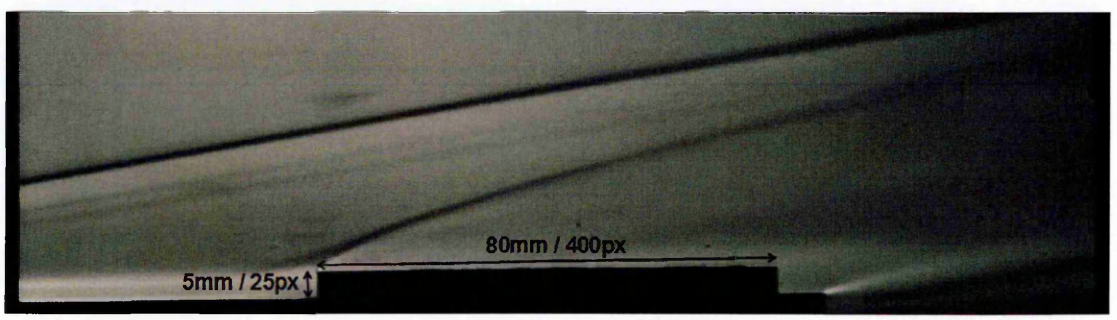

Figure C.3 Calculation of image resolution based on α=90° protuberance.

The error associated to the discrimination of the boundary layer edge varied between laminar and turbulent boundary layers. Transitional boundary layers look similar to turbulent boundary layers in the visualisations. The edge of the laminar boundary layer is very sharp and is determined within ±1 pixel accuracy, while in the turbulent boundary layer cases this is within ±3 pixel accuracy as shown in Figs. C.4 and C.5. Considering the image resolution, the margin in determining the boundary layer edge is:

$$\delta(bl_e) = \pm 0.2mm \text{ for a laminar boundary layer [Eq. C.34]}$$

$$\delta(bl_e) = \pm 0.6mm \text{ for a turbulent or transitional boundary layer [Eq. C.35]}$$

A ±1 pixel resolution (±0.2mm) in the discrimination of the flat plate edge needs also to be accounted for to assess the total uncertainty in determining the boundary layer thickness. The total uncertainties are therefore:

$$\delta(bl_{lam}) = 2.5 \pm 0.4mm = 2.5mm \pm 16\% \text{ for a laminar boundary layer} \quad [\text{Eq. C.36}]$$

$$\delta(bl_{turb}) = 5 \pm 0.8mm = 5mm \pm 16\% \text{ for a turbulent boundary layer} \quad [\text{Eq. C.37}]$$

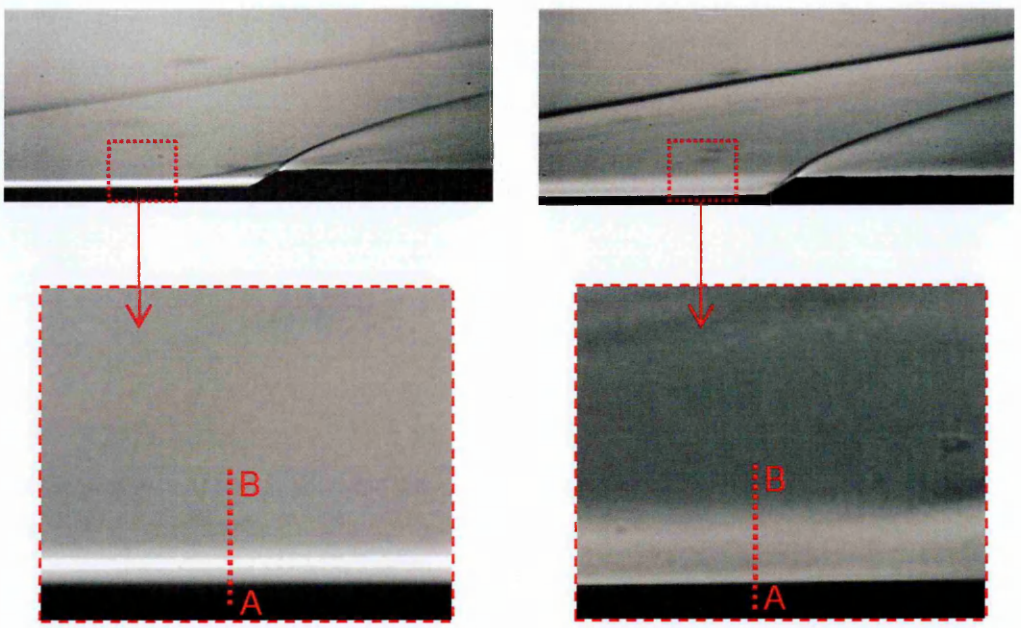

(a) Laminar flow (b) Turbulent flow

Figure C.4 Representative boundary layers, M_∞=8.2, Re_∞/m=9.35x10^6, α=30°. Line A-B is used in Fig. C.5.

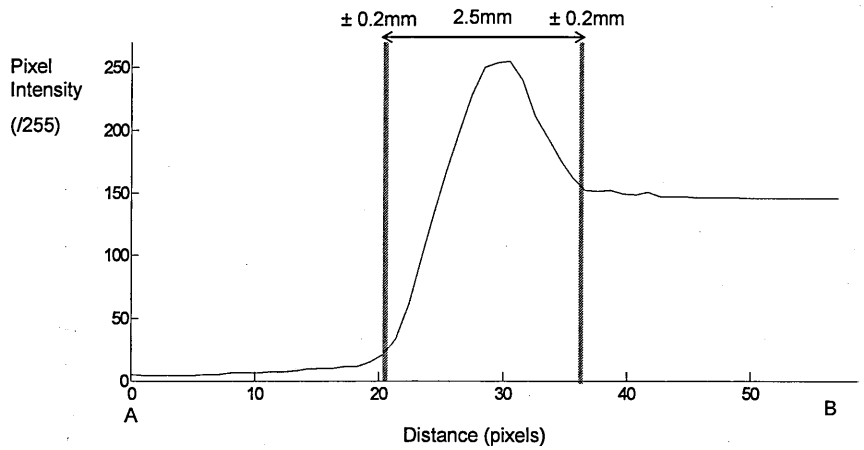

(a) Laminar boundary layer

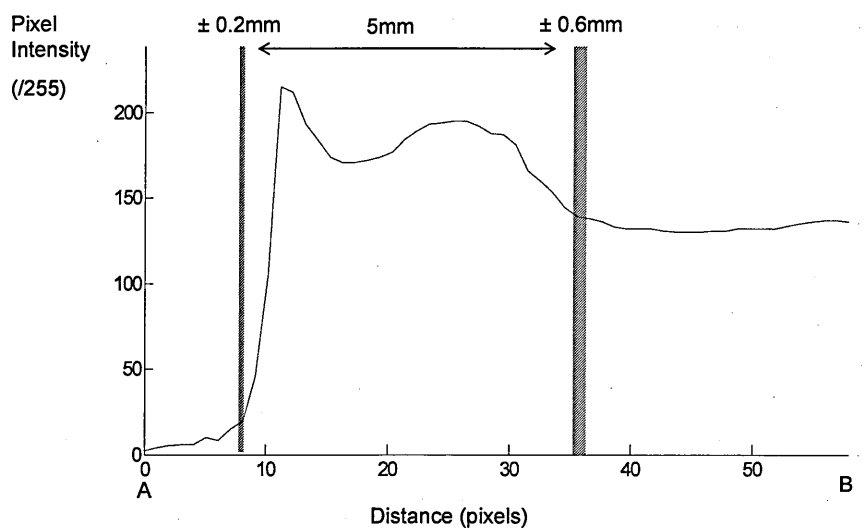

(b) Turbulent boundary layer

Figure C.5 Boundary layer profiles across lines A-B in Fig. C.5.

C.3.2 Measurement of separation length

The main difficulty in determining the separation length ahead of the protuberance is associated with the extrapolation of the separation shock wave, which cannot be clearly distinguished inside the boundary layer. While it is difficult to put an uncertainty to it, the estimation error is based on the maximum and minimum extrapolation margin as shown in Fig. C.6 for a reference supercritical interaction. Based on this analysis, a reasonable estimate is to assume a maximum uncertainty in the extrapolation of the separation shock wave of 10%. The calculation of the separation distance ahead of the protuberance is further compared with the corresponding heat flux measurement in Fig. C.6. In the present sample case the heat flux starts increasing between 24.5mm and 19.5mm and thus the method to calculate the separation length is shown to be within the specified margin based on the agreement with the separation length interpreted from the schlieren image, which is 23.8mm.

$$\frac{\delta(L)}{L} = \pm 10\% \quad \text{[Eq. C.38]}$$

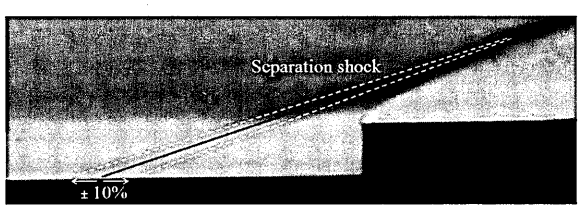

(a) Schlieren image

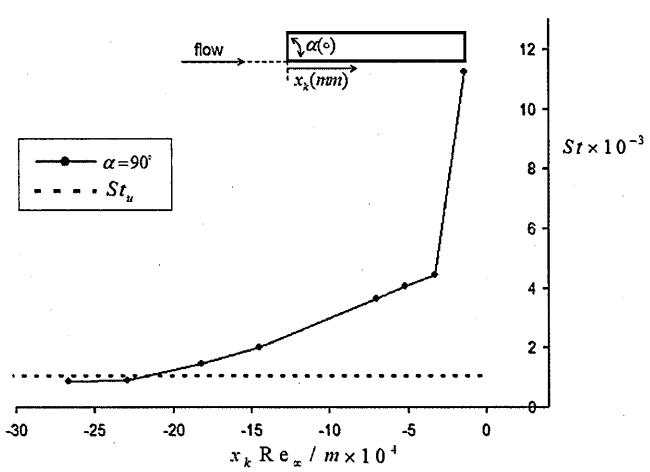

(b) Heat flux in front of the protuberance.

Figure C.6 Protuberance interactions: turbulent, M_∞=8.2, Re_∞/m=9.35x10^6, α=90°.

C.4 Summary

A list of selected uncertainties estimated within this analysis are summarised in Table C.5.

Measurement	Uncertainty
q	±7%
St	±10%
δ	±16%
L	±10%

Table C.5 Summary of uncertainty estimates

APPENDIX D

Comparison with CFD

A comparison between the present experimental results and the numerical simulations performed by Haas (2009) is presented in this appendix. Full-scale (1:1) Reynolds Averaged Navier-Stokes (RANS) simulations were carried out with the commercial code Cobalt. The datum test conditions of Mach 8.2 and $Re_\infty/m=9.35x10^6$ with a turbulent boundary layer ($\delta_u \approx 5mm$) were simulated and the $\alpha=30°$, $\alpha=60°$ and $\alpha=90°$ protuberances were considered.

D.1 Flow field

While the application of numerical simulations to hypersonic heat transfer studies is not established as yet, the main advantage of CFD is the large amount of qualitative information that can be obtained. In particular, information on the basic aspect of the flow field is of interest. For example, Fig. D.1 shows two temperature contours of the flow field in the symmetry plane along the protuberance centreline for the $\alpha=30°$ and the $\alpha=90°$ cases. These contours qualitatively demonstrate that the highest heat flux on the protuberances occur at the top of the leading edge face. The high temperatures in the separated flow region correspond to the cores of the embedded vortices and to the reattaching flow.

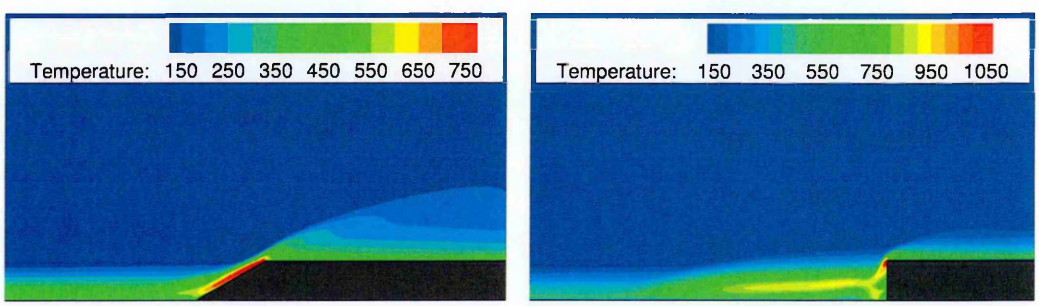

(a) $\alpha=30°$ (b) $\alpha=90°$

Figure D.1 Temperature contour in symmetry plane, in K.

The separation and reattachment of the flow in the present interactions has a strong effect on the surface heat flux. One of the principal flow features of supercritical interactions is the length of the separated region upstream of the protuberance. This varies significantly depending on the turbulence model employed. In this study, simulations were performed with three different turbulence models: the Spalart-Allmaras (SA), k-ω and k-ω Shear-Stress Transport (SST). A comparison of the predicted separation lengths L ahead of the protuberances is presented in Table D.1.

Case	α=30°	α=60°	α=90°
SA	2.5 ± 0.25mm	12 ± 0.25mm	16 ± 0.25mm
k- ω	8 ± 0.25mm	31 ± 0.25mm	35 ± 0.25mm
k- ω SST	6.5 ± 0.25mm	26 ± 0.25mm	31.5 ± 0.25mm
Experiments	0mm	19.3 ± 0.20mm	23.8 ± 0.25mm

Table D.1 Separation length ahead of the protuberances.

At the simulated conditions, the k-ω and k-ω SST models predict separation regions about twice as long as those predicted by the SA model. In Fig. D.2, two illustrations of the flow field show the difference between the SA and the k-ω SST predictions based on the flow streamlines along the symmetry plane. The flow field in the k-ω simulations was very similar to this predicted with the k-ω SST model given that both models use the same near wall formulation. While in the SA simulations the separation length is underpredicted by 30-40% with respect to the experiments, in the k-ω simulations this is overpredicted by 50%-60% and by 30-40% in the k-ω SST simulations. The k-ω SST turbulence model (Menter, 1993) therefore seems to be slightly more suitable than the k-ω model (Wilcox, 1992) in this case. The discrepancies between the separation lengths in the experiments and the numerical predictions with the SA and k-ω SST models are an indication of the high complexity in predicting such interactions. This is of particular importance in quasi-critical interactions (e.g. α=30° protuberance) since weak supercritical interactions can be interpreted to be subcritical and vice versa as found in the present case.

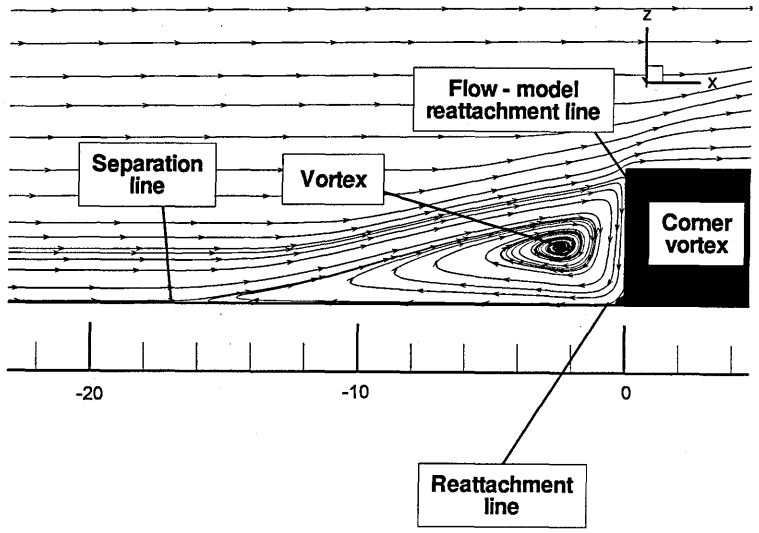

(a) SA turbulence model

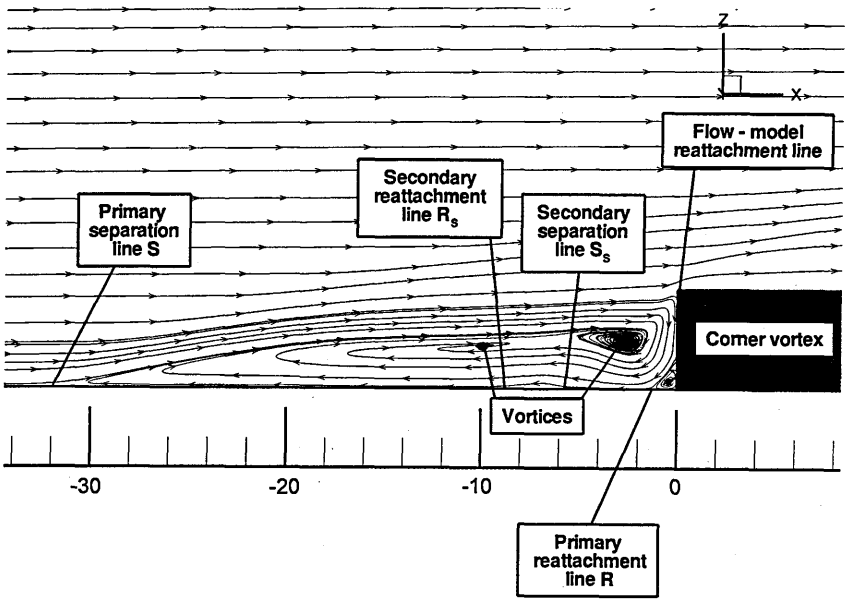

(b) k-ω SST turbulence model

Figure D.2 Flow separation ahead of supercritical protuberance.

D.2 Surface heat flux

One of the main simplifications of the present interactions was to assume symmetry conditions along the protuberance centreline as observed in the surface heat flux contours in the vicinity of the α=30°, α=60° and α=90° protuberances in Fig. D.3. A qualitatively good agreement with the present experimental results is observed: the highest heat flux induced by the α=30° protuberance is found to the side of the device and this induced by the α=60° and α=90° protuberances takes place ahead of the protuberance and with significantly higher values at the higher deflection angles. It is nevertheless noticed that a heat flux dip not observed during the experiments is predicted close to the centreline. This phenomenon is attributed to the symmetry conditions along the interaction centreline and is one of the principal faults of the numerical simulations. Such symmetry effects seem to disappear at distances far from the centreline (y_{cl}>4mm) in the contour plots, however, comparison with simulations considering the full protuberances showed large discrepancies in the prediction of the hot spot ahead of it (>100% higher than with the half protuberance).

The different turbulence models were also subject to significant discrepancies in the prediction of the heat flux along the separated flow region. In general, the SA model predicted larger peak heat transfer rates than the k-ω and k-ω SST models. However, the comparison between the predicted and measured peak fluxes is not straightforward given the simulated turbulence level was suspected not to match that reproduced using the vortex generators in the gun tunnel. While the present simulations were performed at a turbulence intensity of 0.1%, preliminary simulations at 10% turbulence intensity predicted undisturbed boundary layer heat flux rates 75% higher and with a very good agreement with the present experimental undisturbed heat flux. Due to time restrictions, simulations were only performed at the lower turbulence level but comparison with the present experimental results can be done by non-dimensionalising St with respect to St_u which is a general practice in similar studies. Comparison is also made in terms of Stanton number for completeness. A comparison of the numerical and experimental hot spots in the form of St_{max} and St_{max}/St_u is shown in Table D.2, where large discrepancies between the different turbulence models are observed in a similar way as in the prediction of the separation length ahead of the protuberance (Table D.1).

Case	St_u	α=30°		α=60°		α=90°	
		St_{max}	St_{max}/St_u	St_{max}	St_{max}/St_u	St_{max}	St_{max}/St_u
SA	0.54	1.38	2.56	8.62	15.96	22.97	42.54
k-ω SST	0.52	1.33	2.56	3.71	7.13	8.50	16.34
k-ω	0.48	1.41	2.94	3.76	7.83	9.64	20.08
Experiments	1.0	2.9	2.9	5.5	5.5	11.2	11.2

Table D.2 Comparison of highest heat flux in different protuberance cases.

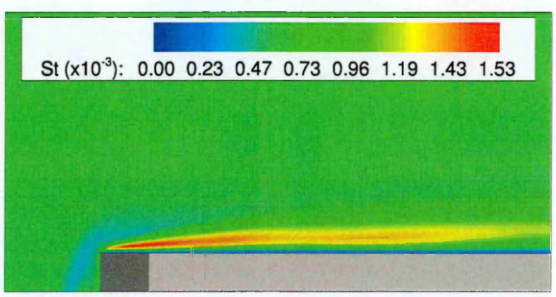

(a) α=30°

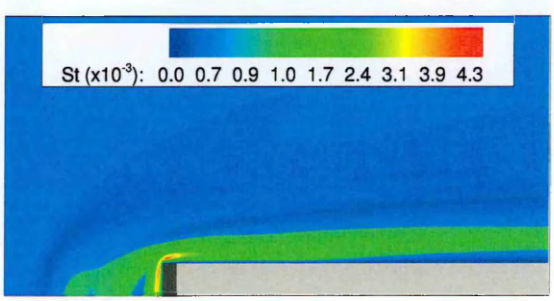

(b) α=60°

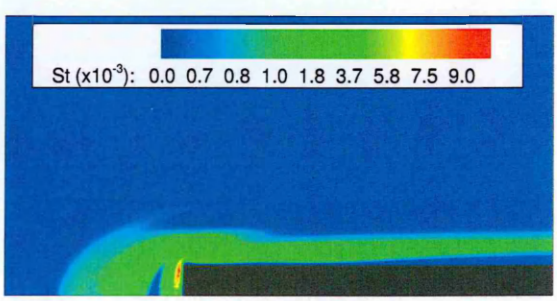

(c) α=90°

Figure D.3 Heat flux distribution in the vicinity of protuberances.

A full comparison of the experimental heat flux measurements in the vicinity of the α=30°, α=60° and α=90° protuberances with the numerical simulations is presented in Figs. D.6 – D.11 in the form of St and St/St_u. From these results it is observed that:

i. The prediction of the heat flux in the α=30° interaction is excellent in terms of St/St_u. However, in terms of St the experimental measurements are significantly larger than the numerical results.

ii. At the higher deflection angles (α=60° and α=90°) the opposite trend is observed: there is relatively good agreement in St form in the regions close to the protuberance (y_{cl}=0mm, 4mm, and 8mm) while far from the protuberance the best agreement is observed in the form of St/St_u.

These results further corroborate that there is a fundamental difference between the mechanisms which induce the hot spot ahead of supercritical interactions and those which induce the side hot spot in subcritical and weak supercritical interactions. Little confidence can be placed in the present numerical results due to the high sensitivity to turbulence model and boundary conditions, amongst a number of other factors. Hence, no further conclusions can be drawn with confidence.

To conclude, these simulations are a good example of the limitations of the current CFD capability to predict hypersonic heat transfer. While CFD is able to offer qualitative information from the flow, quantitative predictions are subject to very large uncertainties in cases of strong flow separation, and generally with insufficient accuracy for engineering applications. CFD is a promising tool which is benefitting from the constantly increasing computer power and from the generally easier use and lower costs in comparison to experimental studies, however, further advances in this area clearly rely on experimental investigations.

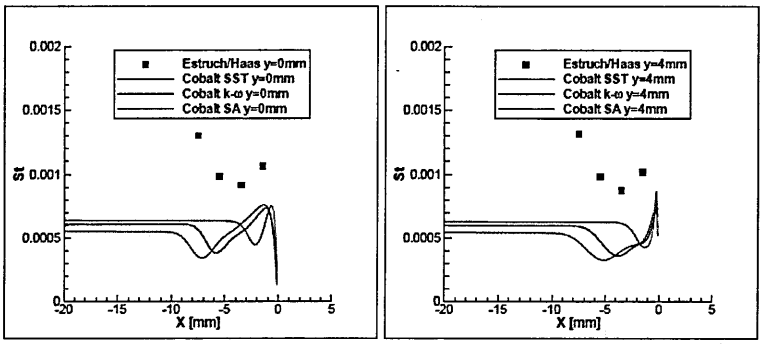

(a) y_{cl}=0mm (b) y_{cl}=4mm

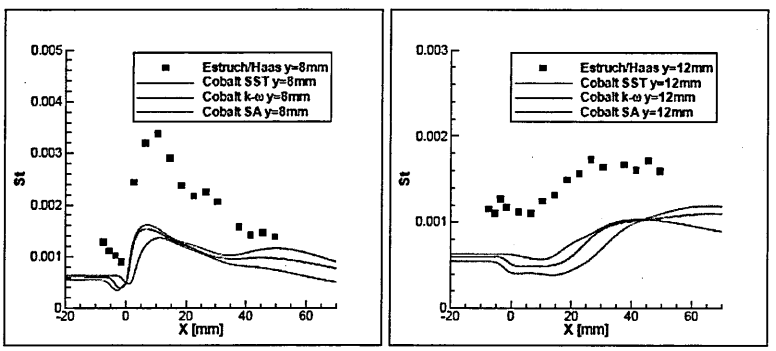

(c) y_{cl}=8mm (d) y_{cl}=12mm

Figure D.4 St in the vicinity of α=30° protuberance.

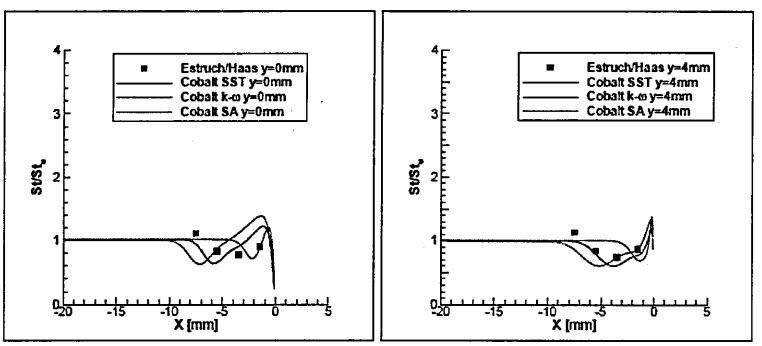

(a) y_{cl}=0mm (b) y_{cl}=4mm

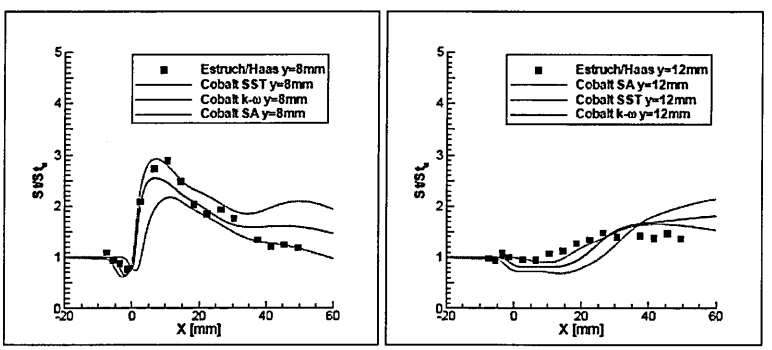

(c) y_{cl}=8mm (d) y_{cl}=12mm

Figure D.5 St/St_u in the vicinity of α=30° protuberance.

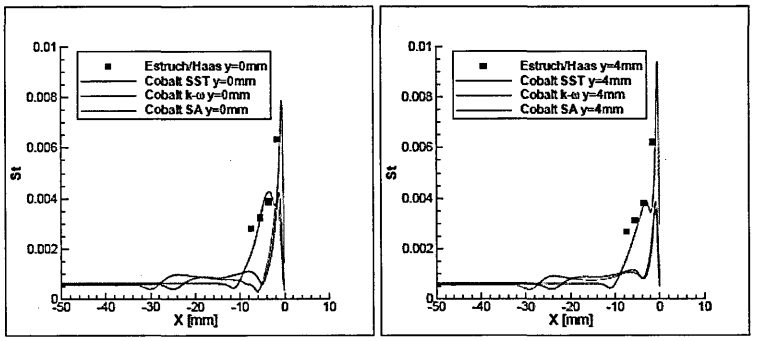

(a) y_{cl}=0mm (b) y_{cl}=4mm

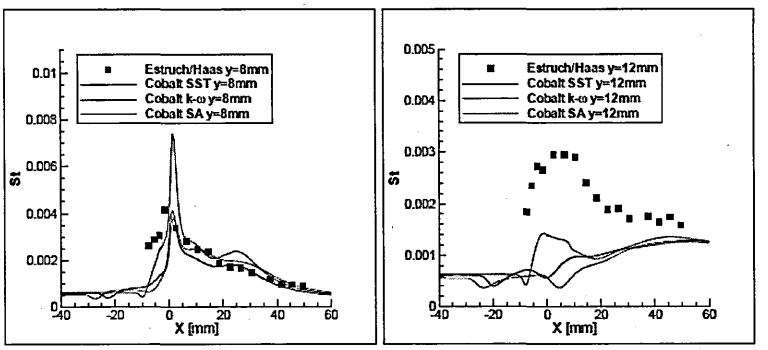

(c) y_{cl}=8mm (d) y_{cl}=12mm

Figure D.6 St in the vicinity of α=60° protuberance.

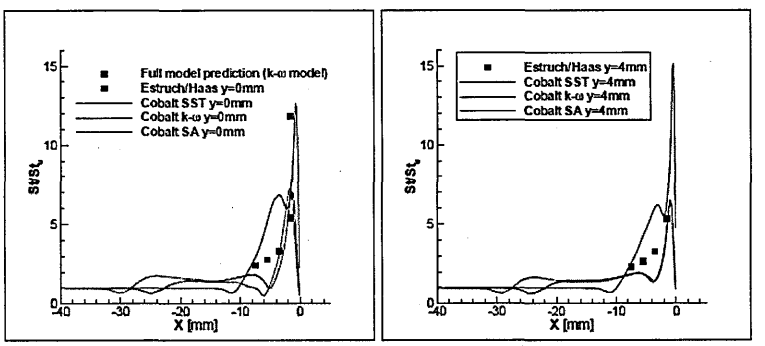

(a) y_{cl}=0mm (b) y_{cl}=4mm

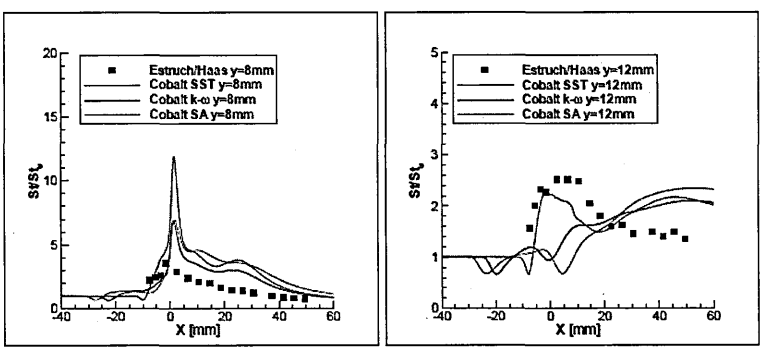

(c) y_{cl}=8mm (d) y_{cl}=12mm

Figure D.7 St/St_u in the vicinity of α=60° protuberance.

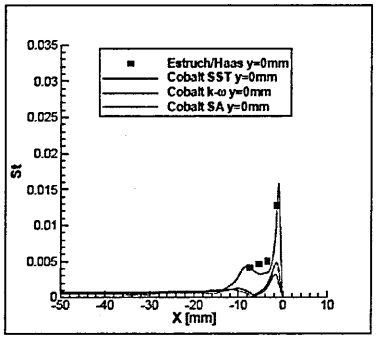

(a) y_{cl}=0mm

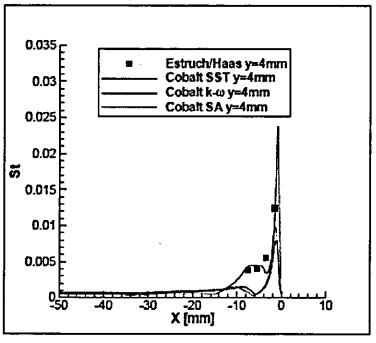

(b) y_{cl}=4mm

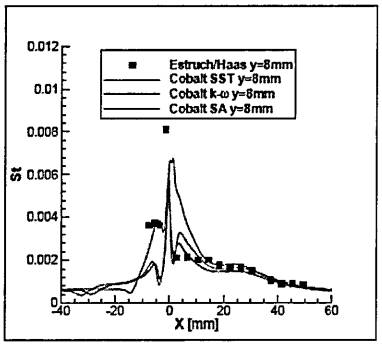

(c) y_{cl}=8mm

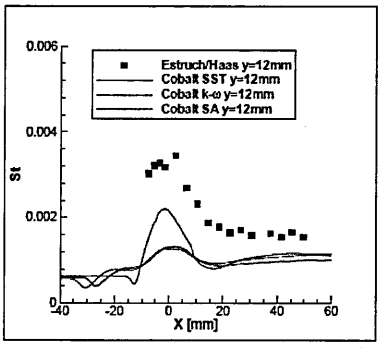

(d) y_{cl}=12mm

Figure D.8 St in the vicinity of α=90° protuberance.

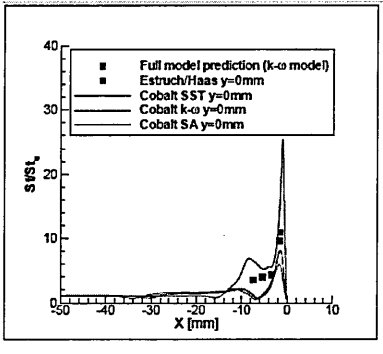

(a) y_{cl}=0mm

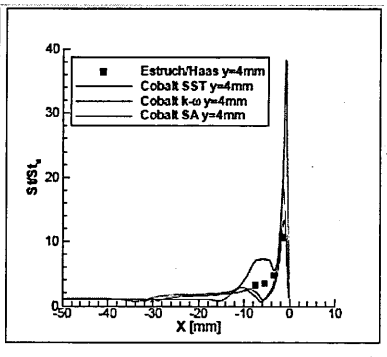

(b) y_{cl}=4mm

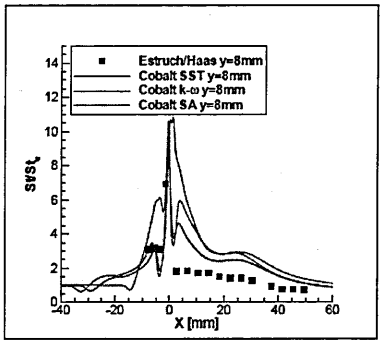

(c) y_{cl}=8mm

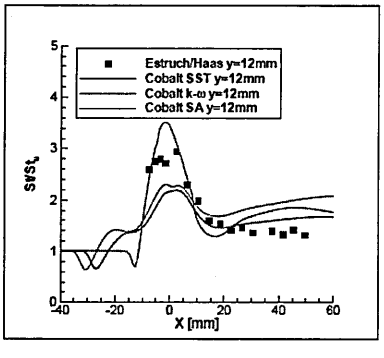

(d) y_{cl}=12mm

Figure D.9 St/St_u in the vicinity of α=90° protuberance.